

## Electrochemical activation of photo- and electrochemical water oxidation catalysts

Trzesniewski, Bartek

**DOI**

[10.4233/uuid:d01639ad-f2ab-40d8-ad29-0c86c31ff3f4](https://doi.org/10.4233/uuid:d01639ad-f2ab-40d8-ad29-0c86c31ff3f4)

**Publication date**

2018

**Document Version**

Final published version

**Citation (APA)**

Trzesniewski, B. (2018). *Electrochemical activation of photo- and electrochemical water oxidation catalysts*. [Dissertation (TU Delft), Delft University of Technology]. <https://doi.org/10.4233/uuid:d01639ad-f2ab-40d8-ad29-0c86c31ff3f4>

**Important note**

To cite this publication, please use the final published version (if applicable).  
Please check the document version above.

**Copyright**

Other than for strictly personal use, it is not permitted to download, forward or distribute the text or part of it, without the consent of the author(s) and/or copyright holder(s), unless the work is under an open content license such as Creative Commons.

**Takedown policy**

Please contact us and provide details if you believe this document breaches copyrights.  
We will remove access to the work immediately and investigate your claim.

# **Electrochemical activation of photo- and electrochemical water oxidation catalysts**

Bartłomiej Jacek “Bartek” TRZEŚNIEWSKI



# **Electrochemical activation of photo- and electrochemical water oxidation catalysts**

## **Proefschrift**

ter verkrijging van de graad van doctor  
aan de Technische Universiteit Delft,  
op gezag van de Rector Magnificus, Prof.dr.ir. T.H.J.J. van der Hagen,  
voorzitter van het College voor Promoties,  
in het openbaar te verdedigen op  
maandag 11 juni 2018 om 12:30 uur

door

Bartłomiej Jacek “Bartek” TRZEŚNIEWSKI  
Master of Science in Materials Science and Engineering,  
AGH University of Science and Technology, Polen  
geboren te Krakau, Polen



This dissertation has been approved by the promotor:

Dr. W.A. Smith

Prof. dr. B. Dam

Composition of the doctoral committee:

Rector Magnificus                      chairman

Dr. W.A. Smith                          Delft University of Technology, promotor

Prof. dr. B. Dam                        Delft University of Technology, promotor

Independent members:

Prof. dr. Ir. R. van de Krol            Helmholtz-Zentrum Berlin, Germany

Prof. dr. S. Gimenez                  Universitat Jaume I, Spain

Prof. dr. G. Mul                        University of Twente

Prof. dr. J.J.C. Geerlings            Delft University of Technology

Dr. A.J. Houtepen                    Delft University of Technology

Prof. dr. L.D.A. Siebbeles           Delft University of Technology, reserve member

Cover artwork: Vincent van Gogh, Wheatfield with Crows, July 1890

Credits: Van Gogh Museum, Amsterdam (Vincent van Gogh Foundation),  
in agreement with regulations for non-commercial use

ISBN number: 978-94-6186-932-6

Printed by GVO drukkers & vormgevers B.V.

© Bartłomiej Jacek “Bartek” Trześniewski, 2018

The work described in this thesis was carried out in the Materials for Energy Conversion and Storage (MECS) group, Department of Chemical Engineering, Faculty of Applied Sciences, Delft University of Technology. This research was funded by FOM/NWO (FOM TNW 10.327), under the agenda of the BioSolarCells consortium.

Dedykuję rodzicom i tym dwojgu,  
którzy odeszli



# Table of Contents

<b>1. Introduction.....</b>	<b>11</b>
1.1 Global Energy Landscape.....	11
1.2 Photoelectrochemical (PEC) water splitting .....	15
1.3 Bismuth vanadate ( $\text{BiVO}_4$ ) .....	18
1.3.1 Introduction .....	18
1.3.2 Overview of photoelectrochemical processes in $\text{BiVO}_4$ .....	20
1.3.3 Defining synthetic vs. post-synthetic modification .....	22
1.3.4 (a) Post-synthetic improvement of charge separation .....	24
1.3.4 (b) Post-synthetic removal of recombination sites .....	24
1.3.4 (c) Post-synthetic production of free carriers .....	27
1.3.4 (d) Summary .....	30
1.3.5 (b) Removal of surface recombination sites .....	31
1.3.5 (c) Near-surface doping and surface state alteration .....	33
1.3.5 (d) Summary .....	37
1.3.6 Theoretical limits.....	38
1.3.7 Post-synthetic treatments – overview .....	41
1.4 Electrochemical Water Oxidation.....	42
1.5 This Thesis.....	45
1.6 References .....	47
<b>2. Photocharged <math>\text{BiVO}_4</math> Photoanodes for Improved Solar Water Splitting ....</b>	<b>54</b>
2.1 Introduction.....	55
2.2 Experimental.....	57
2.2.1 Preparation of $\text{BiVO}_4$ thin film photoanodes .....	57
2.2.2 Photoelectrochemical (PEC) measurements.....	57
2.2.3 X-ray photoelectron spectroscopy (XPS).....	58
2.3 Results and Discussion.....	58

2.3.1 Photoelectrochemical (PEC) measurements .....	58
2.3.2 Photovoltage of BiVO <sub>4</sub> .....	62
2.3.3 Photocharged BiVO <sub>4</sub> .....	65
2.3.4 Material properties of photocharged BiVO <sub>4</sub> .....	68
2.4 Conclusions .....	70
2.5 Acknowledgements .....	71
2.6 References .....	71
<b>Appendix I .....</b>	<b>73</b>
Experimental .....	73
Preparation of BiVO <sub>4</sub> thin film photoanodes .....	73
Material characterization .....	74
Results .....	74
Table of contents (TOC) graphic .....	78
<b>3. Near-complete suppression of surface losses and total internal quantum efficiency in BiVO<sub>4</sub> photoanodes .....</b>	<b>79</b>
3.1 Introduction .....	80
3.2 Results and discussion .....	83
3.2.1 Influence of pH on PC BiVO <sub>4</sub> under illumination .....	83
3.2.2 Spectroscopic study of PC BiVO <sub>4</sub> .....	88
3.2.3 In-situ X-ray absorption spectroscopy (XAS) .....	92
3.2.4 Impedance Spectroscopy (IS) .....	94
3.3 Conclusions .....	100
3.4 Experimental .....	101
3.4.1 Preparation of BiVO <sub>4</sub> thin film photoanodes .....	101
3.4.2 Photoelectrochemical (PEC) measurements .....	102
3.4.3 In-situ UV-vis spectroscopy .....	103
3.4.4 Quantum Efficiency .....	103
3.4.5 X-ray absorption spectroscopy (XAS): X-ray absorption near edge structure (XANES) and Extended X-ray absorption fine structure (EXAFS) .....	103

3.4.6 Impedance Spectroscopy (IS) .....	104
3.4.7 Scanning Electron Microscopy (SEM) .....	104
3.4.8 X-ray photoelectron spectroscopy (XPS) .....	105
3.5 Acknowledgements .....	105
3.6 References .....	105
<b>Appendix II .....</b>	<b>109</b>
Preparation of BiVO <sub>4</sub> thin film photoanodes .....	109
Results .....	110
Broader Context and Table of contents (TOC) graphic .....	117
<b>4. In Situ Observation of Active Oxygen Species in Fe-Containing Ni-Based Oxygen Evolution Catalysts: The Effect of pH on Electrochemical Activity..</b>	<b>118</b>
4.1 Introduction .....	119
4.2 Experimental Section .....	121
4.2.1 Preparation of Ni(Fe)-B <sub>i</sub> and Ni(Fe)OOH thin films on FTO .....	121
4.2.2 Electrochemical performance of Ni(Fe)-B <sub>i</sub> and Ni(Fe)OOH thin films on FTO .....	122
4.2.3 UV-vis spectroscopy .....	122
4.2.4 Surface Enhanced Raman experiments .....	123
4.2.5 X-ray Absorption Spectroscopy .....	124
4.2.6 Atomic Force Microscopy (AFM) .....	125
4.2.7 X-ray Photoelectron Spectroscopy (XPS) .....	125
4.3 Results and Discussion .....	126
4.3.1 Cyclic voltammetry of nickel(II) hydroxide and nickel borate during electrochemical water oxidation in alkaline media .....	126
4.3.2 In situ electrochemical UV-vis spectroscopy of nickel(II) hydroxide and nickel borate during electrochemical water oxidation in alkaline media .....	128
4.3.3 In situ Surface Enhanced Raman Spectroscopy (SERS) of nickel(II) hydroxide and nickel borate during electrochemical water oxidation in alkaline media ....	130
4.3.4 In situ X-ray Absorption Spectroscopy measurements of nickel(II) hydroxide and nickel borate during electrochemical water oxidation in alkaline media ....	138

4.4 Conclusions .....	141
4.5 Acknowledgements .....	142
4.6 References .....	142
<b>Appendix III .....</b>	<b>145</b>
General .....	145
X-ray Photoelectron Spectroscopy (XPS) .....	148
Atomic Force Microscopy (AFM) .....	149
The pH dependence of the electrocatalytic activity of NiFe double hydroxide ..	150
Preparation NiFe double hydroxide (DH) .....	150
pH dependence of the NiFe DH activity towards oxygen evolution .....	151
Extended X-ray Absorption Fine Structure (EXAFS) results .....	152
References .....	154
<b>5. Summary .....</b>	<b>155</b>
<b>6. Samenvatting .....</b>	<b>159</b>
<b>7. Acknowledgements .....</b>	<b>164</b>
<b>8. List of Publications .....</b>	<b>167</b>
<b>9. Curriculum Vitae .....</b>	<b>169</b>

# 1. Introduction

## 1.1 Global Energy Landscape

Human beings are the most influential, intelligent and widespread animal species on planet Earth. Over the centuries we have invented and discovered: fire, the wheel, writing, printing, electricity, transistors and the internet. We have driven agricultural, industrial and digital revolutions. We know how to make advanced tools and art, how to learn and communicate, how to make science and philosophy. We have been to the moon and we have been to the depths of the oceans. We have revealed the secrets of DNA, created weapons of mass destruction and managed to find cures to many diseases. Looking at the big picture, one could ask, what was it that allowed us to achieve so much? And looking ahead, what is it that we need to survive and to thrive in the coming decades and centuries? In 2005 Nobel laureate in Chemistry Richard Smalley presented the "Top Ten Problems of Humanity for Next 50 Years" list,<sup>1</sup> on which he positioned Energy at the top place. Energy is the resource that enables taking care of any other task on the global scale. Indeed, if we had access to unlimited amounts of energy, a lot of the pending world problems could be easily resolved.

The world energy consumption has been steadily growing over the past decades. It currently equals to 17.6 TW and is projected to keep on increasing and to reach 30 TW in year 2050.<sup>2-5</sup> Part of this expected increase is due to the population growth. As of now there are approximately 7.6 billion people living on Earth. This number is expected to rise by 29 %, up to 9.8 billion in 2050, mostly due to developing countries in Asia and Africa.<sup>6</sup> Even more significantly, the cumulative global GDP

---

Part of this chapter has been published as: B. Lamm,\* B. J. Trześniewski,\* H. Döscher, W. A. Smith, M. Stefik, ACS Energy Lett. 2018, 3, 112–124, \*equal contribution, (10.1021/acsenergylett.7b00834)



growth between 2016 and 2050 is expected to reach 130%.<sup>7</sup> Importantly, the emerging economies are expected to grow at least twice faster than the advanced ones, resulting in a new global order, with China, India, Indonesia, Brazil, Mexico and Nigeria in the top 10 GDP-wise. Such a drastic increase in the overall global wealth will inevitably call for higher energy demand. But do we have enough resources to provide the western life-style to 10 billion people? Where to get all this extra energy from?

Currently, fossil fuels (oil, gas and coal) account for roughly 85 % of the world energy mix<sup>8</sup> (Figure 1a). Their proven reserves are sufficient for the next 50 (oil and gas) up to 150 years (coal), assuming the current status quo.<sup>4,5</sup> Moreover, so far the reserves have been growing roughly twice faster than the consumption, constantly postponing the final depletion date. But while we certainly have enough of fossil fuels for the current century, recovering those resources is becoming more economically strenuous. That is because a lot of the remaining reserves require expensive and complex excavation methods (deep water, arctic, unconventional oil, etc). In other words, most of what was easy to recover has already been burnt. But regardless of the accessibility, even if the remaining fossil fuels resources are sizable, they will still run out at some point in the future. And to facilitate a smooth energy transition the replacement strategies have to be ready fast.

Still, there is one far more important argument to stop using fossil fuels immediately: global climate change. Burning fossil fuels accounts for huge CO<sub>2</sub> emissions (36 GT in 2015),<sup>9,10</sup> which is a well-known greenhouse gas. The global atmospheric concentration of CO<sub>2</sub> has been growing rapidly in the last two centuries driven by human activities, initially at ~275 ppm to reach 412 ppm now<sup>11</sup> (Figure 1b). Global climate change has a number of serious consequences, such as: sea level rise, ocean acidification, more frequent and more severe extreme weather events (floods, draughts, hurricanes), reduced bio-diversity, and political and social unrest. Besides the harmful CO<sub>2</sub> emissions, burning fossil fuels also causes secondary air pollution (NO<sub>x</sub>, SO<sub>x</sub>, PM<sub>2.5</sub>, VOCs, Pb, Hg), which can directly be harmful to animal and plant life on Earth.

Consequently, to meet the future energy demands, to gradually terminate the consumption of fossil fuels, and to lower CO<sub>2</sub> emissions, a transition towards sustainable and clean energy sources is necessary. There is a number of possible green energy options to consider: wind, hydro, geothermal, biomass, nuclear and solar. Quite

likely all these different forms of renewable energy will be present in the future energy landscape, since different local conditions may favour different solutions. However, there is only one source that alone can provide us with all the energy we need – the Sun. 95 PW of solar energy reaches the Earth’s surface,<sup>12,13</sup> out of which 28 PW is accessible on land, which is roughly 1000 times more than our needs in 2050.

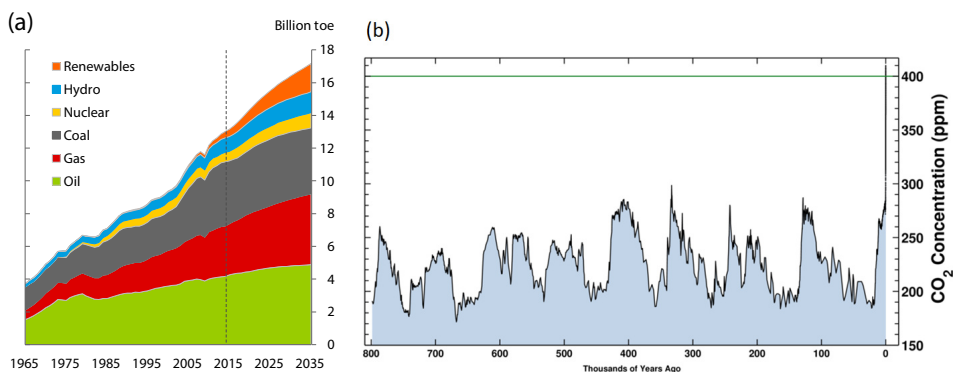


Figure 1. (a) Primary energy consumption by fuel<sup>4,5</sup> (b) The global average concentration of CO<sub>2</sub> in Earth's atmosphere<sup>11</sup>

The prices of photovoltaic (PV) systems have been falling steadily ever since the commercialization of the technology, driven by the scale effect. As a result, grid parity for PV-generated electricity had been reached by 19 countries by January 2014.<sup>14</sup> It is therefore natural to think, why don't we just cover all the deserts around the globe with PV panels and consider the problem solved? This introduces the biggest drawback of solar energy: it is intermittent. There is the day-night cycle, the seasonal cycle, and the random nature of cloud cover which can all curtail electricity generation from PV panels. Clearly, to ensure a sufficient supply of energy 24 hours a day, that is to compensate for the lack of Sun during the night and weak irradiation during the winters and cloudy days, a storage solution is necessary. Thus, solar energy captured during the sunny days can be used upon demand.

There are several available energy storage solutions, developed to different degrees: mechanical (pumped-storage hydroelectricity), electrical (supercapacitors), electrochemical (batteries), thermal and chemical (fuels). Arguably, no other solution can match the outstanding storage properties of fuels. Their gravimetric and

volumetric energy densities are several orders of magnitude higher than of any battery or capacitor. There are several possible fuels to consider: hydrogen, methane, methanol, higher order hydrocarbons, ammonia, etc. The carbon containing fuels seem to be an attractive solution from the standpoint of possible CO<sub>2</sub> capture and utilization (CCU). Besides, the carbon-based fuels are attractive because there already exists a global infrastructure set up for their use, thus all we need to do is change the feedstock/conversion technology, and deployment can happen immediately. However, even production of single-carbon compounds such as methane or methanol directly from CO<sub>2</sub> is very challenging. Such reactions involve transfer of 6 or 8 electrons and protons and very high inherent energy efficiency losses. Moreover, such reactions entail very complex pathways, going through multiple different intermediates, making the selectivity towards a single product a big challenge. Additionally, no large-scale atmospheric CO<sub>2</sub> capture technologies exist yet. Hydrogen on the other hand is the simplest fuel that one can imagine. It does not require any carbon source. The renewable production of hydrogen can be realized with the water splitting reaction. Water, just like sunlight, is one of the most abundant resources that we have on Earth and is therefore a great possible feedstock for the production of solar fuels (i.e. synthetic chemical fuels produced via solar to chemical energy conversion process). H<sub>2</sub> can be later combusted in a fuel cell, to efficiently produce water and electricity. However, when producing green hydrogen, we are not limited to using it as the final product. Once the CO<sub>2</sub> air capture technology becomes efficient, or simply considering concentrated CO<sub>2</sub> sources, H<sub>2</sub> and CO<sub>2</sub> can be combined in the reverse water-gas shift reaction to produce CO and H<sub>2</sub>O. CO with additional H<sub>2</sub> (syngas) can be further fed in the Fischer-Tropsch reaction to produce hydrocarbons. Thus, even if the utopian “hydrogen economy” vision does not come true, H<sub>2</sub> still has the potential to play a key role in the future energy storage technologies. More detailed considerations regarding the hydrogen production via electrochemical water splitting are presented in the next section.

Looking at the current energy landscape, there are several additional important issues to consider. Firstly, the share of energy used for electricity generation has increased drastically, from 26 % in 1965, up to 42 % in 2017, and is expected to continue increasing (47 % by 2035),<sup>4,5</sup> mostly due to rapidly growing demand in developing countries. This electrification trend gives solar technology the chance to offer non-centralized solutions for local communities where there is currently no

infrastructure at all. Consequently, this development may allow emerging economies to skip a fossil-based step in the electricity generation, in a similar way that some African countries went straight to mobile phones with no prior history of landlines. Secondly, some sectors requiring very high power densities are simply impossible to electrify. e.g. it is highly unlikely that fuel any other than liquid hydrocarbons will ever be used to power airplanes or large shipping vessels. Running some industrial plants purely on electricity also remains doubtful due to their high energy demands. Therefore, even if the sun was available 24/7, there still would be a need to store some of its energy in the form of a chemical fuel. Lastly, one should consider that the power output of solar-powered plants should be enough not only to produce all the electricity needed during the day, but also to store all the energy needed for the night-time electricity generation, and store the energy for the sectors which require a power source different than electricity. That implies that the target energy output for photo-driven plants lies way beyond that of fossil fuel powered ones. All in all, the renewable production of hydrogen via water splitting seems like an attractive solution to harvest the energy of the Sun, store it and release it upon demand.

## 1.2 Photoelectrochemical (PEC) water splitting

The water splitting reaction requires a moderate amount of energy to proceed and is therefore an attractive solution for energy storage. The overall reaction can be written as follows:



There are two major pathways to produce solar hydrogen via water splitting reaction: direct photoelectrochemical (PEC) and indirect PV + electrolysis routes. In this thesis, we focus on the former. PV + electrolysis remains an attractive alternative, and only the future will tell which of the two solutions will prevail on both technological and economic basis. Nonetheless, the PEC approach offers several advantages over the PV + electrolysis approach. Firstly, commercial electrolyzers typically operate at very high current densities, which generally require high

overpotentials and consequently decreased conversion efficiencies and low energy efficiency. Secondly, to provide voltages sufficient for electrolyzers, typically three Si PV cells need to be connected in series, therefore a lot more area and materials are necessary. Thirdly, electrolyzers are expensive since they use precious metal catalysts. Lastly, the PEC approach offers a possibility to combine all the functionalities in a single device which can give an advantage in terms of balance of systems, materials cost, and maintenance.

PEC water splitting is realised with a PEC cell, schematically presented in Figure 2a. In the most simple configuration a PEC cell consists of an n-type semiconducting photoanode and a metallic cathode, immersed in aqueous electrolyte and connected with an external wire. The key component of any PEC cell is the light active semiconducting photoelectrode, in our case a photoanode. The working principle of a PEC cell is as follows. Upon illumination with light, the semiconductor absorbs photons with energy higher than the bandgap ( $E_g$ ). Light absorption leads to charge generation: electrons from the valence band get excited to the conduction band, leaving positively charged holes behind. These charge carriers are then separated by drift and diffusion, driven by an internal electric field and charge gradients respectively. Next, they are transported to the corresponding electrode/electrolyte interfaces: holes towards the anode and electrons towards the cathode via the external circuit. Finally, the charge carriers are utilized to drive the catalytic reactions; holes oxidize water to evolve oxygen and electrons reduce water to produce hydrogen. The schematic of the process is shown in Figure 2b.

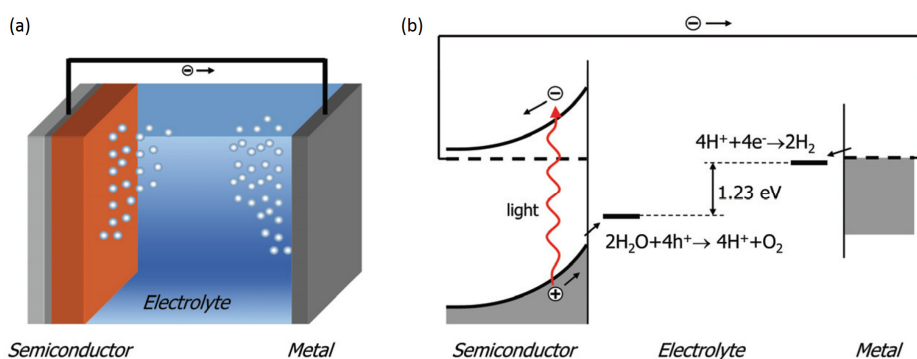
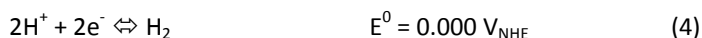


Figure 2. (a) Simple scheme of a PEC cell (b) band diagram of a PEC cell based on an n-type photoanode and metal counter electrode<sup>2</sup>

The two half reactions of water splitting occur on the spatially separated electrodes. In an alkaline electrolyte, the reduction and oxidation reactions proceed as follows:



For an acidic environment:



Thus, the thermodynamic potential to split water is 1.23 V (equivalent to light of 1008 nm). However, due to a number of loss mechanisms (electrolyte, contact and series resistances, inherent overpotentials), the potential needed to split water with reasonable efficiencies is closer to 1.9 V.<sup>15–17</sup> Looking at the two half-reactions of water splitting, the hydrogen evolution reaction (HER) can be regarded as more simple. It involves the transfer of two electrons and protons, and only a single intermediate. Significantly, catalysts that can drive this reaction with virtually no overpotential exist.<sup>18</sup> The oxygen evolution reaction (OER) is far more complex and troublesome. It involves the transfer of four electrons and protons, and three different intermediates. Consequently, OER typically proceeds far from the equilibrium potential of 1.23 V<sub>RHE</sub>. These inherently large overpotentials cause large energy losses in the overall water splitting process.<sup>18,19</sup>

Therefore, the understanding and improvement of the water oxidation half-reaction can be regarded as the biggest challenge in the field of water splitting. Only once we tackle all the bottlenecks in the OER, highly efficient solar water splitting can be realized to enable large-scale renewable energy storage. Accordingly, the following section of this chapter focuses on bismuth vanadate (BiVO<sub>4</sub>), a promising metal oxide photoanode material, widely studied for applications in the solar driven oxidation of water. Section 1.3 discusses all different post-synthetic approaches that have been demonstrated to improve its activity towards OER. Furthermore, section 1.4 looks at oxygen evolution catalysts (OECs), in particular nickel oxyhydroxide (Ni(Fe)OOH), the

best OEC based on cheap earth-abundant elements, working in alkaline media. In both sections we pay special attention to focus not on the materials alone, but on the electrochemical system as a whole, i.e. the material and the electrochemical environment it is surrounded by. We believe that much too often the materials are studied and optimized in conditions chosen in an arbitrary way. Meanwhile, electrolytes of different composition and different pH can significantly change the properties and performance (i.e. activation, stability, selectivity) of the electrodes, and therefore greatly affects the perspective to use them in a future device. Thus, we take a broader view and look at the electrode + electrolyte system as a whole, in an effort to understand how electrochemical environment affects the (currently) most active metal oxide photoanodes ( $\text{BiVO}_4$ ) and the most active OECs ( $\text{Ni(Fe)OOH}$ ).

## 1.3 Bismuth vanadate ( $\text{BiVO}_4$ )

### 1.3.1 Introduction

Monoclinic bismuth vanadate ( $\text{BiVO}_4$ ) is a promising and widely studied photoanode for solar-assisted water splitting,<sup>20,21</sup> made from cheap source compounds.  $\text{BiVO}_4$  has an indirect bandgap energy of approximately 2.4-2.5 eV (~500-520 nm band edge),<sup>22,23</sup> with absorption into the visible and UV range of light, and with a maximum theoretical photocurrent of  $\sim 7 \text{ mA cm}^{-2}$  under 1 sun AM 1.5G illumination. Additionally, a wider direct bandgap (ca. 2.7 eV) is also present in  $\text{BiVO}_4$ .<sup>23</sup> The conduction band edge (CB) lies near 0  $V_{\text{RHE}}$  (versus reversible hydrogen electrode), placing the valence band edge (VB) near 2.4  $V_{\text{RHE}}$ , and providing significant excess potential for holes to photooxidize water while electrons maintain a potential appropriate for hydrogen evolution at the counter electrode with moderate external bias. A thorough review of  $\text{BiVO}_4$  photoelectrochemical (PEC) properties and challenges was recently published.<sup>22</sup> Post-synthetic treatments have recently emerged as a way to significantly improve PEC performance with treatments that occur after the synthesis of electrodes. These post-synthetic treatments are based upon illumination, chemistry, electrochemistry, or combinations thereof, improving the PEC performance

of active materials in ways that typically cannot be achieved via direct fabrication methods. This section highlights recent findings with BiVO<sub>4</sub> post-synthetic treatments and identifies important avenues of future inquiries.

The efficiency of solar fuels production requires consideration of both the photocurrent and the applied voltage bias. The role of photocurrent is apparent and linearly scales with the energy stored. Most oxide based PEC devices require some externally applied voltage bias ( $E_{app}$ ). Thus the resulting fuel contains energy from both the external voltage source and the PEC device itself. The use of excessive bias voltage diminishes the balance of solar energy stored. The applied bias photon-to-current efficiency (ABPE) takes this important applied potential into account when expressing the efficiency of conversion from solar to chemical energy,<sup>24,25</sup> where  $J_{photo}$  is the measured photocurrent at a particular applied potential ( $E_{app}$ ),  $P_{photo}$  is the power density of AM 1.5G (100 mW cm<sup>-2</sup>), and  $E_{rc}$  corresponds to the cell potential of the redox couple; 1.23 V<sub>RHE</sub> corresponds to the standard cell potential for water splitting.

$$ABPE(\%) = \left[ \frac{(J_{photo})(\text{mA cm}^{-2}) \times (E_{rc} - E_{app})(V)}{P_{photo}(\text{mW cm}^{-2})} \right]_{AM\ 1.5G} \times 100 \quad (6)$$

It is important to distinguish between the ABPE calculated with a 2-electrode configuration ( $E_{app}$  is between the working and counter electrodes) for overall water-splitting versus the ABPE calculated with a 3-electrode configuration ( $E_{app}$  is between the working and reference electrodes). The ABPE values in Figure 3b were calculated from 3-electrode data to provide a level comparison between samples since 3-electrode data is the most readily available in publications. Photocurrents as high as 6.7 mA cm<sup>-2</sup> (90% of the theoretical limit) have been reported for BiVO<sub>4</sub> with  $E_{app}=1.23$  V<sub>RHE</sub>,<sup>26</sup> however, operation at this voltage corresponds to an ABPE of 0% (Figure 3a). Including both photocurrent and applied voltage shows maximum demonstrated ABPE values of 2.2-2.3% for BiVO<sub>4</sub> (Figure 3b, 0.6 V<sub>RHE</sub>, 3.2-3.4 mA cm<sup>-2</sup>).<sup>25,27</sup> A simple theoretical upper limit of 6.4-7.7% ABPE for water splitting may be estimated by considering the theoretical photocurrent limit (6.2-7.5 mA cm<sup>-2</sup> for a bandgap of 2.5-2.4 eV, respectively) and band positions (neglecting HER and OER overpotential losses; i.e. photocurrent saturation at 0.2 V<sub>RHE</sub> with 100% fill factor). Clearly, there remains much room for ABPE improvement by focusing on improving low-bias-voltage



operation. Design strategies should thus work to maximize both charge separation and charge injection of BiVO<sub>4</sub> with low applied bias voltage.

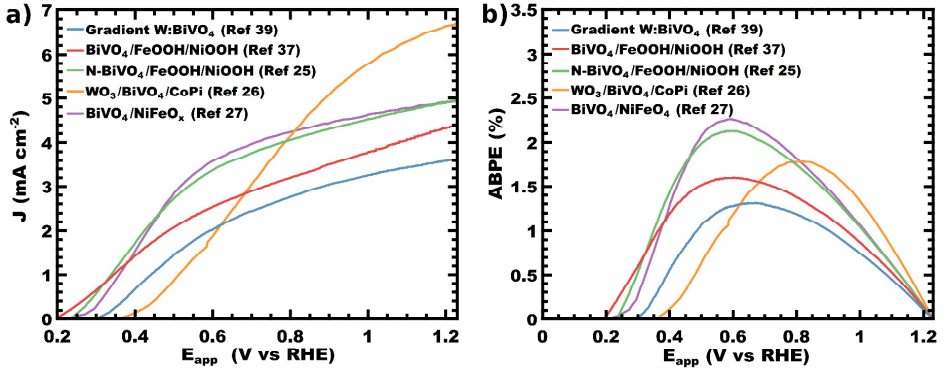


Figure 3. (a) J–V characteristics of BiVO<sub>4</sub> photoanodes and (b) applied bias photocurrent conversion efficiencies of high-performing BiVO<sub>4</sub>-based photoanodes. All data were obtained with a 3-electrode configuration to exclude variable counter electrode contributions.

### 1.3.2 Overview of photoelectrochemical processes in BiVO<sub>4</sub>

For any photoelectrode material, the overall PEC performance, measured by  $J_{photo}$ , is determined by the combination of several phenomena, including the charge separation efficiency, the charge injection efficiency, and light harvesting efficiency (LHE), and can be expressed as follows:

$$J_{photo}(V) = J_{abs} \cdot \phi_{sep}(V) \cdot \phi_{inj}(V) \quad (7)$$

Here,  $J_{abs}$  is the photon absorption rate expressed as a current density (determined from LHE and the illumination spectrum), and  $\phi_{sep}$  and  $\phi_{inj}$  are the charge separation and charge injection efficiencies, respectively (Figure 4a).<sup>28,29</sup>

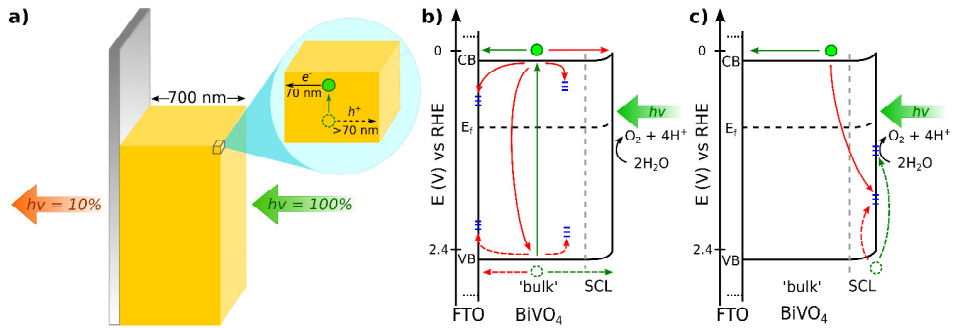


Figure 4. For solid films, there is a trade-off between light-harvesting efficiency and charge separation efficiency (a). Band diagrams of BiVO<sub>4</sub> showing stepwise processes toward water splitting with (b) light-harvesting and charge separation ( $\phi_{sep}$ ) followed by (c) charge injection ( $\phi_{inj}$ ). The green paths support water splitting, whereas the red paths are loss pathways.

For pure BiVO<sub>4</sub>,  $\phi_{sep}$  is often limited by bulk recombination and trapping of charge carriers (Figure 4b)<sup>30–35</sup> whereas  $\phi_{inj}$  is typically limited by slow water oxidation kinetics and surface recombination (Figure 4c), although these can effectively be mitigated with the addition of co-catalyst layers.<sup>36–38</sup> The efficiency of each step is dependent on physical and chemical processes within the bulk or at the surface of the material. The relative rates of water oxidation ( $k_{wo}$ ) and recombination ( $k_{rec}$ ) determine the charge injection efficiency  $\phi_{inj}$  at the surface (assuming 100% faradaic efficiency).<sup>36,38</sup>

$$\phi_{inj}(V) = \frac{k_{wo}(V)}{k_{rec}(V) + k_{wo}(V)} \quad (8)$$

Charge separation is accomplished by a combination of drift from an external applied potential or from the internal potential from the space charge layer (SCL), as well as diffusive charge transport. For pristine (undoped) BiVO<sub>4</sub>, the SCL width can be as high as 90 nm;<sup>36</sup> this would enhance  $\phi_{sep}$  of very thin, <90 nm, films. In contrast, thicker films (>200 nm) are needed to achieve reasonable LHE values, dimensions where  $\phi_{sep}$  is considerably reduced since most carriers are produced outside of the SCL. This may be mitigated by enhancing the extent of band bending with gradient-doping.<sup>39</sup> Use of a large external bias voltage can enhance charge separation at the cost of significant loss of overall ABPE. The separation of charge carriers produced far from the SCL is limited by low carrier conductivity as well as recombination sites within the film or at the substrate-BiVO<sub>4</sub> interface.<sup>30,32</sup> Here, since BiVO<sub>4</sub> is normally operated with bias voltage,

improvements to conductivity (product of mobility and carrier concentration) can improve charge separation.

### 1.3.3 Defining synthetic vs. post-synthetic modification

Synthetic strategies to improve the PEC properties of  $\text{BiVO}_4$  – such as nanostructuring films, designing heterostructures, applying oxygen evolution catalysts (OECs), adding dopants to  $\text{BiVO}_4$ , among others – have been developed and used to great effect, and were reviewed elsewhere.<sup>22,40,41</sup> Post-synthetic treatments have been concurrently developed and have enabled many of the highest photocurrents reported to date.<sup>25–27</sup> These treatments are applied after the synthesis of  $\text{BiVO}_4$ , and are based upon illumination, chemistry, electrochemistry, or combinations thereof (Figure 5). Post-synthetic treatments are intended to modify the defect chemistry of existing material rather than to deposit additional material. For this reason, treatments that deposit metallic elements are not considered as post-synthetic treatments. For example, here we consider annealing  $\text{BiVO}_4$  under  $\text{H}_2$  or  $\text{N}_2$  gases to be post-synthetic treatments whereas the deposition of passivation or catalytic layers (e.g.  $\text{FeOOH}$ ,  $\text{CoPi}$ , etc.) is a synthetic treatment. Broadly, post-synthetic treatments affect  $\phi_{\text{sep}}$ ,  $\phi_{\text{inj}}$ , or both to improve the overall ABPE performance of  $\text{BiVO}_4$ .

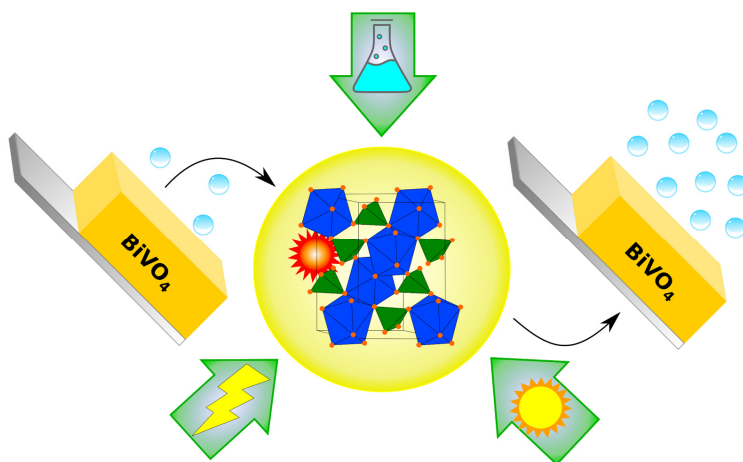


Figure 5. Schematic representation of postsynthetic treatments.

An electrochemical treatment of Mo:BiVO<sub>4</sub> was reported in 2011;<sup>42</sup> this was followed by H<sub>2</sub>-annealed BiVO<sub>4</sub> in 2013 and subsequent follow-ups.<sup>43–46</sup> In 2015, N<sub>2</sub>-annealed BiVO<sub>4</sub> was demonstrated to attain one of the highest ABPEs on record,<sup>25</sup> second only to a report on electrochemically-treated catalyzed BiVO<sub>4</sub> in 2016.<sup>27</sup> Two illumination-dependent treatments, UV-curing and photocharging of BiVO<sub>4</sub>, were published in 2015,<sup>47,48</sup> with later follow-up reports.<sup>49,50</sup> In 2016, a significantly accelerated PEC activation used a combination of light, electrolyte, and applied potential.<sup>51</sup>

The defect changes during post-synthetic treatments are sometimes subject to multiple equivocal interpretations as many of the proposed mechanisms are consistent with the often limited experimental data. For example, the addition of both hydrogen interstitials<sup>49</sup> and hydrogen anti-site on oxygen,<sup>45</sup> and both the addition<sup>43</sup> and removal<sup>45</sup> of oxygen vacancies have been supported by similar shifts in vanadium X-ray photoelectron spectroscopy (XPS) data; such contradictory defect chemistries clearly require additional investigation. Additionally, multiple intrinsic: e.g. oxygen, bismuth, or vanadium vacancies ( $v_O^{2\bullet}$ ,  $v_{Bi}^{3'}$ , and  $v_V^{5'}$ ), interstitials ( $O_{int}^{2'}$ ,  $Bi_{int}^{3\bullet}$ , and  $V_{int}^{5\bullet}$ ), and anti-sites ( $Bi_V^{2'}$  and  $V_{Bi}^{2\bullet}$ ), and extrinsic: e.g. hydrogen interstitial or substitution ( $H_{int}^{\bullet}$  or  $H_O^{3\bullet}$ ) defects are proposed to exist in BiVO<sub>4</sub>, either directly after synthesis or after exposure to PEC conditions (i.e. illumination and electrolyte).<sup>45,46,49</sup> Additionally, defect clusters – e.g. double or triple vacancies like  $v_{Bi}^{3'}v_O^{2\bullet}$ ,  $v_{Bi}^{3'}v_O^{2\bullet}v_{Bi}^{3'}$ , or  $v_{Br}^{\bullet}v_{Bi}^{3'}v_O^{2\bullet}$  – are also proposed to affect the catalytic activity of semiconductor photoelectrodes.<sup>52</sup> Differentiating between these numerous possible defect chemistries will require more detailed follow up studies using experimental techniques that can probe local electronic environments, and subsequently study charge carrier kinetics to elucidate defect activity (e.g. as trap, donor, and/or catalytic sites). Furthermore, the synthetic route dependence on subsequent post-synthetic behaviors is rarely considered – is it not reasonable that the native material defects should affect the results of a post-synthetic treatment?

The emergence of post-synthetic treatments highlights new opportunities to understand and improve photoelectrodes. Similar mechanisms may be of further utility as researchers turn more focus towards the development of novel multinary metal oxide photoabsorbers where, like BiVO<sub>4</sub>, there is a combinatorial expansion of the candidate point defect chemistries. Lastly, post-synthetic treatments also elucidate

possible electrode changes under extended service and can provide new strategies to enable extended device performance. This perspective will provide an overview of a variety of reported post-synthetic treatments and attempt to describe unifying features between treatments as well as paths forward towards a deeper understanding.

#### **1.3.4 (a) Post-synthetic improvement of charge separation**

Synthetic approaches to improve  $\phi_{\text{sep}}$  are based on two main approaches: increasing the free carrier density by substituting V with higher valent metals (e.g. Mo, W)<sup>29,32,39,42,53–56</sup> and limiting recombination at the back-interface by adding “hole blocking layers,” such as SnO<sub>2</sub> or WO<sub>3</sub>, between BiVO<sub>4</sub> and the substrate.<sup>26,30–32,57,58</sup> Post-synthetic techniques have recently emerged with similarly significant improvements to charge separation.

#### **1.3.4 (b) Post-synthetic removal of recombination sites**

Bismuth vanadate photoelectrodes have been synthesized using numerous techniques including sol-gel,<sup>29,59</sup> spray pyrolysis,<sup>30</sup> electrodeposition and conversion,<sup>27,37,60</sup> magnetron sputter deposition,<sup>56,61,62</sup> chemical vapor deposition (CVD),<sup>63</sup> and atomic layer deposition (ALD),<sup>51,64</sup> where each method results in varying performance, partially due to the nature of the inherent defects. The combination of mobility and carrier lifetime results in a limited ~70 nm transport length of electrons within BiVO<sub>4</sub>, with holes able to diffuse farther.<sup>32</sup> This characteristic is why numerous BiVO<sub>4</sub> publications report higher photocurrents with back-side illumination to minimize the transport distance for electrons.

Many of these synthetic techniques have been utilized to create high-surface area architectures in an effort to enhance charge separation. The nanostructuring of pure BiVO<sub>4</sub> improves minority carrier (hole) transport to the surface,<sup>27,37</sup> whereas host-guest approaches are needed to improve electron transport to the substrate.<sup>26,58,65–68</sup> Thus far, the methods used for the production of BiVO<sub>4</sub> host-guest nanostructures have all utilized non-uniform depositions or cathodic electrodepositions that limit the use of hole-blocking layers at the BiVO<sub>4</sub>-substrate interface.<sup>26,58,65,66</sup> Atomic layer

deposition (ALD) stands out as a method to fabricate conformal BiVO<sub>4</sub> coatings within complex device architectures while retaining compatibility with hole-blocking layers and radial dopant profiles.<sup>64</sup> Surface functionalized ALD (SF-ALD) was recently shown to enable phase pure scheelite BiVO<sub>4</sub>.<sup>51</sup>

The  $\phi_{\text{sep}}$  of SF-ALD BiVO<sub>4</sub> was remarkably sensitive to post-synthetic treatment. Post-synthetic enhancements were maximized with a treatment that involved exposing the sample to AM 1.5G simulated illumination while applying an external bias of 0.6 V<sub>RHE</sub> for 1 h. Corresponding to this treatment (PEC activation), film optical absorbance decreased,  $\phi_{\text{sep}}$  increased, and both absorbed and incident photon-to-current efficiencies increased (APCE and IPCE, respectively; Figure 6a), with an increase of ABPE from 0.18 to 0.28% for 75 nm-thick films in electrolyte with hole scavenger (sulfite,  $E_{\text{rc}} = 0.93 \text{ V}_{\text{RHE}}$  in equation 6).<sup>51,69</sup> Note that  $\phi_{\text{inj}}$  is assumed to be unity in the presence of hole scavenger; no water oxidation data was presented. The simultaneous increase of transparency with photocurrent is counterintuitive given the relationship between LHE and photocurrent in equation 7. This effect is attributed to the removal of metallic defects during treatment (*vide infra*), which is expected to improve  $\phi_{\text{sep}}$  by removing photoabsorbing trap sites, thus decreasing the overall optical absorption. The post-synthetic enhancements were shown to be stable for at least 17 h. During PEC activation, an oxidative photocurrent was observed to increase and plateau; this was attributed to the combined oxidation of hole scavenger and BiVO<sub>4</sub> defects. XPS (Figure 6b) analysis suggested that reduced metal defects in calcined SF-ALD samples (Bi<sup>0</sup> and V<sup>4+</sup>) were fully oxidized (Bi<sup>3+</sup> and V<sup>5+</sup>) following PEC activation. The ALD of bismuth titanates with the same Bi<sup>3+</sup> precursor was previously shown to result in a mixture of Bi<sup>3+</sup> and Bi<sup>0</sup>,<sup>70</sup> highlighting the connection of synthetic route with point defect chemistries. Related post-synthetic treatments such as UV-curing and photocharging also involve illumination;<sup>48,49</sup> however, control experiments demonstrated that the applied bias with PEC activation leads to larger improvements to  $\phi_{\text{sep}}$  and occur much faster within 1 hr. The ability of bismuth vanadate to self-heal may explain its label as a “defect tolerant” material.<sup>32</sup> More work is needed to establish the precise nature of the defects present in the untreated BiVO<sub>4</sub>, and to determine if any other phenomenon are taking place – e.g. hydrogen or proton uptake or surface state alteration.<sup>45,46,49</sup>

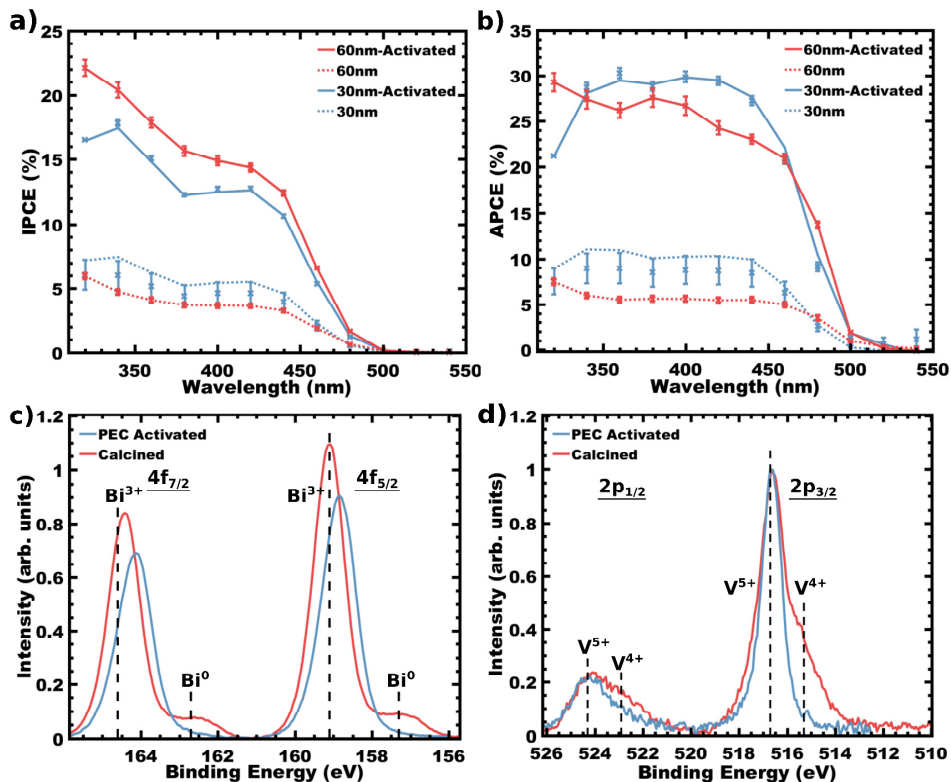


Figure 6. Effect of a postsynthetic PEC activation treatment on 30 and 60 nm films prepared by SF-ALD: (a) IPCE, (b) APCE, and XPS of (c) Bi 4f and (d) V 2p comparing as-made and activated SF-ALD  $\text{BiVO}_4$ .

Annealing  $\text{BiVO}_4$  films in  $\text{H}_2$  was found to increase the concentration of  $\text{V}^{4+}$  species while removing or passivating trap states.<sup>43,45,46</sup>  $\text{H}_2$ -annealing has been demonstrated to improve the onset potential and photocurrent of the photoelectrodes (93 mV shift to onset potential and increase to photocurrent from 1.23 to 1.43  $\text{mA cm}^{-2}$  at 1.23  $\text{V}_{\text{RHE}}$  between as-grown and 290 °C  $\text{H}_2$ -annealed  $\text{BiVO}_4$ , respectively),<sup>43,45</sup> corresponding to an increase in ABPE for sulfite oxidation from 0.18 to 0.27% between as made and  $\text{H}_2$ -annealed  $\text{BiVO}_4$ . Optimal annealing conditions were reported as 15 min at 290 °C under 1 atm of  $\text{H}_2$ .<sup>45</sup>  $\text{H}_2$  annealing primarily improves  $\phi_{\text{sep}}$ ; however, a decrease in  $\phi_{\text{inj}}$  was also reported,<sup>46</sup> possibly due to surface H affecting water oxidation kinetic activity.<sup>46,71,72</sup> Additionally, changes to the surface hydroxyl ( $-\text{OH}$ ) concentration were reported;<sup>44</sup> such alterations were reported to affect  $\phi_{\text{inj}}$  in

BiVO<sub>4</sub>.<sup>47,48</sup> This treatment was found to improve photocurrent regardless of synthetic procedure,<sup>46</sup> and was helpful in improving the photocurrent of other photoanode materials.<sup>73–75</sup> In the initial report,<sup>43</sup> density functional theory (DFT) calculations suggested that elemental H was occupying both interstitial and oxygen sites within the BiVO<sub>4</sub> lattice, with both types of defects expected to act as shallow donors. A follow-up report identified two local hydrogen environments by <sup>1</sup>H-NMR spectroscopy that were attributed to interstitial hydrogen (H<sub>int</sub>) and substitutional hydrogen (H<sub>O</sub>).<sup>45</sup> Notably, H<sub>O</sub> also had a trace presence in as-made BiVO<sub>4</sub>. This was further supported by a second follow-up report that quantitatively analyzed the loading of hydrogen into BiVO<sub>4</sub> by <sup>15</sup>N nuclear reaction analysis, finding about 5x the amount of hydrogen in annealed films (0.7 vs 0.14 at% for H-BiVO<sub>4</sub> and BiVO<sub>4</sub>, respectively).<sup>46</sup> Initially, the partial reduction of V from 5+ to 4+ was attributed to the formation of oxygen vacancies, v<sub>O</sub>.<sup>43</sup> However, subsequent investigations correlated H<sub>2</sub>-annealing to a reduced photoluminescence (attributed to removal of v<sub>O</sub>)<sup>45</sup> and increase in charge carrier lifetime, suggesting a decrease in trap concentration by the removal or passivation of traps (proposed to be interstitial V or V anti-site on Bi, V<sub>int</sub> or V<sub>Bi</sub>).<sup>46</sup> Follow-up reports also agree on the presence of one of the aforementioned hydrogen defects (H<sub>int</sub>, bonded to a bridging O), and that increasing the v<sub>O</sub> content is not the source of improved  $\phi_{sep}$ . There remains some question as to the nature of the trap states removed or passivated (e.g. v<sub>O</sub>, V<sub>int</sub>, or V<sub>Bi</sub>).<sup>45,46</sup> Furthermore, there is disagreement as to the effect of H<sub>2</sub>-annealing on charge carrier conductivity.<sup>45,46</sup> Considering that both v<sub>O</sub> and H<sub>O</sub> can yield the same XPS observation of partially reduced vanadium, follow up studies on hydrogenated photoelectrode materials would benefit by parsing the multiple causal pathways with further measurements such as electron energy loss spectroscopy (EELS)<sup>76–78</sup> or X-ray absorption near edge structure (XANES)<sup>79</sup> to probe changes to local electronic environment caused by specific defect chemistries.

### 1.3.4 (c) Post-synthetic production of free carriers

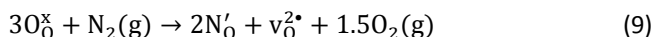
Doping BiVO<sub>4</sub> with metals and non-metals – commonly W and Mo – has been widely utilized to synthetically alter the carrier density and conductivity of BiVO<sub>4</sub>-based photoanodes.<sup>30,32,42,47,53–56,80</sup> Recently, several post-synthetic techniques have been utilized to similarly increase free carrier density.<sup>25,27,81</sup> It has been suspected that V<sup>4+</sup> plays a role in the native conductivity of BiVO<sub>4</sub> photoanodes,<sup>82</sup> typically attributed to



the formation of O vacancies ( $v_O$ ) as a shallow donor state.<sup>83</sup> Consequently, several post-synthetic treatments have related effects to conductivity and ABPE to alterations in V oxidation state.<sup>27,43,81</sup> However, recent work has shown that the mobility of charge carriers in  $\text{BiVO}_4$  is not improved by increasing  $v_O$  concentration,<sup>45,46</sup> suggesting that an alternative mechanism may be present.

To achieve one of the highest reported ABPEs, researchers activated their electrodes with a simple cyclic voltammetry treatment in alkaline media prior to depositing the catalytic Ni-borate layer.<sup>27</sup> This treatment (five cycles of voltammetric scans from 0 to 1  $V_{\text{RHE}}$  at 40  $\text{mV s}^{-1}$ ) was suggested to involve the reversible redox between  $\text{V}^{5+}$  and  $\text{V}^{4+}$ . Improvements to  $\phi_{\text{sep}}$  following this treatment were attributed to an improved (lower gradient) distribution of  $\text{V}^{4+}$  near the surface of the film.<sup>27</sup> The authors noted that others had observed a 5 nm “reduction shell” at the surface of  $\text{BiVO}_4$ ; however, those observations were on commercial powders that had not carried out PEC, and the scanning transmission electron microscopy (STEM) imaging may have itself induced changes.<sup>77</sup> Within this reduction shell, vanadium primarily exists in the 4+ state – compared to the 5+ state of bulk V – producing a  $n^+-n$  homojunction that is deleterious to charge separation.<sup>27,77</sup> It was also noted that onset potential was affected by vanadium redox changes. An anodic shift to onset potential was observed with starting potentials of 0.05 to 0.25  $V_{\text{RHE}}$  in current-potential scans, indicating overly-reduced  $\text{V}^{4+}$  produces charge recombination sites.<sup>27</sup> An alternative mechanism for film activation could involve the incorporation of hydrogen defects ( $\text{H}_{\text{int}}$  or  $\text{H}_O$ , for example), which would also reduce vanadium while introducing shallow donors; further measurements could clarify the changes to defect chemistry caused by such treatments. Calculation of the relative ABPE enhancement would require electrochemical data from the as-made sample.<sup>27</sup>

Doping  $\text{BiVO}_4$  with  $\text{N}_2$  ( $\text{N-BiVO}_4$ ) was also shown to primarily improve photocurrent and  $\phi_{\text{sep}}$ .<sup>25</sup> Charge injection efficiency was calculated to slightly increase as well. This treatment was reported to incorporate N in the lattice, accompanied by the generation of  $v_O$ . Using Kröger-Vink notation, the proposed reaction was:<sup>25</sup>



where  $O_O^x$  denotes oxygen on an oxygen site,  $N'_O$  denotes nitrogen on an oxygen site, and  $v_O^{2\bullet}$  denotes an oxygen vacancy. N-BiVO<sub>4</sub> was achieved by annealing under N<sub>2</sub> at 350 °C for 2 h. N-BiVO<sub>4</sub> resulted in a reduced bandgap (~0.2 eV less) compared to untreated BiVO<sub>4</sub> by increasing the VB maximum, as suggested by DFT calculations and IPCE measurements. Whereas  $v_O$  are proposed by some to yield localized trap states in BiVO<sub>4</sub>,<sup>25,45</sup> the  $v_O$  production in N-BiVO<sub>4</sub> was also accompanied by a shift of the valence band towards the conduction band, enhancing activation of  $v_O$  as donor states. The charge mobility increased by 25%, corresponding to an improvement in  $\phi_{sep}$  from 88 to 94% at 1.0 V<sub>RHE</sub>. The concomitant reduction of bandgap notably also improved optical absorbance.<sup>25</sup> The authors noted that the changes in the XPS spectrum were not suggestive of changes to the Bi nor V oxidation states, unlike several other post-synthetic treatments discussed thus far. Overall, N-BiVO<sub>4</sub> produced one of the highest ABPEs reported to date (2.16%); in comparison, untreated BiVO<sub>4</sub> samples demonstrated an ABPE of 1.63%. Additionally, the photocurrent for sulfite oxidation was stable for 50 h without decay;<sup>25</sup> and water oxidation photocurrents decayed after 30 h due to film degradation (perhaps caused by the use of a phosphate buffer).<sup>25,27,84</sup> Further investigation into the defect chemistry specific to BiVO<sub>4</sub> synthesized in this manner (i.e. electrodeposition and conversion) could be particularly insightful, given the exceptionally high performance (ABPE) of this and similar reports (for example, refs <sup>27</sup> and <sup>37</sup>).

Although the partial reduction of vanadium species is often correlated with improved PEC properties (e.g.  $\phi_{sep}$  or  $\phi_{inj}$ ), the direct (electro)chemical reduction of BiVO<sub>4</sub> is not as effective.<sup>81</sup> For example, BiVO<sub>4</sub> was reduced electrochemically for 3 min at ca. -0.3 V<sub>RHE</sub> followed by chemical reduction in 0.1 M NaBH<sub>4</sub> for 3 min which enhanced the photocurrent from 0.5 to 1.4 mA cm<sup>-2</sup> at 1.2 V<sub>RHE</sub> and was ascribed to an enhanced free-carrier density from the production of  $v_O$  and the associated reduced vanadium oxidation states, as evidenced by XPS.<sup>81</sup> ABPE increased from 0.04 to 0.16% following this combined treatment. However, the benefits of this treatment were stable for only 40 min before the photocurrent began to decay significantly, returning to the initial (untreated) photocurrent after 75 min. The instability of this treatment might be due to the over-reduction of BiVO<sub>4</sub>,<sup>45</sup> possibly resulting in the re-oxidation of species within the electrode. Additionally, more mild reducing treatments (e.g. annealing in Ar to induce  $v_O$  formation or less aggressive electrochemical treatment) have resulted in little to no change to BiVO<sub>4</sub> water oxidation performance.<sup>42,46</sup>

Briefly we note that the conductivity of  $\text{BiVO}_4$  may also be enhanced thermally or by significantly increasing photon flux. The low minority carrier mobility in  $\text{BiVO}_4$  is caused by localization of the carriers as small polarons.<sup>85</sup> A modest temperature increase from 10 to 42 °C was shown to activate minority carrier hopping in  $\text{BiVO}_4$  and significantly enhance the PEC activity from 1.8 to 4.0  $\text{mA/cm}^2$  at 1.0  $V_{\text{RHE}}$ .<sup>55</sup> Similarly, increasing the concentration of incident photons (from  $\sim 10^{18}$  photons  $\text{cm}^{-2} \text{s}^{-1}$  for AM 1.5 to  $\sim 10^{24}$ - $10^{28}$  photons  $\text{cm}^{-2} \text{s}^{-1}$ ) can overcome trapping mechanisms for both charge carriers and significantly enhance mobility.<sup>32,34,35,46</sup>

### 1.3.4 (d) Summary

Conventional methods of improving  $\phi_{\text{sep}}$  in  $\text{BiVO}_4$ -based photoanodes have primarily been confined to hetero-metal dopants and hole blocking layers.<sup>30,53,58</sup> Post-synthetic techniques that have recently emerged can supplement or replace synthetic approaches by removing common and/or synthesis-specific bulk defects, and increasing the free carrier density.<sup>25,27,43,45,46,51</sup> The development of these post-synthetic techniques continues to improve the understanding of  $\text{BiVO}_4$  defect chemistry and highlights the differences between various synthetic methods.<sup>45,46,51</sup>

It is important to note that two of the techniques discussed produced stable improvements through mild (photo)electrochemical treatments.<sup>27,51</sup> One may expect that these treatments only affect the near-surface, however the improvements to  $\phi_{\text{sep}}$  suggest that bulk changes may be occurring e.g. intercalation of hydrogen. Further data are needed to better understand these changes.

### 1.3.5 (a) Post-synthetic improvement of charge injection at the surface

Post-synthetic treatments have been developed to modify the surface and near-surface regions of  $\text{BiVO}_4$ -based electrodes. As described briefly in the introduction, the  $\phi_{\text{inj}}$  suffers from slow water oxidation kinetics, which causes an accumulation of holes within the SCL, particularly at  $\text{BiO}_8$  polyhedra.<sup>86</sup> This accumulation makes the back-recombination of holes and electrons kinetically viable.<sup>36</sup> Recombination can also occur at surface defects at the  $\text{BiVO}_4$ -electrolyte interface.<sup>42,54,87</sup> Furthermore, the build-up of holes within the SCL and near the surface

of BiVO<sub>4</sub>-based photoanodes was linked to photocorrosion,<sup>20,22</sup> in particular when immersed in alkaline electrolytes.<sup>84,88</sup> Clearly, the best strategies to improve  $\phi_{inj}$  and prevent electrode degradation should involve either increasing the rate of water oxidation or decreasing the rate of near-surface recombination (equation 8). Commonly, layers of additional materials as protective layers or catalysts – e.g. amorphous TiO<sub>2</sub>,<sup>54,57,88</sup> CoPi,<sup>29,31,89</sup> NiOOH,<sup>25,37</sup> etc.<sup>27,87,88,90–92</sup> – are used to either block native defects, store holes to mitigate side reactions, or to catalyze the water oxidation reaction; however, simple post-synthetic modifications have also been used to mitigate surface defects.<sup>42,48,49,87</sup>

### 1.3.5 (b) Removal of surface recombination sites

Surface recombination sites can be removed or blocked by simple post-synthetic treatments in both doped and pristine BiVO<sub>4</sub>. These treatments provide simple routes to decrease  $k_{rec}$  and improve  $\phi_{inj}$ , as described in equation 8. Simulations of BiVO<sub>4</sub> surfaces suggest that hole localization and subsequent recombination at the electrode-electrolyte interface is caused by native crystal distortions;<sup>86</sup> while experimental evidence supports a second recombination mechanism via segregated surface species.<sup>42</sup>

Ion segregation, or enrichment of a material constituent, at the surface of photoelectrodes has been known to form recombination centers.<sup>42,93</sup> In the case of Mo-doped BiVO<sub>4</sub> (Mo:BiVO<sub>4</sub>), Mo<sup>6+</sup> aggregates at the surface were dissolved by an electrochemical treatment of 30 cyclic voltammetry scans from -0.3 – 1.16 V<sub>RHE</sub>, causing the photocurrent at ~1.2 V<sub>RHE</sub> to approximately double when illuminated from the front of the photoelectrode, based on XPS and PEC characterization, corresponding to an increase in ABPE from 0.09 to 0.24%. Comparatively, non-doped BiVO<sub>4</sub> electrodes showed no effect on photocurrent following the same electrochemical treatment, suggesting that the untreated Mo<sup>6+</sup> locations are recombination sites at the semiconductor/electrolyte interface.<sup>42</sup> Additionally, Mott-Schottky analysis suggested that bulk properties (e.g. carrier concentration) were not altered by the treatment; i.e. only  $\phi_{inj}$  was affected.<sup>42</sup> Interestingly, a Bi-rich surface layer was observed following the electrochemical treatment, suggesting that V was also dissolved from the surface. The effect on photocurrent or stability caused by dissolving V from the surface or the

enrichment of Bi at the surface was not reported,<sup>42</sup> though it should be noted that Bi-enriched BiVO<sub>4</sub> surfaces were previously shown to improve photocurrent stability.<sup>94</sup> It should also be noted that while this treatment and the EC/chemical treatment discussed in the previous section<sup>81</sup> both apply cathodic potentials to reduce electrode material, the potential discussed here was only applied for a brief time before sweeping to higher (oxidizing) voltages, compared to holding -0.3 V<sub>RHE</sub> for 3 min.<sup>42,81</sup> For this treatment, cathodic potentials (versus V<sup>4+</sup>/V<sup>5+</sup>, E<sub>app</sub> < ~0.1 V<sub>RHE</sub>)<sup>27</sup> are only applied for ~6.5 s per scan before the sweep becomes anodic (~36.5 s for 0.1 < V<sub>RHE</sub> < 1.2). It would seem that any reduction of V or other species within these BiVO<sub>4</sub> films is reversed by the oxidation involved in each sweep, with the exception of surface Mo<sup>6+</sup> which is apparently dissolved irreversibly into solution. Additional differing results between this treatment and the previously discussed EC scanning treatment<sup>27</sup> can be at least partially explained by the electrolytes used (sodium sulfate at pH 6.5 versus potassium borate at pH 9.4), as pH is known to strongly affect post-synthetic treatment.<sup>49</sup> However, direct experimental comparison would be needed to confirm these hypotheses. This electrochemical treatment was found to be stable after storing treated electrodes in air or vacuum for 12 h.<sup>42</sup>

While not strictly a post-synthetic treatment by our definition, etching of an NiO<sub>x</sub> catalytic layer on BiVO<sub>4</sub> was proposed to block recombination sites ascribed to BiO<sub>8</sub> polyhedra at the electrode surface.<sup>86,87</sup> Computational modelling suggested that lattice distortions within the first ~2 nm of BiVO<sub>4</sub> surfaces create an environment favorable for hole trapping.<sup>86</sup> Bi<sup>3+</sup> surface sites were reportedly blocked by the selective etching of nickel borate surface layers in a potassium phosphate solution.<sup>87</sup> The etching procedure exposed VO<sub>4</sub> sites while the remaining, non-catalytic NiO<sub>x</sub> was primarily located on BiO<sub>8</sub> sites. The resulting films exhibited a significant improvement to  $\phi_{inj}$ , improving the stable photocurrent at 1.23 V<sub>RHE</sub> from 0.34 mA cm<sup>-2</sup> to 1.09 mA cm<sup>-2</sup>,<sup>87</sup> and improving ABPE to 0.39% from 0.07 and 0.15% for untreated and NiO<sub>x</sub> catalyzed films, respectively. A small improvement of  $\phi_{sep}$  for both catalytic and etched NiO<sub>x</sub>/BiVO<sub>4</sub> samples over bare BiVO<sub>4</sub> can be observed in photocurrent data with hole scavenger (sulfite) present.<sup>87</sup> This work emphasizes the crucial role of surface termination, particularly with multinary materials. Future work on this treatment could be directed towards improving the treatment route – e.g. by directing the passivating material to the recombination sites initially and removing the need to etch – and

investigating the surface chemistry of BiVO<sub>4</sub> (for example, the role of different exposed metal sites and the passivation mechanism of NiO<sub>x</sub> sites).

These post-synthetic techniques target both the electrode-electrolyte interface and improve  $\phi_{inj}$  by removing or blocking surface recombination sites, and represent facile approaches to enhance the performance of both doped and pristine BiVO<sub>4</sub> photoanodes.<sup>42,87</sup> These diverse results highlight that there is not a specific ideal surface termination since both Bi and V surface-rich terminations were observed with improved charge injection, depending on the particular report.

### 1.3.5 (c) Near-surface doping and surface state alteration

In the near-surface regime (i.e. 2-10 nm),<sup>86</sup> partial reduction of V through photochemical treatment has been associated with improved  $\phi_{sep}$  and  $\phi_{inj}$ .<sup>47-49</sup> Photochemical treatments have been demonstrated with both ultra-violet (UV) and visible light and the resulting effects can be achieved either in or out of electrolyte, depending on the report.<sup>47-49</sup> Soaking BiVO<sub>4</sub> in AgNO<sub>3</sub> can also improve  $\phi_{inj}$  significantly.<sup>94</sup>

Relatively early in the PEC research on BiVO<sub>4</sub>, it was noticed that the photocurrent in pristine BiVO<sub>4</sub> decayed as much as 50% within 30 min, yet the photocurrent could be partially restored by cyclic voltammetry or storing the electrodes in the dark for 24 h.<sup>94</sup> Based on the existing knowledge of photoelectrode surface modifications, this work exposed BiVO<sub>4</sub> to a number of metal salts (0.01 M, 12 h) to adsorb metal ions into BiVO<sub>4</sub>. Of the different salts tested, AgNO<sub>3</sub> solutions showed the most improvement in photocurrent. Following AgNO<sub>3</sub> treatment,  $\phi_{inj}$  was improved to near-unity and  $\phi_{sep}$  was slightly improved at high potentials (1.15-1.55 V<sub>RHE</sub>); ABPE was improved from 0.06 to 0.21%. BiVO<sub>4</sub> treated with AgNO<sub>3</sub> demonstrated a stable photocurrent (1 h) plateauing at nearly twice the saturation photocurrent of untreated BiVO<sub>4</sub>. Following an XPS analysis on the effect of 1 h of photoreaction (e.g. PEC water splitting) on treated and untreated BiVO<sub>4</sub>, it was found that V dissolved from the surface of both treated and untreated samples; however, the surface of treated BiVO<sub>4</sub> was capped by a Bi-rich layer. The surface of AgNO<sub>3</sub> treated BiVO<sub>4</sub> was etched following photoreaction; beneath the surface, Bi and V were found to be stoichiometrically matched even with 1.8 at% Ag<sup>+</sup> present, and Bi was found to

be both in the normal  $\text{Bi}^{3+}$  and reduced  $\text{Bi}^0$  oxidation states; here it should be noted that by incorporating metal species to  $\text{BiVO}_4$ , this treatment is not strictly a post-synthetic treatment. The researchers attributed the improved photocurrent and stability to both the protective Bi-rich surface layer and the  $\text{Ag}^+$  ion exchange layer formed at the surface of  $\text{AgNO}_3$  treated  $\text{BiVO}_4$ .<sup>94</sup> Additionally, it was hypothesized that the addition of  $\text{Ag}^+$  to the near-surface region of  $\text{BiVO}_4$  would raise the VB maximum within this spatial region;<sup>22,95</sup> thus narrowing the bandgap and improving charge separation as well as absorption. Further evidence would be needed to support this hypothesis.

For W-doped  $\text{BiVO}_4$  (W: $\text{BiVO}_4$ ), curing electrodes in air with UV light ( $\sim 10 \text{ mW cm}^{-2}$ , 20 h) significantly enhanced both  $\phi_{\text{sep}}$  and  $\phi_{\text{inj}}$  (Figure 7a).<sup>47</sup> The improvement of  $\phi_{\text{sep}}$  was demonstrated by comparing photocurrents before and after treatment in the presence of a hole scavenger ( $\text{H}_2\text{O}_2$ ). Evidence of  $\phi_{\text{inj}}$  improvement was shown by the change in photovoltage from 0.17 to 0.41 V,<sup>47,96</sup> as well as the comparison of water oxidation photocurrents in relation to the photocurrents in a hole scavenger. UV-cured W: $\text{BiVO}_4$  films showed an improved ABPE for water oxidation (0.20%) over untreated samples (0.07%). The improvements of  $\phi_{\text{inj}}$  were attributed to a change in the ratio of dangling to bridging (oxy)hydroxyl group surface groups at the electrolyte-electrode interface, where the amount of bridging O was increased following UV-curing. Alterations to film crystallinity and texture were also observed, and would be expected to affect  $\phi_{\text{sep}}$ .<sup>47</sup> Further analysis on the effects of this treatment (e.g. defect chemistry, carrier kinetics) in relation to other photo(electro)chemical treatments could offer important insights into the differences between pristine and doped  $\text{BiVO}_4$ .

A separate light-based treatment was demonstrated to address the limitations of  $\text{BiVO}_4$ , denoted as 'photocharging',<sup>48,49</sup> which uses long-time exposure of the  $\text{BiVO}_4$  photoanodes to AM 1.5G illumination under open circuit conditions in a cell filled with electrolyte. Photocharging leads to greatly enhanced photocurrent, a strong cathodic shift of the photocurrent onset, and improved J-V fill factor (Figure 7b). The photocharging-driven activation of  $\text{BiVO}_4$  photoanodes is facilitated especially under alkaline conditions, with slightly alkaline electrolyte (pH 10) showing the greatest performance enhancements and slightly acidic media (pH 4) showing no effect following photocharging;<sup>49</sup> photocharged samples in pH 10 buffer were found to have an ABPE of 1.67%, versus an ABPE of 0.16% for untreated films. It is worth noting here

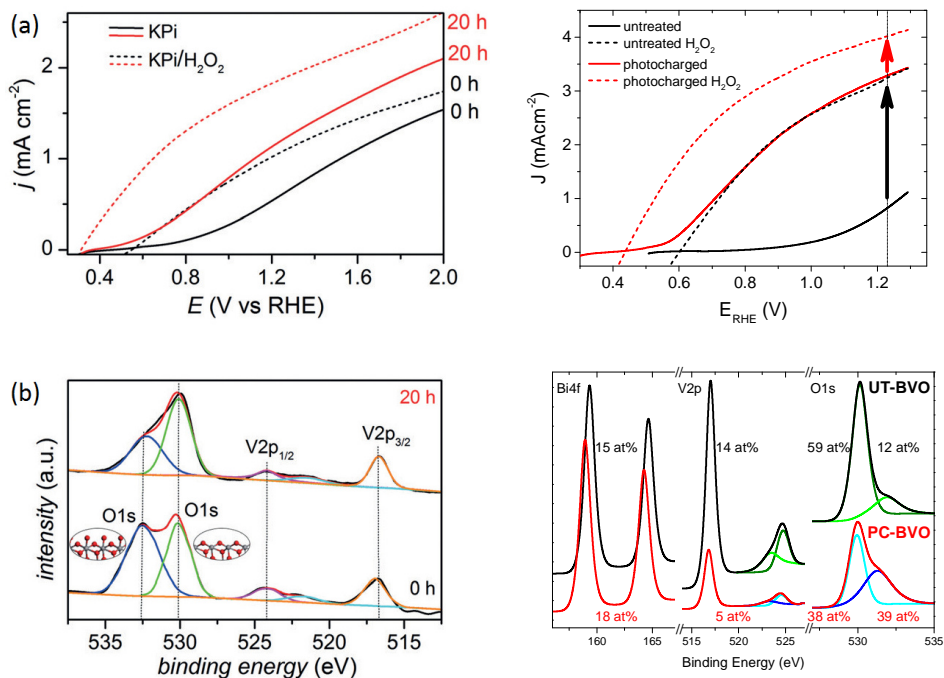
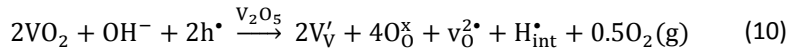


Figure 7. (a) (left) Photocurrent densities of BiVO<sub>4</sub> photoanodes, before and after exposure to 20 h of UV curing, in KPi buffered solutions (solid) and after the addition of 0.1 M H<sub>2</sub>O<sub>2</sub> (dashed), at pH 7; (right) J–V scans of 200 nm thick BiVO<sub>4</sub> under back-side AM 1.5 illumination, in 0.1 M K-Pi buffer (pH 7.2). Arrows denote catalytic limitations for untreated (black) and photocharged (red) material. (b) (left) O 1s and V 2p peaks of BiVO<sub>4</sub> with 0 h (black) and 20 h (red) UV curing in XPS spectra normalized to V 2p<sub>3/2</sub> signal. The inset images represent the possible structures of crystalline oxygen (530.3 eV) and oxygen-based defect sites (532.3 eV) on the surface. The red spheres represent O atoms, and gray spheres represent V atoms. (right) XPS spectra of BiVO<sub>4</sub> photoanodes before and after photocharging in 0.1 M PBA buffer, pH 10, under AM 1.5G simulated illumination.

that not all basic media are appropriate for BiVO<sub>4</sub>-based electrodes; phosphate buffers especially are known to etch BiVO<sub>4</sub> to the detriment of film performance and stability.<sup>27,84</sup> The combination of requirements – principally alkaline electrolyte and visible light illumination – led to the conclusion that photogenerated holes (h<sup>+</sup>) and hydroxide ions cause two main effects; i) hydrogenation of the near-surface region, proposed as the formation of interstitial positively charged defects (H<sub>int</sub><sup>+</sup>), resulting in V<sup>4+</sup> and oxygen vacancies (v<sub>O</sub><sup>2+</sup>), and ii) saturation of the electrode surface with hydroxyl groups, which act as intermediates in the OER.<sup>49</sup> The proposed defect



chemistry reaction, described using Kröger-Vink notation and shown in equation 10, presents self-doping of the  $V_2O_5$  sublattice with reduced  $VO_2$  species, in alkaline conditions ( $OH^-$ ) and under illumination ( $h^*$ ). Here care should be taken to distinguish between a vanadium in vanadium site ( $V_V'$ ) and a vacant oxygen site ( $v_O^{2\bullet}$ ). Furthermore, the ( $O_O^x$ ) denotes the oxygen atoms occupying the regular oxygen sites.



These surface and near-surface alterations result in a record high photocurrent for undoped and uncatalyzed  $BiVO_4$  of  $4.3 \text{ mA cm}^{-2}$  at  $1.23 \text{ V}_{RHE}$ , an onset potential of  $0.25 \text{ V}_{RHE}$  corresponding to a doubling of the photovoltage, improved  $\phi_{inj}$  and  $\phi_{sep}$ , and near-unity internal quantum efficiency.<sup>48,49</sup> Electrochemical impedance spectroscopy (EIS) characterization suggests that photocharging leads to the formation of a surface capacitive layer, which has the ability to accumulate holes, and hence reduces the surface recombination. The formation of this capacitive layer involves the increase of hydroxyl groups at the surface and the partial reduction of vanadium 5+ to 4+, as supported by X-ray photoelectron spectroscopy (XPS) and X-ray absorption spectroscopy (XAS) measurements,<sup>49</sup> and more recently by intensity modulated photocurrent spectroscopy (IMPS).<sup>50</sup> IMPS results further elucidated that  $\phi_{inj}$  improvements (caused by the aforementioned surface state changes) increased charge transfer while decreasing recombination ( $k_{WO}$  and  $k_{rec}$  in equation 8, respectively).<sup>50</sup>

Contrary to the UV-curing study, which can enhance performance even when illuminated in air, photocharging could only be performed in an aqueous solution. While the surface states were observed to change following both treatments, the trends were opposite – i.e. increasing amount of dangling  $-OH$  surface sites in case of photocharging in an electrolyte and passivation of  $-OH$  in case of UV-curing in air (Figure 7b).<sup>47,49</sup> These differences between UV-cured  $W:BiVO_4$  and photocharged  $BiVO_4$  might be caused by either the differences in deposition method (sol-gel spin coating vs spray pyrolysis, respectively) which can cause different intrinsic surface or bulk defects,<sup>48</sup> or by the addition of W to  $BiVO_4$  in the UV-curing case which is known to form extrinsic trap states.<sup>32,46</sup> As noted previously, doping  $BiVO_4$  can cause significant alterations to the surface of  $BiVO_4$ ,<sup>42</sup> furthermore, doping  $BiVO_4$  with W is known to form additional trap states (versus pristine  $BiVO_4$ ), adversely affecting charge carrier mobilities and lifetimes.<sup>32</sup> More work is needed to confirm either of these hypotheses.

Notably, the mechanism proposed for photocharging is very similar to that for H<sub>2</sub>-annealed BiVO<sub>4</sub> and the role of hydrogen in BiVO<sub>4</sub>, as discussed in the previous section.<sup>45</sup> Both treatments – H<sub>2</sub> annealing and photocharging – are proposed to introduce hydrogen defects (H<sub>o</sub>, H<sub>int</sub>) and v<sub>o</sub>, as well as altering the surface states at the semiconductor-electrolyte interface. Both treatments have also been shown to improve  $\phi_{sep}$  and increase the concentration of surface dangling –OH groups,<sup>44,48</sup> which were shown to improve  $\phi_{inj}$  in photocharged samples.<sup>49</sup> In addition to the treatment conditions, the most significant difference between the electrodes is the localization of vanadium reduction to the near-surface (top 5-10 nm, based on XPS, XAS, and XANES results) of photocharged BiVO<sub>4</sub> compared to no reported localization in H<sub>2</sub>-annealed BiVO<sub>4</sub>. Similarities also exist between the photocharging treatment and some of the (photo)electrochemical treatments discussed in the previous section.<sup>27,48,49,51</sup> All of these treatments take place, optimally, in alkaline media and are accompanied by changes in the V oxidation state for an overall enhancement of photocurrent and improved onset potential. Indeed, the photocharging effect works best in alkaline media and not at all in acidic media.<sup>49</sup> Additionally, the initial report on photocharged BiVO<sub>4</sub> indicated that the treatment was reversible (i.e. unstable) when stored in the dark overnight in buffer;<sup>48</sup> however, EC-treated BiVO<sub>4</sub> was reported as stable over extended measurements (10 h PEC, 10 days in borate electrolyte), perhaps owing to the deposition of a catalytic layer following the electrochemical treatment.<sup>27</sup>

These similarities point towards a relationship between three effective post-synthetic treatments for improving the PEC efficiency of BiVO<sub>4</sub>, where H<sub>2</sub> annealing, photocharging, and electrochemical treatments achieve similar results based on possibly related underlying mechanisms.<sup>27,45,46,49,51</sup> Further data are needed to develop a deeper understanding and to find the most effective treatments for further performance gains. Bringing new measurement techniques to bare on BiVO<sub>4</sub> will certainly help illuminate changes.<sup>97–99</sup>

### 1.3.5 (d) Summary

Post-synthetic treatments offer powerful ways of removing a variety of surface recombination sites and improving (near)-surface kinetic properties of BiVO<sub>4</sub>-based photoanodes. Importantly, the type of defect present (and therefore the

synthetic method utilized) has a significant impact on the effectiveness of a given technique. For example, two similar treatments – UV curing and photocharging – are not interchangeable and seem to have opposite effects on different BiVO<sub>4</sub>-based electrodes.<sup>49</sup> Likewise, two seemingly disparate treatments – PEC activation (oxidation) and electrochemical cycling – both improve electrodes similarly, presumably because the initial-state after synthesis has different native defects.<sup>42,51</sup> Therefore, as research on BiVO<sub>4</sub> electrodes continues, it is important to carefully characterize the types and location of defects present within BiVO<sub>4</sub> before and after treatments. This is especially important when comparing different synthetic routes, but is equally relevant for the same synthesis where small changes to instrumentation can produce significantly different materials.<sup>46</sup>

### 1.3.6 Theoretical limits

Enhanced theoretical models<sup>100</sup> based on the detailed balance concept<sup>101</sup> predict fundamental prospects of solar water splitting devices and enable precise guidance for their development.<sup>102</sup> These models include fundamentally inevitable losses such as radiative recombination, thermalization, and transmission. However, oxide materials with highly non-ideal semiconductor properties, such as BiVO<sub>4</sub>, still represent significant challenges for both theoretical prediction and experimental implementation. Figure 8 compares the idealized optoelectronic performance limit for BiVO<sub>4</sub> (black line, in a hypothetical PV configuration) with present day record current-voltage characteristics (red/blue lines, PEC configuration, see also Figure 3). The theoretical calculation (black line, Figure 8) assumes idealized material by neglect of nonradiative recombination, of lattice imperfections, and of system losses (including catalysis, band offsets, resistances, etc.) that largely diminish the performance of experimental BiVO<sub>4</sub> PEC devices. Fundamentally, its 2.4 eV band gap ( $E_{bg}$ ) enables BiVO<sub>4</sub> to provide up to 2.1 V open circuit voltage ( $V_{oc}$ ) and 14.5% PV efficiency at a load of about 1.95 V (maximum power point, mpp). In the light of more than 700 mV sacrificial overvoltage (in excess of the thermodynamic water splitting potential of 1.23 V) even bias-free PEC operation of a single-junction absorber may appear conceivable. However a single-junction approach has not been achieved in practice due to major material deficiencies (recombination and poor band alignment) demanding a much higher overvoltage budget.

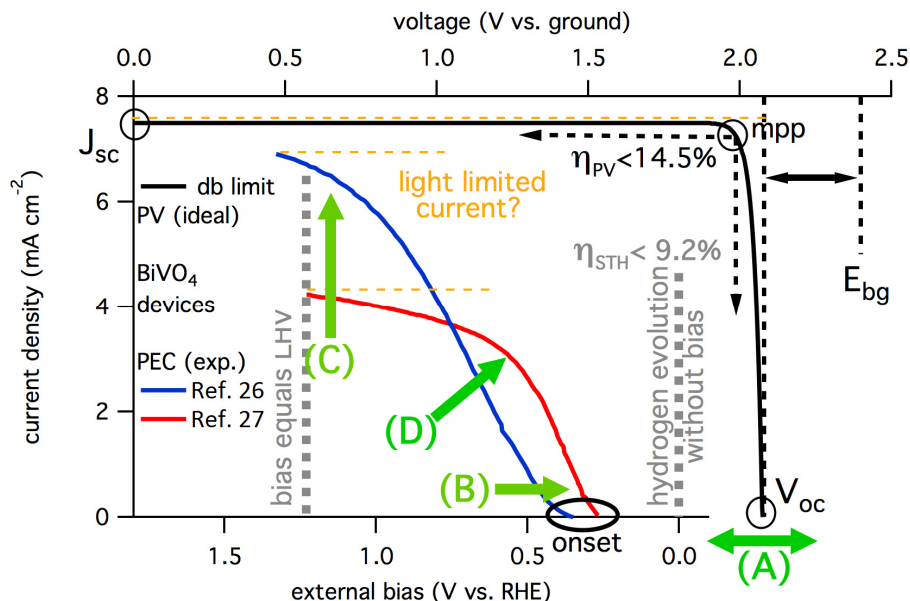


Figure 8. Comparison of I–V characteristics of experimental BiVO<sub>4</sub> PEC devices (blue/red, bottom axis) relative to the theoretical detailed balance limit for BiVO<sub>4</sub> photovoltaics (black, top axis).

Experimental PEC performance of BiVO<sub>4</sub> (Figures 3 & 8) lags far behind that ideal, but at least positive net energy contributions (up to ~2% ABPE, see above)<sup>25,27</sup> have been realized. Present and future development deals with three major bottlenecks restricting solar-to-hydrogen (STH) energy conversion with BiVO<sub>4</sub>: (i) non-radiative recombination, (ii) unfavorable band alignment, and (iii) an excessively large band gap energy. Engineering solutions such as host-guest architecture<sup>26,58,68</sup> decouple the mismatch of diffusion and absorption lengths enabling impressive photocurrents (Figure 8C). Gradient doping improves charge carrier extraction,<sup>39</sup> and thus effectively further suppresses the impact of non-radiative recombination events towards a more rectangular IV characteristic (Figure 8D). Both concepts also promise minor improvements of the photocurrent onset potential (Figure 8C), but are limited by the intrinsically non-ideal band alignment of BiVO<sub>4</sub> to the water oxidation/reduction potentials.

A priori, the transfer between absolute PV (upper axis) and relative PEC (lower axis) potential metrics remains unclear (Figure 8). Despite its high band gap and theoretical voltage prospects, BiVO<sub>4</sub> is considered incapable of driving unbiased water

splitting as its band edges do not straddle both water splitting half-reaction potentials.<sup>103</sup> However, appropriate engineering solutions such as surface modification with dipoles<sup>104</sup> or a buried p-n junction<sup>102</sup> may lessen or even resolve the misalignment. Tandem operation represents a more practical solution already demonstrated today.<sup>39,105,106</sup> Utilization of inevitable transmission losses (photons <2.4 eV) by a subsequently absorbing bottom PV structure may provide plenty additional (built-in) bias voltage. Figure 9 maps detailed balance tandem STH efficiency limits over both top and bottom absorber band gaps. Optimum structures may tolerate up to 2.3 V of overvoltage loss before severely restricting the performance prospects. The popular concept of combining BiVO<sub>4</sub> with multiple bottom junctions accommodates even higher losses.<sup>39,105,106</sup> Achieved performance gains indirectly demonstrate insufficient material quality of concurrent BiVO<sub>4</sub>, where its I-V characteristics virtually never saturate to a light-limited photocurrent regime with low applied bias. Engineering concepts promise to combine more ideal performance with better photocurrent onset.

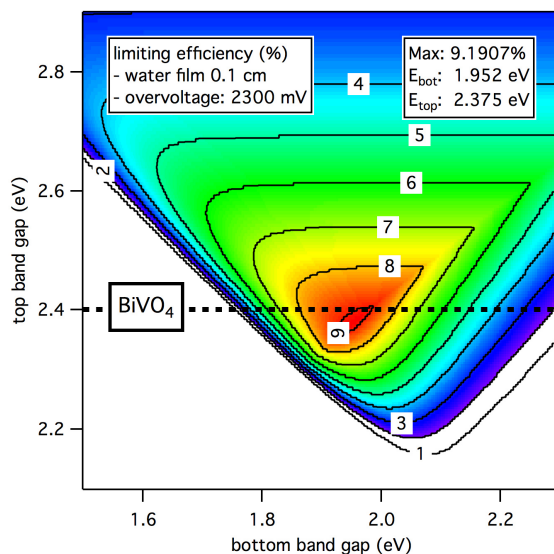


Figure 9. Detailed balance contour plots of the fundamental solar-to-hydrogen conversion efficiency limit for dual-junction watersplitting devices over the band gap energies of top and bottom absorber material for thin (1 mm) illumination length through the electrolyte and high (2300 mV) overvoltage loss.

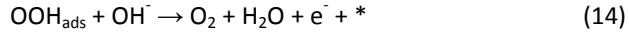
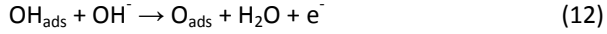
### 1.3.7 Post-synthetic treatments – overview

Bismuth vanadate is a well-studied and interesting material for use in solar-assisted water splitting. Recently, a variety of post-synthetic modifications have emerged to improve the ABPE performance of  $\text{BiVO}_4$ . Postsynthetic treatments have provided insights into  $\text{BiVO}_4$  defect chemistry at the surface and within the bulk of the material, yielding significant enhancements to charge injection and charge separation, respectively. Importantly, it has become apparent that probing the oxidation states by XPS alone cannot distinguish between the multiple posited changes to defect chemistries. For example thermal hydrogenation,<sup>43,45,46</sup> proton intercalation,<sup>48,49</sup> production of oxygen vacancies,<sup>25,43,48,49</sup> and electrochemical reduction<sup>27,81</sup> all are expected to yield reduced vanadium states. XPS measurements of vanadium oxidation states alone are not sufficient to distinguish between these various defect mechanisms. New insights will be drawn from future studies that attempt to parse these multiple causal pathways in the presently reported observations. Techniques to probe local electronic environments – e.g. solid-state NMR ( $^1\text{H}$ ,  $^{51}\text{V}$ , and  $^{209}\text{Bi}$ ),<sup>45,107–109</sup> Raman and IR spectroscopy,<sup>107,110</sup> electron energy loss spectroscopy (EELS),<sup>76–78</sup> STEM,<sup>77,111</sup> and X-ray absorption near edge structure (XANES)<sup>79</sup> – could be used in conjunction with computational methodologies to identify changes to specific defect chemistries. Here, inelastic X-ray techniques have yielded recent insights into changes at the  $\text{BiVO}_4$ /electrolyte interface<sup>97,99</sup> and to electronic structure with changing defect chemistry.<sup>23,98,112,113</sup> Once the defects are identified with specificity, then techniques that probe charge carrier dynamics (such as transient diffuse reflectance and time-resolved conductivity)<sup>35,46</sup> or trap states (such as photoluminescence)<sup>45</sup> could provide valuable insights into the role of those defects sites (e.g. catalytic site, trap site, and/or donor). Beyond immediate performance, post-synthetic treatments may also elucidate possible electrode changes under extended service and provide new strategies to enable extended device performance, furthering the development of commercial PEC water splitting devices.

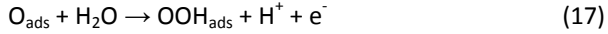
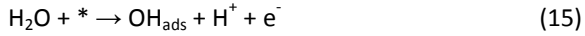
## 1.4 Electrochemical Water Oxidation

As previously mentioned, the water oxidation half-reaction is significantly more complex than water reduction. The oxygen evolution reaction (OER) proceeds through three different intermediates and involves the transfer of four electrons and protons. The detailed mechanism for OER<sup>19,114–116</sup> is presented in equations (11) – (14) for alkaline media and in equations (15) – (18) for acidic media:

Alkaline:



Acidic:



Due to such complexity, the kinetics of OER are rather slow, limiting the efficiency of energy storage via water splitting. Therefore, understanding, designing and investigating more active catalysts for OER is crucial to improve the efficiency of overall water splitting. Typically, the search for an optimal catalyst for a given reaction entails optimization of the binding energies for all the intermediates, such that each of the intermediates binds not too strongly and not too weakly to the catalyst. Thus, the free energies of all the reaction steps can be minimized and the reaction can proceed close to the thermodynamic equilibrium potential. However, the well-known problem with the OER is that the binding energies of two of the intermediates, OH and OOH,

are strongly correlated.<sup>19,114,115</sup> Therefore, it is impossible to optimize the binding energy of one, without affecting the other, an effect called the ‘scaling relationship’. Consequently, there exists an intrinsic thermodynamic limitation for the OER, i.e. no conventional catalyst can drive the OER with overpotential smaller than ~250 mV.<sup>19</sup>

The most widely studied electrocatalysts for OER are based on transition metal oxides. They provide reasonably high activity, selectivity and stability for water oxidation to oxygen. Out of this class of materials, the most active catalysts for OER are iridium and ruthenium oxides, excelling in acid and alkaline media respectively.<sup>117,118</sup> However, both those elements are too scarce and expensive to consider using them on a massive scale. Thus, one of the best alternatives to IrO<sub>2</sub> and RuO<sub>2</sub> are catalysts based on widely earth-abundant Ni. Nickel-based OECs operating in alkaline media have proven to oxidize water with activity similar to that of RuO<sub>2</sub> and IrO<sub>2</sub> catalysts.<sup>117,118</sup> Except for standard NiOx / NiOOH catalysts, a nickel–borate (Ni–B<sub>i</sub>) OEC optimized for mildly alkaline conditions has been recently presented.<sup>119–121</sup>

Pure metallic nickel itself is thermodynamically unstable under alkaline conditions, as suggested by the Pourbaix diagram of Ni.<sup>117</sup> Under open circuit conditions or potentials below ~1.4 V<sub>RHE</sub> metallic Ni spontaneously turns into nickel hydroxide Ni(OH)<sub>2</sub>, which is the reduced, non-active form of the catalyst. When sufficiently positive potential is applied, Ni(OH)<sub>2</sub> transforms into nickel oxyhydroxide (NiOOH), the oxidized, active form of the catalysts. Importantly, there are two primary phase systems in the nickel-water family: β-Ni(OH)<sub>2</sub>/β-NiOOH and α-Ni(OH)<sub>2</sub>/γ-NiOOH.<sup>122</sup> The β/β system is typical for fresh, as deposited films, has Ni in the average oxidation state of 2+/3+ (β-OH/β-OOH), and is catalytically less active.<sup>121</sup> The α/γ system is typical for anodically conditioned films, has Ni average oxidation state of 2+/3.6+ (α-OH/γ-OOH) and is catalytically more active.<sup>121</sup> All those nickel compounds crystalize in the form of closely packed sheets, with only weak interactions in between them. γ-NiOOH is known to possess extra water molecules and cations in between the sheets, causing the interplanar distance to be larger than in the β-counterpart, facilitating better ion transport and charge conductivity.<sup>123</sup> Recently it has been shown that Fe plays a big role in the β/β => α/γ phase transformation.<sup>123–126</sup> NiOOH fabricated and conditioned in rigorously Fe-pure electrolyte, recognized as β phase, shows very low OER activity. On the other hand, the Ni(Fe)OOH and pure NiOOH conditioned in Fe-rich electrolyte, recognized as γ phase, shows superior OER activity. To summarize,



there are 3 transformations in the Ni system: (1) spontaneous  $\text{Ni} \Rightarrow \text{Ni(OH)}_2$ , (2) potential driven  $\text{Ni(OH)}_2 \rightleftharpoons \text{NiOOH}$ , (3) Fe induced  $\beta/\beta \Rightarrow \alpha/\gamma$ .

Most photoanode materials do not have sufficient catalytic activity to drive OER with reasonable efficiencies. Thus, not surprisingly Ni-based OECs have been used as co-catalysts for photoanodes, in particular  $\text{BiVO}_4$ , to enhance their catalytic functionalities.<sup>27,37,91</sup> Typically a thin film of a Ni-based OEC would be deposited on top of the photoanode, thereby creating a stack where different functionalities are split over different layers, to create the most efficient device.  $\text{NiOOH}$  has been recently described as electrolyte-permeable catalyst, able to create a so-called adaptive junction when placed on a photoanode in a PEC cell.<sup>127–131</sup> It has several different consequences on the catalyst-semiconductor tandem energetics: the adaptive OECs screen the electronic charge on the catalyst, preventing formation of the potential drop across the catalyst, the interface energetics change during operation, i.e. the effective barrier height for the electron exchange depends on the potential of the catalyst, resulting in suppression of the Fermi level pinning and high photovoltages.<sup>128</sup>

Currently,  $\text{Ni(Fe)OOH}$  seems to be the best available OEC composed from earth-abundant elements.<sup>132</sup> Consequently, it is also the best candidate to be used in a future PEC device, when both efficiency and cost are to be considered. Therefore, it is imperative to gain thorough understanding of  $\text{Ni(Fe)OOH}$  system functioning. Only then the more efficient, fully optimized PEC photoanode – cocatalyst devices can be designed and created, to facilitate large-scale energy conversion and storage systems. Furthermore, even though Ni is a very active OER, the influence of electrolyte conditions (pH) have not been clearly shown yet, and learning how electrolyte affects the phase transformations of  $\text{NiOOH}$  may lead to greater understanding that can provide a blueprint for further catalyst/electrolyte optimization.

## 1.5 This Thesis

The general aim of this thesis is to study and engineer the oxygen evolution side of the PEC cell, where most of the bottlenecks in the solar water splitting lie. The focus is put on two materials, that together form an efficient tandem for light-driven OER:  $\text{BiVO}_4$  photoanodes and  $\text{Ni(Fe)OOH}$  OECs. Regarding  $\text{BiVO}_4$ , the goals are: (1) to investigate the possibilities of mitigating the bulk and surface limitations with approaches alternative to well-established techniques, thus to yield high photocurrents from  $\text{BiVO}_4$  with simple means, (2) to understand how different conditions govern the PEC properties of  $\text{BiVO}_4$ , thus to optimize the efficiency of the overall device and (3) to learn about the energetics at the  $\text{BiVO}_4$ -electrolyte junction. Regarding  $\text{Ni(Fe)OOH}$  the goals are: (1) to gain insights into the mechanism of OER on  $\text{Ni(Fe)OOH}$ , to (2) to understand the role of electrochemical environment on the properties and efficiency of Ni-based OECs and (3) to show any structural and functional differences between  $\text{Ni(Fe)OOH}$  and  $\text{Ni-B}_i$ . All the aims combined are geared towards creation of more efficient and better thought-out PEC solar water splitting systems. The secondary aim is to demonstrate the key role of the electrochemical environment in the PEC processes. Electrolytes of different composition and different pH can significantly change the properties and performance of the electrodes, and therefore the perspective to use them in a future PEC device. Therefore, we want to show that PEC systems should be studied as a whole, i.e. the electrode material together with the surrounding electrochemical environment.

In chapter 2 we introduce a novel simple technique to overcome the bulk and surface limitations of  $\text{BiVO}_4$ , which we call 'photocharging' (PC). Indeed, we demonstrate that the activity of  $\text{BiVO}_4$  photoanodes towards water oxidation can be significantly improved by prolonged exposure to AM1.5 illumination, while having the electrodes immersed in the electrolyte and in the open circuit (OC) configuration. We show that PC treatment allows for photocurrents of  $3.3 \text{ mAcm}^{-2}$  at  $1.23 \text{ V}_{\text{RHE}}$ , remarkably high for undoped and uncatalyzed  $\text{BiVO}_4$  at pH 7. Additionally, we demonstrate significantly enhanced catalytic efficiency in a broad potential range. We understand this as a signature of elimination of a major loss pathway at the semiconductor-electrolyte interface. We also observe enhanced photocurrents in the presence of sacrificial hole scavenger before and after the PC treatment, suggesting

improvement of the bulk-related functionalities as well. Furthermore, we observe improved photovoltages extracted from BiVO<sub>4</sub> photoanodes and a corresponding cathodic shift in the photocurrent onset potential.

In chapter 3 we look more deeply into the mechanism of the photocharging treatment and how it gives rise to improved performance of BiVO<sub>4</sub> photoanodes. Firstly, we investigate how different conditions affect the PC treatment. We discover that alkaline conditions are especially advantageous; we show that BiVO<sub>4</sub> photoanodes subjected to PC in pH 10 achieve record high photocurrent for undoped and uncatalyzed BiVO<sub>4</sub> of 4.3 mAcm<sup>-2</sup> @ 1.23 V<sub>RHE</sub>, as well as very low onset potential of 0.25 V<sub>RHE</sub> and a very steep photocurrent onset. Further, we investigate changes in the optical, structural, chemical and electronic properties of photocharged BiVO<sub>4</sub> to learn about the chemical and physical mechanisms behind the PC phenomenon and distinguish between the surface and bulk related effects. We use in-situ UV-vis spectroscopy to trace the optoelectronic properties of BiVO<sub>4</sub> during the treatment. We also look into the quantum efficiency of PC-BiVO<sub>4</sub> to study the spectral PEC response of the photoanodes. We find little qualitative, but huge quantitative improvements: PC-BiVO<sub>4</sub> reaches 75 and 95 % external and internal quantum efficiencies respectively. Additionally, we use in-situ PEC X-ray absorption spectroscopy (XAS) to look for changes in the structural and chemical properties of the bulk of the films. Complementarily, with aid of impedance spectroscopy we study the electronic properties of PC-BiVO<sub>4</sub>. With both of those techniques we find mainly signs for changes in the surface-related properties of PC-BiVO<sub>4</sub>. Based on our findings we present a model of how the photocharging effect possibly works. In our model we speculate about alkaline-conditions-favoured hydrogenation coupled with creation of oxygen vacancies and reduction of vanadium species, possibly accompanied with creation of oxo- water intermediates. We associate most of the observed enhancements with light-driven chemical transformations at the surface, leading to alterations of the energetics at the semiconductor-liquid junction. Those results signify the role of the electrochemical environment on the overall efficiency of a PEC system.

In chapter 4 we investigate two Ni-based OECs in Fe-containing media: nickel oxyhydroxide (Ni(Fe)OOH) and nickel borate (Ni(Fe)-B<sub>i</sub>). We use various in-situ spectroelectrochemical techniques (UV-vis, SERS and XAS) to systematically characterize them. Firstly, we show experimental evidence for the formation of NiOO<sup>-</sup>

sites, deprotonated, negatively charged NiOOH species, proposed in the literature as adsorbed “active oxygen”. We observe that the presence of those NiOO<sup>-</sup> sites on the surface of our catalysts seems to be directly responsible for high OER activity. Complementarily, we establish that the OER activity of Ni(Fe)OOH depends strongly on the alkalinity of the environment, which we attribute to the deprotonation of the catalyst, resulting in the formation of negatively charged surface sites, acting as OER precursors. Importantly, we demonstrate that not only the iron impurities but also the electrolyte plays a major role in activating NiOOH. Lastly, we look for significant structural, electronic, compositional, morphological, and optical differences between Ni(Fe)OOH and Ni(Fe)-B<sub>i</sub> and we fail to find any, suggesting that those two catalysts are surprisingly similar.

## 1.6 References

- (1) Smalley, R. E. *MRS Bull.* **2005**, 30 (6), 412–417.
- (2) van de Krol, R.; Grätzel, M. *Photoelectrochemical Hydrogen Production*; van de Krol, R., Grätzel, M., Eds.; Electronic Materials: Science & Technology; Springer US: Boston, MA, 2012; Vol. 102.
- (3) IEA, *Key world energy statistics*; 2016.
- (4) BP Statistical Review of World Energy; 2017.
- (5) BP Energy Outlook; 2017.
- (6) UN World Population Prospects; 2017.
- (7) Price waterhouse Coopers, *The World in 2050*; 2017.
- (8) EIA, *International Energy Outlook*; 2017.
- (9) Netherlands Environmental Assessment Agency, *CO2 time series 1990-2015 per region/country*; 2015.
- (10) *Unburnable Carbon*; 2014.
- (11) Scripps Institution of Oceanography at UC San Diego scripps.ucsd.edu (accessed May 12, 2018).
- (12) Loeb, N. G.; Wielicki, B. A.; Doelling, D. R.; Smith, G. L.; Keyes, D. F.; Kato, S.; Manalo-Smith, N.; Wong, T. J. *J. Clim.* **2009**, 22 (3), 748–766.

- (13) Trenberth, K. E.; Fasullo, J. T.; Kiehl, J. *Bull. Am. Meteorol. Soc.* **2009**, *90* (3), 311–323.
- (14) *Deutsche Bank Markets Research, 2014 Outlook: Let the Second Gold Rush Begin*; 2014.
- (15) Bolton, J. R.; Strickler, S. J.; Connolly, J. S. *Nature* **1985**, *316* (6028), 495–500.
- (16) WEBER, M.; DIGNAM, M. *Int. J. Hydrogen Energy* **1986**, *11* (4), 225–232.
- (17) MURPHY, A.; BARNES, P.; RANDENIYA, L.; PLUMB, I.; GREY, I.; HORNE, M.; GLASSCOCK, J. *Int. J. Hydrogen Energy* **2006**, *31* (14), 1999–2017.
- (18) Koper, M. T. M. *J. Electroanal. Chem.* **2011**, *660* (2), 254–260.
- (19) Man, I. C.; Su, H.-Y.; Calle-Vallejo, F.; Hansen, H. a.; Martínez, J. I.; Inoglu, N. G.; Kitchin, J.; Jaramillo, T. F.; Nørskov, J. K.; Rossmeisl, J. *ChemCatChem* **2011**, *3* (7), 1159–1165.
- (20) Kudo, A.; Ueda, K.; Kato, H.; Mikami, I. *Catal. Letters* **1998**, *53* (3/4), 229–230.
- (21) Tokunaga, S.; Kato, H.; Kudo, A. *Chem. Mater.* **2001**, *13* (12), 4624–4628.
- (22) Park, Y.; McDonald, K. J.; Choi, K.-S. *Chem. Soc. Rev.* **2013**, *42* (6), 2321–2337.
- (23) Cooper, J. K.; Gul, S.; Toma, F. M.; Chen, L.; Liu, Y.-S.; Guo, J.; Ager, J. W.; Yano, J.; Sharp, I. D. *J. Phys. Chem. C* **2015**, *119* (6), 2969–2974.
- (24) Walter, M. G.; Warren, E. L.; McKone, J. R.; Boettcher, S. W.; Mi, Q.; Santori, E. A.; Lewis, N. S. *Chem. Rev.* **2010**, *110* (11), 6446–6473.
- (25) Kim, T. W.; Ping, Y.; Galli, G. A.; Choi, K.-S. *Nat. Commun.* **2015**, *6*, 8769.
- (26) Pihosh, Y.; Turkevych, I.; Mawatari, K.; Uemura, J.; Kazoe, Y.; Kosar, S.; Makita, K.; Sugaya, T.; Matsui, T.; Fujita, D.; Tosa, M.; Kondo, M.; Kitamori, T. *Sci. Rep.* **2015**, *5* (1), 11141.
- (27) Kuang, Y.; Jia, Q.; Nishiyama, H.; Yamada, T.; Kudo, A.; Domen, K. *Adv. Energy Mater.* **2016**, *6* (2), 1501645.
- (28) Dotan, H.; Sivula, K.; Grätzel, M.; Rothschild, A.; Warren, S. C. *Energy Environ. Sci.* **2011**, *4* (3), 958–964.
- (29) Zhong, D. K.; Choi, S.; Gamelin, D. R. *J. Am. Chem. Soc.* **2011**, *133* (45), 18370–18377.
- (30) Liang, Y.; Tsubota, T.; Mooij, L. P. A.; van de Krol, R. *J. Phys. Chem. C* **2011**, *115* (35), 17594–17598.
- (31) Abdi, F. F.; van de Krol, R. *J. Phys. Chem. C* **2012**, *116* (17), 9398–9404.
- (32) Abdi, F. F.; Savenije, T. J.; May, M. M.; Dam, B.; van de Krol, R. *J. Phys. Chem. Lett.* **2013**, *4* (16), 2752–2757.
- (33) Ravensbergen, J.; Abdi, F. F.; van Santen, J. H.; Frese, R. N.; Dam, B.; van de Krol, R.; Kennis, J. T. M. *J. Phys. Chem. C* **2014**, *118* (48), 27793–27800.
- (34) Butler, K. T.; Dringoli, B. J.; Zhou, L.; Rao, P. M.; Walsh, A.; Titova, L. V. *J. Mater.*

- Chem. A* **2016**, *4* (47), 18516–18523.
- (35) Suzuki, Y.; Murthy, D. H. K.; Matsuzaki, H.; Furube, A.; Wang, Q.; Hisatomi, T.; Domen, K.; Seki, K. *J. Phys. Chem. C* **2017**, *121* (35), 19044–19052.
  - (36) Ma, Y.; Pendlebury, S. R.; Reynal, A.; Le Formal, F.; Durrant, J. R. *Chem. Sci.* **2014**, *5* (8), 2964–2973.
  - (37) Kim, T. W.; Choi, K.-S. *Science (80-. )*. **2014**, *343* (6174), 990–994.
  - (38) Zachäus, C.; Abdi, F. F.; Peter, L. M.; van de Krol, R. *Chem. Sci.* **2017**, *8* (5), 3712–3719.
  - (39) Abdi, F. F.; Han, L.; Smets, A. H. M.; Zeman, M.; Dam, B.; van de Krol, R. *Nat. Commun.* **2013**, *4*, 2195.
  - (40) Tolod, K.; Hernández, S.; Russo, N. *Catalysts* **2017**, *7* (1), 13.
  - (41) Tan, H. L.; Amal, R.; Ng, Y. H. *J. Mater. Chem. A* **2017**, *5* (32), 16498–16521.
  - (42) Luo, W.; Li, Z.; Yu, T.; Zou, Z. *J. Phys. Chem. C* **2012**, *116* (8), 5076–5081.
  - (43) Wang, G.; Ling, Y.; Lu, X.; Qian, F.; Tong, Y.; Zhang, J. Z.; Lordi, V.; Rocha Leao, C.; Li, Y. *J. Phys. Chem. C* **2013**, *117* (21), 10957–10964.
  - (44) Singh, A. P.; Kodan, N.; Dey, A.; Krishnamurthy, S.; Mehta, B. R. *Int. J. Hydrogen Energy* **2015**, *40* (12), 4311–4319.
  - (45) Cooper, J. K.; Scott, S. B.; Ling, Y.; Yang, J.; Hao, S.; Li, Y.; Toma, F. M.; Stutzmann, M.; Lakshmi, K. V.; Sharp, I. D. *Chem. Mater.* **2016**, *28* (16), 5761–5771.
  - (46) Jang, J.-W.; Friedrich, D.; Müller, S.; Lamers, M.; Hempel, H.; Lardhi, S.; Cao, Z.; Harb, M.; Cavallo, L.; Heller, R.; Eichberger, R.; van de Krol, R.; Abdi, F. F. *Adv. Energy Mater.* **2017**, *1701536*, 1701536.
  - (47) Li, T.; He, J.; Peña, B.; Berlinguette, C. P. *Angew. Chemie Int. Ed.* **2016**, *55* (5), 1769–1772.
  - (48) Trześniewski, B. J.; Smith, W. A. *J. Mater. Chem. A* **2016**, *4* (8), 2919–2926.
  - (49) Trześniewski, B. J.; Digdaya, I. A.; Nagaki, T.; Ravishankar, S.; Herraiz-Cardona, I.; Vermaas, D. A.; Longo, A.; Gimenez, S.; Smith, W. A. *Energy Environ. Sci.* **2017**, *10* (6), 1517–1529.
  - (50) Liu, E. Y.; Thorne, J. E.; He, Y.; Wang, D. *ACS Appl. Mater. Interfaces* **2017**, *9* (27), 22083–22087.
  - (51) Lamm, B.; Sarkar, A.; Stefik, M. *J. Mater. Chem. A* **2017**, *5* (13), 6060–6069.
  - (52) Ding, J.; Dai, Z.; Tian, F.; Zhou, B.; Zhao, B.; Zhao, H.; Chen, Z.; Liu, Y.; Chen, R. *J. Mater. Chem. A* **2017**, *5* (45), 23453–23459.
  - (53) Parmar, K. P. S.; Kang, H. J.; Bist, A.; Dua, P.; Jang, J. S.; Lee, J. S. *ChemSusChem* **2012**, *5* (10), 1926–1934.
  - (54) Eisenberg, D.; Ahn, H. S.; Bard, A. J. *J. Am. Chem. Soc.* **2014**, *136* (40), 14011–14014.

- (55) Zhang, L.; Ye, X.; Boloor, M.; Poletayev, A.; Melosh, N. A.; Chueh, W. C. *Energy Environ. Sci.* **2016**, 9 (6), 2044–2052.
- (56) Gutkowski, R.; Khare, C.; Conzuelo, F.; Kayran, Y. U.; Ludwig, A.; Schuhmann, W. *Energy Environ. Sci.* **2017**, 10 (5), 1213–1221.
- (57) Kalanur, S. S.; Yoo, I.-H.; Park, J.; Seo, H. J. *Mater. Chem. A* **2017**, 5 (4), 1455–1461.
- (58) Shi, X.; Choi, I. Y.; Zhang, K.; Kwon, J.; Kim, D. Y.; Lee, J. K.; Oh, S. H.; Kim, J. K.; Park, J. H. *Nat. Commun.* **2014**, 5, 4775.
- (59) Galembeck, A.; Alves, O. L. *Thin Solid Films* **2000**, 365 (1), 90–93.
- (60) Seabold, J. A.; Choi, K. J. *Am. Chem. Soc.* **2012**, 134 (4), 2186–2192.
- (61) Chen, L.; Alarcón-Lladó, E.; Hettick, M.; Sharp, I. D.; Lin, Y.; Javey, A.; Ager, J. W. *J. Phys. Chem. C* **2013**, 117 (42), 21635–21642.
- (62) Gong, H.; Freudenberg, N.; Nie, M.; van de Krol, R.; Ellmer, K. *AIP Adv.* **2016**, 6 (4), 45108.
- (63) Alarcón-Lladó, E.; Chen, L.; Hettick, M.; Mashouf, N.; Lin, Y.; Javey, A.; Ager, J. W. *Phys. Chem. Chem. Phys.* **2014**, 16 (4), 1651–1657.
- (64) Stefik, M. *ChemSusChem* **2016**, 9 (13), 1727–1735.
- (65) Zhang, L.; Reisner, E.; Baumberg, J. J. *Energy Environ. Sci.* **2014**, 7 (4), 1402.
- (66) Su, J.; Guo, L.; Bao, N.; Grimes, C. a. *Nano Lett.* **2011**, 11 (5), 1928–1933.
- (67) Zhou, L.; Zhao, C.; Giri, B.; Allen, P.; Xu, X.; Joshi, H.; Fan, Y.; Titova, L. V.; Rao, P. M. *Nano Lett.* **2016**, 16 (6), 3463–3474.
- (68) Zhou, L.; Yang, Y.; Zhang, J.; Rao, P. M. *ACS Appl. Mater. Interfaces* **2017**, 9 (13), 11356–11362.
- (69) *CRC Handbook of Chemistry and Physics*, 92nd ed.; Hayes, W., Lide, D. R., Eds.; Taylor & Francis: Boca Raton, 2011.
- (70) Schuisky, M.; Kukli, K.; Ritala, M.; Hårsta, A.; Leskelä, M. *Chem. Vap. Depos.* **2000**, 6 (3), 139–145.
- (71) Fidelsky, V.; Toroker, M. C. *J. Phys. Chem. C* **2016**, 120 (44), 25405–25410.
- (72) Diaz-Morales, O.; Ferrus-Suspedra, D.; Koper, M. T. M. *Chem. Sci.* **2016**, 7 (4), 2639–2645.
- (73) Wang, G.; Ling, Y.; Wang, H.; Yang, X.; Wang, C.; Zhang, J. Z.; Li, Y. *Energy Environ. Sci.* **2012**, 5 (3), 6180.
- (74) Wang, G.; Wang, H.; Ling, Y.; Tang, Y.; Yang, X.; Fitzmorris, R. C.; Wang, C.; Zhang, J. Z.; Li, Y. *Nano Lett.* **2011**, 11 (7), 3026–3033.
- (75) Lu, X.; Wang, G.; Xie, S.; Shi, J.; Li, W.; Tong, Y.; Li, Y. *Chem. Commun.* **2012**, 48 (62), 7717.
- (76) Zhao, Z.; Li, Z.; Zou, Z. *RSC Adv.* **2011**, 1 (5), 874.

- (77) Rossell, M. D.; Agrawal, P.; Borgschulte, A.; Hébert, C.; Passerone, D.; Erni, R. *Chem. Mater.* **2015**, *27* (10), 3593–3600.
- (78) Torruella, P.; Coll, C.; Martín, G.; López-Conesa, L.; Vila, M.; Díaz-Guerra, C.; Varela, M.; Ruiz-González, M. L.; Piqueras, J.; Peiró, F.; Estradé, S. *J. Phys. Chem. C* **2017**, *121* (44), 24809–24815.
- (79) Pattengale, B.; Ludwig, J.; Huang, J. *J. Phys. Chem. C* **2016**, *120* (3), 1421–1427.
- (80) Nair, V.; Perkins, C. L.; Lin, Q.; Law, M. *Energy Environ. Sci.* **2016**, *9* (4), 1412–1429.
- (81) Qin, D.-D.; Wang, T.; Song, Y.-M.; Tao, C.-L. *Dalt. Trans.* **2014**, *43* (21), 7691.
- (82) Venkatesan, R.; Velumani, S.; Tabellout, M.; Errien, N.; Kassiba, A. *J. Phys. Chem. Solids* **2013**, *74* (12), 1695–1702.
- (83) Yin, W.-J.; Wei, S.-H.; Al-Jassim, M. M.; Turner, J.; Yan, Y. *Phys. Rev. B* **2011**, *83* (15), 155102.
- (84) Toma, F. M.; Cooper, J. K.; Kunzelmann, V.; McDowell, M. T.; Yu, J.; Larson, D. M.; Borys, N. J.; Abelyan, C.; Beeman, J. W.; Yu, K. M.; Yang, J.; Chen, L.; Shaner, M. R.; Spurgeon, J.; Houle, F. a; Persson, K. a; Sharp, I. D. *Nat. Commun.* **2016**, *7* (May), 12012.
- (85) Rettie, A. J. E.; Chemelewski, W. D.; Emin, D.; Mullins, C. B. *J. Phys. Chem. Lett.* **2016**, *7* (3), 471–479.
- (86) Kweon, K. E.; Hwang, G. S. *Appl. Phys. Lett.* **2013**, *103* (13), 131603.
- (87) Liang, Y.; Messinger, J. *Phys. Chem. Chem. Phys.* **2014**, *16* (24), 12014.
- (88) McDowell, M. T.; Lichterman, M. F.; Spurgeon, J. M.; Hu, S.; Sharp, I. D.; Bruntschwig, B. S.; Lewis, N. S. *J. Phys. Chem. C* **2014**, *118* (34), 19618–19624.
- (89) Jeon, T. H.; Choi, W.; Park, H. *Phys. Chem. Chem. Phys.* **2011**, *13* (48), 21392–21401.
- (90) Lai, Y.-H. H.; Palm, D. W.; Reisner, E. *Adv. Energy Mater.* **2015**, *5* (24), 1501668.
- (91) Choi, S. K.; Choi, W.; Park, H. *Phys. Chem. Chem. Phys.* **2013**, *15* (17), 6499.
- (92) Ding, C.; Shi, J.; Wang, D.; Wang, Z.; Wang, N.; Liu, G.; Xiong, F.; Li, C. *Phys. Chem. Chem. Phys.* **2013**, *15* (13), 4589.
- (93) Li, M.; Luo, W.; Liu, B.; Zhao, X.; Li, Z.; Chen, D.; Yu, T.; Xie, Z.; Zhang, R.; Zou, Z. *Appl. Phys. Lett.* **2011**, *99* (11), 112108.
- (94) Sayama, K.; Nomura, A.; Arai, T.; Sugita, T.; Abe, R.; Oi, T.; Iwasaki, Y.; Abe, Y.; Sugihara, H.; Yanagida, M.; Oi, T.; Iwasaki, Y.; Abe, Y.; Sugihara, H. *J. Phys. Chem. B* **2006**, *110* (23), 11352–11360.
- (95) Walsh, A.; Yan, Y.; Huda, M. N.; Al-Jassim, M. M.; Wei, S.-H. *Chem. Mater.* **2009**, *21* (3), 547–551.
- (96) Krishnan Rajeshwar. In *Encyclopedia of Electrochemistry*; Wiley-VCH Verlag GmbH & Co. KGaA: Weinheim, Germany, Germany, 2007; pp 1–53.



- (97) Starr, D. E.; Favaro, M.; Abdi, F. F.; Bluhm, H.; Crumlin, E. J.; van de Krol, R. *J. Electron Spectros. Relat. Phenomena* **2017**, *221*, 106–115.
- (98) Jovic, V.; Laverock, J.; Rettie, A. J. E.; Zhou, J.-S.; Mullins, C. B.; Singh, V. R.; Lamoureux, B.; Wilson, D.; Su, T.-Y.; Jovic, B.; Bluhm, H.; Söhnle, T.; Smith, K. E. *J. Mater. Chem. A* **2015**, *3* (47), 23743–23753.
- (99) Favaro, M.; Abdi, F. F.; Lamers, M.; Crumlin, E. J.; Liu, Z.; van de Krol, R.; Starr, D. E. *J. Phys. Chem. B* **2018**, *122* (2), 801–809.
- (100) Döscher, H.; Geisz, J. F.; Deutsch, T. G.; Turner, J. A. *Energy Environ. Sci.* **2014**, *7* (9), 2951–2956.
- (101) Shockley, W.; Queisser, H. J. *J. Appl. Phys.* **1961**, *32* (3), 510–519.
- (102) Young, J. L.; Steiner, M. A.; Döscher, H.; France, R. M.; Turner, J. A.; Deutsch, T. G. *Nat. Energy* **2017**, *2* (4), 17028.
- (103) Zhou, M.; Bao, J.; Bi, W.; Zeng, Y.; Zhu, R.; Tao, M.; Xie, Y. *ChemSusChem* **2012**, *5* (8), 1420–1425.
- (104) Garner, L. E.; Steirer, K. X.; Young, J. L.; Anderson, N. C.; Miller, E. M.; Tinkham, J. S.; Deutsch, T. G.; Sellinger, A.; Turner, J. A.; Neale, N. R. *ChemSusChem* **2017**, *10* (4), 767–773.
- (105) Döscher, H.; Young, J. L.; Geisz, J. F.; Turner, J. A.; Deutsch, T. G. *Energy Environ. Sci.* **2016**, *9* (1), 74–80.
- (106) Zhang, K.; Ma, M.; Li, P.; Wang, D. H.; Park, J. H. *Adv. Energy Mater.* **2016**, *6* (15), 1600602.
- (107) Hardcastle, F. D.; Wachs, I. E.; Eckert, H.; Jefferson, D. A. *J. Solid State Chem.* **1991**, *90* (2), 194–210.
- (108) Morgan, K.; Sayer, B. G.; Schrobilgen, G. J. *J. Magn. Reson.* **1983**, *52* (1), 139–142.
- (109) Hamaed, H.; Laschuk, M. W.; Tersikh, V. V.; Schurko, R. W. *J. Am. Chem. Soc.* **2009**, *131* (23), 8271–8279.
- (110) Frost, R. L.; Henry, D. A.; Weier, M. L.; Martens, W. *J. Raman Spectrosc.* **2006**, *37* (7), 722–732.
- (111) Tate, M. L.; Blom, D. A.; Avdeev, M.; Brand, H. E. A.; McIntyre, G. J.; Vogt, T.; Evans, I. R. *Adv. Funct. Mater.* **2017**, *27* (8), 1605625.
- (112) Cooper, J. K.; Gul, S.; Toma, F. M.; Chen, L.; Glans, P.-A.; Guo, J.; Ager, J. W.; Yano, J.; Sharp, I. D. *Chem. Mater.* **2014**, *26* (18), 5365–5373.
- (113) Resasco, J.; Zhang, H.; Kornienko, N.; Becknell, N.; Lee, H.; Guo, J.; Briseno, A. L.; Yang, P. *ACS Cent. Sci.* **2016**, *2* (2), 80–88.
- (114) Rossmeisl, J.; Logadottir, A.; Nørskov, J. K. *Chem. Phys.* **2005**, *319* (1–3), 178–184.
- (115) Rossmeisl, J.; Qu, Z.-W.; Zhu, H.; Kroes, G.-J.; Nørskov, J. K. *J. Electroanal.*

- Chem.* **2007**, 607 (1–2), 83–89.
- (116) Dau, H.; Limberg, C.; Reier, T.; Risch, M.; Roggan, S.; Strasser, P. *ChemCatChem* **2010**, 2 (7), 724–761.
  - (117) Digdaya, I. A.; Adhyaksa, G. W. P.; Trześniewski, B. J.; Garnett, E. C.; Smith, W. A. *Nat. Commun.* **2017**, 8 (May), 15968.
  - (118) Lee, Y.; Suntivich, J.; May, K. J.; Perry, E. E.; Shao-Horn, Y. *J. Phys. Chem. Lett.* **2012**, 399–404.
  - (119) Dincă, M.; Surendranath, Y.; Nocera, D. G. *Proc. Natl. Acad. Sci. U. S. A.* **2010**, 107 (23), 10337–10341.
  - (120) Bediako, D. K.; Surendranath, Y.; Nocera, D. G. *J. Am. Chem. Soc.* **2013**, 135 (9), 3662–3674.
  - (121) Bediako, D. K.; Lassalle-Kaiser, B.; Surendranath, Y.; Yano, J.; Yachandra, V. K.; Nocera, D. G. *J. Am. Chem. Soc.* **2012**, 134 (15), 6801–6809.
  - (122) Van der Ven, a.; Morgan, D.; Meng, Y. S.; Ceder, G. *J. Electrochem. Soc.* **2006**, 153 (2), A210–A215.
  - (123) Klaus, S.; Cai, Y.; Louie, M. W.; Trotochaud, L.; Bell, A. T. *J. Phys. Chem. C* **2015**, 119 (13), 7243–7254.
  - (124) Trotochaud, L.; Young, S. L.; Ranney, J. K.; Boettcher, S. W. *J. Am. Chem. Soc.* **2014**, 136 (18), 6744–6753.
  - (125) Smith, A. M.; Trotochaud, L.; Burke, M. S.; Boettcher, S. *Chem. Commun.* **2014**, 51, 5261–5263.
  - (126) Friebel, D.; Louie, M. W.; Bajdich, M.; Sanwald, K. E.; Cai, Y.; Wise, A. M.; Cheng, M.-J.; Sokaras, D.; Weng, T.-C.; Alonso-Mori, R.; Davis, R. C.; Bargar, J. R.; Nørskov, J. K.; Nilsson, A.; Bell, A. T. *J. Am. Chem. Soc.* **2015**, 137 (3), 1305–1313.
  - (127) Laskowski, F. A. L.; Nellist, M. R.; Venkatkarthick, R.; Boettcher, S. W. *Energy Environ. Sci.* **2017**, 10 (2), 570–579.
  - (128) Nellist, M. R.; Laskowski, F. a L.; Lin, F.; Mills, T. J.; Boettcher, S. W. *Acc. Chem. Res.* **2016**, 49 (4), 733–740.
  - (129) Lin, F.; Boettcher, S. W. *Nat. Mater.* **2014**, 13 (1), 81–86.
  - (130) Lin, F.; Bachman, B. F.; Boettcher, S. W. *J. Phys. Chem. Lett.* **2015**, 6 (13), 2427–2433.
  - (131) Mills, T. J.; Lin, F.; Boettcher, S. W. *Phys. Rev. Lett.* **2014**, 112 (14), 148304.
  - (132) McCrory, C. C. L.; Jung, S.; Peters, J. C.; Jaramillo, T. F. *J. Am. Chem. Soc.* **2013**, 135 (45), 16977–16987.

## 2. Photocharged BiVO<sub>4</sub> Photoanodes for Improved Solar Water Splitting

Bismuth vanadate (BiVO<sub>4</sub>) is a promising semiconductor material for the production of solar fuels via photoelectrochemical water splitting, however, it suffers from substantial recombination losses that limit its performance to well below its theoretical maximum. Here we demonstrate for the first time that the photoelectrochemical (PEC) performance of BiVO<sub>4</sub> photoanodes can be dramatically improved by prolonged exposure to AM1.5 illumination in the open circuit (OC) configuration. Photoanodes subjected to such light treatment achieve a record photocurrent for undoped and uncatalysed BiVO<sub>4</sub> of 3.3 mAcm<sup>-2</sup> at 1.23 V<sub>RHE</sub>. Moreover, photoelectrochemical tests with a sacrificial agent yield significantly enhanced catalytic efficiency over the whole operating potential range, suggesting elimination of major losses at the semiconductor-electrolyte interface. Finally, we demonstrate that this so-called ‘photocharging’ technique induces a considerable cathodic shift in the photocurrent onset potential and increases the photovoltage extracted from BiVO<sub>4</sub> photoanodes.

---

This chapter has been published as: B. J. Trześniewski and W. A. Smith, *J. Mater. Chem. A*, 2016, 4, 2919–2926 (10.1039/c5ta04716a)

## 2.1 Introduction

Photoelectrochemical (PEC) water splitting offers an efficient and sustainable way to store solar energy in the form of chemical bonds.<sup>1–3</sup> One of the most attractive ways to achieve this solar driven water splitting is by using light-absorbing semiconductors to capture and convert sunlight into chemical energy by driving the corresponding water reduction and oxidation reactions. Bismuth vanadate ( $\text{BiVO}_4$ ) is a promising n-type semiconducting material for photoelectrochemical water splitting devices due to its ability to absorb visible light (band-gap energy  $\sim 2.4$  eV), a favorable conduction band edge position (just below the water reduction potential), and its relative stability in near-neutral aqueous environments. Moreover, it is made of cheap, non-toxic, earth-abundant elements and can be easily produced on a large scale. In order to make the production of solar hydrogen with  $\text{BiVO}_4$  viable, its performance bottlenecks and limitations have to be identified and addressed accordingly.

Based on its band gap energy,  $\text{BiVO}_4$  should be able to produce upwards of  $\sim 7.5$   $\text{mA}/\text{cm}^2$  of photocurrent under AM 1.5 irradiation.<sup>4,5</sup> However, to date, this photoanode has achieved far less than its full potential. It has been suggested that  $\text{BiVO}_4$  suffers from poor surface catalytic activity, and thus many strategies have focused on passivating or putting dedicated oxygen evolution catalysts (OECs) on its surface. The results of both passivation and co-catalysis have achieved significantly enhanced photoactivity at reduced overpotentials, but the mechanism for how these methods work are limited. In fact, a new performance benchmark for  $\text{BiVO}_4$  photoanodes has recently been set by Kim and Choi,<sup>6</sup> who observed photocurrent densities of  $1.7$   $\text{mAcm}^{-2}$  (at  $1.23$   $V_{\text{RHE}}$ ) for undoped nanostructured  $\text{BiVO}_4$ , and  $4.5$   $\text{mAcm}^{-2}$  (at  $1.23$   $V_{\text{RHE}}$ ) for  $\text{BiVO}_4$  catalysed with a dual layer  $\text{FeOOH}/\text{NiOOH}$  OEC. Many other attempts have been made to improve the surface catalytic reactivity of  $\text{BiVO}_4$  by the addition of other OEC's such as Co-Pi, Co-Bi and Ni-Bi.<sup>7–10</sup> However, strong parasitic light absorption by OECs (up to 20% for layers as thin as 2 nm)<sup>11</sup> can make them prohibitive to use in tandem water splitting devices that require illumination through the electrolyte/OEC interface. In addition, the catalytic activity at low bias potentials remains low for photoanodes even when modified with co-catalysts. It is therefore of paramount importance to understand the physical and chemical nature of the semiconductor/electrolyte interface in  $\text{BiVO}_4$  photoanodes, specifically the role of

electronic surface states that may constitute the favorable pathways for unwanted recombination. Therefore new strategies to tackle surface catalytic reactivity are necessary.

In addition to its poor surface catalytic reactivity,  $\text{BiVO}_4$  also suffers from poor charge separation efficiency due to bulk recombination losses. It has been reported that spray deposited  $\text{BiVO}_4$  photoanodes have 35% charge separation efficiency at 1.23  $V_{\text{RHE}}$ ,<sup>12</sup> showing that bulk processes are severely limiting its performance. Previous research has aimed at tackling this problem by introducing elemental doping, most notably with W and Mo.<sup>12–14</sup> Of particular note, the most significant improvement in the charge separation efficiency was reported by utilizing a novel W-gradient doping profile in the  $\text{BiVO}_4$ , which significantly increased the charge separation efficiency in the bulk of the photoanode.<sup>15</sup>

Herein we report a new photoanode treatment technique made possible by so-called ‘photocharging’. We demonstrate that the PEC performance of  $\text{BiVO}_4$  photoanodes can be dramatically improved by prolonged exposure to AM1.5 illumination in the open circuit (OC) configuration. Such a light treatment results in double the record benchmark photocurrent density for undoped and uncatalyzed  $\text{BiVO}_4$  at 1.23  $V_{\text{RHE}}$ , a 0.3 V cathodic shift of the photocurrent onset potential, and near unity catalytic efficiency in the operational potential range. Preliminary analysis shows that this overall performance enhancement is largely due to improvements in the surface of the  $\text{BiVO}_4$  photoanodes, though it was also observed that bulk modifications may also play a role in the enhanced activity as well. Ultimately, we demonstrate a novel approach to investigate and improve the nature of the  $\text{BiVO}_4$ /electrolyte interface leading to a new benchmark performance for un-doped and un-catalyzed  $\text{BiVO}_4$  photoanodes.

## 2.2 Experimental

### 2.2.1 Preparation of BiVO<sub>4</sub> thin film photoanodes

Thin films of 200 nm thick BiVO<sub>4</sub> were prepared by spray pyrolysis on FTO coated glass substrates. Details of the deposition procedure are described elsewhere<sup>5,12</sup> and are also available in Appendix I. Prior to deposition of the BiVO<sub>4</sub>, a SnO<sub>2</sub> interfacial layer (~80 nm) was deposited onto the FTO substrate at 425 °C to prevent recombination at the FTO/BiVO<sub>4</sub> interface.<sup>16</sup> The substrate temperature during spraying of BiVO<sub>4</sub> was maintained at 450 °C. After deposition, the samples were further annealed for 2 h in a tube furnace at 450 °C in air.

### 2.2.2 Photoelectrochemical (PEC) measurements

Photoelectrochemical characterization of BiVO<sub>4</sub> photoanodes was carried out in an electrochemical cell using a three-electrode configuration. A 0.1 M phosphate buffer (0.1 K-P<sub>i</sub>) was used as electrolyte, prepared by dissolving K<sub>2</sub>HPO<sub>4</sub> (98%, Sigma) and KH<sub>2</sub>PO<sub>4</sub> (99%, Sigma) in Milli-Q water (18.2 MΩcm) to obtain pH 7.2. The potential of the working electrode was controlled by a multi-channel potentiostat (Parstat MC, Princeton Applied Research). An Ag/AgCl electrode (XR300, saturated KCl + AgCl solution (KS120), Radiometer Analytical) and a coiled Pt wire were used as the reference and counter electrodes, respectively. Measurements under illumination were performed with a Newport Sol3A Class AAA solar simulator (type 94023A-SR3) producing simulated AM1.5 solar illumination (100 mW/cm<sup>2</sup>). In all the experiments involving illumination, BiVO<sub>4</sub> samples were illuminated from the back-side, i.e. the light came through the substrate side first.

The photovoltage of BiVO<sub>4</sub> photoanodes was investigated with a series of open circuit (OC) measurements; potential of the working electrode ( $V_{WE}$ ) was monitored in the dark and under AM1.5 illumination until an equilibrium plateau in the  $V_{WE}(t)$  was reached.

The photocharging of BiVO<sub>4</sub> photoanodes was performed in OC conditions under illumination. BiVO<sub>4</sub> samples were placed in the electrochemical cell and exposed to AM 1.5 light until the plateau of  $V_{WE}(t)$  was reached (10 hours on average).

Cyclic voltammetry scans were taken at a scan speed of 50 mV/s unless stated otherwise. To examine the catalytic efficiency, 1.5 ml of H<sub>2</sub>O<sub>2</sub> (30%, Merck) was added to the electrolyte solution.

### 2.2.3 X-ray photoelectron spectroscopy (XPS)

XPS experiment was performed using the Thermo Scientific K-alpha apparatus equipped with an Al K-alpha X-ray Source and a Flood Gun. Parameters used for the measurements were: spot size of 400  $\mu$ m, pass energy of 50 eV, energy step size of 0.1 eV, dwell time of 50 ms, 10 scans in the vicinity of V2p orbital binding energy. XPS spectra were corrected for the C peak position.

## 2.3 Results and Discussion

### 2.3.1 Photoelectrochemical (PEC) measurements

The PEC performance of the untreated BiVO<sub>4</sub> photoanodes was first measured under AM 1.5 irradiation to obtain the photocurrent density as a function of the applied potential, as shown in Figure 1. The untreated samples show a photocurrent onset potential ( $V_{on}$ ) of  $\sim 0.7 V_{RHE}$ , and a photocurrent density of  $0.8 \text{ mAcm}^{-2}$  at  $1.23 V_{RHE}$  (solid black curve). Within the range of potentials applied, the current density vs. voltage (J-V) curve has a very poor slope, a concave shape, and doesn't obtain a saturated current density, suggesting a substantial amount of surface recombination. It has been previously shown,<sup>12</sup> that H<sub>2</sub>O<sub>2</sub> is an excellent hole scavenger for BiVO<sub>4</sub> photoanodes in these conditions, and thus it is proposed that when using H<sub>2</sub>O<sub>2</sub> in the electrolyte solution, the performance can be estimated to yield near 100% catalytic efficiency. Therefore, using an electrolyte with H<sub>2</sub>O<sub>2</sub> provides the benchmark for the

highest expected activity that these photoelectrodes can achieve if there are no surface recombination losses. When the un-treated  $\text{BiVO}_4$  photoanodes were measured in an electrolyte containing  $\text{H}_2\text{O}_2$ , the JV curves show a remarkable, but expected, improvement in both the on-set potential ( $V_{\text{on}} = 0.6 V_{\text{RHE}}$ ) and photocurrent density at 1.23 V vs. RHE ( $J = 3.3 \text{ mA/cm}^2$ ), as shown in the dashed black curve in Figure 1. The PEC performance of the  $\text{BiVO}_4$  photoanodes in  $\text{H}_2\text{O}$  and in an  $\text{H}_2\text{O}_2$  containing electrolyte are used to act as a reference for the activity of our untreated samples in an aqueous solution, and with no surface catalytic losses.

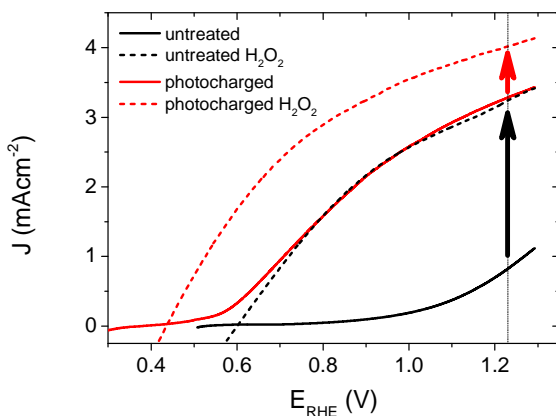


Figure 1. J-V scans of 200 nm thick  $\text{BiVO}_4$  under back-side AM1.5 illumination, in 0.1 M K-P<sub>i</sub> buffer (pH 7.2), scan rate  $50 \text{ mVs}^{-1}$ , anodic sweeps. Arrows denote catalytic limitations for untreated (black) and photocharged (red) material.

After obtaining the JV characteristics of the pure  $\text{BiVO}_4$  photoanodes, the samples were subjected to a simple pre-treatment technique. The  $\text{BiVO}_4$  photoanodes were placed in the PEC cell and held in OC conditions (i.e. no applied bias) and exposed to AM 1.5 illumination until an equilibrium potential was observed (10 hours on average). We subsequently refer to this process as photocharging. Immediately following this photocharging treatment, the JV characteristics under AM 1.5 illumination were measured for the treated samples (shown in Figure 1, red solid curve), and the photocharged photoanodes show strikingly different PEC features than the untreated films.



After the photocharging treatment, the shape of the JV characteristic becomes convex and a record photocurrent of  $3.3 \text{ mAcm}^{-2}$  at  $1.23 \text{ V}_{\text{RHE}}$  for undoped and uncatalyzed  $\text{BiVO}_4$  was achieved. In addition, the treated photoanodes show a substantial cathodic shift of the  $V_{\text{on}}$  by  $\sim 0.3 \text{ V}$ . Remarkably, the J-V of the photocharged photoanode follows almost exactly the photocurrent of the un-treated  $\text{BiVO}_4$  measured in the presence of  $\text{H}_2\text{O}_2$ . The shape of the J-V curve suggests<sup>17</sup> major suppression of the surface recombination due to the very steep photocurrent slope, relatively low applied potential required to achieve a saturated current density, and convex shape of the curve. The PEC performance of the photocharged  $\text{BiVO}_4$  samples was similarly tested after adding  $\text{H}_2\text{O}_2$  to the electrolyte, as shown in the dashed red curve in Figure 1. Surprisingly, the JV characteristics under these conditions showed a further decreased onset potential,  $V_{\text{on}} = 0.43 \text{ V}_{\text{RHE}}$ , and a larger photocurrent density at  $1.23 \text{ V}_{\text{RHE}}$ ,  $J = 4.0 \text{ mA/cm}^2$ .

To further quantify the change in the surface reactivity for each of the  $\text{BiVO}_4$  photoanodes (before and after photocharging), the catalytic efficiency,  $\eta_{\text{cat}}$ , was calculated using the method developed by Dotan et al.,<sup>18</sup> where the current density in the normal aqueous solution is directly compared to that obtained in the presence of  $\text{H}_2\text{O}_2$ , as shown in Figure 2. It is confirmed that the untreated  $\text{BiVO}_4$  photoanode has very poor catalytic activity, shown by a very low  $\eta_{\text{cat}}$  (maximum of 25% at  $1.23 \text{ V}_{\text{RHE}}$ ). In contrast, the  $\eta_{\text{cat}}$  of the photocharged sample showed significant improvements as shown in the dashed and solid red curves. If the photocharged  $\text{BiVO}_4$  photoanode was compared to the initial untreated sample measured in  $\text{H}_2\text{O}_2$ , the dashed red curve in Figure 2 is obtained, showing unity  $\eta_{\text{cat}}$  across the entire potential range. This is expected since the JV curves overlap for the two samples. However, if the photocharged sample was compared to itself with and without  $\text{H}_2\text{O}_2$ , the solid red curve in Figure 2 is obtained. The  $\eta_{\text{cat}}$  for this newly photocharged sample now reaches a maximum of 80% at  $1.23 \text{ V}_{\text{RHE}}$ , and even achieves reasonable efficiencies at lower potentials, with a  $\eta_{\text{cat}}$  of 55% at  $0.8 \text{ V}_{\text{RHE}}$ . These results have three major implications: (1) the photocharging treatment significantly improves the catalytic efficiency of the  $\text{BiVO}_4$  photoanodes, (2) there are still some surface catalytic losses for photocharged electrodes and (3) a bulk/non-surface related improvement was also achieved. Comparing the solid red curve and the solid black curve in Figure 2 clearly shows that there is an enhancement in the catalytic efficiency due to the photocharging treatment. However, if the improvement was achieved only due to the modification of

the surface of  $\text{BiVO}_4$ , then it would be expected that the performance in a solution containing  $\text{H}_2\text{O}_2$  would be identical for the untreated and photocharged samples (dashed black and dashed red in Figure 1), which is not the case. Therefore, since the JV curves of the photocharged  $\text{BiVO}_4$  sample and the untreated sample in  $\text{H}_2\text{O}_2$  overlap, and there is still a further improvement in current when a photocharged sample is measured in presence of  $\text{H}_2\text{O}_2$ , there must be a non-catalytic enhancement, which will be discussed later.

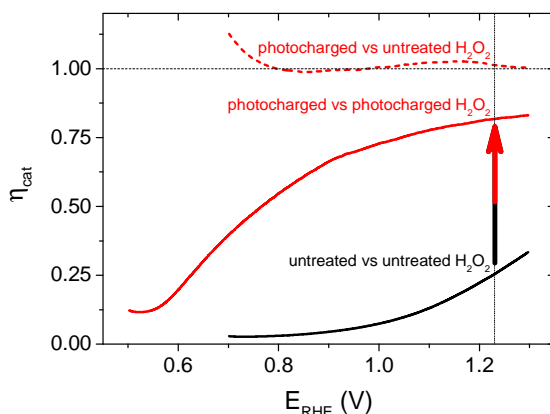


Figure 2. Calculated catalytic efficiency for the untreated (black solid curve) and photocharged  $\text{BiVO}_4$  samples (red curves). The catalytic efficiency for the photocharged samples was estimated using the JV characteristics in the presence of  $\text{H}_2\text{O}_2$  for the untreated sample (dashed red curve) and with the photocharged sample (solid red curve).

The PEC performance of the photocharged photoanodes was found to be stable within 20 voltammetric cycles in the potential range of 0.5 – 1.3  $V_{\text{RHE}}$ , with no observable decrease in the photocurrent density (Fig. S1).

However, a photocharged sample left in the electrochemical cell over-night and re-measured on the next day exhibits very similar J-V characteristics to what is measured initially, before photocharging. This shows that dark OC conditions facilitate the deactivation of the improved PEC performance. Nonetheless, the process of photocharging repeated later on is equally effective and results in recovery of the improved performance (Fig. S2). This finding may limit this technique to have a lasting effect in a practical device for PEC water splitting, but a prospective challenge for

further development would be to 'lock-in' the photocharging effect on the photocharged BiVO<sub>4</sub> surface.

### 2.3.2 Photovoltage of BiVO<sub>4</sub>

Numerous reports have shown that the performance of metal oxide photoanodes can be greatly hindered by the presence of electronic surface states (SuS).<sup>19,20</sup> It has been proposed that the electronic nature of the surface states results in the pinning of the Fermi level ( $E_F$ ), which has a detrimental effect on the obtainable photovoltage ( $V_{ph}$ ). Likewise, it has been demonstrated that these SuS can be passivated, leading to an increased  $V_{ph}$ , a cathodically shifted  $V_{on}$  and higher photocurrent densities.<sup>21–25</sup> Therefore, to better understand whether the observed change in PEC properties of our BiVO<sub>4</sub> photoanodes is related to the presence of SuS, an investigation of the change in  $V_{ph}$  for our samples before and after the photocharging treatment has been conducted.

The equilibration conditions of n-type semiconductors in aqueous-based electrolytes have been described in detail in previously reported literature.<sup>1,26,27</sup> It has been proposed that in the dark and in an OC configuration and ideal conditions, i.e. with a pristine electrode surface with no surface defect states, the Fermi level ( $E_F$ ) of a photoanode equilibrates with the water oxidation potential ( $E_{OH-/O_2}^0 = 1.23 V_{RHE}$ ) (Figure 3a). Whereas under illumination, the quasi-Fermi level of the electrons ( $E_{F,n}$ ) shifts towards the conduction band edge ( $E_C^S$ ) and quasi-Fermi level of the holes ( $E_{F,p}$ ) equilibrates with  $E_{OH-/O_2}^0$  (Figure 3b).

However, when surface states with sufficient density ( $DOS \sim 10^{13}-10^{14}$ )<sup>28</sup> exist at the semiconductor/electrolyte interface, a significant potential drop in the Helmholtz layer is likely to develop.<sup>29</sup> Consequently the  $E_F$  doesn't equilibrate with  $E_{OH-/O_2}^0$  and instead aligns with the energy level of the SuS ( $E_{SuS}$ )<sup>21,27</sup> (Figure 3c). The potential drop in the Helmholtz layer results in a so-called Fermi level pinning effect.<sup>30</sup> Under Fermi level pinning conditions, any change in pH or applied potential is accommodated by a change in the occupation of the SuS and a corresponding change in the potential drop across the Helmholtz layer.<sup>27</sup> As a result, the Fermi level stays virtually fixed and the degree of band bending remains constant, and a significantly lower photovoltage is obtained.

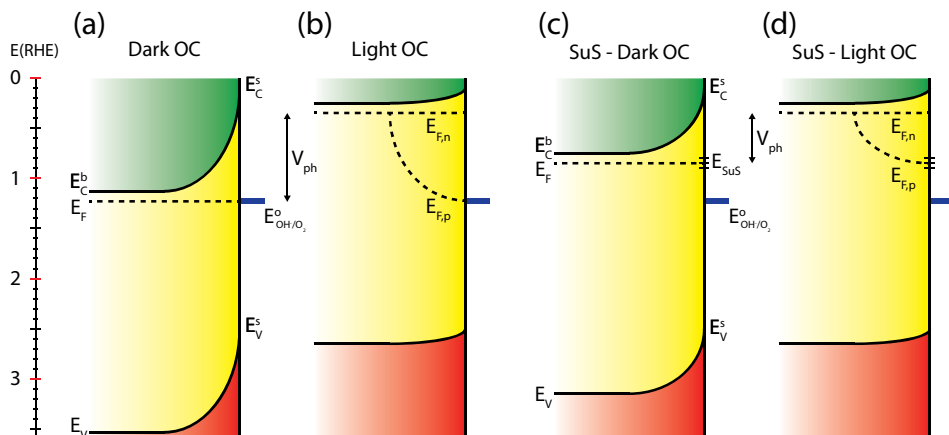


Figure 3. Estimated electronic band diagrams for  $\text{BiVO}_4$  in the OC configuration without surface states present (a) in the dark and (b) under illumination, and with surface states present (c) in the dark, and (d) under illumination.

In our experiments, we performed a set of PEC measurements in the OC configuration to investigate the behaviour of our  $\text{BiVO}_4$  photoanodes in this respect. The potential of the working electrode ( $V_{\text{WE}}$ ) was monitored in the dark and under illumination until a steady state equilibrium was observed, i.e. the potential of the working electrode remained constant over time (Fig. S3 and S4). The photovoltage ( $V_{\text{ph}}$ ) was calculated as  $V_{\text{WE,dark}} - V_{\text{WE,light}}$ . Figure 4 contains a summary of the measured and estimated OC potentials in the dark and under illumination for  $\text{BiVO}_4$  photoanodes in water ( $\text{H}_2\text{O}$ ), in the presence of hydrogen peroxide ( $\text{H}_2\text{O}_2$ ) and after photocharging ( $\text{H}_2\text{O}^{\text{photo}}$ ).

The equilibrium potential of the untreated  $\text{BiVO}_4$  photoanode was found to be more negative than the water oxidation potential by ca. 0.4 V. A likely reason for the mismatch between the observed value of  $E_{\text{F}}$  and  $E_{\text{OH}/\text{O}_2}^0$  is the presence of SuS's on the  $\text{BiVO}_4$  surface. These results are in agreement with studies on  $\alpha\text{-Fe}_2\text{O}_3$  and  $\text{TiO}_2$  electrodes,<sup>20</sup> where equilibration potentials of ca. 0.8  $V_{\text{RHE}}$  have been reported (OC dark conditions), suggesting that this may be an effect typical for metal oxide photoanodes. This consistency implies that surface states are independent of the exact composition of a metal oxide and originate from some surface adsorbate species and/or water oxidation intermediates that bind preferentially to metal oxide surfaces. Furthermore, when a hole scavenger is present in the electrolyte, we observed values

of  $V_{WE} (H_2O_2 \text{ dark})$  much closer to  $1.23 V_{RHE}$ , i.e.  $1.0 V_{RHE}$ . This can be explained by the fact that  $H_2O_2$  is not only an efficient acceptor of photogenerated holes, but can also easily donate electrons to the SuS's of  $BiVO_4$ , as the oxidation potential of  $H_2O_2$  ( $0.68 V_{RHE}$ ) is more negative than  $E_{SuS}$ .

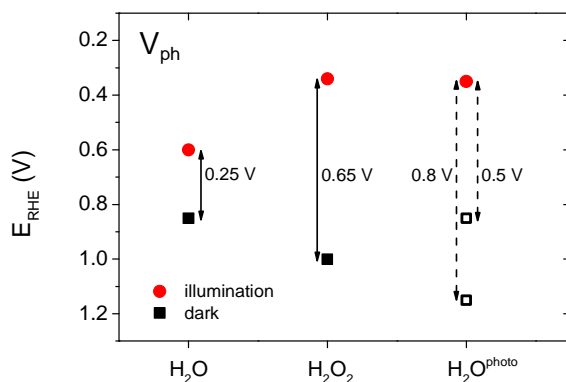


Figure 4. Equilibrium potentials and photovoltage values of  $BiVO_4$  photoanodes in the open circuit configuration: untreated sample in 0.1M K-Pi electrolyte ( $H_2O$ ), in presence of a hole scavenger ( $H_2O_2$ ), photocharged sample ( $H_2O^{photo}$ ).

The dark OC potential of the photocharged anodes could not be directly determined using the standard approach. That is because dark OC conditions facilitate the deactivation of the photocharging effect, therefore the measured dark OC potential corresponds rather to the untreated material. Consequently, two different approaches were used to estimate the photovoltage of the photocharged photoanodes. It has been proposed<sup>21</sup> that there is direct correlation between the onset potential and the position of the dark OC potential. Therefore in the first approach the photovoltage was estimated based on the cathodic shift of the onset potential observed for the photocharged anodes. In the second approach the dark OC potential was assumed to be the same as the one of the untreated photoanodes.

### 2.3.3 Photocharged BiVO<sub>4</sub>

To further explore the PEC properties of the photocharged BiVO<sub>4</sub> photoanodes, dark electrochemical experiments were performed before and after photocharging. Figure 5 shows three consecutive dark JV scans taken immediately after the photo-induced equilibrium of  $E_F$  was reached. An oxidation peak can be observed at potentials of about 0.85 V<sub>RHE</sub>. As such a peak is not present in dark JV curves taken for untreated BiVO<sub>4</sub>, we conclude that upon exposure to illumination in OC conditions, the electrochemical behaviour of our BiVO<sub>4</sub> photoanodes are altered, i.e. they attain some additional negative charge. Once the photoanodes are swept anodically with potential greater than 0.85 V<sub>RHE</sub>, the electrons are removed, which results in the presence of an oxidation peak in the JV scan. This peak appears to be the largest after the first cycle, and becomes successively smaller after each cycle until after >3 cycles the peak is gone, suggesting that within the range of potentials applied (0.2-2.1 V<sub>RHE</sub>) and within the timescale of a CV scan, this effect is irreversible without the addition of light. The position of the observed oxidation peak (0.85 V<sub>RHE</sub>) is consistent with the recorded  $V_{WE}$  dark H<sub>2</sub>O (0.85 V<sub>RHE</sub>), which directly corresponds to the energy level of the proposed SuS.

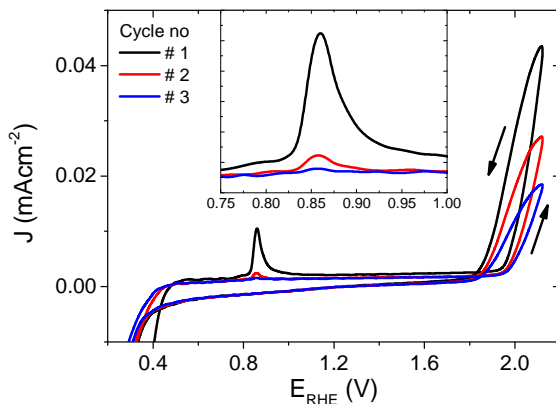


Figure 5. The first three dark JV scans of the BiVO<sub>4</sub> photoanode after 10 hours of photocharging, inset: a zoomed in plot around the observed oxidation peak at ~0.85 V<sub>RHE</sub>.

Additionally, current densities up to  $0.043 \text{ mAcm}^{-2}$  at  $2.1 \text{ V}_{\text{RHE}}$  in the dark can be observed for photocharged  $\text{BiVO}_4$ , suggesting some dark electrocatalytic activity (Figure 5). Untreated  $\text{BiVO}_4$  is a very poor electrocatalyst, with virtually no current at  $2.1 \text{ V}_{\text{RHE}}$  in the dark (Fig. S5). Even with a thin layer of OEC such as Ni-Bi only  $0.011 \text{ mAcm}^{-2}$  can be observed at  $2.1 \text{ V}_{\text{RHE}}$  (Fig. S5). It further confirms that photocharging can successfully modify the surface of  $\text{BiVO}_4$  photoanodes leading to enhanced catalytic activity.

However, it is also possible that the photocharging of  $\text{BiVO}_4$  photoanodes is a non-surface related phenomenon. For untreated  $\text{BiVO}_4$  photoanodes, the first voltammetric cycle under illumination always yields the highest photocurrent density, and subsequent cycles show a gradually decreasing performance (Figure 6a inset). Usually from the 5th cycle onwards, the obtained CVs start to overlap as shown in Figure 6a, where the blue curve is obtained for all CVs recorded after 5 cycles. Interestingly, this decrease in photocurrent over cycling for untreated  $\text{BiVO}_4$  is accompanied with a change in the redox waves intensities and positions at low potentials. Initially a small oxidation wave at  $\sim 0.65 \text{ V}_{\text{RHE}}$  and a reduction wave at  $\sim 0.55 \text{ V}_{\text{RHE}}$  can be observed. Both waves disappear over cycling and a reduction wave at  $\sim 0.75 \text{ V}_{\text{RHE}}$  arises instead. Conversely, the photocharging technique leads to the diminishing of this reduction wave at  $\sim 0.75 \text{ V}_{\text{RHE}}$ , as shown in Figure 6b. The observed redox waves have previously been shown to correspond to the reduction and re-oxidation of vanadium  $\text{V}^{4+} / \text{V}^{5+}$ , which may be a bulk process.<sup>31</sup> The fact that photocurrent density is related to the intensity of the redox waves, and hence to the concentration of  $\text{V}^{4+}$  and  $\text{V}^{5+}$  species, suggests that photocharging leads to alteration of the  $\text{V}^{4+}$  to  $\text{V}^{5+}$  ratio.

To further investigate the possible change in vanadium oxidation state, XPS measurements were performed on the  $\text{BiVO}_4$  photoanodes before and after photocharging. Prior to the XPS experiment two samples were photocharged in K-P<sub>i</sub> buffer pH 7.2; one for 8 h, and another one for 16 h. One other sample, an untreated one, was tested as a reference. Measurements were focused in the energy range expected for vanadium, and the results are presented in Figure 7.

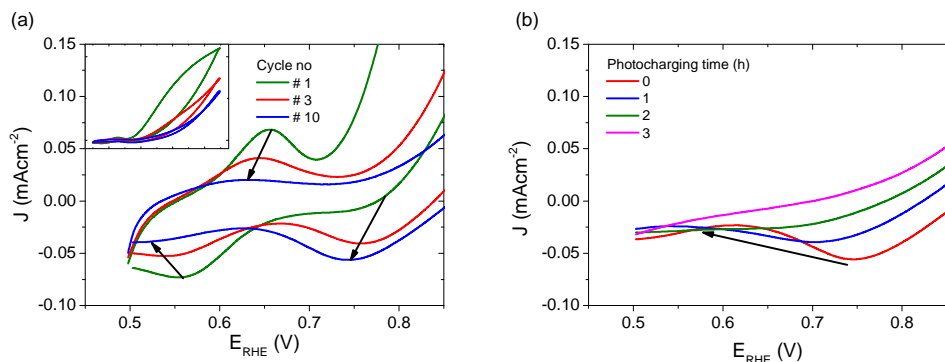


Figure 6. JV scans under illumination, for (a) untreated  $\text{BiVO}_4$ , inset: full potential range, and (b)  $\text{BiVO}_4$  photocharged for different periods of time (cathodic sweeps only).

A clear shift of the V2p peak towards lower binding energies can be observed for photocharged samples (Figure 7a). The position of V2p peak as a function of photocharging time is plotted in Figure 7b. It shows quantitatively that the negative shift of the binding energy for V2p<sub>3/2</sub> orbital scales up linearly with photocharging time. Moreover, it has been previously reported<sup>32</sup> that the binding energy of vanadium in the 5+ oxidation state is found at 517.1 eV, and is correlated to the  $\text{V}_2\text{O}_5$  species, while the binding energy of vanadium in the 4+ oxidation state is 516.4 eV. Comparison of our data with these V2p<sub>3/2</sub> references for different oxidation states (dotted lines on Figure 7b) suggests that photocharging treatment results in gradual reduction of V in our  $\text{BiVO}_4$  films, i.e. the untreated samples are rich in V in 5+ state, while photocharging results in higher and higher fraction of  $\text{V}^{4+}$ .

It is important to note that the XPS technique only gives quantitative information about the oxidation state of the surface of the sample, and therefore we cannot conclude that the oxidation state of vanadium changes in the bulk. Ion beam etching was attempted to probe the oxidation state of vanadium at a depth several nanometers below the surface for our samples, but due to the complex morphology and composition of our films, reliable data was not obtainable. Therefore we can conclude that at least the surface vanadium species reduce during the photocharging process, but further investigations are required to determine if the bulk vanadium also reduces.



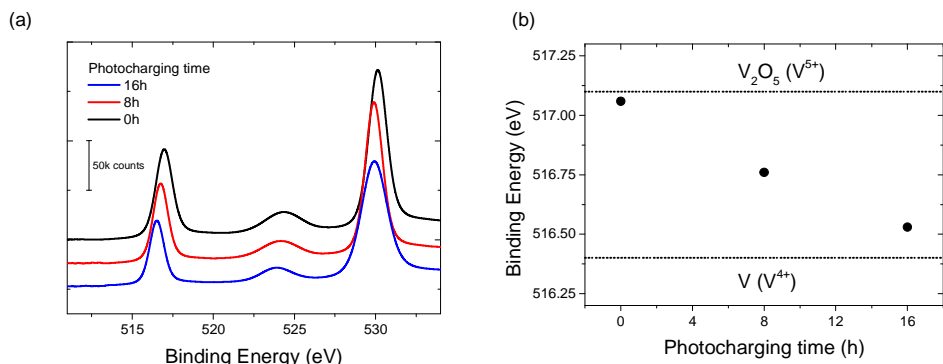


Figure 7. (a) XPS spectra for BiVO<sub>4</sub> photoanodes photocharged for 0 (black), 8 (red) and 16 h (blue) in K-Pi buffer pH 7.2. (b) V2p<sub>3/2</sub> peak position for BiVO<sub>4</sub> samples photocharged for different amount of time. V<sub>2</sub>O<sub>5</sub> and V(IV) binding energies are shown for reference.

### 2.3.4 Material properties of photocharged BiVO<sub>4</sub>

To probe whether the photocharging treatment leads to any changes in the microstructural, structural and/or chemical properties of our BiVO<sub>4</sub> films, a detailed material characterization was performed before and after photocharging. Specifically, the aim was to clarify if the photocharging treatment leads to any corrosion process of BiVO<sub>4</sub>, enhancement/change in the surface area, or any other surface altering phenomena. The faradaic efficiency is also included to test if the enhancement in photocurrent generation is related to water oxidation and not any other reaction.

We investigated the surface morphology before and after photocharging by taking AFM scans of 200 nm thick BiVO<sub>4</sub> samples, as shown in Fig. S6 and S7 respectively. From these images, there are no clearly noticeable changes in the surface morphology before and after the treatment. Our AFM investigation suggests that the photocharging treatment does not alter the microstructure of our films, and therefore the observed enhancement in photocurrent appears not to be related to an increased surface roughness or etching induced nano-structuring. Our SEM study further confirms these conclusions. The surface morphology of BiVO<sub>4</sub> samples before and after photocharging was investigated by SEM, as shown in Fig. S8 and S9 respectively.

Similar to the AFM observations, any qualitative difference in the surface morphology before and after the treatment is not clearly visible.

The crystal structure of  $\text{BiVO}_4$  before and after photocharging was also investigated by collecting XRD scans (Fig. S10). Our spray deposited films show a structure typical for monoclinic scheelite-type  $\text{BiVO}_4$ . Our diffractograms demonstrate that there is no clear difference in the crystal structure between the untreated and photocharged films. This implies that no additional lattice stress or strain inducing defects are responsible for the enhanced performance of the photocharged  $\text{BiVO}_4$  films.

The chronoamperometric (J-t) tests of photocharged  $\text{BiVO}_4$  thin films were performed for three different potentials over the course of an hour for each potential step. We choose moderately anodic potentials to avoid any stability issues related to  $\text{BiVO}_4$  itself, which are more likely to occur at highly oxidative potentials. We also choose these potentials for the sake of applicability of the photocharging treatment. Potentials in the 0.6 – 1.0 V range are close to the intersection points for a  $\text{BiVO}_4/\text{a-Si}$  PV cell tandem device,<sup>15</sup> therefore they represent practical operating potentials for a potential bias free solar water splitting device.

The results of the photocurrent stability measurements are presented in Fig. S11. The photocurrent within the time-frame of our experiment seems to be stable, i.e. for all 3 potentials tested, the J-t curves look fairly flat as a function of time. Larger fluctuations in the photocurrent density at 1.0  $V_{\text{RHE}}$  are related to bubble formation. Our results suggest that the enhancement in current due to the photocharging treatment can be sustained for at least several hours. Any decrease in photocurrent of the photocharged  $\text{BiVO}_4$  held at fixed potential is therefore likely to originate from the instability of the material itself, and not as a result of the photocharging treatment.

To show that the observed enhancement in photocurrent is indeed related to  $\text{O}_2$  evolution, a gas chromatography (GC) measurement was performed. Given the time resolution of our GC apparatus (18 min) and any potential intrinsic stability issues related to the  $\text{BiVO}_4$  itself, we performed the GC measurements under a fixed current density ( $0.65 \text{ mAcm}^{-2}$ ) rather than at a fixed potential. The outcome of the GC investigation is presented in Figure 8. All the experimental data points are in the close proximity of the oxygen evolution trend calculated based on the applied current and

the GC calibration data. Our results suggest that the Faradaic efficiency of the water oxidation process on photocharged  $\text{BiVO}_4$  photoanodes is close to unity, meaning the enhancement in photocurrent is not related to any other electron pathway or side reaction.

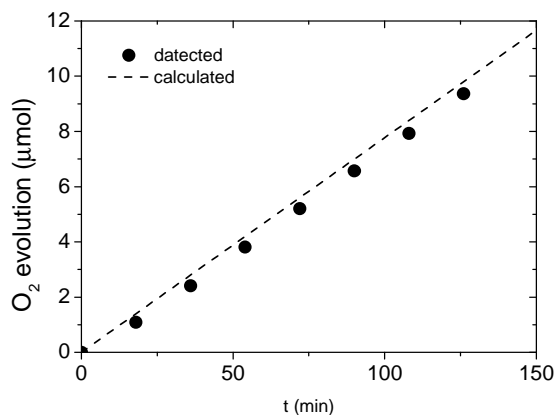


Figure 8. Gas chromatography detection of  $\text{O}_2$  evolved at photocharged  $\text{BiVO}_4$  electrode at constant current of  $0.65 \text{ mAcm}^{-2}$ .

## 2.4 Conclusions

In summary, we showed that prolonged exposure of  $\text{BiVO}_4$  photoanodes to AM1.5 illumination in the OC configuration, a technique that we call ‘photocharging’, greatly improves its PEC properties. We found that such light-induced treatment results in a major suppression of surface recombination, and thus a record photocurrent for bare, undoped, uncatalysed  $\text{BiVO}_4$  photoanodes was achieved. Furthermore, we showed that photocharging induces a significant cathodic shift in the photocurrent onset potential, and an increased photovoltage.

According to our results, the photocharging treatment improves both bulk and surface properties of  $\text{BiVO}_4$ . Therefore we hypothesize about the mechanisms

related to these two effects. Surface related enhancement could possibly be explained by the fact that photocharging leads to a photo-induced passivation of the surface states at the solid-liquid interface. Such passivation would result in a diminished Fermi level pinning effect and consequently in an increase of the photovoltage. Bulk related effect of photocharging could possibly be explained by reduction of  $V^{5+}$  to  $V^{4+}$  in the bulk of the film. Work is in progress to reveal what is the effect of photocharging on physico-chemical properties of  $\text{BiVO}_4$ , and to further determine the exact mechanism of this process and how it leads to the increased photocatalytic activity.

## 2.5 Acknowledgements

We acknowledge the financial support of the Foundation for Fundamental Research on Matter (FOM TNW 10.327). This work has been done under the agenda of the BioSolarCells Consortium. Helpful discussions with Sixto Gimenez, Moreno de Respinis and Bernard Dam are greatly acknowledged.

## 2.6 References

- (1) Walter, M. G.; Warren, E. L.; McKone, J. R.; Boettcher, S. W.; Mi, Q.; Santori, E. A.; Lewis, N. S. *Chem. Rev.* **2010**, *110* (11), 6446.
- (2) Grätzel, M. *Nature* **2001**, *414* (6861), 338.
- (3) Nocera, D. G. *Acc. Chem. Res.* **2012**, *45* (5), 767.
- (4) Tokunaga, S.; Kato, H.; Kudo, A. *Chem. Mater.* **2001**, *13* (12), 4624.
- (5) Abdi, F. F.; van de Krol, R. *J. Phys. Chem. C* **2012**, *116* (17), 9398.
- (6) Kim, T. W.; Choi, K.-S. *Science* (80-. ). **2014**, *343* (6174), 990.
- (7) Jeon, T. H.; Choi, W.; Park, H. *Phys. Chem. Chem. Phys.* **2011**, *13* (48), 21392.
- (8) Zhong, D. K.; Choi, S.; Gamelin, D. R. *J. Am. Chem. Soc.* **2011**, *133* (45), 18370.
- (9) Ding, C.; Shi, J.; Wang, D.; Wang, Z.; Wang, N.; Liu, G.; Xiong, F.; Li, C. *Phys. Chem. Chem. Phys.* **2013**, *15* (13), 4589.
- (10) Choi, S. K.; Choi, W.; Park, H. *Phys. Chem. Chem. Phys.* **2013**, *15* (17), 6499.

- (11) Trotochaud, L.; Mills, T. J.; Boettcher, S. W. *J. Phys. Chem. Lett.* **2013**, 4 (6), 931.
- (12) Abdi, F. F.; Firet, N.; van de Krol, R. *ChemCatChem* **2013**, 5 (2), 490.
- (13) Parmar, K. P. S.; Kang, H. J.; Bist, A.; Dua, P.; Jang, J. S.; Lee, J. S. *ChemSusChem* **2012**, 5 (10), 1926.
- (14) Luo, W.; Yang, Z.; Li, Z.; Zhang, J.; Liu, J.; Zhao, Z.; Wang, Z.; Yan, S.; Yu, T.; Zou, Z. *Energy Environ. Sci.* **2011**, 4 (10), 4046.
- (15) Abdi, F. F.; Han, L.; Smets, A. H. M.; Zeman, M.; Dam, B.; van de Krol, R. *Nat. Commun.* **2013**, 4, 2195.
- (16) Liang, Y.; Tsubota, T.; Mooij, L. P. A.; van de Krol, R. *J. Phys. Chem. C* **2011**, 115 (35), 17594.
- (17) Reichman, J. *Appl. Phys. Lett.* **1980**, 36 (7), 574.
- (18) Dotan, H.; Sivula, K.; Grätzel, M.; Rothschild, A.; Warren, S. C. *Energy Environ. Sci.* **2011**, 4 (3), 958.
- (19) Klahr, B.; Hamann, T. *J. Phys. Chem. C* **2014**, 118 (19), 10393.
- (20) Du, C.; Zhang, M.; Jang, J.; Liu, Y.; Liu, G.; Wang, D. *J. Phys. Chem. C* **2014**, 118 (30), 17054.
- (21) Du, C.; Yang, X.; Mayer, M. T.; Hoyt, H.; Xie, J.; McMahon, G.; Bischooping, G.; Wang, D. *Angew. Chemie (International ed.)* **2013**, 52 (48), 12692.
- (22) Zandi, O.; Hamann, T. W. *J. Phys. Chem. Lett.* **2014**, 5 (9), 1522.
- (23) Eisenberg, D.; Ahn, H. S.; Bard, A. J. *J. Am. Chem. Soc.* **2014**, 136 (40), 14011.
- (24) McDowell, M. T.; Lichterman, M. F.; Spurgeon, J. M.; Hu, S.; Sharp, I. D.; Brunschwig, B. S.; Lewis, N. S. *J. Phys. Chem. C* **2014**, 118 (34), 19618.
- (25) Yang, X.; Liu, R.; Du, C.; Dai, P.; Zheng, Z.; Wang, D. *ACS Appl. Mater. Interfaces* **2014**, 6 (15), 12005.
- (26) Gerischer, H. *Electrochim. Acta* **1990**, 35 (11–12), 1677.
- (27) van de Krol, R.; Grätzel, M. *Photoelectrochemical Hydrogen Production*; van de Krol, R., Grätzel, M., Eds.; Electronic Materials: Science & Technology; Springer US: Boston, MA, 2012; Vol. 102.
- (28) Bard, A. J.; Bocarsly, A. B.; Fan, F. R. F.; Walton, E. G.; Wrighton, M. S. *J. Am. Chem. Soc.* **1980**, 102 (11), 3671.
- (29) Morrison, S. R. *Electrochemistry at Semiconductor and Oxidized Metal Electrodes*; Springer, 1980.
- (30) Pleskov, I. V. *Solar Energy Conversion: A Photoelectrochemical Approach*; Springer, 1990.
- (31) Qin, D.-D.; Wang, T.; Song, Y.-M.; Tao, C.-L. *Dalt. Trans.* **2014**, 43 (21), 7691.
- (32) Biesinger, M. C.; Lau, L. W. M.; Gerson, A. R.; Smart, R. S. C. *Appl. Surf. Sci.* **2010**, 257 (3), 887.

# Appendix I

## Experimental

### Preparation of BiVO<sub>4</sub> thin film photoanodes

Thin films of 200 nm thick BiVO<sub>4</sub> were prepared by spray pyrolysis on FTO coated glass substrates (fluorine-doped tin dioxide, 15 Ω/□, TEC-15, Hartford Glass Co.). FTO substrates were rinsed with a Triton solution, sulphuric acid, acetone and ethanol, and subsequently cleaned using an UV ozone cleaner (Novascan). The precursor solution was made by dissolving 4 mM Bi(NO<sub>3</sub>)<sub>3</sub>·5H<sub>2</sub>O (98%, Alfa Aesar) in acetic acid (98%, Sigma-Aldrich) and adding an equimolar amount of vanadium in the form of VO(AcAc)<sub>2</sub> (99%, Alfa Aesar) dissolved in absolute ethanol (Sigma-Aldrich). The substrate temperature during spraying was maintained at 450 °C, as measured by a thermocouple pressed to the top of the substrate surface. The spray deposition was carried out using an automated spray setup with Quickmist air atomizing spray nozzle driven by an overpressure of 0.06 MPa of nitrogen gas. The nozzle–substrate distance was kept constant at 20 cm. The precursor solution was placed 20 cm below the nozzle and fed to the nozzle via the siphoning effect induced by the nitrogen gas flow. Each spray cycle consisted of 5 s of spray time and 55 s of delay time to allow solvent evaporation, and a total of 200 cycles were used to deposit the films.

Prior to deposition of the BiVO<sub>4</sub>, a SnO<sub>2</sub> interfacial layer (~80 nm) was deposited onto the FTO substrate to prevent recombination at the FTO/BiVO<sub>4</sub> interface. 0.1 M SnCl<sub>4</sub> (99%, Acros Organics) solution in ethyl acetate (99.5%, J.T. Baker) was used as the precursor solution. The SnO<sub>2</sub> layer was deposited at 425 °C using five spray cycles (5 s on, 55 s off) in a gravity-assisted siphoning mode, where the precursor solution was placed 30 cm above the nozzle. After deposition, the SnO<sub>2</sub>/BiVO<sub>4</sub> samples were subjected to an additional 2 h heat treatment in a tube furnace at 450 °C in air. Spray deposition was performed on FTO substrates of 50 x 50 mm in size which were eventually cut into 20 x 10 mm samples.

## Material characterization

AFM surface scans were performed using an NT-MDT Ntegra apparatus coupled with an NT-MDT P8 XPM controller, with an NT-MDT NSG30 cantilever mounted. Scans were taken over an area of 2x2 and 1x1  $\mu\text{m}$ , with a 1 Hz frequency and a resolution of 512x512 points.

The morphology of thin films was investigated with SEM microscopy (JEOL JSM-6010LA instrument equipped with a tungsten hairpin filament). Samples were investigated in the secondary electron imaging mode (SEI), using an Everhart-Thornley type of detector. SEM images were collected using the accelerating voltage of 20 kV, at a working distance of 10 mm.

Structural analysis was performed with a Bruker D8 Advance X-ray diffractometer (Co-K $\alpha$ ,  $\lambda = 0.178897$  nm) equipped with a LynxEye detector in a Bragg-Brentano configuration.

## Results

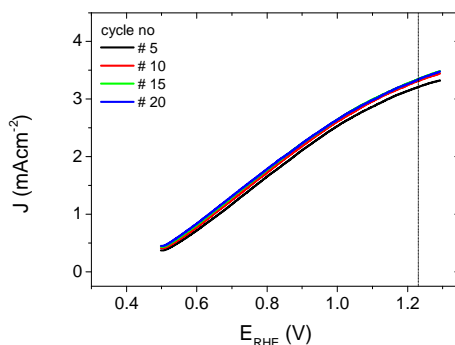


Fig. S1 The JV performance of the photocharged  $\text{BiVO}_4$  for up to 20 cyclic voltammetric sweeps.

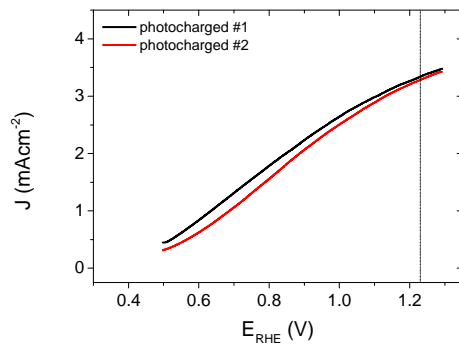


Fig. S2 The JV performance of a photocharged  $\text{BiVO}_4$  photoanode (black), which was subsequently left in the cell for 24 h to discharge under dark conditions and recharged back again (red).

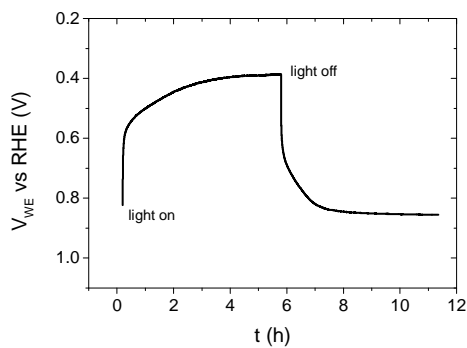


Fig. S3 Transients recorded for  $E_f$  equilibration in the OC configuration,  $\text{BiVO}_4$  in 0.1 K-Pi

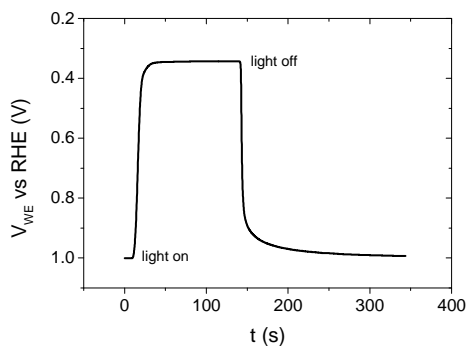


Fig. S4 Transients recorded for  $E_f$  equilibration in the OC configuration,  $\text{BiVO}_4$  in presence of  $\text{H}_2\text{O}_2$



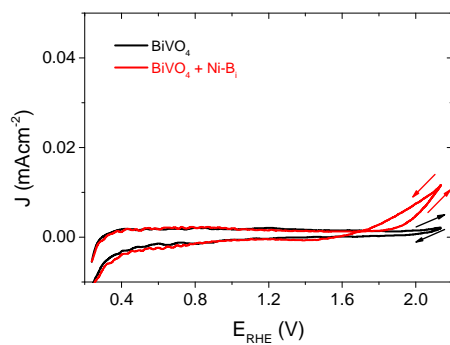


Fig. S5 J-V characteristics for  $\text{BiVO}_4$  and  $\text{BiVO}_4$  catalysed with  $\text{Ni-Bi}$ .

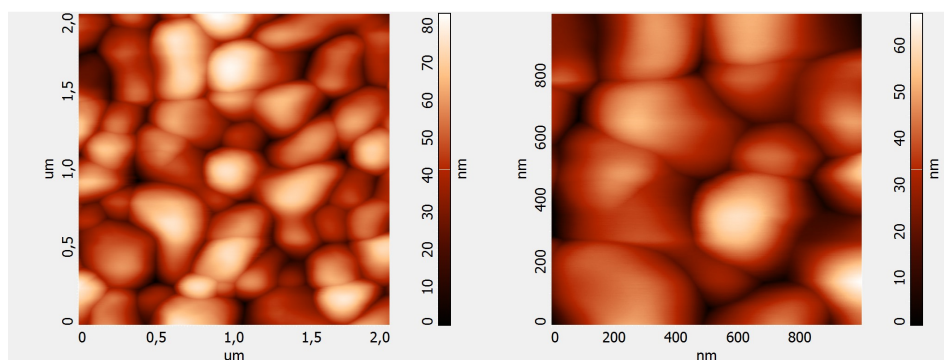


Fig. S6 AFM scans of untreated 200 nm  $\text{BiVO}_4$  films:  $2 \times 2 \mu\text{m}$  and  $1 \times 1 \mu\text{m}$ .

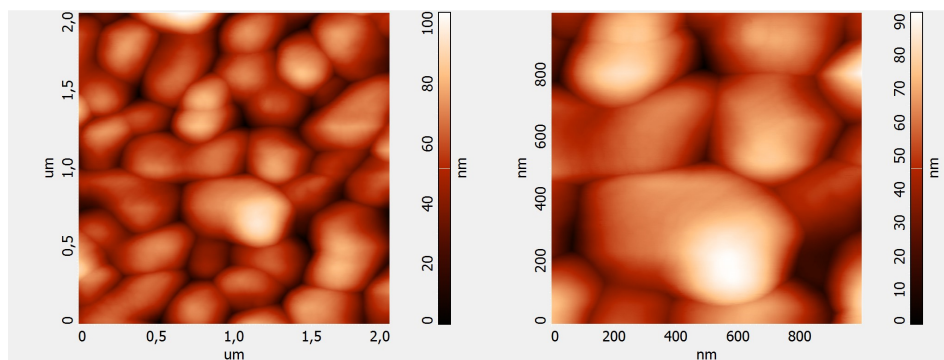


Fig. S7 AFM scans of photocharged 200 nm  $\text{BiVO}_4$  films:  $2 \times 2 \mu\text{m}$  and  $1 \times 1 \mu\text{m}$ .

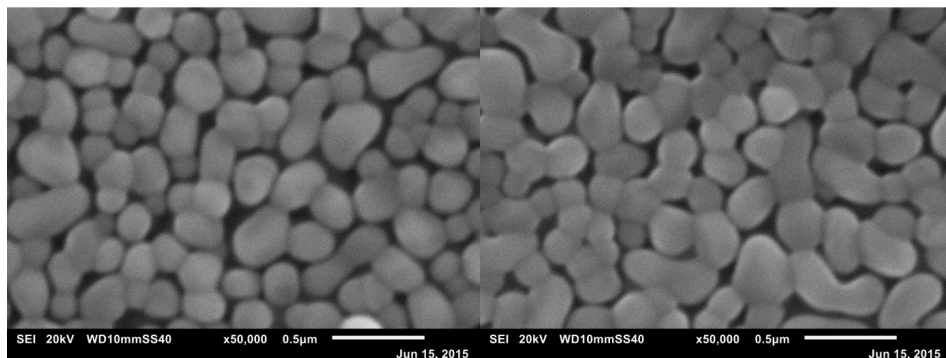


Fig. S8 SEM images of untreated 200 nm  $\text{BiVO}_4$  films.

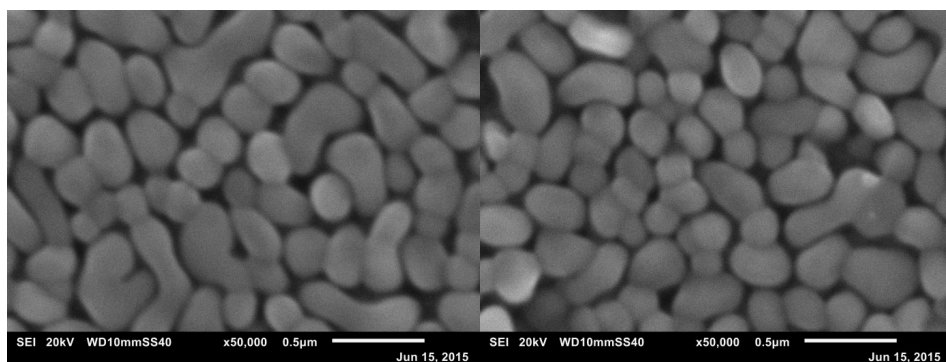


Fig. S9 SEM images of photocharged 200 nm  $\text{BiVO}_4$  films

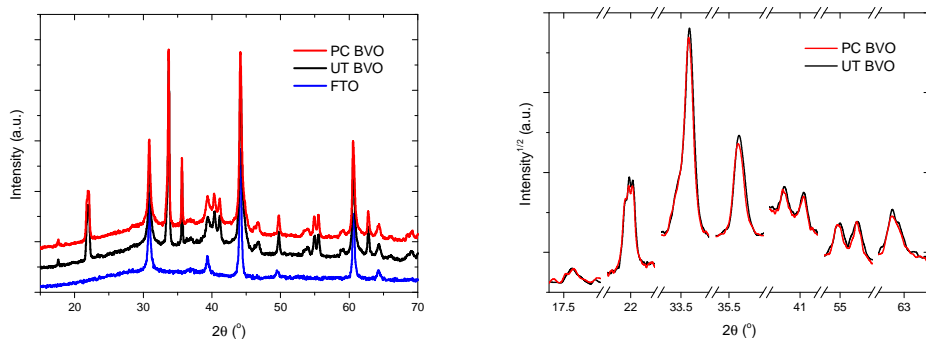


Fig. S10 XRD spectra of 200 nm  $\text{BiVO}_4$  films before and after photocharging: full range (left) and the most intense  $\text{BiVO}_4$  peaks (right).

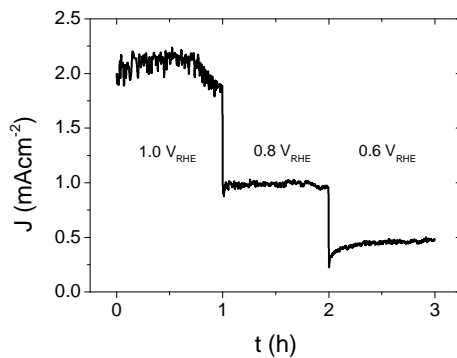
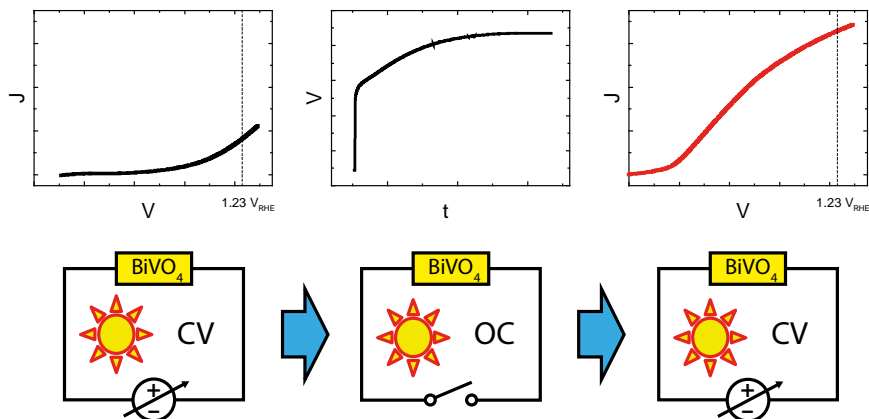


Fig. S11 Chronoamperometric measurements of photocharged  $\text{BiVO}_4$  films held at 1.0, 0.8 and 0.6  $V_{\text{RHE}}$  with a one hour duration per potential step.

## Table of contents (TOC) graphic



Synopsis - Long exposure of  $\text{BiVO}_4$  photoanodes to light under open circuit conditions (photocharging) results in the record high current densities for undoped and uncatalyzed  $\text{BiVO}_4$ .

### 3. Near-complete suppression of surface losses and total internal quantum efficiency in BiVO<sub>4</sub> photoanodes

Bismuth vanadate (BiVO<sub>4</sub>) is one of the most efficient light absorbing metal oxides for solar water splitting. BiVO<sub>4</sub> photoanodes immersed in electrolyte under open circuit configuration and exposed to simulated solar illumination for prolonged time achieve superior photoelectrochemical (PEC) activity. This photocharging (PC) effect is capable of almost completely overcoming the surface and bulk limitations of BiVO<sub>4</sub>. Herein we show that alkaline conditions favor the PC effect, specifically BiVO<sub>4</sub> photoanodes subjected to PC treatment in pH 10 achieve a record high photocurrent for undoped and uncatalyzed BiVO<sub>4</sub> of 4.3 mAcm<sup>-2</sup> @ 1.23 V<sub>RHE</sub>, an outstandingly low onset potential of 0.25 V<sub>RHE</sub>, and a very steep photocurrent onset. Alkaline conditions also facilitate excellent external and internal quantum efficiencies of 75 and 95 % respectively (average in the 440 nm > λ > 330 nm range). Moreover, impedance spectroscopy and in-situ XAS study suggests that electronic, structural and chemical properties of the bulk of these films remain unchanged during the PC treatment. However, appreciable changes in the surface-related properties take place. Ultimately, our results indicate that the improved activity of PC-BiVO<sub>4</sub> is enhanced by surface reaction pathways of the semiconductor liquid junction, which is directly correlated to the electrochemical environment it is modified in.

---

This chapter has been published as: B. J. Trześniewski, I. A. Digdaya, T. Nagaki, S. Ravishankar, I. Herraiz-Cardona, D. A. Vermaas, A. Longo, S. Gimenez and Wilson A. Smith, *Energy Environ. Sci.*, 2017, 10, 1517-1529 (10.1039/c6ee03677e)

### 3.1 Introduction

The storage of intrinsically intermittent solar energy in the form of chemical fuels (e.g.  $H_2$ ) has the potential to simultaneously combat global environmental and energy problems. Photoelectrochemical (PEC) water splitting is one of the most promising approaches for such a renewable and sustainable production of hydrogen.<sup>1–</sup>

<sup>4</sup> Metal oxides have been extensively used<sup>5</sup> as a promising class of photo-electrode material for PEC devices, due to their high (photo)chemical stability, abundance and low cost, as well as suitable optical and electronic properties. However, out of the wide selection of metal oxides, so far only a few materials,  $Fe_2O_3$ ,<sup>6</sup>  $WO_3$ ,<sup>7</sup>  $BiVO_4$ ,<sup>8</sup> and  $Cu_2O$ ,<sup>9</sup> have demonstrated reasonable performance under simulated solar illumination (i.e. photocurrent over  $2\text{ mAcm}^{-2}$  and large photovoltage).

Among the metal oxides, bismuth vanadate ( $BiVO_4$ ) is a material with the highest reported solar to hydrogen (STH) conversion efficiency to date (5.2 %).<sup>10,11</sup>  $BiVO_4$  is an n-type photoanode material, with a bandgap energy of 2.4 eV,<sup>12</sup> a theoretical efficiency of ~9% STH,<sup>13</sup> is made of cheap, relatively earth abundant, non-toxic elements and is reasonably stable in neutral conditions. However, it suffers from surface and bulk recombination losses that limit its performance to well below its theoretical maximum.<sup>13</sup> The deposition of a co-catalyst ( $Co-Pi$ ,<sup>13–16</sup>  $Co-Bi$ ,<sup>17</sup>  $Ni-Bi$ ,<sup>18</sup>  $FeOOH/NiOOH$ ,<sup>19</sup>  $Fe_2O_3/ZrO_2$ <sup>20</sup>) has been reported to successfully mitigate the surface-related limitations of  $BiVO_4$  and has enabled to the ability to achieve close to 100% catalytic efficiencies for the oxygen evolution reaction (OER). Complementarily, the low electronic conductivity of  $BiVO_4$  has been partially overcome via doping with high-valence cations such as  $W$ <sup>13,14,21</sup> or  $Mo$ <sup>21</sup> which substitute for vanadium. Moreover, fabricating  $BiVO_4$  films in a nanostructured morphology has been demonstrated<sup>19,22,23</sup> to overcome the transport limitations caused by the intrinsically short (70 nm)<sup>24</sup> diffusion length of photogenerated charge carriers. Finally, the surface passivation of  $BiVO_4$  films with thin layers of  $TiO_2$  has also been shown<sup>25,26</sup> to significantly improve its stability. While these techniques are mostly successful to improve the overall PEC activity of  $BiVO_4$ , they add extra steps to the material processing and introduce significant complexity in optimizing a practical PEC water splitting device.

In our recent work<sup>27</sup> we have reported for the first time on a photoelectrochemical procedure called photocharging (PC), that enables the ability to successfully improve both bulk and surface limitations of BiVO<sub>4</sub> photoanodes. We have demonstrated that prolonged exposure of BiVO<sub>4</sub> photoanodes in an aqueous solution in open circuit (OC) conditions to simulated solar irradiation can greatly increase its solar water oxidation efficiency via a reduced onset potential and an increased maximum photocurrent density. A similar change in various properties of light active materials exposed to illumination has been widely recognized in the photovoltaic (PV) field as a so-called light soaking effect.<sup>28–31</sup> However, up till now, no analogous effect has been identified in the PEC field. Moreover, it seems that the mechanism of the photocharging effect observed for BiVO<sub>4</sub> may be quite different from PV light soaking. For instance, the light soaking effect observed in PV devices is a purely solid-state phenomenon, i.e. it concerns only the interaction between the solid-state materials and incident electromagnetic radiation. Accordingly, the light soaking effect in the PV cells has been usually ascribed<sup>28–31</sup> to the alteration of the defect structure, change in DOS of trap states or interdiffusion within the light active materials. In contrast, according to our results, the presence of a liquid electrolyte is essential to the PC effect, and no PC can take place without it, i.e. the PC effect does not occur when illuminating the BiVO<sub>4</sub> films in air. These findings indicate that the PC effect should be studied in the context of the semiconductor-liquid junction (SLJ), the key interface in the PEC system.<sup>32–36</sup> The significance of the SLJ stands out by the number of important processes in which it is involved: mediation of the transport of charge carriers, formation and passivation of surface states, and catalysis of the oxygen evolution reaction (OER) via the formation of reaction intermediates.

Herein we provide new insights on the possible mechanisms of photocharging in BiVO<sub>4</sub> photoanodes, and how it directly leads to improved PEC performance. We investigate changes in the PEC, optical, structural, chemical and electronic properties of photocharged BiVO<sub>4</sub> in the context of the SLJ, to provide further insights into the chemical and physical mechanisms behind the PC phenomenon. Firstly, we investigate the effect of the electrolyte pH on the PC efficiency as a function of time to understand if the PC effect is related to the formation of oxy/hydroxyl-based water oxidation intermediates (HO\*, O\*, HOO\*). Since protons/hydroxyl groups are directly involved in all the steps that constitute the OER,<sup>37</sup> we expect that if the PC treatment is promoting the formation of any of the water oxidation intermediates, then a different pH could

heavily affect the PC efficiency. We show that alkaline conditions favour the PC effect, specifically that BiVO<sub>4</sub> photoanodes subjected to the PC treatment in pH 10 achieve a record high photocurrent for undoped and uncatalyzed BiVO<sub>4</sub> of 4.3 mAcm<sup>-2</sup> @ 1.23 V<sub>RHE</sub>, an outstandingly low onset potential of 0.25 V<sub>RHE</sub>, and excellent external and internal quantum efficiencies of 75 and 95 % respectively (average in the 440 nm > λ > 330 nm range). Secondly, we perform an in-situ UV-vis spectroscopic study to examine if PC leads to changes in the optoelectronic properties of BiVO<sub>4</sub>, and hence possibly different electronic transport properties. We observe that PC leads to increased absorption outside the bandgap energy region of BiVO<sub>4</sub> (λ > 520 nm), especially in the PC-facilitating alkaline conditions. However, this increased absorption does not seem to be directly responsible for the photocurrent enhancement, since the external quantum efficiency (IPCE) of PC-BiVO<sub>4</sub> for λ > 520 nm remains negligible. In addition, we use impedance spectroscopy to investigate the effect of PC on the electronic properties of BiVO<sub>4</sub> and observe only negligible changes in the bulk electronic properties of BiVO<sub>4</sub> films before and after the treatment. However, we observe a significant change in surface-related properties; increase in capacitance and decrease in resistance. Lastly, we use in-situ electrochemical X-ray absorption spectroscopy (XAS) to study the chemical and structural properties of BiVO<sub>4</sub> under PEC conditions. Our findings suggest that neither applying bias potential nor the photocharging treatment alters the structure/chemistry of the bulk of our BiVO<sub>4</sub> films; specifically, the oxidation state of vanadium does not seem to change. Overall, our results suggest that PC is related to a light-driven alteration of the surface of BiVO<sub>4</sub>, and is highly preferential in alkaline conditions. Those changes are most likely related to the formation of highly active water oxidation intermediates and/or changes in the chemistry of the surface. We propose a model in which surface of BiVO<sub>4</sub> becomes hydrogenated in alkaline conditions and under illumination, coupled with creation of oxygen vacancies and reduction of vanadium species, and possibly accompanied with creation of oxo- water intermediates. Consequently, electrocatalytic properties become more beneficial for solar driven water splitting applications. Furthermore, any bulk-related effects that we identify are mediated by phenomena occurring at the surface, which highlights the importance of the SLJ for the efficiency of PEC devices.

## 3.2 Results and discussion

### 3.2.1 Influence of pH on PC BiVO<sub>4</sub> under illumination

To understand the importance of the SLJ during photocharging treatments, the effect of the electrolyte pH on the PC efficiency was studied first. Figure 1 presents J-V curves of 200 nm thick BiVO<sub>4</sub> photoanodes under AM 1.5 illumination in PBA buffer at pH 4, 7 and 10 collected before (dashed lines) and after (solid lines) PC for 20 hours. For untreated BiVO<sub>4</sub>, J-V curves recorded in pH 4, 7 and 10 show little difference. Given the sample-to-sample variation, they can be considered similar, though pH 4 gives consistently the lowest activity in terms of photocurrent density. It is apparent that pH has little influence on the photocurrent generation of untreated BiVO<sub>4</sub>. Consequently, we can conclude that different concentrations of H<sup>+</sup> or OH<sup>-</sup> do not significantly influence the light driven oxidation of water on untreated BiVO<sub>4</sub> photoanodes.

In contrast, for photocharged BiVO<sub>4</sub>, J-V curves recorded in pH 4, 7 and 10 show striking differences. There seemingly exists a very strong relationship between the alkalinity of the electrolyte and PEC activity of the photocharged electrodes, in particular, a high pH promotes high photocurrent and low onset potential. We observe photocurrent densities of 1.0, 3.3 and 4.3 mAcm<sup>-2</sup> @ 1.23 V<sub>RHE</sub> in pH 4, 7 and 10 respectively. In our initial study<sup>27</sup> we have reported 3.3 mAcm<sup>-2</sup> @ 1.23 V<sub>RHE</sub> in pH 7, herein we were able to achieve 4.3 mAcm<sup>-2</sup> @ 1.23 V<sub>RHE</sub> using pH 10 electrolyte. This is by far the highest reported photocurrent at 1.23 V<sub>RHE</sub> for undoped and uncatalyzed BiVO<sub>4</sub> photoanodes. Moreover, there is also a very clear difference in the slope of the photocurrent in different media. Slightly acidic conditions at pH 4 results in a very sluggish photocurrent onset; initially the J-V curve is almost flat and a significant overpotential is required to achieve reasonable photocurrent densities. On the other hand, alkaline conditions at pH 10 lead to a very steep photocurrent onset from the very beginning, with no observable inflection point in the J-V curve, a trend more typical for measurement where no surface limitations are present,<sup>38</sup> for example when a sacrificial hole scavenger such as H<sub>2</sub>O<sub>2</sub> is employed.<sup>27</sup> The different slopes suggest that alkaline conditions facilitate major suppression of surface recombination<sup>39</sup> in PC BiVO<sub>4</sub>. Interestingly, the J-V curves in pH 4 recorded before and after the PC treatment overlap, showing that at this pH no PC effect takes place. It seems that there is a



threshold pH for the PC to take place and at conditions acidic enough ( $\text{pH} < 7$ ) no PC can occur. That implies a certain concentration of hydroxyl groups is necessary for the PC treatment to be successful.

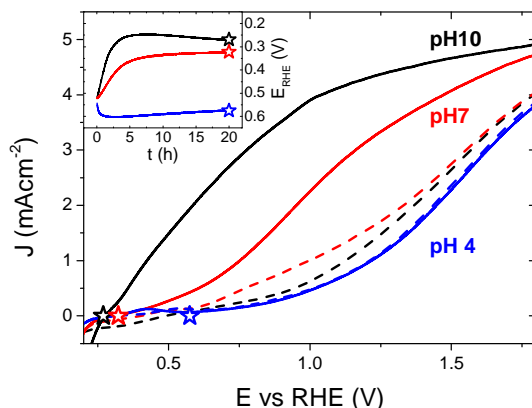


Figure 1. J-V curves of  $\text{BiVO}_4$  in PBA buffer pH 4, 7 and 10, a stable 10<sup>th</sup> anodic scan is shown in each case. Dashed curves – untreated films, solid curves – photocharged films. Each PC treatment was performed in the same pH as the corresponding CV experiment. Inset: E-t OC trends collected during the PC treatment. Stars in both plots denote the final photocharging OC potential. Experimental conditions: back-side AM1.5 illumination, films of 200 nm in thickness, scan rate of 50 mV/s.

Moreover, it seems that no specific anion nor cation is responsible for the PC effect. As presented in Fig. S1, electrolytes with compositions different than  $\text{K-P}_i$  or PBA buffer can successfully facilitate the PC effect, following a pH trend similar to what is demonstrated in Figure 1. In addition, a series of experiments was conducted to measure the photocurrent density as a function of thickness (Fig. S2 black curves). As expected, due to low absorption of  $\text{BiVO}_4$ , the photocurrent density produced by our photoanodes scales up with thickness of the films, up to ca. 200 nm limit. There is no significant gain in current for films thicker than 200 nm since 200 nm thick films already absorb most of the available light<sup>40</sup> and going beyond 200 nm may be detrimental due to the 70 nm diffusion length of charge carriers in  $\text{BiVO}_4$ <sup>24</sup> and consequently any gain related to increased absorption could be potentially consumed by bulk transport and recombination losses. Fig. S2 presents also time evolution trends of the PC process (curves red to blue). JV curves collected every 2 h show a steady

increase in photocurrent, cathodic shift of the photocurrent onset and improvement in the fill-factor. It seems that the biggest changes occur in the first 6 h of the treatment, and further improvements are more moderate.

The inset in Figure 1 shows the time evolution of the  $\text{BiVO}_4$  potential vs RHE recorded during the PC treatment in pH 4, 7 and 10. The dark open circuit potentials for each pH are shown in Appendix II (Fig. S3), where the pH does not show a strong influence ( $E_{\text{OC, dark}}$ ). It can be seen that more strongly alkaline pH's favor lower light induced equilibrium potentials (closer to the  $\text{BiVO}_4$  conduction band-edge). Accordingly, we measured the equilibrium open-circuit (OC) potentials of 0.58, 0.32 and 0.27  $V_{\text{RHE}}$  for pH 4, 7 and 10 respectively. Remarkably, the final OC potentials ( $E_{\text{OC}}$ , marked with stars in both the inset and the main plot) and the photocurrent onset potentials ( $E_{\text{onset}}$ ) seem to be identical for the corresponding pH's. A correlation between  $E_{\text{OC}}$  and  $E_{\text{onset}}$  is something to be expected, since measurements of  $E_{\text{OC}}$  can be used to determine the photovoltage ( $V_{\text{ph}}$ ); any changes in  $V_{\text{ph}}$  are usually reflected in shift of the  $E_{\text{onset}}$ <sup>35</sup> since  $V_{\text{ph}}$  can be simply viewed as amount of bias voltage provided by a photoelectrode itself. However, this exact coincidence of the long-term equilibrium OC potential after photocharging and the photocurrent onset potential of the J-V curves under solar illumination is a unique feature of our photoanodes. It seems that the onset of PEC activity corresponds directly with the photocharged OC potential, and thus the match between these values shows that there has been a significant reduction in overpotential required to evolve oxygen in photocharged samples. It may imply very fast exchange current densities at the SLJ. Importantly, this proposed correlation seems to hold in the whole pH 4 - 10 range, and is therefore not a signature of PC-enhanced performance, but rather a unique feature of our material. Notably, measurements collected at different pH's have very different photocurrent slopes at the onset: very sluggish at pH 4 and very steep at pH 10. Therefore, while the exchange current densities may be very fast in the whole pH range, the losses at the interface still vary significantly depending on the pH. To further prove that the OC potential under illumination correlates directly with the OER onset potential, we performed an  $i(t)$  experiment at a potential slightly (0.1 V) above the OC potential of a photocharged  $\text{BiVO}_4$  anode (Fig. S4 and S5). Our results show that a small anodic bias of 0.1 V vs the OCV (potential too low to drive OER on untreated  $\text{BiVO}_4$ , see Fig. S6 and S7) can result in some non-negligible current over 30 hours, suggesting that the observed current is indeed related to OER.

The potential of a photoelectrode probed by a potentiostat can be considered to be equivalent to its Fermi level position  $E_F$  or quasi-Fermi level position of the electrons  $E_{F,n}$ .<sup>36</sup> While the OC potential measured by the potentiostat corresponds effectively to the back contact and not to the surface, it is assumed that any change in one would trigger a similar change in the other. Therefore, we consider the 'E vs t' measurements (Figure 1, inset) as a technique to monitor *in-situ* the effect of the PC treatment on the  $E_{F,n}$  of  $\text{BiVO}_4$ . Our data shows that under PC conditions facilitating the highest enhancement in the photocurrent (pH 10), the OC potential strongly shifts towards the water reduction potential (0  $V_{\text{RHE}}$ ) during the PC time (Figure 1, inset, black curve). Therefore, we can conclude that a successful PC treatment leads to a shift of the  $\text{BiVO}_4$   $E_{F,n}$  towards the conduction band edge.

The observed shift in the OC potential can be related to pinning of the electron Fermi level by the surface capacitive layer. Pinning of  $E_F$  has been reported to have a strong effect on the obtainable photovoltage ( $V_{\text{ph}}$ ).<sup>35,36,41</sup> Our previous results<sup>27</sup> suggest that the photocharging treatment may be related to changes in the chemical compositions of the surface. Consequently the surface of  $\text{BiVO}_4$  altered during the photocharging seems to give rise to an energetic level at which the Fermi level pins. Our data indicates that Fermi level pinning at the energy level related to this newly formed capacitive layer is more beneficial for water oxidation via an increase of  $V_{\text{ph}}$ . Furthermore, it has been proposed that under heavy Fermi level pinning conditions, an extra bias voltage may be necessary to start driving the OER.<sup>42</sup> This agrees well with our J-V data, which shows that the overpotential to drive OER with untreated  $\text{BiVO}_4$  is significantly higher than for photocharged films (supposedly diminished Fermi level pinning). The electronic properties of this proposed surface capacitive layer are further discussed in the impedance spectroscopy section.

One other possible explanation of this OC potential shift could be related to formation of some oxy/hydroxyl-based water oxidation intermediates at the surface of  $\text{BiVO}_4$ . In general, the chemical nature of the surface adsorbates can be expected to depend strongly on the electrolyte properties. Specifically, in water based electrolytes, the pH will heavily affect the type of the aqueous-based adsorbates on the surface of a photoelectrode. Correspondingly, the properties of the SLJ, in particular the surface adsorbates, can affect in some way the chemical reaction mediated by the surface, in our case water oxidation. It seems plausible that in alkaline conditions, high  $\text{OH}^-$

concentration produces adsorbates that can be readily transformed with the charge carriers excited during the PC treatment into more active water oxidation intermediates, simultaneously resulting in an altered  $E_{F,n}$ . Importantly, it has been proposed<sup>36</sup> that the adsorption of  $H_2O$  molecules and its derivatives is responsible for the surface states observed typically on  $MO_x$  photoanodes. Therefore, both presented hypotheses may in fact share a common mechanism.

Furthermore, in our initial work<sup>27</sup> we reported on limited stability of the photocharging effect in near-neutral conditions. Photoanodes photocharged in pH 7.2 and left in the electrolyte for 24 h under dark OC conditions exhibited J-V characteristics very similar to that of untreated material. Now, using pH 10, we were able to achieve much higher stability. The results of dark “deactivation” of a  $BiVO_4$  film in pH 10 are presented in Fig. S8a. It seems that after 20 h of storage in the dark the deactivation of PC- $BiVO_4$  is only partial and much less severe than in pH 7. The JV curve of “deactivated” PC- $BiVO_4$  is roughly one third in between the photocharged and the untreated state. Therefore, the pH 10 conditions seem not only to be more beneficial in terms of driving the PC effect but also prevent the dark deactivation much better than pH 7. Consequently, pH 10 conditions are much more suitable for a practical PEC water splitting device, since the photocharging effect can remain “locked-in” overnight.

Moreover, on the contrary to what has been recently reported,<sup>43</sup> our  $BiVO_4$  photoanodes do not show any changes in PEC activity when subjected to prolonged illumination in air (Fig. S8b), establishing the necessity of the electrolyte to facilitate the PC effect. Clearly, different deposition techniques used to fabricate  $BiVO_4$  films (spin coating in Berlinguette’s work<sup>43</sup> and spray pyrolysis in our case) inevitably produce films of different composition and different defect structure, what is further supported by our XPS study presented in Figure 2. In the work of Berlinguette, a strong peak at ca 532 eV can be observed for untreated samples, which is ascribed to surface defect sites (e.g., dangling oxo or hydroxy groups). However, we observe exactly the opposite; our initial material demonstrates a relatively weak signal at 532 eV. Further on, since the starting material is quite different, we believe that both treatments lead to a different modification and facilitate some different chemical transformation at the surface. In the work of Berlinguette the oxygen peak at 532 eV diminishes over the UV-curing treatment time, which is ascribed to removal of the surface states. On the

contrary, we observe that it is only once the oxygen peak at 532 eV becomes more pronounced that an enhanced activity for photoelectrochemical water oxidation by our photoanodes can be achieved. We tentatively ascribe this 532 eV peak to hydroxyl groups.<sup>44</sup> Moreover, we observe a significant decrease in the surface vanadium concentration of photoanodes subjected to photocharging treatment. Overall, our XPS study clearly demonstrates that our initial material is different from the one of Berlinguette and that we are driving a different chemical transformation with our photocharging treatment. The surface of the photocharged  $\text{BiVO}_4$  seems to be terminated with some extra hydroxyl groups, to have a decreased concentration of vanadium and to be enriched with oxygen, which happens to make it more active for OER.

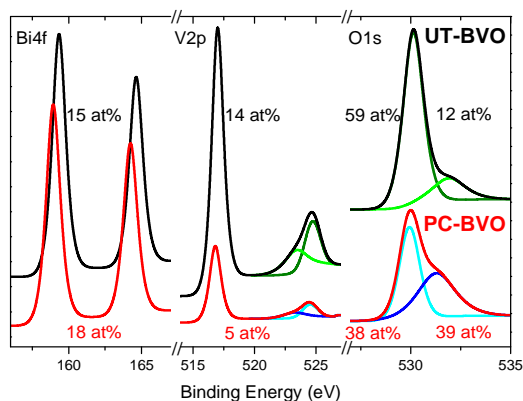


Figure 2. XPS spectra of  $\text{BiVO}_4$  photoanodes before and after photocharging in 0.1 M PBA buffer pH 10 under AM1.5G simulated illumination.

### 3.2.2 Spectroscopic study of PC $\text{BiVO}_4$

To further probe the optoelectronic properties of  $\text{BiVO}_4$  photoanodes during photocharging, we performed in-situ UV-vis spectroscopy to measure the change in optical transmittance of the photoanodes during electrochemical testing. Figure 3 shows the change in transmittance of the films at 550 nm (above the 520 nm bandgap of  $\text{BiVO}_4$ ), collected in-situ during the PC process. It was observed that for all the 3 pH's

studied, the PC treatment leads to a gradual decrease in transmittance at 550 nm, meaning more absorption in the above bandgap region. Moreover, we detect a strong change in transmittance at pH 10 and a very slight one at pH 4. Therefore, regardless of the mechanism for this optical change, the hydroxyl groups seem to be facilitating the darkening effect.

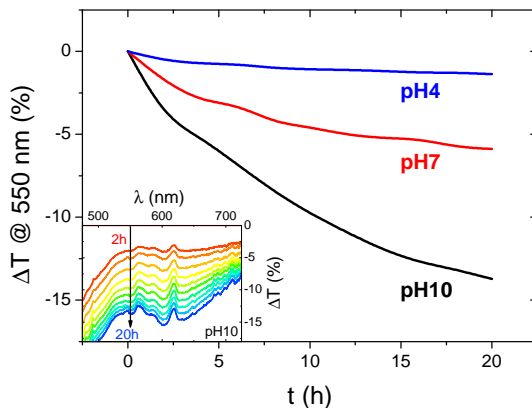


Figure 3. Relative change in optical transmittance at 550 nm wavelength as a function of PC time of  $\text{BiVO}_4$  in PBA buffer pH 4, 7 and 10. Inset – relative change in optical transmittance in the above-bandgap spectral range as a function of PC time of  $\text{BiVO}_4$  in PBA buffer pH 10, shown with a time step of 2h, the arrow indicates the trend.

Our spectral data suggests that there is a direct correlation between the pH and strength of the observed optical effect, i.e. alkaline conditions favor the darkening of  $\text{BiVO}_4$  outside the band gap region. In the previous section we identified a similar correlation between the electrolyte pH and the strength of the PC effect, i.e. the higher the pH the more photocurrent extracted from a photocharged  $\text{BiVO}_4$  sample. This implies that a ‘darker state’ of  $\text{BiVO}_4$  can be associated with higher photocurrents. However, there is no clear plateau in the  $\Delta T/\text{dt}$  trend, suggesting that a full transition to a ‘darker state’ is not a necessary condition to fully photocharge  $\text{BiVO}_4$ .

To understand whether the extra above-the-bandgap absorption of photocharged  $\text{BiVO}_4$  yields an improved photocurrent density, i.e. if it creates charge carriers useful for water oxidation, external quantum efficiency (EQE), or incident

photon to current conversion efficiency (IPCE) experiments were performed. Figure 4a shows the results of the EQE measurements of  $\text{BiVO}_4$  photoanodes before and after PC. All the EQE curves show the onset of the photocurrent at a wavelength of about 520 nm, in good agreement with the bandgap energy of 2.4 eV typically reported for  $\text{BiVO}_4$ .<sup>12</sup> All the curves reach a quasi-plateau at wavelength of about 440 nm. This slow rise in EQE is a direct consequence of optical properties of  $\text{BiVO}_4$ . It is widely believed that a range of weak valence to conduction band transitions in the near bandgap wavelength range<sup>45</sup> is responsible for a slow rise in the absorption coefficient of  $\text{BiVO}_4$ , and consequently the observed trend in EQE.

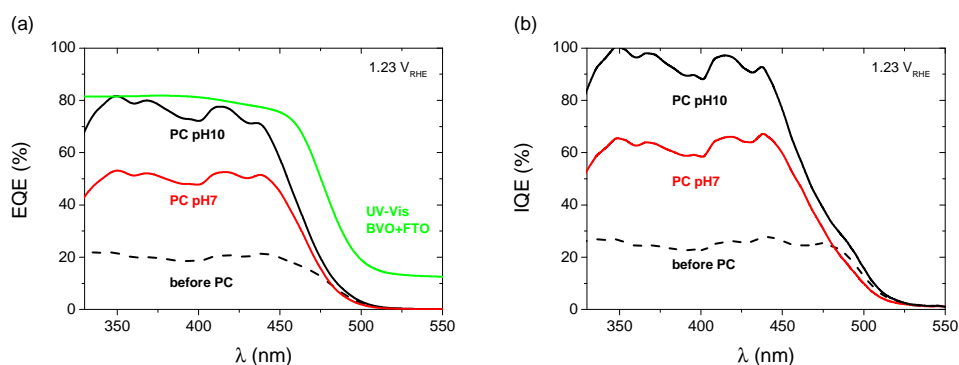


Figure 4. (a) External and (b) Internal Quantum Efficiency measurements of 200 nm  $\text{BiVO}_4$  in PBA buffer pH 7 and 10 before and after PC collected at  $1.23 \text{ V}_{\text{RHE}}$  bias voltage. Green curve – absorption trend of a  $\text{BiVO}_4$ -FTO sample.

Our EQE results clearly show that PC has a remarkable impact on the quantum efficiency of  $\text{BiVO}_4$  photoanodes. Untreated  $\text{BiVO}_4$  demonstrates average IPCE of 20%, while PC  $\text{BiVO}_4$  shows average IPCE of 75% and 50% for pH 10 and pH 7 respectively (440 nm >  $\lambda$  > 330 nm range). The EQE results follow a trend similar to the voltammetry measurements, i.e. a high pH favours a high quantum efficiency Figure 4b presents the internal quantum efficiency (IQE), or absorbed photon to current conversion efficiency (APCE) data obtained by integrating the absorption spectra of the films with the EQE/IPCE. For pH 10, we can calculate the average internal quantum efficiency to be around 95% in the 330 to 440 nm wavelength range. This remarkable result shows clearly that the PC treatment allows our  $\text{BiVO}_4$  photoanodes to convert almost all of the absorbed photons into extractable photocurrent, suggesting that the

PC treatment in pH 10 can eliminate both catalytic and bulk limitations almost entirely. This is an unprecedented result for a non-doped, non-catalyst modified photoelectrode, and represents a benchmark for photo-to-chemical conversion for solar water oxidation.

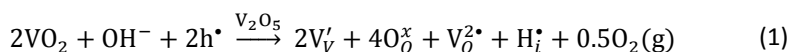
To further strengthen our claim about near complete suppression of surface losses we also present the catalytic efficiency trends of our  $\text{BiVO}_4$  photoanodes as a function of potential for different conditions (Fig. S9). We believe that the observed near unity quantum efficiency is also facilitated by the morphology of our films. Although the investigated photoanodes are 200 nm thick, yet they're not fully compact and flat. As demonstrated in Fig. S10,  $\text{BiVO}_4$  films fabricated via spray pyrolysis are highly porous and intrinsically nanostructured, such that the distance for the charge carriers to travel is significantly less than 200 nm and close to the diffusion length of photogenerated charge carriers reported for  $\text{BiVO}_4$  (70 nm). Furthermore, it is also possible that the photocharging treatment affects positively the diffusion length of the charge carriers in  $\text{BiVO}_4$ , without affecting the surface morphology at any pH (Fig. S10).

Interestingly, the quantum efficiency in the above-bandgap wavelength region remains zero after PC. Therefore we can conclude that the additional portion of light absorbed by PC  $\text{BiVO}_4$  in the above-bandgap region, demonstrated as the previously described darkening effect, does not contribute to the increased photocurrent. Increased absorption in the above-bandgap range and unchanged EQE onset could suggest incorporation of H into the near surface layer of our films, since similar optical effects have been reported for hydrogenated  $\text{BiVO}_4$ .<sup>46</sup> Likewise, the darkening effect could possibly be explained by reduction of vanadium species in  $\text{BiVO}_4$ , similarly to what has been reported by Qin et al.,<sup>47</sup> who observed enhanced absorption beyond the bandgap in reduced monoclinic  $\text{BiVO}_4$ .

The most likely way for hydrogen to get incorporated into the  $\text{BiVO}_4$  lattice is via intercalation into interstitial sites,<sup>46</sup> leading to formation of positively charged ( $\text{H}_i^\bullet$ ) defects. For the sake of conservation of charge, it is possible that formation of those interstitial hydrogen impurities is accompanied with reduction of vanadium, leading to formation of negatively charged vanadium species ( $\text{V}_V'$ ). This mechanism is consistent with the XPS study of PC- $\text{BiVO}_4$  which we have presented in our initial report,<sup>27</sup> and which shows that surface vanadium undergoes reduction from 5+ to 4+ oxidation state during the PC treatment. If we now consider self-doping of the  $\text{V}_2\text{O}_5$  sublattice with



VO<sub>2</sub> species, we may expect that oxygen ions will occupy four out of five oxygen sites in the V<sub>2</sub>O<sub>5</sub> sublattice (O<sub>O</sub><sup>x</sup>), leaving the fifth oxygen site empty and leading to formation of an oxygen vacancy (V<sub>O</sub><sup>2•</sup>). In this particular case special care needs to be taken in order not to confuse the Vanadium and vacancy descriptor (V<sub>V</sub><sup>•</sup> and V<sub>O</sub><sup>2•</sup>). Overall, we can propose the mechanism of light-triggered hydrogenation of the BiVO<sub>4</sub> surface layer coupled with the reduction of vanadium surface species; equation (1) illustrates the possible defect chemistry reaction using Kröger–Vink notation:



Since our experimental results indicate that both light and alkaline conditions are critical for the PC effect to take place, thus photogenerated holes (h<sup>•</sup>) and hydroxyl groups (OH<sup>•</sup>) are included as reactants with VO<sub>2</sub>. The alteration of the surface chemistry via the formation of hydrogen interstitials and oxygen vacancies could lead to increased absorption outside the BiVO<sub>4</sub> band gap energy and improve the catalytic properties of our photoanodes, which is in agreement with the results from Wang et al.,<sup>46</sup> which show that hydrogen treatment leads to improved photocurrents in BiVO<sub>4</sub> photoanodes.

### 3.2.3 In-situ X-ray absorption spectroscopy (XAS)

It is unclear whether the whole bulk of BiVO<sub>4</sub> films becomes affected by the photocharging treatment. Therefore, in order to investigate any possible impact of the PC treatment on the chemical and structural properties of bulk BiVO<sub>4</sub>, specifically to identify any changes in the average bulk oxidation state of vanadium and in the local environment, we performed an in-situ XAS study.

Figure 5 presents Vanadium K-edge XAS spectra collected in-situ as the function of the (a) PC treatment time and (b) applied bias potential. For BiVO<sub>4</sub> films subjected to PC treatment for 8 h, no changes in the XAS spectrum were observed throughout the experiment. Likewise, ex-situ conditions and dark OC conditions yield the same spectra (Figure 5a). Similarly, for BiVO<sub>4</sub> films poised at potentials of 0.3, 0.7 and 1.1 V<sub>RHE</sub> there was essentially no shift in the XANES edge energy (Figure 5b). Ultimately, for all the experimental conditions studied, the XAS spectra in the XANES

range show a nearly perfect overlap. Therefore, we conclude that neither photocharging treatment nor applying bias potential ( $0.3 - 1.1 \text{ V}_{\text{RHE}}$ ) alters the structure/chemistry of the bulk of  $\text{BiVO}_4$  films; specifically, our films do not display any signatures of changes in the average bulk vanadium oxidation state, despite significantly different PEC properties.

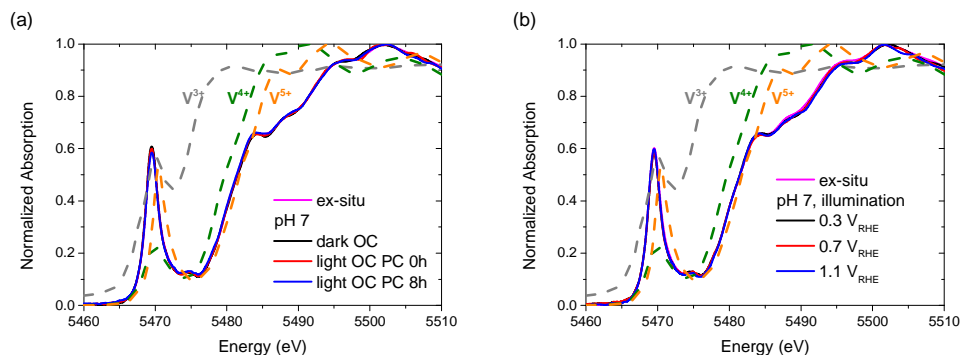


Figure 5. Vanadium K-edge XAS spectra collected (a) ex situ and in-situ under OC conditions, in the dark and under illumination (b) ex situ and under illumination and with applied bias potential.

Figure 5 includes also reference spectra of  $\text{V}_2\text{O}_3$ ,  $\text{VO}_2$  and  $\text{V}_2\text{O}_5$ . Clearly, the edge position of vanadium oxides shifts to higher energies with increased formal oxidation state (approx. 5470, 5474 and 5476 eV for  $\text{V}^{3+}$ ,  $\text{V}^{4+}$  and  $\text{V}^{5+}$  respectively). Based on the spectra of vanadium oxides the oxidation state of V in  $\text{BiVO}_4$  films was estimated. Notably, the edge position of a XANES spectrum is only an approximate indicator of the oxidation state of metals owing to the several parameters that contribute to the XANES spectra (i.e., charge density, ligand symmetry, and spin density).<sup>48,49</sup> However, given significant differences between edge positions of different vanadium oxides and a similar chemical environment of vanadium atoms both in  $\text{VO}_x$  and in  $\text{BiVO}_4$ , the oxidation state of V in our films can be determined quite confidently. The edge position of  $\text{BiVO}_4$  films is alike to that of  $\text{V}_2\text{O}_5$ , indicating a mean oxidation state of +5. Since, like discussed in the previous paragraph, all the  $\text{BiVO}_4$  XAS spectra are essentially the same, we can conclude that bulk vanadium in our films always preserves the +5 oxidation state.

To verify the local arrangement of vanadium in our films and to monitor any possible changes in the spectrum, XANES calculations have been performed.  $\text{BiVO}_4$  is known to exist in three polymorphs: orthorhombic pucherite, tetragonal dreyerite, and monoclinic clinobisvanite. However, the only thermodynamically stable phase is clinobisvanite. According to the simulations presented in Fig. S11 the main atomic arrangement shown by our films is typical for the crystallographic structure of clinobisvanite. Therefore, we can further confirm that bulk vanadium in our films has a dominant oxidation state of +5.

### 3.2.4 Impedance Spectroscopy (IS)

In an effort to find the correlation between the photocharging treatment and charge transfer behavior, we performed cyclic voltammetry (CV) on the untreated (UT) and photocharged (PC)  $\text{BiVO}_4$ , as shown in Figure 6. In the presence of trap states (*i.e.*, surface states), one or more reduction peaks are usually present in the cathodic voltammetry scan, which can be attributed to charging or filling of electrons from the conduction band to the surface state as the electron Fermi level shifts upward during the cathodic sweep.<sup>50–52</sup> In the dark voltammetry, thus in the absence of photogenerated holes, such trap-related reduction peaks are irreversible. The irreversibility of these capacitive cathodic peaks has been related to the equilibration between trap states and conduction band.<sup>52</sup> In order to unambiguously identify any trap-related peaks, the CV is typically performed in the dark, to avoid masking the possible trap capacitive effects by the photocurrent. CV scan of the UT sample shown in Figure 6a depicts both anodic and cathodic peaks, which cannot be assigned to deep surface traps (which are irreversible). The reversible peaks, however, can be ascribed to the reduction and re-oxidation of the redox system of  $\text{V}^{5+}$  to  $\text{V}^{4+}$ . It is noticeable that these redox peaks are barely visible in the dark and significantly more pronounced under illumination (Fig. S12), since the photogenerated charge also contributes to the oxidation and reduction of these redox states. Moreover, slightly higher capacitance can be derived from the hysteresis of the PC cyclic voltammetry curve in Figure 6a.

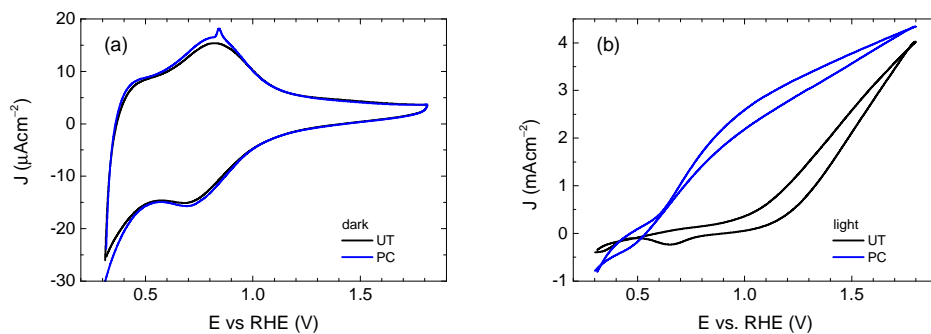


Figure 6. Cyclic voltammetry of untreated (UT) and photocharged (PC)  $\text{BiVO}_4$  (a) in the dark and (b) under illumination.

Consequently, we carried out impedance spectroscopy (IS) measurements to characterize the carrier dynamics in the bulk and on the surface on the untreated (UT) and photocharged (PC)  $\text{BiVO}_4$  in the dark and under illumination using physical models (*i.e.*, equivalent circuit, EC) that have been used extensively for n-type metal oxide semiconductors when surface states are present (see Fig. S13).<sup>53–55</sup> Figure 7a shows the bulk capacitance of UT and PC  $\text{BiVO}_4$  in the dark and under illumination as a function of applied potentials obtained from the IS measurements. This capacitance shows a peak at ca.  $0.7 V_{\text{RHE}}$  which increases both under illumination and after the PC treatment. This behavior is consistent with the cyclic voltammetry study demonstrated in Figure 6 and Fig. S12, and can be ascribed to the redox process of  $\text{V}^{4+}/\text{V}^{5+}$ . However, we found that the photocharging treatment involving reduction of  $\text{V}^{5+}$  to  $\text{V}^{4+}$  does not affect the bulk electronic properties, as indicated by the constant bulk resistance for the untreated and the photocharged samples, shown in Figure 7b. This likely suggests that the onset potential shift and increase of the photocurrent observed in our photocharged samples is not related to the bulk conductivity of the material.

Further on, we looked for signatures of any changes in the band structure of  $\text{BiVO}_4$  occurring during the photocharging process. Figure 7c presents the bulk capacitance versus applied voltage, plotted as a Mott-Schottky dependence. The Mott-Schottky plot allows for estimation of the flat band potential ( $V_{\text{fb}}$ ) of our samples. Due to a significant overlap of the redox capacitance (the peak at  $0.7 V_{\text{RHE}}$ ) with the space charge capacitance of  $\text{BiVO}_4$ , the potential window available for the linear Mott-

Schottky dependence is very narrow. However, the extraction of the space charge capacitance is still possible, as shown in Figure 7d. We noticed that the flat band potential shifts anodically upon photocharging treatment, which is consistent with hole accumulation at the capacitive layer. In any case, the positive shift does not contribute to the cathodic shift of photocurrent onset potential of the photocharged  $\text{BiVO}_4$ . This cathodic shift of photocurrent is related reduced surface recombination, improving the performance of the photoanodes.

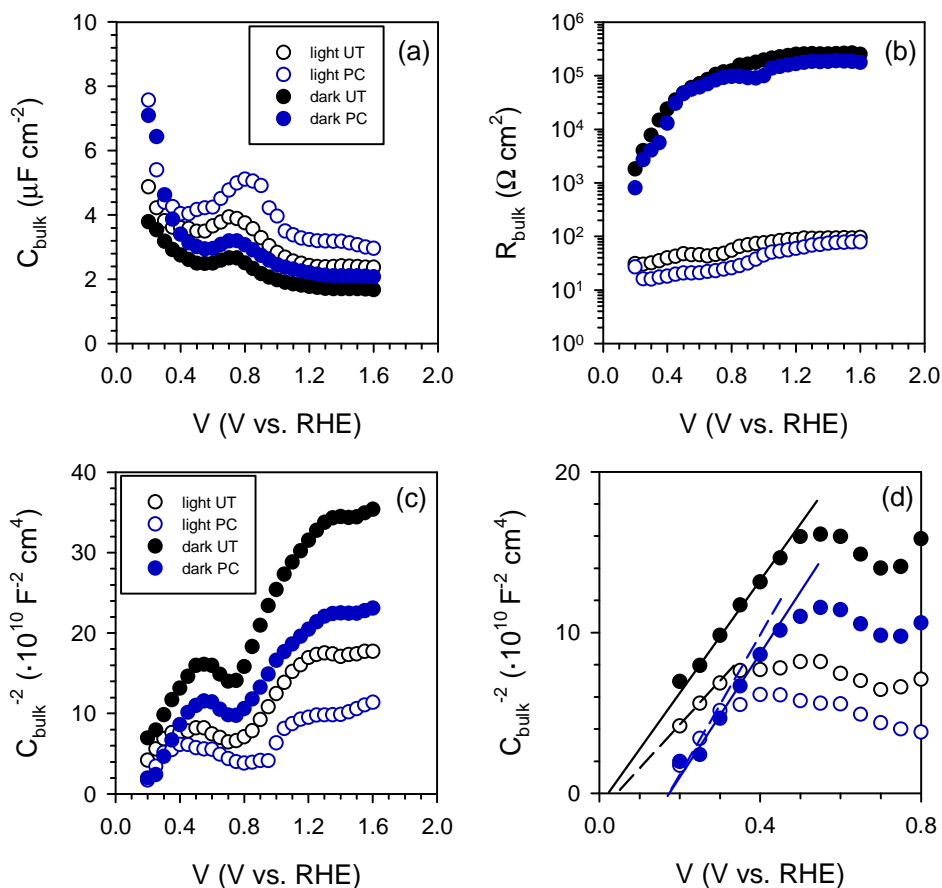


Figure 7. Untreated (UT) and photocharged (PC)  $\text{BiVO}_4$  at pH 10 - (a) Bulk capacitance ( $C_{\text{bulk}}$ ) and (b) bulk resistance ( $R_{\text{bulk}}$ ) as a function of potential, (c) and (d) Mott-Schottky plots

The IS response of illuminated  $\text{BiVO}_4$  photoanodes also showed some distinctive feature in the low frequency regime. Such a feature can be usually attributed to a surface signature, such as charging/discharging of the surface states<sup>54</sup> and/or catalytic layers.<sup>55,56</sup> In order to properly address this phenomenon, the evolution of both the surface capacitance ( $C_s$ ) and charge transfer resistance ( $R_{ct}$ ) with potential was studied, as depicted in Figure 8.

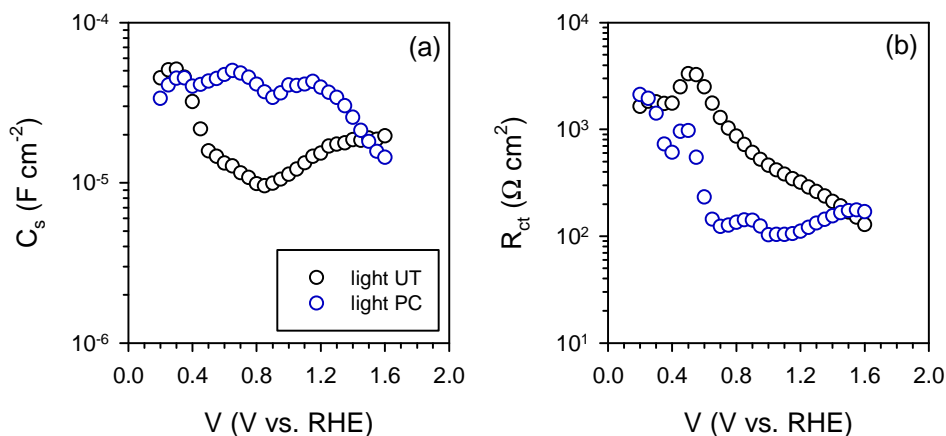


Figure 8. (a) Surface capacitance ( $C_s$ ) (b) charge transfer resistance ( $R_{ct}$ ) of the untreated (UT) and the photocharged (PC)  $\text{BiVO}_4$  under illumination at pH 10.

From Figure 8a we note that the values of the surface capacitance increase on the photocharged sample, suggesting that surface modification indeed took place during the photocharging treatment. The surface capacitance of PC samples does not demonstrate the typical Gaussian distribution that is generally obtained for a system containing localized surface states.<sup>54,57</sup> In fact, it remains almost constant in a wide potential window (ca. 1 V), which is similar to that reported in water splitting systems when a catalytic layer is deposited on the surface of a photoanode.<sup>55,56</sup> Hence, we attribute this capacitance to the formation of a surface layer formed by the photocharging process due to the adsorption of oxy/hydroxyl species as previously discussed, rather than a localized surface trap. This hypothesis is further supported by the evolution of charge transfer resistance shown in Figure 8b. The resistance does not significantly evolve over a large potential window and its minima do not correspond to

the maxima of the surface capacitance as expected for a surface trap. The surface capacitive layer pins the electron Fermi level which leads to the anodic shift of the flatband potential as observed from Figure 7c for photocharged samples.

This has been illustrated in the cartoon of Figure 9, highlighting the proposed mechanisms involved in the photocharging process: intercalation of hydrogen and reduction of surface vanadium favoured under alkaline conditions and formation of the capacitive layer. In the mechanistic cartoon of Figure 9, the reduced band bending in the photocharged material is due to the shift of the Fermi level towards the conduction band of  $\text{BiVO}_4$ , as a result of the photocharging effect. The shift of the flatband potential to positive potentials is consistent with the accumulation of holes at the interface. The diagram depicts also the increase in the photovoltage of PC  $\text{BiVO}_4$  ( $V_{\text{ph2}}$ ) vs the photovoltage of the untreated material.

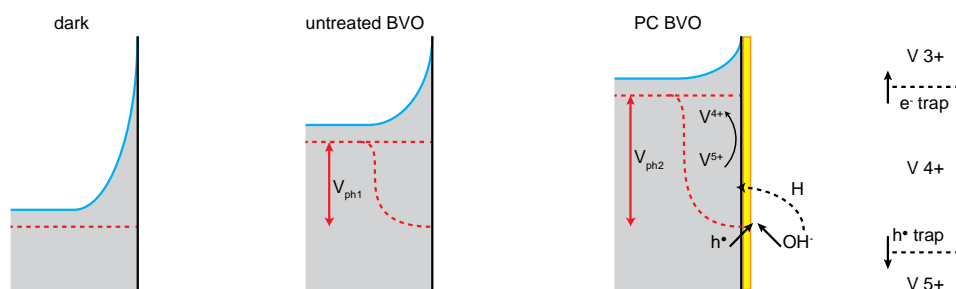


Figure 9. Band diagrams of  $\text{BiVO}_4$  in the dark and under illumination before and after photocharging treatment, including the simplified photocharging mechanism model. The green star indicates the energetic level related to the surface capacitive layer, causing the Fermi level pinning.

Though the flatband potential moves to more anodic potentials, the capacitive layer acts as a 'hole reservoir' and minimises recombination, leading to an onset potential of about 0.4 V vs  $V_{\text{RHE}}$ , as observed from Figure 6b. From this study it can be concluded that the photocharging treatment accelerates the creation of the OER intermediates on the  $\text{BiVO}_4$  surface which act as a hole reservoir, in the same manner as a catalytic layer. The origin of this early formation of reaction promoters can be connected to the  $\text{V}^{5+}$  reduction process in favourable pH electrolyte conditions. The mechanism of the photocatalytic effect by the existence of  $\text{V}^{4+}$  has been largely described on V multiple valence materials such as  $\text{V}_2\text{O}_5$  doped  $\text{TiO}_2$ ,  $\text{CaV}_2\text{O}_6$  and  $\text{BiVO}_4$ .

nanorods.<sup>58–60</sup> Furthermore, it has been demonstrated on BiVO<sub>4</sub> nanorods that the presence of V<sup>4+</sup> defects induce oxygen vacancies (V<sub>O</sub>) on the surface of nanoparticles.<sup>60</sup> V<sub>O</sub> can strongly adsorb O<sup>2-</sup> and OH<sup>-</sup> species on the surface, which leads to an enhanced photocatalytic effect.

To further elucidate on the capacitive behaviour of our photoanodes, a chopped light chronoamperometry experiment was performed. Similar study<sup>55</sup> has demonstrated that Co-Pi deposited onto α-Fe<sub>2</sub>O<sub>3</sub> can efficiently collect and store photogenerated holes from the hematite electrodes. Co-Pi layers of different thickness have different charge storage capacity and therefore demonstrate different decay times in chopped light transients. An analogous study performed on Fh/Ta<sub>3</sub>N<sub>5</sub><sup>61</sup> describes a “surface charging” process, demonstrated by increase in the photocurrent. This effect is attributed to accumulation of surface trapped holes, resulting in enhancement of photocurrent. Fig. S14 and S15 present respectively the anodic and cathodic transients of untreated and photocharged BiVO<sub>4</sub> photoanodes. The fast decay observed for untreated films (Fig. S14a) could suggest<sup>55</sup> hole accumulation/trapping, charging of the surface states or oxidation of some surface species. On the other hand, photocharged films demonstrate build-up of photocurrent (Fig. S14b), which suggest<sup>61</sup> capacitance-related effect such as surface charging. Cathodic transients show much faster decay in case of untreated BiVO<sub>4</sub> (Fig. S15a), when compared with photocharged material (Fig. S15b). It could be indicative of higher charge storage capacity of PC-BiVO<sub>4</sub>, in agreement with our EIS results. Overall, photocharged BiVO<sub>4</sub> seems to demonstrate some traits typical for catalyzed photoanodes.

A more in depth analysis of the anodic transients is troublesome since within the potential range used in our study the capacitive and faradaic currents are convoluted, therefore it is difficult to extract the integrated capacitive charge. However, the total charge stored in the case of the cathodic transients can be calculated using equation (2):

$$\Delta Q = \int J dt \quad (2)$$



From the observation of the transients, it is clear that higher charge is accumulated at the PC specimens. Further on, the surface capacitance can be calculated using equation (3):

$$C_s = \frac{d\Delta Q}{dE} \quad (3)$$

The capacitance values based on cathodic transients presented in Fig. S15 and obtained using equations (2) and (3) are 0.05 and 0.4 mFcm<sup>-2</sup> for untreated and photocharged material respectively. These values confirm significant differences in the charge storage capabilities of BiVO<sub>4</sub> before and after the PC treatment, and are in agreement with qualitative trends presented in Figure 8a.

### 3.3 Conclusions

BiVO<sub>4</sub> photoanodes immersed in electrolyte under the OC configuration and exposed to simulated solar illumination for prolonged time achieve superior PEC activity. This photocharging effect is capable of dramatically improving both, bulk and surface functionalities of BiVO<sub>4</sub>. New insights into the mechanisms of PC in BiVO<sub>4</sub> photoanodes and how it leads to improved PEC performance are necessary for its application in real devices.

There seems to exist a strong correlation between the pH of the electrolyte and PEC properties of PC BiVO<sub>4</sub>: alkaline conditions facilitate the PC effect while acidic conditions prevent it from happening. Specifically PC performed in alkaline conditions pH 10 yields high photocurrents, low onsets and high fill-factors, as well as very high quantum efficiencies (near 100% internal quantum efficiency), suggesting that both bulk and surface limitations of BiVO<sub>4</sub> can be overcome with PC alone. The strong pH dependence of the PC effect suggests that the SLJ plays a key role on the PC mechanism.

IS study reveals the photocharging effect is connected with the development of a capacitive layer, which has the ability to accumulate holes, and hence leads to reduced surface recombination. In addition, optical properties of  $\text{BiVO}_4$  subjected to PC treatment change, namely PC  $\text{BiVO}_4$  starts to absorb light beyond the bandgap range. However, this apparent increase in absorption does not lead to formation of charge carriers useful for water oxidation but it is rather a signature of transformation of material into a more PEC active state. This darkening effect could be potentially related to intercalation of hydrogen conjunct to reduction of vanadium in the surface layer of the films. Importantly, in-situ XAS study quite convincingly rules out the possibility that PC treatment leads to reduction of vanadium from 5+ to 4+ state within the whole bulk of the films.

Overall, our results suggest that PC is related to light-driven alteration of the surface of  $\text{BiVO}_4$ , preferential in alkaline conditions. Those changes result in properties becoming more beneficial for solar driven water splitting applications. Furthermore, any bulk-related effects are mediated by phenomena occurring at the surface, which highlights the importance of the SLJ for the efficiency of PEC devices. From a technological perspective, the advantages of the PC effect can be fully exploited under continuous operation of a  $\text{BiVO}_4$ -based photoelectrochemical device, and consequently, redesign of the operation protocols of these devices is imperative to successfully implement this PC effect.

## 3.4 Experimental

### 3.4.1 Preparation of $\text{BiVO}_4$ thin film photoanodes

Thin films of 50, 100, 200 and 300 nm thick  $\text{BiVO}_4$  were prepared by spray pyrolysis on FTO coated glass substrates. Details of the deposition procedure are described elsewhere<sup>13,16</sup> and are also available in Appendix II. Prior to deposition of  $\text{BiVO}_4$ , a  $\text{SnO}_2$  interfacial layer (~80 nm) was deposited onto the FTO substrate at 425 °C to prevent recombination at the FTO/ $\text{BiVO}_4$  interface.<sup>62</sup> The substrate temperature

during spraying of  $\text{BiVO}_4$  was maintained at 450 °C. After deposition, the samples were further annealed for 2 h in a tube furnace at 450 °C in air.

### 3.4.2 Photoelectrochemical (PEC) measurements

A 0.1 M phosphate buffer (K- $\text{P}_i$ ) and 0.1 M phosphate-borate-acetate (PBA) buffer were used as electrolyte. K- $\text{P}_i$  was prepared by dissolving a mixture of  $\text{KH}_2\text{PO}_4$  (Sigma Aldrich, 99.0%) and  $\text{K}_2\text{HPO}_4$  (Sigma Aldrich, 99.0%) in Milli-Q water (18.2 M $\Omega$ cm), to obtain pH 7.2 and to preserve 0.1 M overall concentration of  $\text{PO}_4^{3-}$ . PBA buffer was prepared by dissolving  $\text{KH}_2\text{PO}_4$  (Sigma Aldrich, 99.0%),  $\text{H}_3\text{BO}_3$  (Sigma Aldrich, 99.5%) and acetic acid (Sigma Aldrich, 99.7%) in Milli-Q water (18.2 M $\Omega$ cm). The concentration of each component was set to 0.1 M. The pH was adjusted to a desired value by titrating the PBA solution with KOH (Sigma Aldrich, 99%), and with a pH meter immersed. Throughout this work the PBA buffer pH 4, 7 and 10 was used.

PEC characterization of  $\text{BiVO}_4$  photoanodes was carried out in an electrochemical cell using a three-electrode configuration. The potential of the working electrode was controlled by a multi-channel potentiostat (Parstat MC, Princeton Applied Research). An Ag/AgCl electrode (XR300, saturated KCl + AgCl solution (KS120), Radiometer Analytical) and a coiled Pt wire were used as the reference and counter electrodes, respectively. Measurements under illumination were performed with a Newport Sol3A Class AAA solar simulator (type 94023A-SR3) producing simulated AM 1.5 solar illumination (100 mWcm<sup>-2</sup>). In all the experiments involving illumination,  $\text{BiVO}_4$  samples were illuminated from the back-side, i.e. the light came through the substrate side first. Cyclic voltammetry scans were taken at a scan rate of 50 mVs<sup>-1</sup> unless stated otherwise.

The photocharging of  $\text{BiVO}_4$  photoanodes was performed in OC conditions under illumination.  $\text{BiVO}_4$  samples were placed in the electrochemical cell and exposed to AM 1.5 light until the plateau of  $V_{\text{WE}}(t)$  was reached (10 hours on average).

### 3.4.3 In-situ UV-vis spectroscopy

The spectral data was collected using the OceanOptics USB2000+ spectroradiometer and SpectraSuite software. The spectroradiometer was placed behind the cell to measure the intensity of light transmitted through a BiVO<sub>4</sub> sample.

### 3.4.4 Quantum Efficiency

Monochromatic photocurrents were measured with a 300 W Xe lamp (Oriel LSE340 interface, LSH302 lamp housing, LSN252 power supply, LSB530 lightbulb) coupled into a grating monochromator (ActonSpectraPro 150i). An electronic shutter (Uniblitz LS6) was used, and a long-pass coloured glass filter (Schott, 3 mm thick) was placed between the monochromator and the sample to remove second-order diffracted light. The shutter was actuated every 10 s, and the photocurrent was taken as the difference between the current when the shutter is opened and closed (3 s integration time and ~1.5 nm step size). The light intensity was measured with a calibrated photodiode (Ophir PD300-UV) and ranged between 0.3 and 8 mWcm<sup>-2</sup>. The incident photon to current efficiency (IPCE, sometimes called the external quantum efficiency or EQE) was calculated based on the formula (2):

$$IPCE(\lambda) = \frac{1240(V \times nm) \times J(mAcm^{-2})}{P(mWcm^{-2}) \times \lambda(nm)} \quad (4)$$

### 3.4.5 X-ray absorption spectroscopy (XAS): X-ray absorption near edge structure (XANES) and Extended X-ray absorption fine structure (EXAFS)

V K-edge (5465 eV) XAFS spectra of thin films of BiVO<sub>4</sub> were collected at the Dutch-Belgian Beamline (DUBBLE) at the European Synchrotron Radiation Facility (ESRF).<sup>63</sup> The energy of the X-ray beam was tuned by a double-crystal monochromator operating in fixed-exit mode using a Si(111) crystal pair. All the measurements were performed at ambient temperature and pressure. Spectra of vanadium foil needed for energy calibration and reference spectra of vanadium oxides (V<sub>2</sub>O<sub>3</sub>, VO<sub>2</sub> and V<sub>2</sub>O<sub>5</sub>) were collected in transmission mode using Ar/He-filled ionization chambers. EXAFS

spectra of thin films of  $\text{BiVO}_4$  were collected in fluorescence mode using a 9-element Ge detector (Ortec Inc.).

The XAS investigation of  $\text{BiVO}_4$  was performed using a cell specially designed for in-situ PEC measurements. For the sake of probing the vanadium K-edge, characterized with a relatively low energy of 5465 eV, the electrolyte layer thickness was maintained at  $\sim 10\text{ }\mu\text{m}$ . The cell was equipped with a standard 3-electrode configuration, controlled with a potentiostat and continuously flushed with electrolyte (0.1 M K- $\text{P}_i$ ).  $\text{BiVO}_4$  samples were illuminated from the back-side with a Xe lamp equipped with an optical fiber.

The XANES spectra, three scans per sample, were energy-calibrated, averaged and further analysed using FDMNES package program using the multiple scattering theory based on the muffin-tin approximation on the potential shape.<sup>64,65</sup> The muffin-tin radii were tuned to have a 10% overlap between the different spherical potentials. The Hedín–Lundqvist exchange potential was used. The XANES spectrum of a  $\text{BiVO}_4$  crystal was calculated, considering in the calculation all the atoms surrounding the absorber V within a 7 Å radius sphere. The approximation of non-excited absorbing atoms was used, which better reproduces the experimental data. A similar calculation with the FEFF8 code<sup>66</sup> gave similar results. We have not considered the effect of the structural disorder in the XANES simulations. To simulate the XANES spectra, a core-hole broadening of 1.0 eV was used.

#### **3.4.6 Impedance Spectroscopy (IS)**

IS measurements were carried out in the same set up configuration as the PEC measurements by applying a 20 mV AC signal and scanning in a frequency range between 1 MHz and 50 mHz, at different applied bias. The numerical fitting of the impedance data was carried out using the Zview software (Scribner Associates).

#### **3.4.7 Scanning Electron Microscopy (SEM)**

The morphology of thin films was investigated with SEM microscopy (JEOL JSM-6010LA instrument equipped with a tungsten hairpin filament). Samples were

investigated in the secondary electron imaging mode (SEI), using an Everhart-Thornley type of detector. SEM images were collected using the accelerating voltage of 20 kV, at a working distance of 10 mm.

#### 3.4.8 X-ray photoelectron spectroscopy (XPS)

XPS experiment was performed using the Thermo Scientific K-alpha apparatus equipped with an Al K-alpha X-ray Source and a Flood Gun. Parameters used for the measurements were: spot size of 400  $\mu\text{m}$ , pass energy of 50 eV, energy step size of 0.1 eV, dwell time of 50 ms, 10 scans in the vicinity of the orbital binding energy of the elements of interest. XPS spectra were corrected for the C peak position.

### 3.5 Acknowledgements

We acknowledge the financial support of the Foundation for Fundamental Research on Matter (FOM TNW 10.327). This work has been done under the agenda of the BioSolarCells Consortium supported by the Dutch Ministry of Economic Affairs, Agriculture and Innovation. We acknowledge The Netherlands Organisation for Scientific Research (NWO) for financial support of the measurements at ESRF. We also thank financial support from the University Jaume I through the project P1-1B2011-50.

### 3.6 References

- (1) Grätzel, M. *Nature* **2001**, *414* (6861), 338.
- (2) Walter, M. G.; Warren, E. L.; McKone, J. R.; Boettcher, S. W.; Mi, Q.; Santori, E. A.; Lewis, N. S. *Chem. Rev.* **2010**, *110* (11), 6446.
- (3) Nocera, D. G. *Acc. Chem. Res.* **2012**, *45* (5), 767.

- (4) van de Krol, R.; Grätzel, M. *Photoelectrochemical Hydrogen Production*; van de Krol, R., Grätzel, M., Eds.; Electronic Materials: Science & Technology; Springer US: Boston, MA, 2012; Vol. 102.
- (5) van de Krol, R.; Liang, Y.; Schoonman, J. *J. Mater. Chem.* **2008**, *18* (20), 2311.
- (6) Tilley, S. D.; Cornuz, M.; Sivula, K.; Grätzel, M. *Angew. Chemie (International ed.)* **2010**, *49* (36), 6405.
- (7) Solarska, R.; Królikowska, A.; Augustyński, J. *Angew. Chemie (International ed.)* **2010**, *49* (43), 7980.
- (8) Sayama, K.; Nomura, A.; Arai, T.; Sugita, T.; Abe, R.; Oi, T.; Iwasaki, Y.; Abe, Y.; Sugihara, H.; Yanagida, M.; Oi, T.; Iwasaki, Y.; Abe, Y.; Sugihara, H. *J. Phys. Chem. B* **2006**, *110* (23), 11352.
- (9) Paracchino, A.; Laporte, V.; Sivula, K.; Grätzel, M.; Thimsen, E. *Nat. Mater.* **2011**, *10* (6), 456.
- (10) Han, L.; Abdi, F. F.; van de Krol, R.; Liu, R.; Huang, Z.; Lewerenz, H.-J.; Dam, B.; Zeman, M.; Smets, A. H. M. *ChemSusChem* **2014**, *7* (10), 2832.
- (11) Ager III, J. W.; Shaner, M.; Walczak, K.; Sharp, I. D.; Ardo, S. *Energy Environ. Sci.* **2015**, *8*, 2811.
- (12) Tokunaga, S.; Kato, H.; Kudo, A. *Chem. Mater.* **2001**, *13* (12), 4624.
- (13) Abdi, F. F.; Firet, N.; van de Krol, R. *ChemCatChem* **2013**, *5* (2), 490.
- (14) Zhong, D. K.; Choi, S.; Gamelin, D. R. *J. Am. Chem. Soc.* **2011**, *133* (45), 18370.
- (15) Jeon, T. H.; Choi, W.; Park, H. *Phys. Chem. Chem. Phys.* **2011**, *13* (48), 21392.
- (16) Abdi, F. F.; van de Krol, R. *J. Phys. Chem. C* **2012**, *116* (17), 9398.
- (17) Ding, C.; Shi, J.; Wang, D.; Wang, Z.; Wang, N.; Liu, G.; Xiong, F.; Li, C. *Phys. Chem. Chem. Phys.* **2013**, *15* (13), 4589.
- (18) Choi, S. K.; Choi, W.; Park, H. *Phys. Chem. Chem. Phys.* **2013**, *15* (17), 6499.
- (19) Kim, T. W.; Choi, K.-S. *Science (80-. )*. **2014**, *343* (6174), 990.
- (20) Haro, M.; Solis, C.; Blas-Ferrando, V. M.; Margeat, O.; Dhkil, S. Ben; Videlot-Ackermann, C.; Ackermann, J.; Di Fonzo, F.; Guerrero, A.; Gimenez, S. *ChemSusChem* **2016**, *9* (21), 3062.
- (21) Parmar, K. P. S.; Kang, H. J.; Bist, A.; Dua, P.; Jang, J. S.; Lee, J. S. *ChemSusChem* **2012**, *5* (10), 1926.
- (22) Rao, P. M.; Cai, L.; Liu, C.; Cho, I. S.; Lee, C. H.; Weisse, J. M.; Yang, P.; Zheng, X. *Nano Lett.* **2014**, *14* (2), 1099.
- (23) Pihosh, Y.; Turkevych, I.; Mawatari, K.; Uemura, J.; Kazoe, Y.; Kosar, S.; Makita, K.; Sugaya, T.; Matsui, T.; Fujita, D.; Tosa, M.; Kondo, M.; Kitamori, T. *Sci. Rep.* **2015**, *5* (1), 11141.
- (24) Abdi, F. F.; Savenije, T. J.; May, M. M.; Dam, B.; van de Krol, R. *J. Phys. Chem. Lett.* **2013**, *4* (16), 2752.

- (25) Eisenberg, D.; Ahn, H. S.; Bard, A. J. *J. Am. Chem. Soc.* **2014**, *136* (40), 14011.
- (26) McDowell, M. T.; Lichterman, M. F.; Spurgeon, J. M.; Hu, S.; Sharp, I. D.; Brunschwig, B. S.; Lewis, N. S. *J. Phys. Chem. C* **2014**, *118* (34), 19618.
- (27) Trześniewski, B. J.; Smith, W. A. *J. Mater. Chem. A* **2016**, *4* (8), 2919.
- (28) Gostein, M.; Dunn, L. In *2011 37th IEEE Photovoltaic Specialists Conference*; IEEE, 2011; pp 003126–003131.
- (29) Listorti, A.; Creager, C.; Sommeling, P.; Kroon, J.; Palomares, E.; Fornelli, A.; Breen, B.; Barnes, P. R. F.; Durrant, J. R.; Law, C.; O'Regan, B. *Energy Environ. Sci.* **2011**, *4* (9), 3494.
- (30) Lim, F. J.; Set, Y. T.; Krishnamoorthy, A.; Ouyang, J.; Luther, J.; Ho, G. W. *J. Mater. Chem. A* **2015**, *3* (1), 314.
- (31) Liu, C.; Fan, J.; Zhang, X.; Shen, Y.; Yang, L.; Mai, Y. *ACS Appl. Mater. Interfaces* **2015**, *7* (17), 9066.
- (32) Lin, F.; Boettcher, S. W. *Nat. Mater.* **2014**, *13* (1), 81.
- (33) Mills, T. J.; Lin, F.; Boettcher, S. W. *Phys. Rev. Lett.* **2014**, *112* (14), 148304.
- (34) Lin, F.; Bachman, B. F.; Boettcher, S. W. *J. Phys. Chem. Lett.* **2015**, *6* (13), 2427.
- (35) Du, C.; Yang, X.; Mayer, M. T.; Hoyt, H.; Xie, J.; McMahon, G.; Bischooping, G.; Wang, D. *Angew. Chemie (International ed.)* **2013**, *52* (48), 12692.
- (36) Du, C.; Zhang, M.; Jang, J.; Liu, Y.; Liu, G.; Wang, D. *J. Phys. Chem. C* **2014**, *118* (30), 17054.
- (37) Man, I. C.; Su, H.-Y.; Calle-Vallejo, F.; Hansen, H. a.; Martínez, J. I.; Inoglu, N. G.; Kitchin, J.; Jaramillo, T. F.; Nørskov, J. K.; Rossmeisl, J. *ChemCatChem* **2011**, *3* (7), 1159.
- (38) Shi, X.; Herraiz-Cardona, I.; Bertoluzzi, L.; Lopez-Varo, P.; Bisquert, J.; Park, J. H.; Gimenez, S. *Phys. Chem. Chem. Phys.* **2016**, *18* (13), 9255.
- (39) Reichman, J. *Appl. Phys. Lett.* **1980**, *36* (7), 574.
- (40) Abdi, F. F.; Firet, N.; Dabirian, A.; van de Krol, R. *MRS Proc.* **2012**, *1446* (3), mrss12.
- (41) Yang, X.; Du, C.; Liu, R.; Xie, J.; Wang, D. *J. Catal.* **2013**, *304*, 86.
- (42) Sivula, K. *J. Phys. Chem. Lett.* **2013**, *4* (10), 1624.
- (43) Li, T.; He, J.; Peña, B.; Berlinguette, C. P. *Angew. Chemie Int. Ed.* **2016**, *55* (5), 1769.
- (44) Mullet, M.; Khare, V.; Ruby, C. *Surf. Interface Anal.* **2008**, *40* (3–4), 323.
- (45) Cooper, J. K.; Gul, S.; Toma, F. M.; Chen, L.; Glans, P.-A.; Guo, J.; Ager, J. W.; Yano, J.; Sharp, I. D. *Chem. Mater.* **2014**, *26* (18), 5365.
- (46) Wang, G.; Ling, Y.; Lu, X.; Qian, F.; Tong, Y.; Zhang, J. Z.; Lordi, V.; Rocha Leao, C.; Li, Y. *J. Phys. Chem. C* **2013**, *117* (21), 10957.



- (47) Qin, D.-D.; Wang, T.; Song, Y.-M.; Tao, C.-L. *Dalt. Trans.* **2014**, 43 (21), 7691.
- (48) Bianconi, A. *X-ray Absorption: Principles, Applications, Techniques of EXAFS, SEXAFS and XANES*; Koningsberger, D. C., Prins, R., Eds.; Wiley: New York, 1988.
- (49) Bediako, D. K.; Lassalle-Kaiser, B.; Surendranath, Y.; Yano, J.; Yachandra, V. K.; Nocera, D. G. *J. Am. Chem. Soc.* **2012**, 134 (15), 6801.
- (50) Klahr, B.; Hamann, T. *J. Phys. Chem. C* **2014**, 118 (19), 10393.
- (51) Zandi, O.; Hamann, T. *J. Phys. Chem. Lett.* **2014**, 5 (9), 1522.
- (52) Bertoluzzi, L.; Badia-Bou, L.; Fabregat-Santiago, F.; Gimenez, S.; Bisquert, J. *J. Phys. Chem. Lett.* **2013**, 4 (8), 1334.
- (53) Bertoluzzi, L.; Bisquert, J. *J. Phys. Chem. Lett.* **2012**, 3 (17), 2517.
- (54) Klahr, B.; Gimenez, S.; Fabregat-Santiago, F.; Hamann, T.; Bisquert, J. *J. Am. Chem. Soc.* **2012**, 134 (9), 4294.
- (55) Klahr, B.; Gimenez, S.; Fabregat-Santiago, F.; Bisquert, J.; Hamann, T. *J. Am. Chem. Soc.* **2012**, 134 (40), 16693.
- (56) Badia-Bou, L.; Mas-Marza, E.; Rodenas, P.; Barea, E. M.; Fabregat-Santiago, F.; Gimenez, S.; Peris, E.; Bisquert, J. *J. Phys. Chem. C* **2013**, 117 (8), 3826.
- (57) Gimenez, S.; Dunn, H. K.; Rodenas, P.; Fabregat-Santiago, F.; Miralles, S. G.; Barea, E. M.; Trevisan, R.; Guerrero, A.; Bisquert, J. *J. Electroanal. Chem.* **2012**, 668, 119.
- (58) Zhang, Z.; Shao, C.; Zhang, L.; Li, X.; Liu, Y. *J. Colloid Interface Sci.* **2010**, 351 (1), 57.
- (59) Yu, R.; Xue, N.; Huo, S.; Li, J.; Wang, J. *RSC Adv.* **2015**, 5 (78), 63502.
- (60) Zhang, Y.; Guo, Y.; Duan, H.; Li, H.; Sun, C.; Liu, H. *Phys. Chem. Chem. Phys.* **2014**, 16 (44), 24519.
- (61) Liu, G.; Shi, J.; Zhang, F.; Chen, Z.; Han, J.; Ding, C.; Chen, S.; Wang, Z.; Han, H.; Li, C. *Angew. Chemie (International ed.)* **2014**, 53 (28), 7295.
- (62) Liang, Y.; Tsubota, T.; Mooij, L. P. A.; van de Krol, R. *J. Phys. Chem. C* **2011**, 115 (35), 17594.
- (63) Nikitenko, S.; Beale, A. M.; van der Eerden, A. M. J.; Jacques, S. D. M.; Leynaud, O.; O'Brien, M. G.; Detollenaere, D.; Kaptein, R.; Weckhuysen, B. M.; Bras, W. *J. Synchrotron Radiat.* **2008**, 15 (Pt 6), 632.
- (64) Bunău, O.; Joly, Y. *J. Phys. Condens. Matter* **2009**, 21 (34), 345501.
- (65) Joly, Y. *Phys. Rev. B* **2001**, 63 (12), 125120.
- (66) Ankudinov, A.; Ravel, B.; Rehr, J.; Newville, M. *FEFFFIT Man. within FEFF Proj. Univ. Washington, Seattle, USA.*

## Appendix II

### Preparation of BiVO<sub>4</sub> thin film photoanodes

Thin films of 50, 100, 200 and 300 nm thick BiVO<sub>4</sub> were prepared by spray pyrolysis on FTO coated glass substrates (fluorine-doped tin dioxide, 15  $\Omega/\square$ , TEC-15, Hartford Glass Co.). FTO substrates were rinsed with a Triton solution, sulphuric acid, acetone and ethanol, and subsequently cleaned using an UV ozone cleaner (Novascan). The precursor solution was made by dissolving 4 mM Bi(NO<sub>3</sub>)<sub>3</sub>·5H<sub>2</sub>O (98%, Alfa Aesar) in acetic acid (98%, Sigma-Aldrich) and adding an equimolar amount of vanadium in the form of VO(AcAc)<sub>2</sub> (99%, Alfa Aesar) dissolved in absolute ethanol (Sigma-Aldrich). The substrate temperature during spraying was maintained at 450 °C, as measured by a thermocouple pressed to the top of the substrate surface. The spray deposition was carried out using an automated spray setup with Quickmist air atomizing spray nozzle driven by an overpressure of 0.06 MPa of nitrogen gas. The nozzle–substrate distance was kept constant at 20 cm. The precursor solution was placed 20 cm below the nozzle and fed to the nozzle via the siphoning effect induced by the nitrogen gas flow. Each spray cycle consisted of 5 s of spray time and 55 s of delay time to allow solvent evaporation, and a total of 200 cycles were used to deposit the films.

Prior to deposition of the BiVO<sub>4</sub>, a SnO<sub>2</sub> interfacial layer (~80 nm) was deposited onto the FTO substrate to prevent recombination at the FTO/BiVO<sub>4</sub> interface. 0.1 M SnCl<sub>4</sub> (99%, Acros Organics) solution in ethyl acetate (99.5%, J.T. Baker) was used as the precursor solution. The SnO<sub>2</sub> layer was deposited at 425 °C using five spray cycles (5 s on, 55 s off) in a gravity-assisted siphoning mode, where the precursor solution was placed 30 cm above the nozzle. After deposition, the SnO<sub>2</sub>/BiVO<sub>4</sub> samples were subjected to an additional 2 h heat treatment in a tube furnace at 450 °C in air. Spray deposition was performed on FTO substrates of 50 x 50 mm in size which were eventually cut into 20 x 10 mm samples. Outer edge of the FTO substrate was masked with some Al-foil to avoid contamination of the back-contact.

## Results

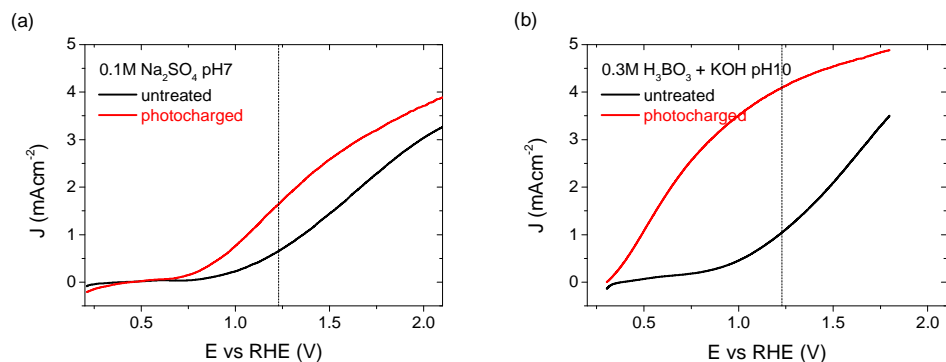


Fig. S1. JV curves of 200 nm thick BiVO<sub>4</sub> films photocharged in (a) 0.1 M Na<sub>2</sub>SO<sub>4</sub> pH 7 and (b) 0.3 M borate buffer pH 10.

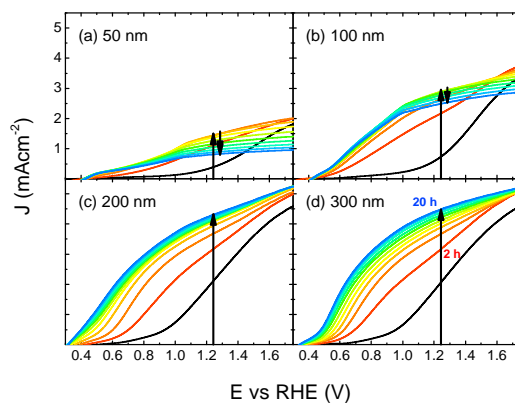


Fig. S2. JV curves of 50, 100, 200 and 300 nm thick BiVO<sub>4</sub> in PBA buffer pH 10, photocharged for a different amount of time, shown with a time step of 2h, the arrows indicates the trends @ 1.23 V<sub>RHE</sub>.

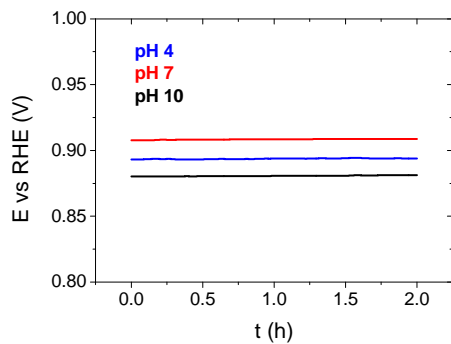


Fig. S3. Steady state OC potentials of  $\text{BiVO}_4$  photoanodes collected in the dark and in various pHs.

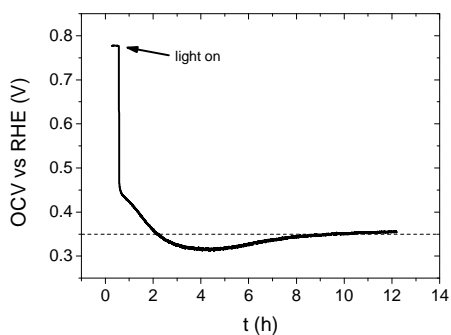


Fig. S4. Open circuit potential of  $\text{BiVO}_4$  photoanode immersed in 0.1 M PBA buffer pH 10 under AM1.5G simulated illumination.

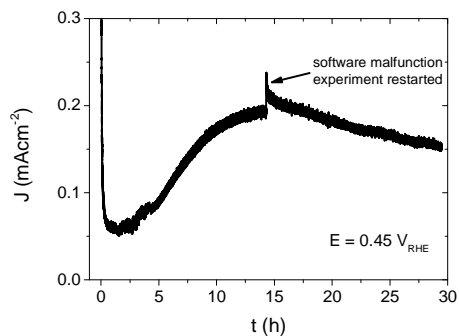


Fig. S5. Chronoamperometry measurement of  $\text{BiVO}_4$  photoanode held at  $0.45 V_{\text{RHE}}$ , 0.1 V more anodic vs the reference OC potential, subsequent to Fig. S7.

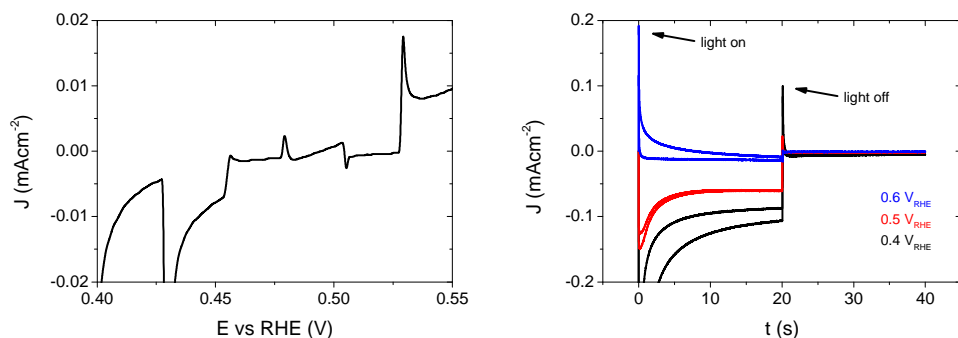


Fig. S6. Chopped illumination JV curve of an untreated  $\text{BiVO}_4$  photoanode in 0.1 M PBA buffer pH 10.

Fig. S7. Chronoamperometry measurement of an untreated  $\text{BiVO}_4$  photoanode held at 0.4, 0.5 and 0.6  $\text{V}_{\text{RHE}}$ , under chopped AM1.5G simulated sunlight in 0.1 M PBA buffer pH 10.

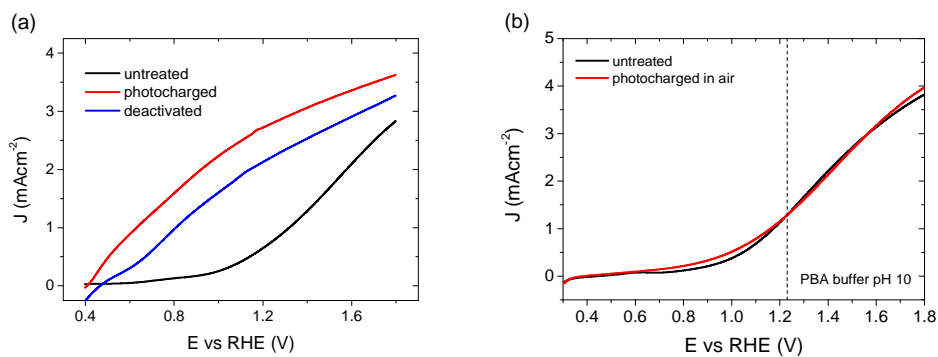


Fig. S8. (a) Cyclic voltammetry of a  $\text{BiVO}_4$  photoanode tested in pH 10: untreated (black), photocharged (red), and left inside the cell and in the dark for 20 h (blue).

Fig. S8. (b) JV curves of 200 nm thick  $\text{BiVO}_4$  film: untreated (black line) and right after 20 h of illumination in the air (red line). Both measurements were performed in PBA buffer pH 10.

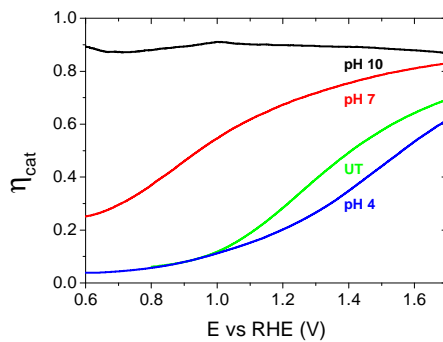
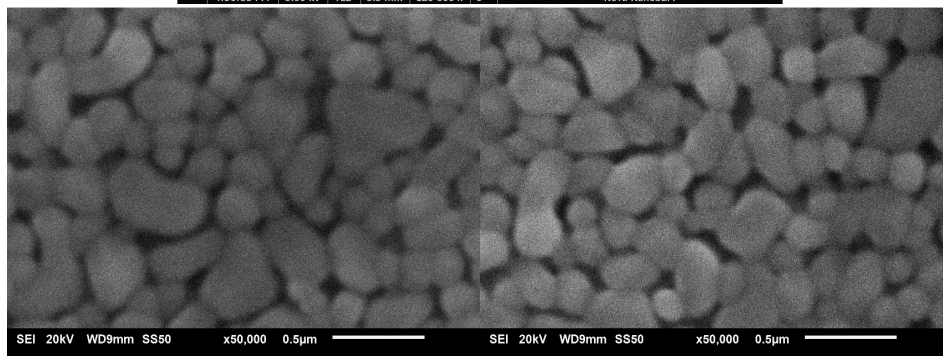
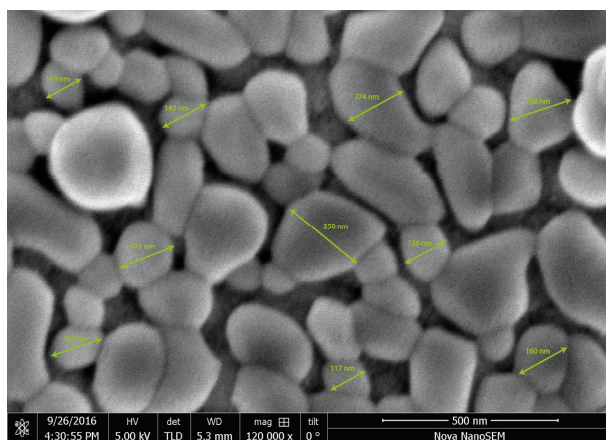
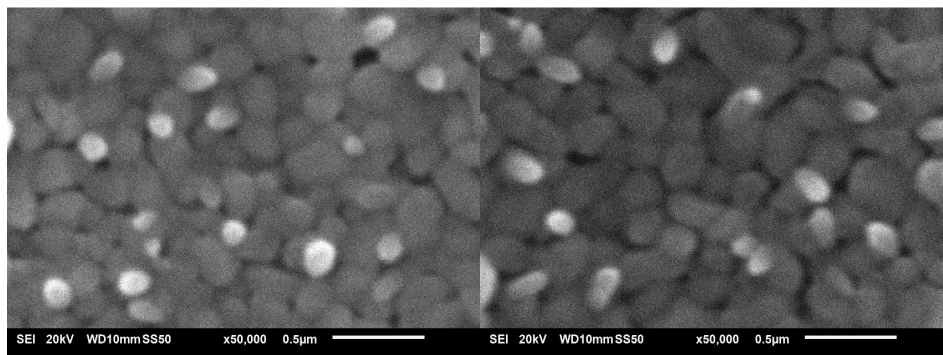


Fig. S9. Catalytic efficiencies of  $\text{BiVO}_4$  photoanodes: untreated and photocharged in PBA buffer pH 4, 7 and 10.

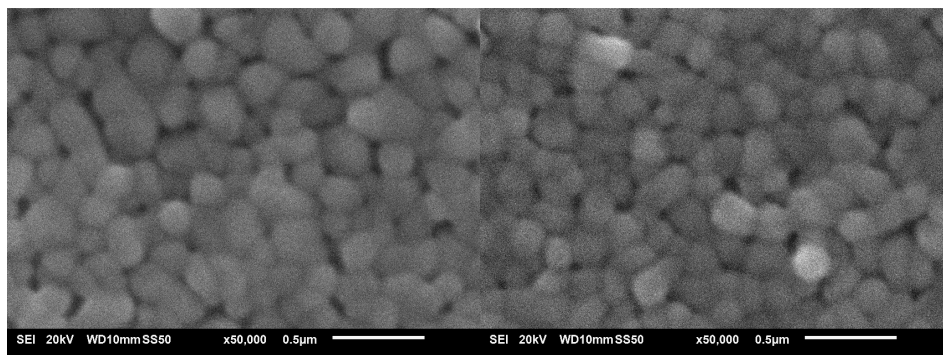
a) pristine



b) PC pH 4



c) PC pH 7



d) PC pH 10

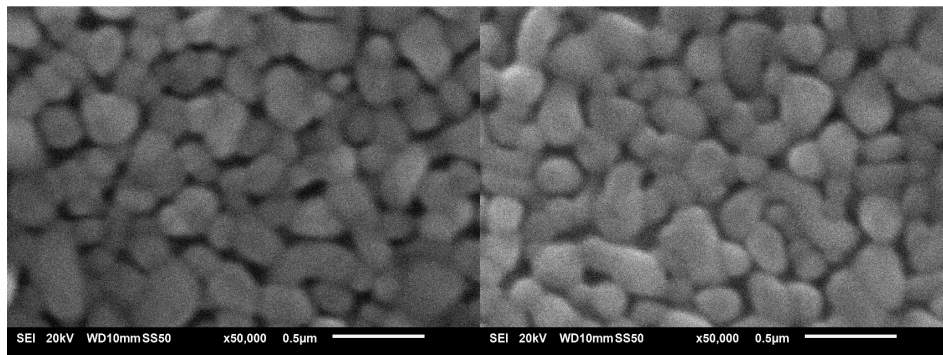


Fig. S10. SEM pictures of 200 nm thick BiVO<sub>4</sub> films before and after photocharging

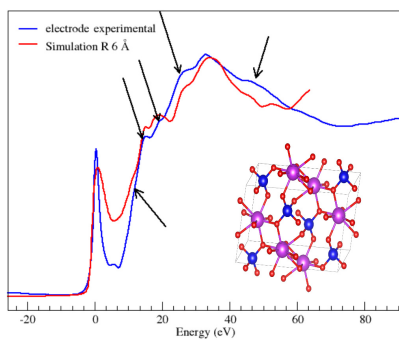


Fig. S11. XANES spectrum of  $\text{BiVO}_4$  collected at the V K edge (blue line) and simulated spectrum according to the clinobisvanite structure (red line). The arrows indicate the main features of the XANES spectrum.

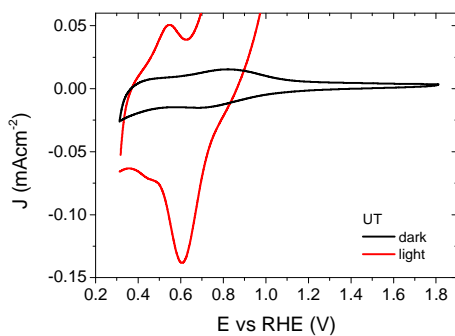


Fig. S12. Cyclic voltammetry of untreated ( $\text{UT}$ )  $\text{BiVO}_4$  in the dark and under illumination. Zoom in of Figures 6 (a) and (b) combined.



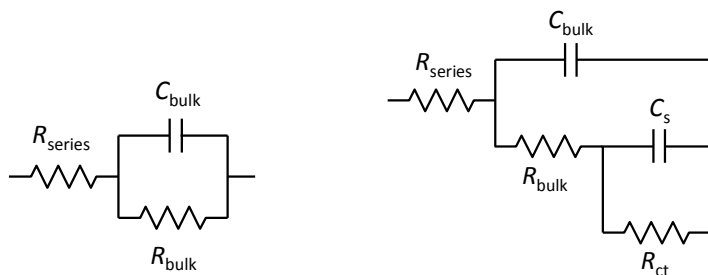


Fig. S13. Equivalent circuit used to fit impedance spectroscopy data of  $\text{BiVO}_4$  in the dark (left), and under illumination (right).

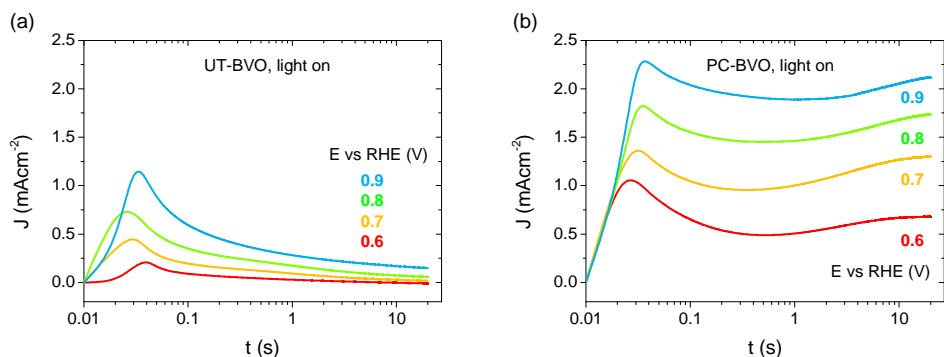


Fig. S14. Anodic transients of an (a) untreated and (b) photocharged  $\text{BiVO}_4$  photoanode immersed in 0.1 M PBA buffer pH 10, under AM1.5G simulated illumination and at applied bias of 0.6, 0.7, 0.8 and 0.9 V vs RHE.

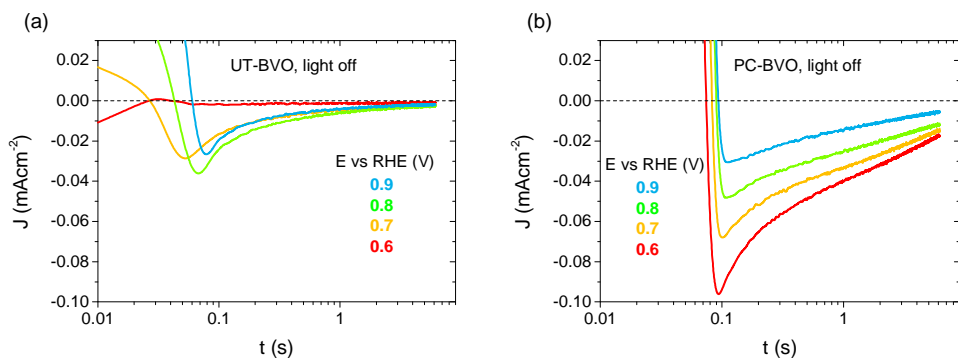
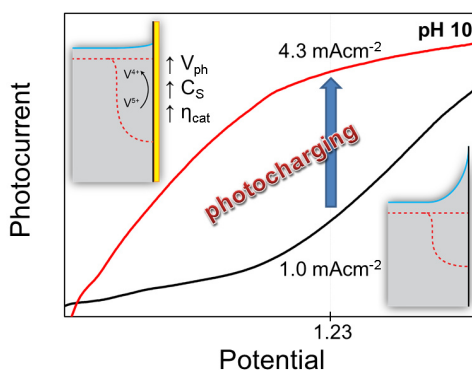


Fig. S15. Cathodic transients of an (a) untreated and (b) photocharged  $\text{BiVO}_4$  photoanode immersed in 0.1 M PBA buffer pH 10, in the dark and at applied bias of 0.6, 0.7, 0.8 and 0.9 V vs RHE.

## Broader Context and Table of contents (TOC) graphic

Photoelectrochemical (PEC) water splitting is an attractive route to capture, convert and store the energy from the sun in the form of chemical bonds. This approach allows for sustainable production of solar fuels (typically  $\text{H}_2$ ), and thereby addresses the challenges of new energy technologies needed in the pathway towards a carbon-free economy. Solar water splitting relies on PEC cells, consisting of semiconducting photoelectrodes, which directly utilise photo-generated charge carriers to drive the water oxidation and reduction half-reactions on the corresponding solid/liquid interfaces. Metal oxides have been heavily studied as a class of photoelectrode materials for PEC devices due to their low cost and stable operation. Specifically, bismuth vanadate,  $\text{BiVO}_4$ , has proven to demonstrate significant activity as a photoanode material. However, due to its inherent bulk- and surface-related limitations, complex strategies such as doping or co-catalysis are typically necessary for  $\text{BiVO}_4$  to reach high yields for  $\text{O}_2$  production. Herein, we investigate photocharging (PC), a simple and novel treatment that can dramatically improve the water splitting capabilities of  $\text{BiVO}_4$ . We demonstrate that illumination combined with alkaline conditions alters the chemistry at the semiconductor-electrolyte interface to form a  $\text{BiVO}_4$  surface with superior activity for the oxygen evolution reaction.



## 4. In Situ Observation of Active Oxygen Species in Fe-Containing Ni-Based Oxygen Evolution Catalysts: The Effect of pH on Electrochemical Activity

Ni-based oxygen evolution catalysts (OECs) are cost-effective and very active materials that can be potentially used for efficient solar-to-fuel conversion process towards sustainable energy generation. We present a systematic spectroelectrochemical characterization of two Fe-containing Ni-based OECs, namely nickel borate ( $\text{Ni(Fe)-B}_i$ ) and nickel oxyhydroxide ( $\text{Ni(Fe)OOH}$ ). Our Raman and X-ray absorption spectroscopy results show that both OECs are chemically similar, and that the borate anions do not play an apparent role in the catalytic process at pH 13. Furthermore, we show spectroscopic evidence for the generation of negatively charged sites in both OECs ( $\text{NiOO}^-$ ), which can be described as adsorbed “active oxygen”. Our data conclusively links the OER activity of the Ni-based OECs with the generation of those sites on the surface of the OECs. The OER activity of both OECs is strongly pH dependent, which can be attributed to a deprotonation process of the Ni-based OECs, leading to the formation of the negatively charged surface sites that act as OER precursors. This work emphasizes the relevance of the electrolyte effect to obtain catalytically active phases in Ni-based OECs, in addition to the key role of the Fe impurities. This effect should be carefully considered in the development of Ni-based compounds meant to catalyze the OER at moderate pHs. Complementarily, UV-vis spectroscopy measurements show strong darkening of those catalysts in the catalytically active state. This coloration effect is directly related to the oxidation of nickel and can be an important factor limiting the efficiency of solar-driven devices utilizing Ni-based OECs.

---

This chapter has been published as: B. J. Trześniewski,\* O. Diaz-Morales,\* D. A. Vermaas, A. Longo, W. Bras, M. T. M. Koper, and W. A. Smith, *J. Am. Chem. Soc.* 2015, 137, 15112–15121, \*equal contribution, (10.1021/jacs.5b06814)

## 4.1 Introduction

The development of clean, efficient and sustainable alternatives to fossil fuels has become one of the most pressing issues facing humanity today. Renewable electricity generation through solar and wind power could provide enough energy to power the planet for the foreseeable long-term future.<sup>1-3</sup> However, large-scale storage of the energy produced by such intermittent sources remains a major challenge. One of the most promising methods to store renewable electricity is through the electrolysis of water ( $\text{H}_2\text{O} \rightarrow \text{H}_2 + \frac{1}{2} \text{O}_2$ ). The hydrogen and oxygen produced via water electrolysis can be subsequently recombined in a fuel cell to produce electricity and water, thus making the overall energy conversion cycle complete.<sup>3,4</sup> In order to make this technology scalable, cheap and efficient, catalysts are needed to drive the hydrogen and oxygen evolution reactions. The hydrogen evolution reaction implies the transfer of two protons and two electrons, and there are catalysts that can drive this reaction near to the equilibrium potential (0 V vs RHE).<sup>5</sup> However, the oxygen evolution reaction (OER) involves the transfer of four protons and four electrons and it proceeds far from the equilibrium potential (1.23 V vs RHE), which causes large energy losses in the overall water splitting process.<sup>5,6</sup> Therefore, a focus on understanding the OER in order to improve its kinetics is paramount for enabling large-scale renewable energy storage.

Ni-based catalysts are one of the best alternatives<sup>6-12</sup> to the most active, yet prohibitively expensive catalysts based on scarcely abundant ruthenium and iridium oxides. Therefore, the anodes for large scale commercial alkaline electrolyzers are mostly based on nickel and its alloys.<sup>13-15</sup> Nickel-based OECs are known to oxidize water in alkaline media with activity comparable to  $\text{RuO}_2$  and  $\text{IrO}_2$  benchmark catalysts.<sup>6-12</sup> In particular,  $\text{Ni(OH)}_2/\text{NiOOH}$  has a beneficial three dimensionally porous brucite structure that facilitates easy ion transport and charge conductivity.<sup>16</sup> This catalyst has been recently used in direct photoelectrochemical water splitting cells, where it forms a so-called adaptive junction when placed on semiconductor photoelectrodes.<sup>17,18</sup> In the past few years, a new form of this catalyst has been developed to form a nickel-borate ( $\text{Ni-B}_i$ ) OEC.<sup>19</sup> This heterogeneous catalyst can be electrodeposited as a thin film from solutions containing  $\text{Ni}_{(\text{aq})}^{2+}$  and the proton-accepting borate anions.  $\text{Ni-B}_i$  can mediate the OER under mild conditions and with

high activity.<sup>20</sup> It is believed that Ni-B<sub>i</sub> is composed of nanosized, molecular-like clusters/domains of NiOOH, which results in a much larger fraction of surface-exposed, catalytically-active nickel centers, relative to NiOOH.<sup>21</sup> However, a recent study from the Boettcher group finds that the activity of Ni-B<sub>i</sub> is mainly due to the Fe impurities and not the Ni sites,<sup>22</sup> a result that is also consistent with previous findings of the beneficial role that Fe plays in the catalytic activity of pure NiOOH.<sup>23–26</sup> It is therefore important to note that previous Ni-based OEC systems demonstrating low onset potentials are actually reporting on materials that have some iron incorporated, as shown indisputably by the Boettcher group.<sup>22,23</sup> Therefore, given the importance of Fe for the OER activity, we assume that all the Ni-based OECs obtained in our study from non-purified media should be referred to as Ni(Fe)OOH / Ni(Fe)-B<sub>i</sub>.

To further understand the mechanisms and functionalities of these promising catalysts and to exploit the potential of their high catalytic activity, it is imperative to track the changes occurring in them during the OER reaction. Spectroelectrochemical characterization techniques allow to study *in situ* the processes at the electrode interface during the catalytic reaction without affecting the performance of the catalyst, and can therefore be used to track the changes in the nickel-based OECs during electrochemical water oxidation.

This work presents an electrochemical and UV-vis/Raman/XAS spectroelectrochemical study of the structural and electronic changes of Ni(Fe)OOH and Ni(Fe)-B<sub>i</sub> catalysts during the electrochemical water oxidation reaction. Our results indicate that both Ni(Fe)OOH and Ni(Fe)-B<sub>i</sub> structurally and electronically change in a very similar manner, indicating a similar composition, morphology, and physical characteristics. We also demonstrate a significant effect of electrolyte pH on the activity of both catalysts towards oxygen evolution. Surface Enhanced Raman Spectroscopy (SERS) measurements indicate the formation of negatively charged surface sites in the OECs (adsorbed “active oxygen”) due to a deprotonation process. Those “active oxygen” species act as an OER precursor what explains the pH sensitivity of the OER catalytic activity. The deprotonation process has a crucial effect on the OER activity of Ni-based OECs at moderate pHs, which should be considered separate from the effect of the Fe impurities in the electrolyte, reported to enhance the catalytic activity of Ni-based electrocatalyst towards OER.<sup>23,25,26</sup>

## 4.2 Experimental Section

### 4.2.1 Preparation of Ni(Fe)-B<sub>i</sub> and Ni(Fe)OOH thin films on FTO

Thin layers (~20 monolayers) of Ni(Fe)-B<sub>i</sub> and Ni(Fe)OOH were electrodeposited on fluorine-doped tin oxide coated glass substrates (FTO, 15 Ω/cm, TEC-15, Hartford Glass Co.). Prior to the deposition process substrates were cleaned by three successive cycles of ultrasonic rinsing in a 10% aqueous triton solution, acetone and isopropanol, for 15 min each time. All the chemicals were used as received, without any further purification. The 0.5 M borate buffer (K-B<sub>i</sub>) pH 9.2 was prepared from 0.5 M aqueous solution of H<sub>3</sub>BO<sub>3</sub> (99.8%, Alfa Aesar) titrated with KOH (99%, Sigma Aldrich) to pH 9.2. The Ni(Fe)-B<sub>i</sub> catalysts were electrodeposited from a 0.5 mM aqueous solution of Ni(NO<sub>3</sub>)<sub>2</sub>·6H<sub>2</sub>O (98.5%, Sigma Aldrich), using 0.5 M K-B<sub>i</sub> pH 9.2 as supporting electrolyte. The Ni(Fe)OOH catalysts were electrodeposited from a 5 mM aqueous solution of Ni(ClO<sub>4</sub>)<sub>2</sub>·6H<sub>2</sub>O (Sigma Aldrich), using KCl (≥ 99%, Sigma Aldrich) with a total ionic strength of 0.1 M. The water used to prepare all solutions was deionized and ultrafiltrated by a Milipore Milli-Q system (resistivity > 18.2 MΩ·cm). The electrodeposition was performed in a single compartment electrochemical cell, using an Ag/AgCl (sat. KCl, sat. AgCl) (XR300, Radiometer Analytical) as reference electrode and a coiled Pt wire as a counter electrode. All potentials are reported versus the reversible hydrogen electrode (RHE), calculated according to the equation (1):

$$E^{\text{RHE}} = E^{\text{Ag/AgCl (sat. KCl)}} + E^0_{\text{Ag/AgCl (sat. KCl)}} + 0.059\Delta\text{pH} \quad (1)$$

Where  $E^{\text{RHE}}$  is the potential versus RHE,  $E^{\text{Ag/AgCl (sat. KCl)}}$  is the potential applied experimentally and  $E^0_{\text{Ag/AgCl (sat. KCl)}}$  is the standard potential of the Ag/AgCl (sat. KCl) versus the normal hydrogen electrode (0.197 V),<sup>27</sup> ΔpH accounts for the difference in pH of the working solution respect to the normal hydrogen electrode (pH zero). The electrodeposition was performed with a potentiostat / galvanostat (EG&G PAR 283). The Ni-based electrocatalysts were deposited both potentiostatically and galvanostatically. The potentiostatic electrodeposition of Ni(Fe)-B<sub>i</sub> was carried out at 1.7 V vs RHE. During the galvanostatic electrodeposition the current was kept constant at 10/-10 μA for Ni(Fe)-B<sub>i</sub> and Ni(Fe)OOH respectively. The electrodeposition of Ni(Fe)-

B<sub>i</sub> and Ni(Fe)OOH was performed for a period of time ensuring formation of *ca.* twenty monolayers of coverage. The time for Ni(Fe)OOH electrodeposition was calculated according to the real surface area of the working electrode in order to deposit twenty times  $663 \mu\text{C cm}^{-2}$ , which corresponds to the charge needed to deposit one monolayer of closely packed metallic nickel from a Ni<sup>2+</sup> solution (atomic radius of nickel  $0.124 \text{ nm}^{28}$ ). Theoretical estimation of time needed to fabricate Ni(Fe)-B<sub>i</sub> films of desired thickness is difficult, since water oxidation reaction can readily occur at potentials facilitating Ni(Fe)-B<sub>i</sub> deposition. Consequently, Ni(Fe)-B<sub>i</sub> films of thicknesses comparable to Ni(Fe)OOH were electrodeposited with the aid of the in situ UV-vis setup described later in this section. Thus, a typical electrodeposition of a Ni(Fe)-B<sub>i</sub> film was terminated when the change in the optical transmission of the sample (monitored in situ) was the same as for a Ni(Fe)OOH film held at potential equal to the one used during the Ni(Fe)-B<sub>i</sub> deposition.

#### **4.2.2 Electrochemical performance of Ni(Fe)-B<sub>i</sub> and Ni(Fe)OOH thin films on FTO**

The same setup as described in the previous section was used for voltammetric measurements. Samples were examined either right after the preparation or after electrochemical conditioning. The polarization curves were obtained by cyclic voltammetry in the potential range 1.1 – 1.9 V vs RHE, scanning at 10 mV/s in KOH 0.1 M or K-B<sub>i</sub> 0.5 M. The electrochemical conditioning procedure consisted of 200 voltammetric cycles between 1.25 – 2.0 V vs RHE, with a scan speed of 500 mV/s.

#### **4.2.3 UV-vis spectroscopy**

The ultraviolet-visible (UV-vis) measurements were performed with a home-made setup. It consisted of a deuterium-halogen UV-vis lamp (Ocean Optics DH-2000-BAL), optical fibers (Ocean Optics, 200  $\mu\text{m}$  fiber core diameter), a single compartment with 3-electrodes electrochemical cell and a spectrometer (Ocean Optics, Maya 2000 Pro). All these elements were aligned together in such a way that UV-vis light was shined on the back side of a sample mounted in an electrochemical cell and the transmission signal was collected on the other side by a spectrometer (see Fig. S1). The

change in transmission was recorded in situ while performing the electrochemical experiment. Cyclic voltammetry experiments were performed using the same setup as described above. The samples of Ni(Fe)-B<sub>i</sub> and Ni(Fe)OOH mounted in this setup were scanned with cyclic potential (potential range 1.1 – 1.9 V vs RHE, scan rate of 10 mV/s) in KOH 0.1 M or K-B<sub>i</sub> 0.5 M and the change in transmission was simultaneously monitored.

#### 4.2.4 Surface Enhanced Raman experiments

The glassware was thoroughly cleaned before starting experiments by boiling in a 1:3 mixture of concentrated HNO<sub>3</sub>/concentrated H<sub>2</sub>SO<sub>4</sub> to remove organic contaminations after which it was boiled five times in water. The water used to clean glassware and to prepare solutions was demineralized and ultra-filtrated by a Milipore MiliQ system (resistivity > 18.2 MΩ cm and TOC < 5ppb). Electrolyte solutions were prepared with high quality chemicals, KOH (Sigma-Aldrich, semiconductor grade), H<sub>3</sub>BO<sub>3</sub> (Merck, pro-analysis), Ni(NO<sub>3</sub>)<sub>2</sub>·6H<sub>2</sub>O (Sigma-Aldrich, trace metals).

The experiments were performed in a confocal Raman microscope (LabRam HR, Horiba Yobin Yvon), using a 50X objective. The excitation source was a HeNe laser (633 nm). Backscattered light was filtered by an edge filter, directed to the spectrograph and to the detector. Details of the setup can be found in refs 29 and 30. The electrochemical SERS experiments were performed with a potentiostat / galvanostat (μAutolab Type III, Metrohm), using a home-made three-electrode and two compartment cell with the reference electrode separated by a Luggin capillary. The counter electrode used was a gold spiral, an Ag/AgCl (sat. KCl, sat. AgCl) was used as reference electrode and a roughened gold surface as working electrode. SERS experiments were made both in 0.1 M KOH and 0.5 M K-B<sub>i</sub> pH 9.2.

All potentials for these experiments are reported versus the reversible hydrogen electrode (RHE) in the working pH, otherwise stated. The potentials of reference electrode versus RHE were calculated according the equation (1), and verified by measuring the equilibrium potential of a Pt wire electrode at the working solution saturated with H<sub>2</sub>.



Prior to each measurement, the working electrode was mechanically polished to mirror finish using alumina slurries (Buehler) with different grain sizes to 0.3  $\mu\text{m}$ , rinsed with MilliQ water and sonicated in 1 M KOH during 5 min to remove all residuals of mechanical polishing. Next, the gold electrode was electrochemically polished by scanning 200 cycles of voltammetry in  $\text{HClO}_4$  0.1 M, scanning in the potential range 0 - 1.75 V vs RHE at 1000 mV/s. The electrode was roughened by 25 oxidation-reduction cycles (ORC) in KCl solution 0.1 M. The ORC were performed by scanning the potential from -0.30 to 1.30 V vs Ag/AgCl (sat. KCl, sat. AgCl) at 1000 mV/s and scanning the potential back at 500 mV/s. The potential was held for 30 s at the negative limit and for 1.3 s at the positive limit, this method is reported to produce a brownish surface that is SERS active.<sup>31</sup>

The roughened gold electrode was thoroughly rinsed with water to measure a cyclic voltammetry in the potential range 0 – 1.75 V vs RHE in  $\text{HClO}_4$  0.1 M at 50 mV/s. The surface area of the electrode was estimated based on the charge of the reduction peak of the gold oxide, assuming  $390 \mu\text{C cm}^{-2}$  for the charge for one monolayer of gold oxide.<sup>32</sup>

Nickel(II) hydroxide was formed on the roughened gold electrode by electrochemical oxidation of metallic nickel, which was plated galvanostatically from a  $\text{Ni}(\text{NO}_3)_2 \cdot 6\text{H}_2\text{O}$  solution 5 mM, using KCl 0.1 M as supporting electrolyte. The electrodeposition was carried out by applying cathodic currents (-10  $\mu\text{A}$ ) for a given time, in order to get *ca.* twenty monolayers of coverage.

$\text{Ni}(\text{Fe})\text{-B}_i$  was deposited potentiostatically on the roughened gold electrode from a  $\text{Ni}(\text{NO}_3)_2 \cdot 6\text{H}_2\text{O}$  solution 0.5 mM, using 0.5 M  $\text{K-B}_i$  pH 9.2 as supporting electrolyte. The electrodeposition was carried out by applying 0.95 V vs Ag/AgCl (sat. KCl, sat. AgCl) for a period of 60 s.

#### 4.2.5 X-ray Absorption Spectroscopy

In situ X-ray Absorption Near Edge Fine Structure (XANES) and Extended X-ray Absorption Fine Structure (EXAFS) measurements at the Ni K-edge (8.333 keV) were collected at the Dutch-Belgian Beamline (DUBBLE) at the European Synchrotron Radiation Facility (ESRF).<sup>33</sup> The energy of the X-ray beam was tuned by a double-crystal

monochromator operating in fixed-exit mode using a Si(111) crystal pair. *In situ* XANES and EXAFS spectra of the samples were collected in fluorescence mode using a 9-element Ge detector (Ortec Inc.), whereas reference spectra of the metallic Ni foil and the Ni Oxide were collected in transmission mode using Ar/He-filled ionization chambers at ambient temperature and pressure. The EXAFS spectra, three scans per sample, were energy-calibrated, averaged and further analyzed using GNXAS.<sup>34,35</sup> In this approach, the local atomic arrangement around the absorbing atom is decomposed into model atomic configurations containing 2, ...,  $n$  atoms. The theoretical EXAFS signal  $\chi(k)$  is given by the sum of the  $n$ -body contributions  $\gamma^2, \gamma^3, \dots, \gamma^n$ , which take into account all the possible single and multiple scattering (MS) paths between the  $n$  atoms. The fitting of  $\chi(k)$  to the experimental EXAFS signal allows to refine the relevant structural parameters of the different coordination shells; the suitability of the model is also evaluated by comparison of the experimental EXAFS signal Fourier transform (FT) with the FT of the calculated  $\chi(k)$  function. The coordination numbers and the global fit parameters that were allowed to vary during the fitting procedure were the distance  $R(\text{\AA})$ , Debye-Waller factor ( $\sigma^2$ ) and the angles of the  $\gamma^n$  contributions which were defined according to the crystallographic structures used in the data analysis. The threshold energy  $E_k=0$  was defined at 8333 eV according to the Ni foil value.

#### 4.2.6 Atomic Force Microscopy (AFM)

AFM surface scans were performed using an NT-MDT Ntegra apparatus coupled with an NT-MDT P8 XPM controller and with an NT-MDT NSG30 cantilever mounted. Scans were taken over an area of  $1 \times 1 \mu\text{m}$ , with a 1 Hz frequency and a resolution of  $512 \times 512$  points.

#### 4.2.7 X-ray Photoelectron Spectroscopy (XPS)

XPS experiment was performed using the Thermo Scientific K-alpha apparatus equipped with an Al K-alpha X-ray Source and a Flood Gun. Parameters used for the measurements were: spot size of  $400 \mu\text{m}$ , pass energy of 50 eV, energy step size of 0.1

eV, dwell time of 50 ms, 20 scans in the vicinity of Ni2p and O1s orbitals binding energy. XPS spectra were corrected for the C peak position.

## 4.3 Results and Discussion

### 4.3.1 Cyclic voltammetry of nickel(II) hydroxide and nickel borate during electrochemical water oxidation in alkaline media

The electrochemical properties of both nickel based oxygen evolution catalysts were first examined in different electrolyte media. It is important to mention that chemicals used throughout this work were not scrubbed of the Fe content. It has been shown that in rigorously iron-free environment the onset for OER is about 1.8 V<sub>RHE</sub>,<sup>23,25,26</sup> whereas the reasonably low onset of 1.55 V<sub>RHE</sub> that we observe in our case is indicative of Fe contamination.<sup>22,23</sup> We are therefore certain that a non-negligible content of Fe was unintentionally incorporated into our materials. Thus, given the enormous effect of iron impurities on activity of Ni-based OECs towards OER, the studied compounds should be considered as Ni(Fe)OOH and Ni(Fe)-B<sub>i</sub> and not as NiOOH and Ni-B<sub>i</sub>.

Figure 1 shows the cyclic voltammetry of nickel(II) hydroxide in 0.1 M KOH pH 13 (dotted black line). The pair of peaks in the potential region 1.25 – 1.50 V vs RHE is attributed to the Ni<sup>2+</sup>/Ni<sup>3+</sup> redox couple,<sup>36,37</sup> followed by the electrochemical oxygen evolution at potentials higher than 1.6 V vs RHE.

Ni(OH)<sub>2</sub> is reported to crystallize in a disordered  $\alpha$ -Ni(OH)<sub>2</sub> phase, that oxidizes to form  $\gamma$ -NiOOH at *ca.* 1.35 V vs RHE.<sup>36,37</sup> The  $\alpha/\gamma$  transition correspond to the Ni<sup>2+</sup>/Ni<sup>3+</sup> redox couple of the nickel-based catalyst and will be referred as the  $\alpha/\gamma$  transition in the rest of the work. The potential region for the  $\alpha/\gamma$  transition measured in this work corresponds well with the previously reported data.<sup>24,36</sup> The catalytic activity of Ni(Fe)(OH)<sub>2</sub> was also studied in a borate buffer electrolyte held at pH 9.2 in order to understand the effect of the borate anion on the catalytic activity of the hydroxide towards the oxygen evolution reaction. The study of the electrocatalytic

activity of  $\text{Ni(Fe)(OH)}_2$  in borate media allows us to get a better understanding of the catalytic activity measured for  $\text{Ni(Fe)-B}_i$ , which will be presented later. From the cyclic voltammetry of a sample of  $\text{Ni(Fe)(OH)}_2$  in borate buffer pH 9.2 (Figure 1, dotted blue line) is noticeable that the potential for the  $\text{Ni(OH)}_2/\text{NiOOH}$  transition shifts to higher potentials by about 0.1 V, and the activity towards oxygen evolution is seriously inhibited when compared with the activity observed in KOH.

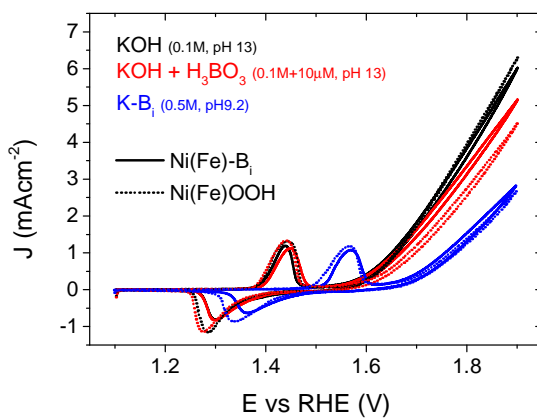


Figure 1. Polarization curves of  $\text{Ni(Fe)-B}_i$  (solid lines) and  $\text{Ni(Fe)OOH}$  (dotted lines) in 0.1 M KOH (black) 0.1 M KOH + 0.01 M  $\text{H}_3\text{BO}_3$  (red) and 0.5 M  $\text{K-B}_i$  (blue). Scan rate: 10 mV/s.

We also investigated the electrochemical properties of  $\text{Ni(Fe)(OH)}_2$  in KOH with the slight addition of  $\text{H}_3\text{BO}_3$  (Figure 1, dotted red line) to test if the borate anions are the cause of the observed inhibitory effect in  $\text{K-B}_i$ . Boric acid was added to KOH 0.1 M to give a nominal  $\text{H}_3\text{BO}_3$  concentration of 0.01 M. The pH of this solution was approximately 12.5, which is very close to the pH 13 of pure KOH 0.1 M, so we can neglect the pH effect. The results indicate that at pH 13 the borate anion does not influence the catalytic activity of  $\text{Ni(Fe)(OH)}_2$  towards water oxidation, but the enhanced activity is rather related to the effect of the electrolyte pH.

The catalytic activity towards oxygen evolution was also studied for  $\text{Ni(Fe)-B}_i$ . The cyclic voltammetry of nickel borate in KOH (Figure 1, solid black line) shows the typical  $\alpha/\gamma$  transition in the potential region 1.25 – 1.50 V vs RHE, similar to the region where the transition occurs in nickel(II) hydroxide. The current density for oxygen

evolution in KOH 0.1 M catalyzed by Ni(Fe)-B<sub>i</sub> is similar to the values obtained for the reaction catalyzed by Ni(Fe)(OH)<sub>2</sub>. Ni(Fe)-B<sub>i</sub> was also tested in borate buffer pH 9.2, and the results of cyclic voltammetry are shown in Figure 1 (solid blue line). The results look quite similar to the voltammogram of Ni(Fe)(OH)<sub>2</sub> in the same media. Again, the  $\alpha/\gamma$  transition shifts to more positive potentials and the current density associated with oxygen evolution is lower than the one observed in 0.1 M KOH. Importantly, no significant differences in the electrochemical characteristics of the two studied OECs were observed.

To further decouple the role of pH and borate concentration in the inhibitory effect of K-B<sub>i</sub> pH 9.2, we tested Ni(Fe)OOH in electrolyte with a fixed borate concentration of 0.5 M while changing the amount of KOH to control the pH in the range 9.2 – 13. We decided to release the restraint of constant total ionic concentration and not use any supporting electrolyte in order to avoid specific adsorption of other anions that could drastically change the chemistry at the solid/liquid interface and hence mask the effect of the borate anions. The results are presented in Fig. S2 as JV curves. The cyclic voltammeteries obtained in the pH range 9.2 – 10 clearly show higher OER-related Tafel slopes than for measurements performed above pH 11. The Tafel slopes in pH 11 - 13 are quite the same as in 0.1 M KOH pH 13 (the small differences observed can be attributed to the difference in ionic strength). The data in Fig. S2 clearly show that borate hinders the catalytic activity below pH 10, results that agree well with the kinetic study reported by Bediako et al.<sup>20</sup> In addition to that, we have shown that borate anions do not affect the OER catalytic activity of Ni(Fe)OOH at highly alkaline pHs (above pH 11).

#### **4.3.2 In situ electrochemical UV-vis spectroscopy of nickel(II) hydroxide and nickel borate during electrochemical water oxidation in alkaline media**

To further confirm the structural changes in our catalysts during voltammetric cycling, a UV-vis study was performed. The results obtained by UV-vis spectroscopy are summarized in Figure 2a-b as contour plots of the normalized transmission ( $T/T_0$ ) as a function of wavelength and potential, obtained during cycling voltammetric experiments on Ni(Fe)-B<sub>i</sub> (Figure 2a) and Ni(Fe)OOH (Figure 2b) catalyst.

The transmission values for a number of selected wavelengths were plotted against the electrode potential and they are shown with the corresponding polarization curves in Fig. S3a-b for Ni(Fe)-B<sub>i</sub> and Ni(Fe)OOH catalysts.

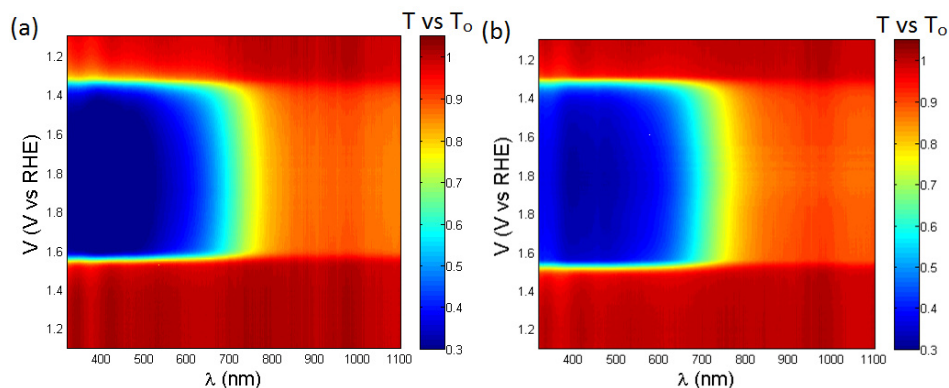


Figure 2. Contour plots of normalized transmission as a function of wavelength and potential for (a) Ni(Fe)-B<sub>i</sub> and (b) Ni(Fe)OOH in 0.5 M K-B<sub>i</sub> electrolyte, pH 9.2.

During the anodic voltammetric sweep, the transmission of Ni(Fe)OOH drops very sharply, down to about 35% of the initial value. When scanning back in the negative direction, we record an opposite change as the transmission increases. These optical transitions occur reversibly, *i.e.* during cathodic sweeps the optical properties are reverted back to the initial state at the end of each voltammetric cycle. Interestingly, the potentials at which the optical transitions occur coincide very well with the potentials at which the oxidation and reduction waves are observed (Fig. S3). When scanning anodically, at potentials corresponding to the onset of the Ni<sup>2+</sup>/Ni<sup>3+</sup> oxidation wave (*ca.* 1.5 V vs RHE), the transmission starts to decrease. The end of the transition coincides well with the offset of the Ni<sup>2+</sup>/Ni<sup>3+</sup> oxidation wave (*ca.* 1.6 V vs RHE). In the OER potential regime the transmission remains relatively unchanged. During a cathodic sweep, a reverse optical transition can be observed in between potentials corresponding to the Ni<sup>3+</sup>/Ni<sup>2+</sup> reduction wave onset and offset (*ca.* 1.4 and 1.25 V vs RHE). Importantly, these redox waves correspond to the catalyst activation. These results imply that significant light absorption by these OECs is inherent to the catalytically active state.

Corrigan *et al.* have performed an extensive study of electrochromism in thin films of  $\text{NiO}_x$  and  $\text{Ni(OH)}_2$ .<sup>38–41</sup> They showed huge differences in optical properties of  $\text{NiO}_x$  films subjected to various potentials: initially transparent  $\text{NiO}_x$  attains brownish color upon oxidation. Our results are in agreement with their findings. Furthermore, results from the group of Lampert<sup>42</sup> show that coloring of  $\text{Ni(OH)}_2$  occurs more rapidly than bleaching of  $\text{NiOOH}$ . This is consistent with our results, *i.e.* the potential window at which the optical transition occurs is more narrow in case of the anodic sweep than the cathodic one, resulting in a steeper slope of the transmission versus potential hysteresis. Likewise, the oxidation wave itself is narrower than the reduction one. Our results are also in agreement with a recent report from the Boettcher group,<sup>43</sup> which has shown that in-situ spectrophotometry can be successfully applied to study electrochromic effects in OECs undergoing redox reactions.

The spectral characteristics of the observed optical transition in Figure 2 are dominated by a strong and broad absorption feature observed for wavelengths below 800 nm. This feature may correspond to a nickel d-d interband transition. Importantly, no significant differences between  $\text{Ni(Fe)-B}_i$  and  $\text{Ni(Fe)OOH}$  were observed in our UV-vis spectral investigation, in agreement with our electrochemical study which did not show major differences between  $\text{Ni(Fe)-B}_i$  and  $\text{Ni(Fe)OOH}$  (as shown in Figure 1).

#### **4.3.3 In situ Surface Enhanced Raman Spectroscopy (SERS) of nickel(II) hydroxide and nickel borate during electrochemical water oxidation in alkaline media**

The Raman spectra of the  $\text{Ni(Fe)(OH)}_2$  in KOH 0.1 M, measured in the potential region 1.0 – 1.9 V vs RHE are shown in Figure 3a. The spectra in the potential region previous to the nickel oxidation (1.0 – 1.3 V vs RHE) show two peaks at *ca.* 450 and 500  $\text{cm}^{-1}$ . Those peaks have been assigned to  $A_{1g}$  stretching modes of Ni-OH and Ni-O, respectively.<sup>37,44–46</sup> The alpha phase of nickel hydroxide is a hydrated compound that would easily deprotonate by applying anodic potentials,<sup>44</sup> this deprotonation effect explains the evolution of the peak at *ca.* 500  $\text{cm}^{-1}$  when the applied potential becomes more positive.

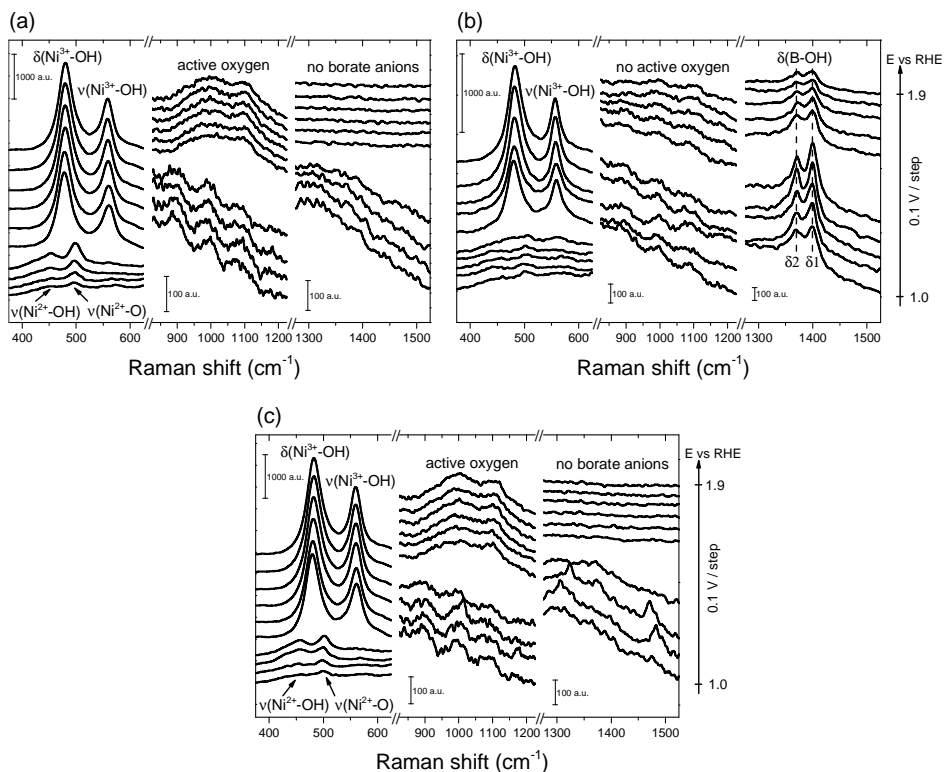


Figure 3. SER spectra of freshly prepared  $\text{Ni(Fe)(OH)}_2$  acquired in the potential range 1.0-1.9 V vs RHE in: (a) 0.1 M KOH pH 13, (b) 0.5 M K-Bi, pH 9.2 and (c) 0.1 M KOH + 0.01 M  $\text{H}_3\text{BO}_3$ . The measurements were performed potentiostatically.

When the applied potential is higher than 1.4 V vs RHE, the  $\alpha/\gamma$  transition takes place and the Raman spectra shows two peaks at *ca.*  $479\text{ cm}^{-1}$  and  $562\text{ cm}^{-1}$ . These peaks match well with the  $e_g$  bending vibration and the  $A_{1g}$  stretching vibration of Ni-O in  $\gamma\text{-NiOOH}$ .<sup>36,37,44,47</sup> Furthermore, Figure 3a shows that the Raman spectra develop rather broad peaks in the region *ca.*  $900\text{-}1150\text{ cm}^{-1}$  when the  $\gamma\text{-NiOOH}$  is formed. Merrill and co-workers<sup>48</sup> reported the same signals during the charge-discharge process of  $\text{Ni(OH)}_2$  in concentrated KOH and attribute the signal to formation of “active oxygen” on the surface of the charged nickel hydroxide ( $\text{NiOOH}$ ), they also described this species as “ $\text{O}^0$ ”. The question that rises around this signal is what is the nature of that activated oxygen and how does it relate with the OER activity. The SERS



study in moderately alkaline pH (pH 9.2) provides evidence to address that question and lead to conclusions about its effect on the OER activity.

Figure 3b shows the Raman spectra of  $\text{Ni(Fe)(OH)}_2$  in 0.5 M K-B<sub>i</sub> at pH 9.2 obtained in the potential region 1.0 – 1.9 V vs RHE. The wavenumber region 400 – 600  $\text{cm}^{-1}$  looks similar to the one observed in KOH 0.1 M that is two peaks that can be assigned to the  $A_{1g}$  stretching modes of Ni-OH and Ni-O (see Figure 3a). The main difference that can be observed is the delay in the appearance of the intense peaks at *ca.* 479 and 562  $\text{cm}^{-1}$ . These peaks now appear at potentials higher than 1.5 V vs RHE which is in agreement with the results obtained from the cyclic voltammetry, where it can be seen that the  $\alpha/\gamma$  transition occurs at higher potentials in 0.5 M K-B<sub>i</sub> pH 9.2 when compared with the results in 0.1 M KOH (see Figure 1). Furthermore, the Raman spectra of  $\text{Ni(Fe)(OH)}_2$  collected in K-B<sub>i</sub> differs substantially from the signals observed in KOH in the wavenumber region 800 – 1500  $\text{cm}^{-1}$ . There are no peaks in the region 900 – 1150  $\text{cm}^{-1}$ , which suggests that the formation of “active oxygen  $\text{O}^0$ ” during  $\alpha/\gamma$  transition is somehow hindered in K-B<sub>i</sub> pH 9.2. Additionally, the spectra acquired in borate buffer show two peaks at *ca.* 1370 and 1400  $\text{cm}^{-1}$  that can be assigned to the in-plane bending vibration of the B-OH in  $[\text{B(OH)}_4]^-$  ions present in the buffer solution.<sup>49,50</sup>

The spectra in Figure 3a show the formation of the “active oxygen” species, similar to the results reported in literature.<sup>48</sup> However, there are no Raman peaks corresponding to this species when freshly prepared  $\text{Ni(Fe)(OH)}_2$  is oxidized in K-B<sub>i</sub> pH 9.2 (Figure 3b), which indicates that the formation of this “ $\text{O}^0$ ” species strongly depends on the electrolyte pH. Furthermore, the catalytic activity of  $\text{Ni(Fe)(OH)}_2$  for OER is higher in 0.1 M KOH than in 0.5 M K-B<sub>i</sub> pH 9.2 (see Figure 1) so one might wonder whether the generation of “active oxygen” sites in the  $\text{Ni(Fe)OOH}$  enhances its OER activity.

To address the effect of the borate anions on the generation of the “active oxygen” species, we also collected Raman spectra of  $\text{Ni(Fe)(OH)}_2$  in 0.1 M KOH spiked with boric acid to give a nominal  $\text{H}_3\text{BO}_3$  concentration of 0.01 M (Figure 3c), the pH of this solution is approximately 12.5 so close to the pH 13 of pure 0.1 M KOH thus isolating the role of the borate anions. The spectra in Figure 3c show the Raman peaks at *ca.* 479  $\text{cm}^{-1}$  and 562  $\text{cm}^{-1}$ , assigned to the  $\delta(\text{Ni}^{3+}\text{-OH})$  and  $\nu(\text{Ni}^{3+}\text{-OH})$  modes respectively. Those peaks appear above 1.4 V vs RHE, similar to the peaks observed in 0.1 M KOH (see Figure 3a). Most interestingly, the oxidized  $\text{Ni(Fe)OOH}$  shows the peaks

between  $900 - 1150\text{ cm}^{-1}$ , which are assigned to “active oxygen”. The spectra in Figure 3c provides clear evidence that the borate anions do not play an inhibitory role in the formation of the “active oxygen” at pH 13, and therefore they do not affect the OER activity of the Ni(Fe)OOH catalyst at pH 13.

Our spectroelectrochemical results are consistent with the kinetic data reported by Nocera and co-workers, where they demonstrated that borate anions have an inhibitory effect on the OER activity of a nickel-based catalyst (Ni-B<sub>i</sub>) at pH 9.2.<sup>20</sup> Furthermore, we now present results that suggest the lack of inhibitory effect of borate anions on the OER activity of nickel-based catalysts at pH 13. It is important to consider that the isoelectric point of nickel(II) hydroxide lies in the pH range 10 – 11,<sup>51</sup> thus the NiOOH catalyst is expected to be negatively charged at pH 13 and the adsorption of the borate anions to be hindered. It is consistent with results shown in Fig. S2, where a distinct change in the Tafel slope in the pH range 10 – 11 can be observed. Moreover, the inhibitory effect of borate anions at pH 9.2 can be observed in our electrochemical results (see Figure 1) and further verified with the spectroscopic data in Figure 3b, where one can see that the formation of the OER active Ni(Fe)OOH is delayed in borate buffer. Furthermore, Ni(Fe)(OH)<sub>2</sub> does not seem to oxidize in the buffer electrolyte until the borate anions are depleted from the surface as it is shown in the plot of the integrals of the  $\delta(\text{Ni}^{3+}\text{-OH})$ ,  $\nu(\text{Ni}^{3+}\text{-OH})$  and  $\delta(\text{B-OH})$  peaks in Fig. S4a in Appendix III.

Figure 4a shows the Raman spectra of Ni(Fe)-B<sub>i</sub> in 0.1 M KOH pH 13 obtained in the potential region of 1.0 – 1.9 V vs RHE. The spectra show that Ni(Fe)-B<sub>i</sub> oxidizes to form a oxyhydroxide with similar features to the ones observed in the Raman spectra of Ni(Fe)(OH)<sub>2</sub>/Ni(Fe)OOH (see Figure 3a). The SER spectra of Ni(Fe)-B<sub>i</sub> show the two peaks at 479 and 562  $\text{cm}^{-1}$  corresponding to the bending and stretching modes of  $\text{Ni}^{3+}\text{-OH}$  respectively, and the broad peaks in the region *ca.* 900-1150  $\text{cm}^{-1}$  attributed to the formation of the “active oxygen” species. Noteworthy, the peaks at *ca.* 1370 and 1400  $\text{cm}^{-1}$  attributed to the B-OH bending modes of the  $[\text{B}(\text{OH})_4]^-$  anions are not present in Figure 4a. This shows that there are no borate ions bonded to the catalyst in the “nickel borate” compound, which seems to deposit as form of Ni(OH)<sub>2</sub> that gets oxidized to NiOOH. This statement can be also confirmed by looking at the stretching modes of  $\text{Ni}^{2+}\text{-O}$  in the potential region 1.0 – 1.3 V vs RHE (see Figure 4a).

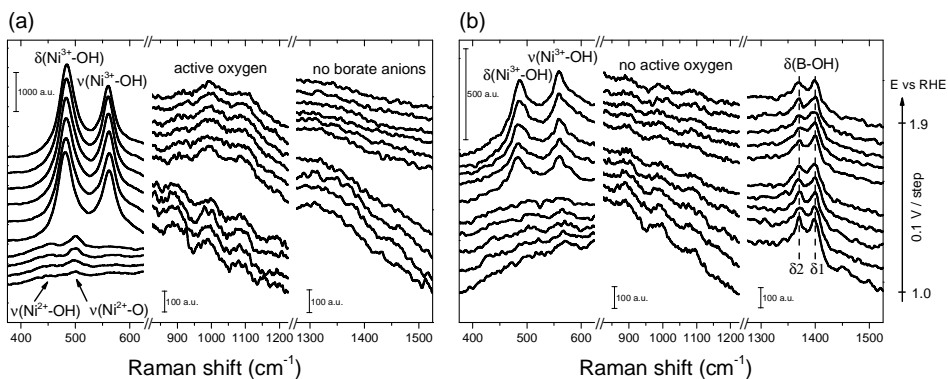


Figure 4. SER spectra of freshly prepared Ni(Fe)-B<sub>i</sub> acquired in the potential range 1.0-1.9 V vs RHE in: (a) 0.1 M KOH pH 13 and (b) 0.5 M K-B<sub>i</sub> pH 9.2. The measurements were performed potentiostatically.

SER spectra of Ni(Fe)-B<sub>i</sub> obtained during the electrochemical water oxidation in K-B<sub>i</sub> (see Figure 4b) resemble the same features observed for the spectra of Ni(Fe)(OH)<sub>2</sub> in K-B<sub>i</sub>: two peaks at *ca.* 480 cm<sup>-1</sup> and 557 cm<sup>-1</sup> appear at potentials above 1.5 V vs RHE, which correspond to formation of nickel oxyhydroxide. Likewise we observe a pair of peaks at 1370 and 1400 cm<sup>-1</sup>, which can be assigned to the borate ions bonded to the catalyst. Again, the peaks in the wavenumber region of 900 – 1150 cm<sup>-1</sup> are absent, suggesting that in K-B<sub>i</sub> pH 9.2 the formation of the “active oxygen” species is hindered, which explain the lacks of activity observed in the cyclic voltammetry in Figure 1. This also supports our hypothesis about the role of the “active oxygen” for the OER electrocatalysis. Furthermore, the spectra in Figure 4b shows that the borate anions are adsorbed on the Ni(Fe)-B<sub>i</sub> catalyst but they need to get depleted in order to form the OER active NiOOH-like catalyst. This can be further verified by looking at the integral of the δ(Ni<sup>3+</sup>-OH), ν(Ni<sup>3+</sup>-OH) and δ(B-OH) peaks in Fig. S4b in Appendix III. From that figure it is clear that the formation of the OER active NiOOH-like form of the catalyst (indicated by increase of the integral of δ(Ni<sup>3+</sup>-OH), ν(Ni<sup>3+</sup>-OH) peaks) occurs with the concomitant depletion of the borate anions (indicated by diminishing of the integral of the δ(B-OH) peak). The spectroelectrochemical evidence show that borate anions do also absorb on the Ni(Fe)-B<sub>i</sub> catalysts at pH 9.2 and act as inhibitors of the OER activity of the catalyst, which is in full agreement with the kinetic data previously reported by Nocera and co-workers.<sup>20</sup>

Regarding the nature of the “active oxygen” species, Merrill and co-workers did not specify the chemical nature of it, neither did our spectroelectrochemical data allow us to unequivocally identify it. However, experimental and DFT data have shown that nickel peroxide and nickel superoxide have vibrational modes in the wavenumber region  $900\text{--}1150\text{ cm}^{-2}$ .<sup>52–54</sup> These reports lead us to think that this “active oxygen” species may have peroxidic or superoxidic nature. Furthermore, the strong pH-dependency of the Raman peak associated with this species indicate that the “active oxygen” is actually formed via deprotonation of the nickel oxyhydroxide to produce a negatively charge nickel oxide ( $\text{NiOO}^-$ ).

Manganese oxide has also been reported to deprotonate in a process that is strongly dependent of the electrolyte pH, and this deprotonation influences the activity of the oxide towards oxygen evolution.<sup>55</sup> The authors propose that the deprotonation of  $\text{Mn}^{3+}\text{-OH}$  sites towards negatively charged  $\text{Mn}^{3+}\text{-O}^-$  is responsible for the activity enhancement. These findings are in full agreement with pH effect on the OER activity reported in this work. We therefore propose that formation of the “active oxygen” species occurs via a deprotonation of nickel oxyhydroxide that produces negatively charged sites on the surface of the nickel oxyhydroxide (with peroxidic or superoxidic nature). This species acts as a precursor for oxygen production in a similar manner as the one reported for manganese oxide.

Looking at the big picture, we believe that ‘active oxygen’ can be regarded as a preferential active site for water oxidation. We speculate that it facilitates a more favorable (i.e. requiring less overpotential) pathway for water oxidation. On the other hand, when the Ni centers are already in the higher valency state and accordingly the ‘active oxygen’ species are present at the surface, once an even more positive bias voltage is applied, the reaction kinetics improve and the reaction proceeds faster and with a higher efficiency, as seen by a typical exponential trend of the current density. However, the number of active sites, and thus the signal from the active oxygen, seem not to scale with potential because the formation of this ‘active’ structure that facilitates the enhanced OER catalysis occurs entirely during the nickel oxidation reaction. Therefore the Raman signal stays unchanged even at highly oxidative potentials (Figure 3a-c and Figure 4a). This implies that we are not creating any more active sites at higher potentials, but we are just driving them with more potential and thereby increasing the kinetics of the OER. This is in agreement with our experimental

findings; the Raman features related to active oxygen appear only in the spectra collected for samples that show a low onset in the CV data (Figure 1, black and red curves). On the other hand, with the samples that do not show the active oxygen feature (both catalysts at pH 9.2), the onset for the OER is larger and the Tafel slope is increased compared to the samples tested at higher pH. This shows that the formation of the active oxygen species, which is favorable for efficient water oxidation, occurs only in strong alkaline media, and thus there is a clear structure/functionality relationship between the catalyst and the electrolyte in which it is tested. In other words, we do not regard the formation of active oxygen species as something inherent to the catalyst alone (presumably a catalyst showing high activity) but rather as something that can be triggered by appropriate coupling of the catalyst and the electrolyte, to result in high overall OER activity.

The similarities between the Ni(Fe)OOH and Ni(Fe)-B<sub>i</sub> catalyst in the catalytically active state were also confirmed by X-ray photoelectron spectroscopy (XPS) (see Fig. S5 in Appendix III), the pristine nickel oxyhydroxide and nickel-borate catalysts exhibit small differences in the Ni2p and O1s binding energies, but those differences disappear when the catalysts are subjected to electrochemical conditioning, after which the XPS spectra are virtually the same, indicating that the chemical state of both electrochemically conditioned catalysts is quite similar.

The microstructure was also verified, using Atomic Force Microscopy (AFM) (see Fig. S6 in Appendix III), the grain size was comparable for both electrocatalysts, although the distribution of the grains is different. The Ni(Fe)-B<sub>i</sub> catalyst deposits in an arrangement of closely packed nanoclusters, whereas the Ni(Fe)OOH compound deposits in a rather chaotic network, without any apparent higher-order structure.

It has been recently reported<sup>23,25,26</sup> that iron impurities present in the electrolyte can improve the electrocatalytic activity towards oxygen evolution of NiOOH. Therefore the question arises whether those impurities might affect the effect of pH on the activity, as presented in this work. The chemicals used during electrodeposition, anodization and cyclic voltammetry were not scrubbed of Fe content, therefore our OEC films can be expected to contain considerable amounts of Fe.<sup>22,23</sup> The KOH and H<sub>3</sub>BO<sub>3</sub> used in this work were reagent grade chemicals with Fe content < 1 ppm, and they were not purified according the method of Trotochaud et al.,<sup>23</sup> so we expect that Fe is present in our films. Both KOH and H<sub>3</sub>BO<sub>3</sub> used have a

similar content of Fe but the measured catalytic activity at pH 9.2 is approximately twice lower than at pH 13. This shows that the catalyst deprotonation towards formation of activated oxygen species has real effect on the catalytic activity, which is not related with the Fe impurities in the electrolyte. We further proved this statement by measuring the catalytic activity towards oxygen evolution on NiFe double hydroxide (50% Fe) in KOH 0.1 M (pH 13) and in phosphate buffer pH 7 (see Fig. S7 in Appendix III). The results of this experiment clearly show that even in the presence of iron, the catalytic activity of Ni(Fe)OOH at pH 7 is negligible, so the deprotonating effect of the alkaline electrolyte plays crucial role for the enhanced catalytic activity towards electrochemical oxygen evolution normally observed in Ni-based catalysts in alkaline media.

It is important to mention that we are not disregarding the effect of Fe impurities in the electrolyte, which is reported to enhance the activity of Ni-based OECs. We acknowledge that the presence of iron is absolutely crucial for efficient OER and it is very well possible that iron is the active site for OER in Ni-based OECs. Nevertheless, in our report we analyse the activity of Ni-based catalysts regardless of Fe content. We focus on coupling of Ni-based OECs with the electrolyte and specifically consider the role of pH and borate concentration. Our evidence shows that the deprotonating effect of hydroxyl anions to form highly oxidized nickel sites in the catalyst also plays a very important role to reach high catalytic activity, and needs to be carefully considered in the development of nickel-based catalysts for the oxygen evolution reaction at moderate pHs. We show that the formation of the active oxygen species is an additional mechanism that can give rise to an even higher OER activity than based on the Fe impurities alone. The formation of the active oxygen species is facilitated by alkaline conditions and seems to be independent of the Fe content in NiOOH i.e. regardless of the exact composition of the catalyst, the active oxygen species can promote higher OER activity. We are confident to ascribe this effect to the electrolyte properties and not the Fe-impurities, since similar observations have been made for Fe-free systems.<sup>56</sup>

#### 4.3.4 In situ X-ray Absorption Spectroscopy measurements of nickel(II) hydroxide and nickel borate during electrochemical water oxidation in alkaline media

Figure 5a-d shows the In situ X-ray Absorption Near Edge Fine Structure (XANES) spectra as function of the applied potential, acquired during potentiostatic experiments for oxygen evolution on Ni(Fe)OOH and Ni(Fe)-B<sub>i</sub> electrocatalysts, in KOH 0.1 M and borate buffer pH 9.2. The edge position in the all XANES spectra shift to higher energies when the electrode potential becomes more positive, which is consistent with the fact that the nickel sites of Ni(Fe)(OH)<sub>2</sub> and Ni(Fe)-B<sub>i</sub> oxidizes at potentials higher than ca. 1.4 V vs RHE (KOH 0.1 M) and 1.5 V vs RHE (borate buffer pH 9.2), as it can be seen in the voltammetries of Figure 1. According to literature data,<sup>21,57</sup> the increase in the oxidation state of nickel in NiOOH induces changes in its local chemical environment, and consequently a crystallographic phase changing from trigonal/rhombohedral to monoclinic occurs.

Interestingly, XANES spectra of both OECs, anodized Ni(Fe)OOH and Ni(Fe)-B<sub>i</sub> collected at various applied potentials look very similar (Figure 5a-b in comparison with Figure 5c-d), this supports the idea that the nickel-borate catalyst in its active state is a form of  $\gamma$ -NiOOH, which is in agreement with the voltammetric and spectroscopic evidence presented in the previous sections. Our results are in agreement with some other XAS studies available in the literature.<sup>21,58</sup> The work of Bediako et al.<sup>21</sup> shows that anodized Ni-B<sub>i</sub> is very similar to  $\gamma$ -NiOOH in terms of the XANES edge position, formal nickel oxidation state and the EXAFS spectra. Likewise, we find virtually no differences between Ni(Fe)-B<sub>i</sub> and Ni(Fe)OOH.

The local environment analysis of Ni catalysts samples was achieved by performing Extended X-ray Absorption Fine Structure (EXAFS) measurements at the Ni K-edge (see Fig. S9-S10 in Appendix III). The experimental data were analyzed according to GNXAS approach which allowed us to construct the signal corresponding to the molecule from known scattering amplitudes and phases. In this way, the structural signal was constructed entirely *ab-initio* and then fitted to the experimental data. To generate the theoretical signals needed to fit the data, the  $\beta$ -NiOOH and  $\gamma$ -NiOOH (swollen phase) crystallographic phase were used.<sup>21,57</sup> These compounds have, respectively, a trigonal / rhombohedral and monoclinic crystal structure.

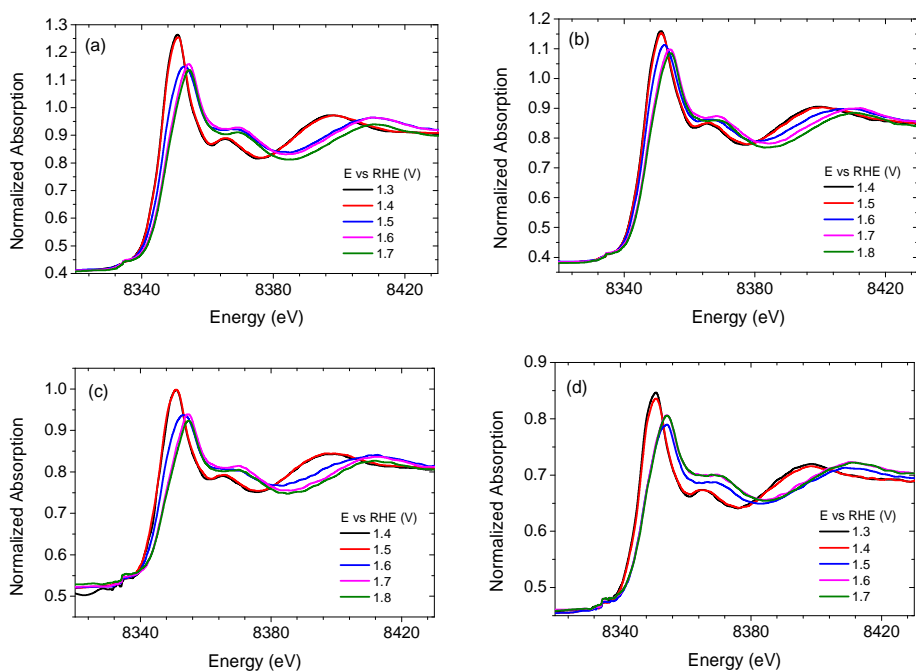


Figure 5. In situ Ni K-edge XAS spectra acquired during potentiostatic OER experiments on anodized Ni(Fe)OOH and Ni(Fe)-Bi electrocatalysts deposited on FTO. (a) XANES spectra of Ni(Fe)OOH during OER in 0.1 M KOH. (b) XANES spectra of Ni(Fe)OOH during OER in borate buffer pH 9.2. (c) XANES spectra of Ni(Fe)-Bi during OER in 0.1 M KOH. (d) XANES spectra of Ni(Fe)-Bi during OER in borate buffer pH 9.2.

The space group that describe the structure of  $\beta$ -NiOOH is  $P\bar{3}m1$ , with the following unit cell parameters:  $a = b = 3.1170 \text{ \AA}$ ,  $c = 4.595 \text{ \AA}$ ,  $\alpha = \beta = 90^\circ$ ,  $\gamma = 120^\circ$ . The space group used to describe the  $\gamma$ -NiOOH phase is  $C2/m$ , with the following unit cell parameters:  $a = b = 2.8295 \text{ \AA}$ ,  $c = 20.9472 \text{ \AA}$ ,  $\alpha = \beta = 90^\circ$ ,  $\gamma = 119.74^\circ$ .

The Ni atoms in both cases coordinate six oxygen atoms but in the  $\beta$ -NiOOH, due to the Jahn-Teller effect, there is a strongly distorted octahedral geometry caused by the elongation of the Ni-O distance along the axial direction.<sup>21</sup> The low symmetry of this structure causes that two different Ni-O distances can be detected in  $\beta$ -NiOOH (Ni-O equatorial:  $1.87 \text{ \AA}$  and Ni-O axial: at  $2.03 \text{ \AA}$ ), but the limited  $k$  range measured makes it impossible to gather this data. This allows the ability to keep the model as simple as possible and to reduce the numbers of fitting parameters. With this approximation,



the local environment of the Ni can be modelled by using two two-body  $\gamma_2^1$  and  $\gamma_2^2$  signals representing the Ni-O and Ni-Ni distances respectively.

The  $\gamma$ -NiOOH structure was modeled with periodically alternating repetitions of edge-shared octahedra arranged into higher ordered layers, which are interstratified with alkali cations and water molecules, which is in agreement with the report from Risch et al. proposes that the structure of Ni-B<sub>i</sub> may be composed of fragments of layered  $\gamma$ -NiOOH separated by water and borate molecules.<sup>58</sup> This approximation makes the model simple and allows us to reduce the numbers of fitting parameters. In this model, the Ni local environment can be simulated by using two two-body  $\gamma_2^1$ ,  $\gamma_2^2$  and two three body signals  $\gamma_3^1$  and  $\gamma_3^2$ .

Figure 6, representing a sketch of a swollen phase, the  $\gamma_2^1$  is relative to the Ni-O distance at 1.985 Å,  $\gamma_2^2$  is the Ni-O at 2.77 Å. The three body configurations  $\gamma_3^1$  and  $\gamma_3^2$ , the  $\gamma_3^1$  is relative to the Ni-O-Ni triangular arrangements with  $\theta \sim 140^\circ$  and having a long Ni-Ni distance at 5.00 Å whereas  $\gamma_3^2$  takes into account the collinear configuration with  $\theta 180^\circ$ , having the Ni-Ni distance at 5.65 Å. In this configuration the only free parameter is the angle. The distances, the Debye Waller factors and the coordination numbers are directly linked by geometrical consideration to the first two shells. It is worth mentioning that the coordination numbers for these distances in the ideal structure are equal to six. The fitting results obtained on the samples are reported in Table S1-S2 in Appendix III and shown in Figure 6.

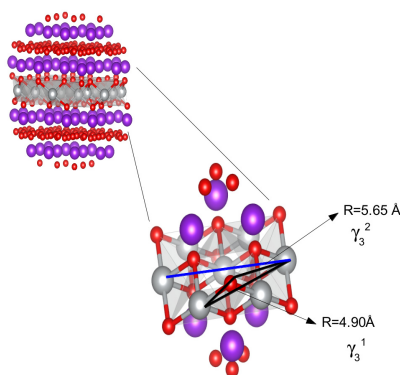


Figure 6. Sketch of the swollen  $\gamma$ -NiOOH phase. For sake of clarity, the direct Ni-O and Ni-Ni distance are not shown but only the two three-body configurations are evidenced in black and in blue lines.

## 4.4 Conclusions

We have presented a systematic spectroelectrochemical study of the electrocatalytic activity towards oxygen evolution of two Ni-based OECs (Ni(Fe)-B<sub>i</sub> and Ni(Fe)OOH). The recorded broad SERS peaks in the region *ca.* 900-1150 cm<sup>-1</sup> clearly show that Ni(Fe)-B<sub>i</sub> and Ni(Fe)OOH get charged prior the actual OER, and those negatively charged sites in the OECs act as OER precursors. We propose that the formation of those “active oxygen” sites occurs via a deprotonation process that strongly depends on the pH of the electrolyte. The chemical identity of the “active oxygen” species is still unclear but its Raman peak appears in the region that nickel peroxide and superoxide have vibrational modes, suggesting that the species may have peroxidic or superoxidic nature. It is noteworthy that the effect of the deprotonation process is crucial at moderate pHs, as even Fe-doped Ni-based catalysts shows negligible activity in neutral pH 7. These results clearly demonstrate that the deprotonating effect in strongly alkaline electrolytes has an important effect on the catalytic activity of nickel-based compounds, and should be carefully considered in addition to the Fe content if one would like to develop Ni-based electrocatalysts meant to catalyze the OER at moderate pHs.

The SERS, UV-vis and XAS evidence collected in this work suggest that  $\alpha$ -Ni(OH)<sub>2</sub> and Ni-B<sub>i</sub> get activated through the formation of very similar oxyhydroxide species. Furthermore, Ni(Fe)-B<sub>i</sub> and Ni(Fe)OOH show similar electrochemical characteristics in a given electrolyte *i.e.* similar OER electrocatalytic activity and electrolyte dependence. We could not find any evidence for the importance of the boron presence in the structure of Ni(Fe)-B<sub>i</sub>. Therefore we conclude that in the active state, Ni(Fe)-B<sub>i</sub> and Ni(Fe)OOH are chemically the same, namely forms of NiOOH.

Furthermore, the *in-situ* UV Vis spectroscopic study of Ni(Fe)-B<sub>i</sub> and Ni(Fe)OOH showed that both OECs absorb a huge portion of light in the catalytically active state. This needs to be taken into consideration when applying this sort of catalyst on photoelectrochemical devices.

Our work has clearly shown that a catalyst should not be studied separately from its environment; in Ni-based OECs the phase-nature and activity of the catalyst is

strongly dependent on the electrolyte properties and therefore such a system should be studied as a whole.

## 4.5 Acknowledgements

This research is financed in part (B.J.T., O.D-M., M.T.M.K. and W.A.S) by the BioSolarCells open innovation consortium, supported by the Dutch Ministry of Economic Affairs, Agriculture and Innovation. A.L. and W.B. acknowledge The Netherlands Organisation for Scientific Research (NWO) for financial support. Helpful discussions with Fatwa Firdaus Abdi and Wim Haije in the initial phase of this work are greatly acknowledged

## 4.6 References

- (1) Hermans, J. *Energy Survival Guide*; Leiden University Press, 2011.
- (2) Hoffert, M. I.; Caldeira, K.; Jain, A. K.; Haites, E. F.; Harvey, L. D. D.; Potter, S. D.; Schlesinger, M. E.; Schneider, S. H.; Watts, R. G.; Wigley, T. M. L.; Wuebbles, D. J. *Nature* **1998**, 395 (October), 881.
- (3) Lewis, N. S.; Nocera, D. G. *Proc. Natl. Acad. Sci. U. S. A.* **2006**, 103 (43), 15729.
- (4) Crabtree, G. W.; Dresselhaus, M. S.; Buchanan, M. V. *Phys. Today* **2004**, 57 (12), 39.
- (5) Koper, M. T. M. *J. Electroanal. Chem.* **2011**, 660 (2), 254.
- (6) Man, I. C.; Su, H.-Y.; Calle-Vallejo, F.; Hansen, H. a.; Martínez, J. I.; Inoglu, N. G.; Kitchin, J.; Jaramillo, T. F.; Nørskov, J. K.; Rossmeisl, J. *ChemCatChem* **2011**, 3 (7), 1159.
- (7) Matsumoto, Y.; Sato, E. *Mater. Chem. Phys.* **1986**, 14 (5), 397.
- (8) Gong, M.; Dai, H. *Nano Res.* **2014**, 8 (1), 23.
- (9) Gong, M.; Li, Y.; Wang, H.; Liang, Y.; Wu, J. Z.; Zhou, J.; Wang, J.; Regier, T.; Wei, F.; Dai, H. *J. Am. Chem. Soc.* **2013**, 135 (23), 8452.
- (10) Lu, Z.; Xu, W.; Zhu, W.; Yang, Q.; Lei, X.; Liu, J.; Li, Y.; Sun, X.; Duan, X. *Chem. Commun.* **2014**, 50 (49), 6479.
- (11) Song, F.; Hu, X. *Nat. Commun.* **2014**, 5, 4477.

- (12) McCrory, C. C. L.; Jung, S.; Peters, J. C.; Jaramillo, T. F. *J. Am. Chem. Soc.* **2013**, *135* (45), 16977.
- (13) Hall, D. E. *J. Electrochem. Soc.* **1983**, *130* (2), 317.
- (14) Trasatti, S. *Electrochim. Acta* **1984**, *29* (11), 1503.
- (15) Li, X.; Walsh, F. C.; Pletcher, D. *Phys. Chem. Chem. Phys.* **2011**, *13* (3), 1162.
- (16) Lyons, M. E. G.; Brandon, M. P. *Int. J. Electrochem. Sci.* **2008**, *3*, 1386.
- (17) Lin, F.; Boettcher, S. W. *Nat. Mater.* **2014**, *13* (1), 81.
- (18) Mills, T. J.; Lin, F.; Boettcher, S. W. *Phys. Rev. Lett.* **2014**, *112* (14), 148304.
- (19) Dincă, M.; Surendranath, Y.; Nocera, D. G. *Proc. Natl. Acad. Sci. U. S. A.* **2010**, *107* (23), 10337.
- (20) Bediako, D. K.; Surendranath, Y.; Nocera, D. G. *J. Am. Chem. Soc.* **2013**, *135* (9), 3662.
- (21) Bediako, D. K.; Lassalle-Kaiser, B.; Surendranath, Y.; Yano, J.; Yachandra, V. K.; Nocera, D. G. *J. Am. Chem. Soc.* **2012**, *134* (15), 6801.
- (22) Smith, A. M.; Trotochaud, L.; Burke, M. S.; Boettcher, S. *Chem. Commun.* **2014**, *51*, 5261.
- (23) Trotochaud, L.; Young, S. L.; Ranney, J. K.; Boettcher, S. W. *J. Am. Chem. Soc.* **2014**, *136* (18), 6744.
- (24) Trotochaud, L.; Ranney, J. K.; Williams, K. N.; Boettcher, S. W. *J. Am. Chem. Soc.* **2012**, *134* (41), 17253.
- (25) Friebe, D.; Louie, M. W.; Bajdich, M.; Sanwald, K. E.; Cai, Y.; Wise, A. M.; Cheng, M.-J.; Sokaras, D.; Weng, T.-C.; Alonso-Mori, R.; Davis, R. C.; Bargar, J. R.; Norskov, J. K.; Nilsson, A.; Bell, A. T. *J. Am. Chem. Soc.* **2015**, *137* (3), 1305.
- (26) Klaus, S.; Cai, Y.; Louie, M. W.; Trotochaud, L.; Bell, A. T. *J. Phys. Chem. C* **2015**, *119* (13), 7243.
- (27) West, R. C. *Handbook of Chemistry and Physics*, 53rd ed.; CRC Press: Cleveland, 1972.
- (28) House, J. *Inorganic Chemistry*, 2nd ed.; Academic Press: Waltham, 2013.
- (29) Lai, S. C. S.; Kleyn, S. E. F.; Rosca, V.; Koper, M. T. M. *J. Phys. Chem. C* **2008**, *112* (48), 19080.
- (30) Diaz-Morales, O.; Calle-Vallejo, F.; de Munck, C.; Koper, M. T. M. *Chem. Sci.* **2013**, *4* (6), 2334.
- (31) Gao, P.; Gosztola, D.; Leung, L.-W. H.; Weaver, M. J. *J. Electroanal. Chem. Interfacial Electrochem.* **1987**, *233* (1–2), 211.
- (32) Trasatti, S.; Petrii, O. A. *J. Electroanal. Chem.* **1992**, *327* (1–2), 353.
- (33) Nikitenko, S.; Beale, A. M.; van der Eerden, A. M. J.; Jacques, S. D. M.; Leynaud, O.; O'Brien, M. G.; Detollenaere, D.; Kaptein, R.; Weckhuysen, B. M.; Bras, W. J.

- Synchrotron Radiat.* **2008**, *15* (Pt 6), 632.
- (34) Filipponi, A.; Di Cicco, A.; Natoli, C. R. *Phys. Rev. B* **1995**, *52* (21), 15122.
  - (35) Filipponi, A.; Di Cicco, A. *Phys. Rev. B* **1995**, *52* (21), 15135.
  - (36) Yeo, B. S.; Bell, A. T. *J. Phys. Chem. C* **2012**, *116* (15), 8394.
  - (37) Cornilsen, B. C.; Shan, X.; Loyselle, P. L. *J. Power Sources* **1990**, *29* (3–4), 453.
  - (38) Corrigan, D. A. *J. Electrochem. Soc.* **1989**, *136* (3), 613.
  - (39) Nazri, G.; Corrigan, D. A.; Maheswari, S. P. *Langmuir* **1989**, *5* (1), 17.
  - (40) Bendert, R. M. *J. Electrochem. Soc.* **1989**, *136* (5), 1369.
  - (41) Conell, R. S.; Corrigan, D. A.; Powell, B. R. *Sol. Energy Mater. Sol. Cells* **1992**, *25* (3–4), 301.
  - (42) Yu, P. C.; Lampert, C. M. *Sol. Energy Mater.* **1989**, *19* (1–2), 1.
  - (43) Trotochaud, L.; Mills, T. J.; Boettcher, S. W. *J. Phys. Chem. Lett.* **2013**, *4* (6), 931.
  - (44) Lo, Y. L.; Hwang, B. J. *Langmuir* **1998**, *14* (4), 944.
  - (45) Hermet, P.; Gourrier, L.; Bantignies, J.-L.; Ravot, D.; Michel, T.; Deabate, S.; Boulet, P.; Henn, F. *Phys. Rev. B* **2011**, *84* (23), 235211.
  - (46) Li, H. B.; Yu, M. H.; Wang, F. X.; Liu, P.; Liang, Y.; Xiao, J.; Wang, C. X.; Tong, Y. X.; Yang, G. W. *Nat. Commun.* **2013**, *4* (May), 1894.
  - (47) Desilvestro, J.; Corrigan, D. A.; Weaver, M. J. *J. Phys. Chem.* **1986**, *90* (24), 6408.
  - (48) Merrill, M.; Worsley, M.; Wittstock, A.; Biener, J.; Stadermann, M. *J. Electroanal. Chem.* **2014**, *717–718*, 177.
  - (49) Devarajan, V.; Gräfe, E.; Funck, E. *Spectrochim. Acta Part A Mol. Spectrosc.* **1974**, *30* (6), 1235.
  - (50) Devi, S. A.; Philip, D.; Aruldas, G. *J. Solid State Chem.* **1994**, *113* (1), 157.
  - (51) Lewis, J. A. *J. Am. Ceram. Soc.* **2000**, *83* (10), 2341.
  - (52) Citra, A.; Chertihin, G. V.; Andrews, L.; Neurock, M. *J. Phys. Chem. A* **1997**, *101* (17), 3109.
  - (53) Uzunova, E. L.; Mikosch, H.; Nikolov, G. S. *J. Chem. Phys.* **2008**, *128* (9), 94307.
  - (54) Holland, P. L. *Dalt. Trans.* **2010**, *39* (23), 5415.
  - (55) Takashima, T.; Hashimoto, K.; Nakamura, R. *J. Am. Chem. Soc.* **2012**, *134* (3), 1519.
  - (56) Diaz-Morales, O.; Ferrus-Suspedra, D.; Koper, M. T. M. *Chem. Sci.* **2016**, *7* (4), 2639.
  - (57) Van der Ven, a.; Morgan, D.; Meng, Y. S.; Ceder, G. *J. Electrochem. Soc.* **2006**, *153* (2), A210.
  - (58) Risch, M.; Klingan, K.; Heidkamp, J.; Ehrenberg, D.; Chernev, P.; Zaharieva, I.; Dau, H. *Chem. Commun.* **2011**, *47* (43), 11912.

# Appendix III

## General

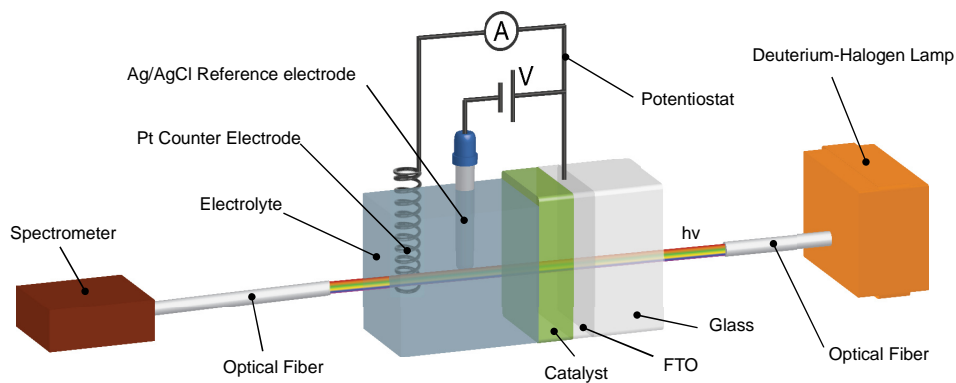


Fig. S1. Schematic view of the electrochemical setup used for the in situ UV-vis measurements.

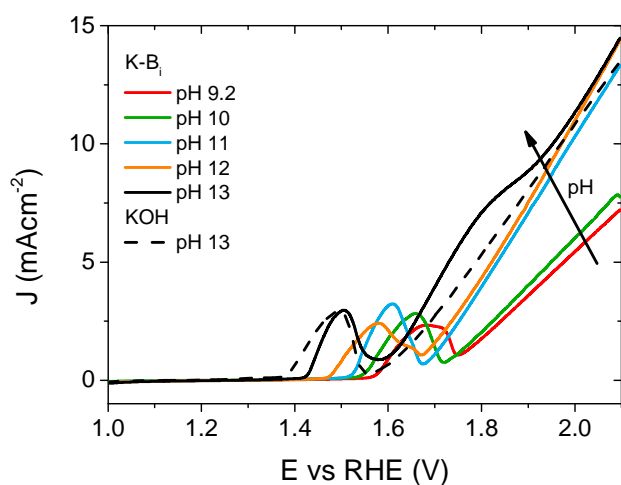


Fig. S2. JV curves of Ni(Fe)OOH collected in 0.5 M K-Bi pH 9.2 – 13 and in 0.1 M KOH pH 13.

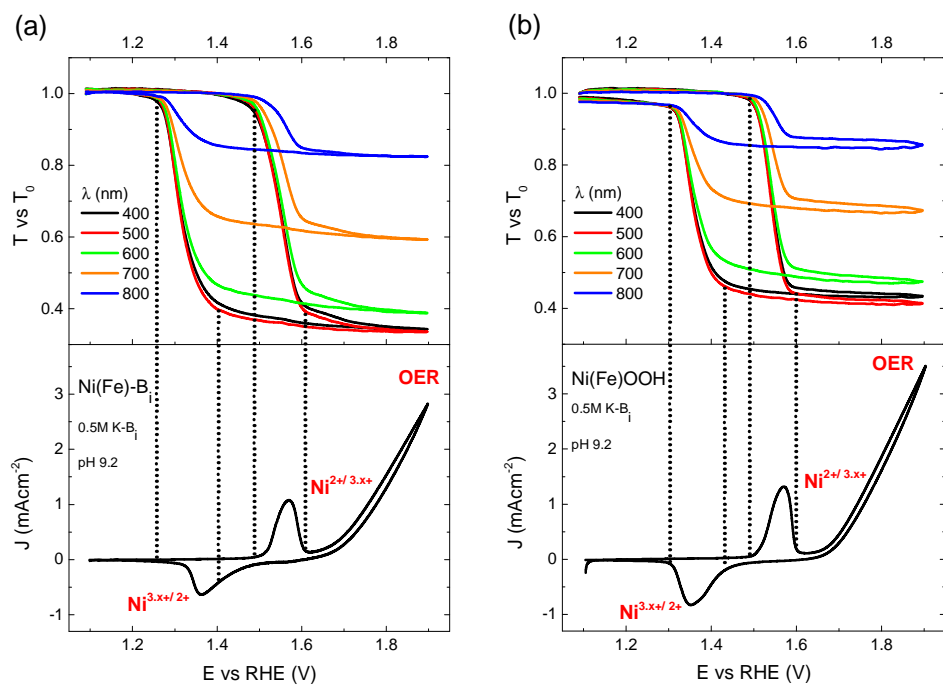


Fig. S3. Transmission vs potential curves for a number of selected wavelengths and the corresponding polarization curves for (a) Ni(Fe)-B<sub>i</sub> and (b) Ni(Fe)OOH in 0.5 M K-B<sub>i</sub> electrolyte pH 9.2, scan rate 10 mV/s. Dotted lines indicate potentials of the onset and offset of the optical transition for  $\lambda = 500$  nm.

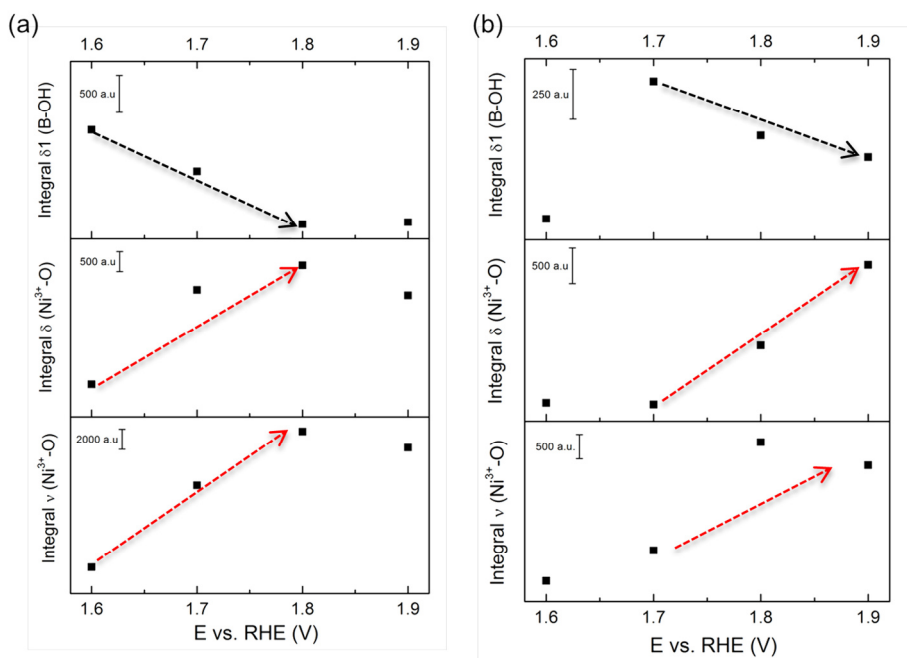


Fig. S4. Evolution of the integral of the Ni-O and B-OH Raman peaks for (a) Ni(Fe)OOH and (b) Ni(Fe)-B<sub>i</sub> catalysts. Measurement obtained from the SER spectra in figures 3b and 4b, respectively (catalysts in borate buffer pH 9.2). The integral of the B-OH peak was calculated from the peak at *ca.* 1400 cm<sup>-1</sup>.



## X-ray Photoelectron Spectroscopy (XPS)

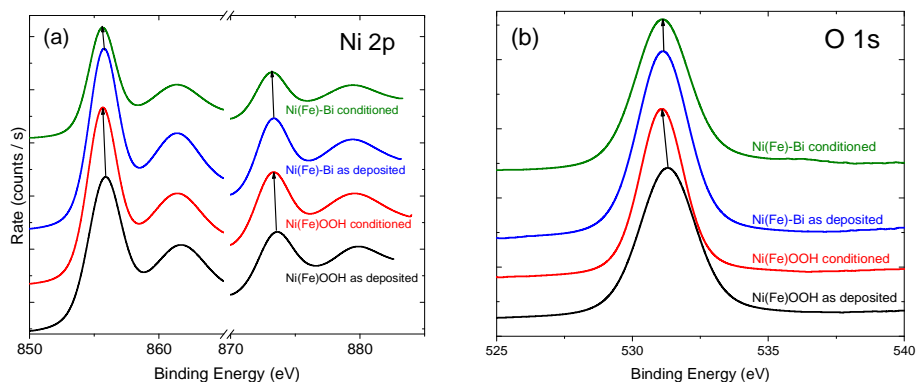


Fig. S5. Collected XPS spectra for as deposited and conditioned samples of Ni(Fe)-Bi and Ni(Fe)OOH. (a) Ni2p and (b) O1s orbital scans.

Ni(Fe)-B<sub>i</sub> and Ni(Fe)OOH electrodes, as deposited and electrochemically conditioned, were tested with X-ray photoelectron spectroscopy, collected data is presented in Fig. S5. The Ni2p and O1s scans for all four samples give features similar in shape and intensity, yet slightly different in specific binding energy. Peaks for as deposited Ni(Fe)-B<sub>i</sub> have slightly higher binding energies than for as deposited Ni(Fe)OOH. For samples subjected to electrochemical conditioning, a shift in the XPS features towards lower binding energies can be observed, more pronounced in case of Ni(Fe)OOH. Consequently, both conditioned samples show virtually the same spectra. In other words, the initial differences in binding energies between the two as deposited samples disappear after the conditioning process, due to a different degree of shift in the binding energy of the XPS features. The electrochemical conditioning process is believed to result in more ordered structure of Ni(OH)<sub>x</sub> type of films. This implies that Ni(Fe)-B<sub>i</sub> as deposited has more ordered structure, however upon conditioning both OECs attain a similar structure. What is more, in case of Ni(Fe)-B<sub>i</sub> we fail to see any effect of boron presence on the obtained spectra. It suggests that boron does not affect significantly the structure of Ni(Fe)-B<sub>i</sub> films.

## Atomic Force Microscopy (AFM)

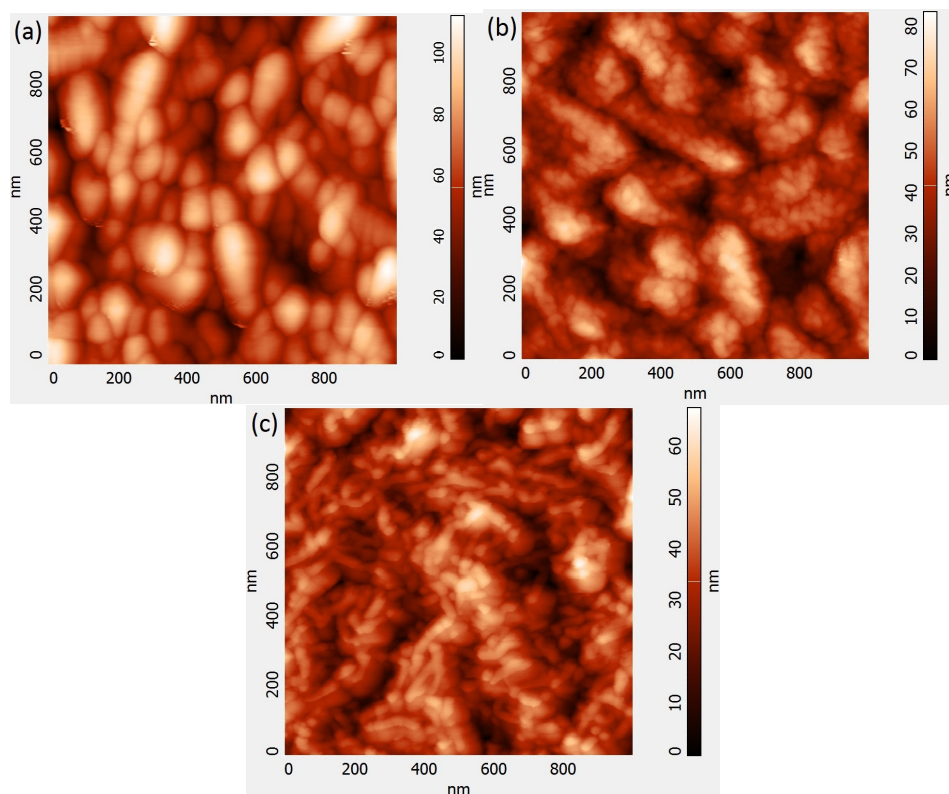


Fig. S6. AFM Scans of (a) FTO substrate (b) Ni(Fe)-Bi sample (c) Ni(Fe)OOH sample.

Fig. S6 shows typical examples of surface topographies for FTO, Ni(Fe)-Bi and Ni(Fe)OOH (Fig. S6 a, b and c respectively). Pristine FTO has grains of about 110 nm in size. In case of Ni(Fe)-Bi, deposited films are in the form of closely packed nanoclusters. On the other hand, the arrangement of nanoparticles in Ni(Fe)OOH films seems to be more chaotic, without any sort of higher-order structure. The grains for both catalysts are comparable in size. Observed differences in microstructures could potentially result in different ion permeability and different catalytically active surface area for the two catalysts.

## The pH dependence of the electrocatalytic activity of NiFe double hydroxide

### Preparation NiFe double hydroxide (DH)

Nickel-iron double hydroxide was prepared by the co-precipitation route,<sup>1</sup> using 0.1 M solutions of  $\text{Ni}(\text{NO}_3)_2$  and  $\text{Fe}(\text{NO}_3)_3$  as precursors. The precipitation was performed at 80 °C by dropping 32 mL of the solution with the metals in 1:1 molar ratio over 10 mL of water previously adjusted to pH 9 with 0.1 M  $\text{Na}_2\text{CO}_3$ . The pH was kept approximately constant at 9 during the synthesis by simultaneous dropping of 0.1 M  $\text{Na}_2\text{CO}_3$  (36 mL). The addition of the  $\text{Ni}^{2+}/\text{Fe}^{3+}$  solution and the  $\text{Na}_2\text{CO}_3$  was completed within 1.5 h, after which the suspension was glass-filtered and thoroughly rinsed with water. The powders were subsequently dried overnight at 120 °C and fine-ground.

The double hydroxide was immobilized on the electrode by drop-casting inks, using Nafion® as binding agent. We used Na-exchanged Nafion to avoid possible corrosion of the hydroxides due to the strong acidity of the commercially available solution. Alkaline Nafion was prepared according to the procedure reported in the literature,<sup>2</sup> by mixing 2 parts in volume of commercially available 5 wt% Nafion solution with 1 part of 0.1 M NaOH, which is reported to have ~ pH 11. The preparation of the inks is similar to previously reported methods to immobilize OER catalysts for RDE experiments,<sup>3,4</sup> with concentrations of  $5 \text{ mg}_{\text{DH}} \text{ mL}_{\text{ink}}^{-1}$  and  $1 \text{ mg}_{\text{Nafion}} \text{ mL}_{\text{ink}}^{-1}$ . The inks were prepared in absolute ethanol, first dispersing the DH within the solvent by sonication for 30 min, subsequently adding the Na-exchanged Nafion, followed by 20 min of further sonication. The catalysts were drop-casted on the Au disk to give a final loading of  $75 \mu\text{g}_{\text{DH}} \text{ cm}^{-2}_{\text{disk}}$  and dried in vacuum, where  $\text{cm}^2_{\text{disk}}$  accounts for the geometrical surface area of the Au disk.<sup>5</sup>

## pH dependence of the NiFe DH activity towards oxygen evolution

The electrocatalytic activity of a Ni-based double hydroxide towards oxygen evolution in neutral media (pH 7) and alkaline media (pH 13) was measured, in order to verify that the effect of pH is real and not caused by differences in Fe impurities in the electrolytes. The results are summarized in Fig. S7. Fig. S7 clearly shows that the effect of pH on the catalytic activity is real, and even a very active catalyst like this NiFe compound shows negligible activity in neutral pH 7.

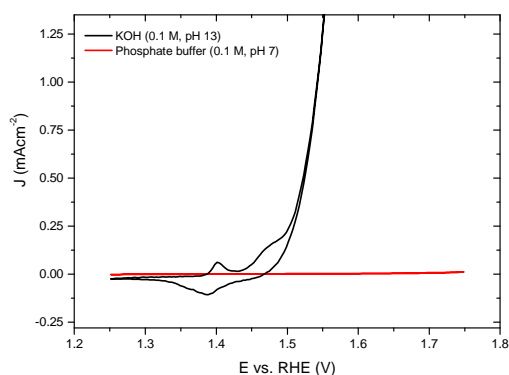


Fig. S7. Polarization curve for oxygen evolution of Ni<sub>0.5</sub>Fe<sub>0.5</sub> double hydroxide, measured in KOH 0.1 M (pH 13) and phosphate buffer (pH7, ionic strength: 0.1 M). Scan rate: 0.01 V/s

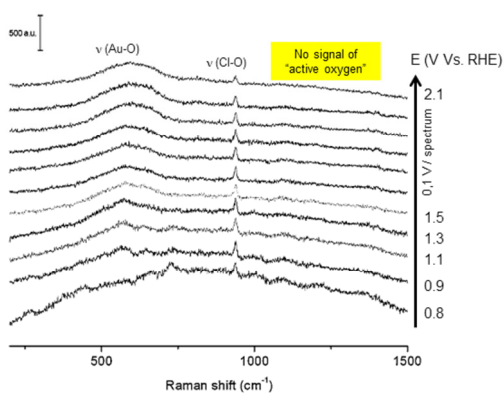


Fig. S8. SER spectra of the gold electrode acquired in the potential range 0.8 – 2.1 V vs RHE in KOH 0.1 M + KClO<sub>4</sub> 0.1 M. The measurements were performed potentiostatically.

## Extended X-ray Absorption Fine Structure (EXAFS) results

Fig. S9-S10 shows the EXAFS results obtained during the electrochemical water oxidation on Ni(Fe)OOH and Ni(Fe)-B<sub>i</sub>, respectively, supported on FTO. The measurements were performed in KOH 0.1 M and borate buffer pH 9.2, and the results are presented in the R-space (Fourier Transform) with the corresponding fitting (fitting parameter are listed in tables S1-S2).

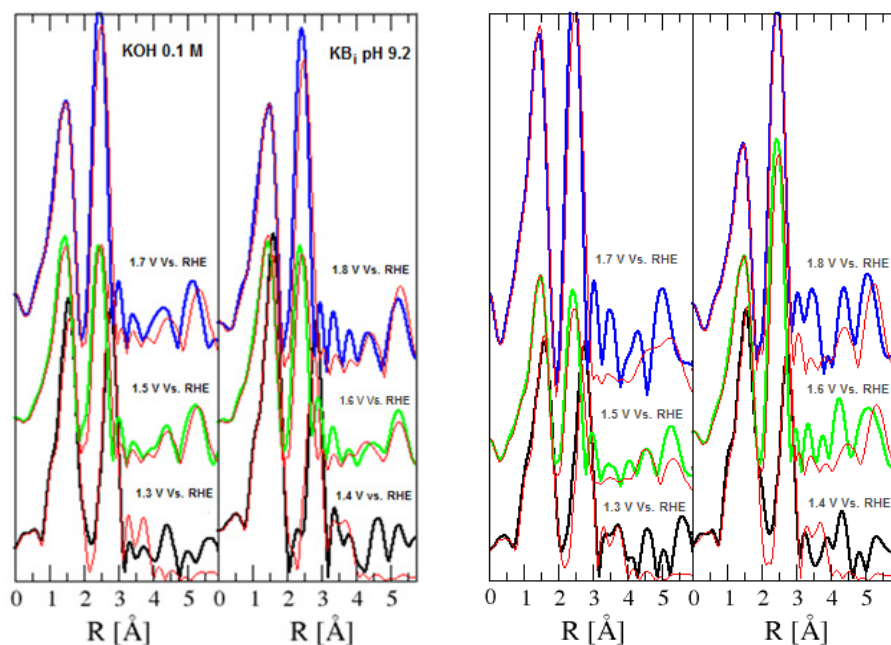


Fig. S9. EXAFS results obtained during the electrochemical water oxidation in Ni(Fe)OOH. The experiment was performed at constant potential in KOH 0.1 M and K-Bi pH 9.2. Results are presented in the R-space (Fourier Transform), with the corresponding fitting (red line).

Fig. S10. EXAFS results obtained during the electrochemical water oxidation in Ni(Fe)-Bi. The experiments were performed at constant potential in KOH 0.1 M and K-Bi pH 9.2. Results are presented in the R-space (Fourier Transform), with the corresponding fitting (red line).

Table S1. Fitting parameters of the EXAFS spectra obtained during the electrochemical water oxidation on Ni(Fe)OOH in KOH 0.1 M and borate buffer pH 9.2. The errors are in the last digit. N indicates the calculated coordination numbers, R corresponds to the shells distances in Å,  $\sigma^2$  are the Debye-Waller factor ( $\text{\AA}^2$ ) and  $\theta$  is the angle of the  $\gamma^n$  contributions.

	0.1 M KOH			Borate buffer pH 9.2			
	1.3	1.5 V <sub>RHE</sub>	1.7 V <sub>RHE</sub>	1.4	1.5 V <sub>RHE</sub>	1.6 V <sub>RHE</sub>	1.8 V <sub>RHE</sub>
<b>N<sub>1</sub></b>	5.1	4.05	5.0	5.1	5.3	4.0	4.2
<b>R<sub>1</sub> Ni-O</b>	1.932	1.895	1.895	1.931	1.90	1.895	1.895
<b><math>\sigma^2</math></b>	0.006	0.006	0.006	0.006	0.008	0.007	0.005
<b>N<sub>2</sub></b>	3.0	2.3	4.4	3.1	3.5	3.0	3.0
<b>R<sub>2</sub> Ni-Ni</b>	2.830	2.840	2.851	2.850	2.842	2.824	2.844
<b><math>\sigma^2</math></b>	0.014	0.003	0.005	0.009	0.008	0.009	0.004
<b>N<sub>3</sub></b>	-	4.05	5	-	-	4.0	3.0
<b>R<sub>3</sub> Ni-Ni (<math>\theta = 140</math>)</b>	-	4.910	4.92	-	-	4.91	4.92
<b><math>\sigma^2</math></b>	-	0.011	0.011	-	-	0.013	0.011
<b>N<sub>4</sub></b>	-	2.3	4.4	-	-	3.0	4.2
<b>R<sub>4</sub> Ni-Ni (<math>\theta = 180</math>)</b>	-	5.533	5.682	-	-	5.646	5.686
<b><math>\sigma^2</math></b>	-	0.008	0.009	-	-	0.007	0.007

Table S2. Fitting parameters of the EXAFS spectra obtained during the electrochemical water oxidation on Ni(Fe)-B<sub>i</sub> in KOH 0.1 M and borate buffer pH 9.2. The errors are in the last digit. *N* indicates the calculated coordination numbers, *R* corresponds to the shells distances in Å,  $\sigma^2$  are the Debye-Waller factor (Å<sup>2</sup>) and  $\theta$  is the angle of the  $\nu^n$  contributions.

	0.1 M KOH			Borate buffer pH 9.2		
	1.3	1.5 V <sub>RHE</sub>	1.7 V <sub>RHE</sub>	1.4	1.6 V <sub>RHE</sub>	1.8 V <sub>RHE</sub>
<b>N<sub>1</sub></b>	6.0	4.0	4.7	6.0	4.3	4.3
<b>R<sub>1</sub> Ni-O</b>	2.040	1.900	1.898	1.940	1.895	1.90
<b><math>\sigma^2</math></b>	0.004	0.003	0.007	0.004	0.006	0.006
<b>N<sub>2</sub></b>	3.1	5.0	5.0	3.0	4.2	2.0
<b>R<sub>2</sub> Ni-Ni</b>	2.816	2.845	2.852	2.820	2.836	2.827
<b><math>\sigma^2</math></b>	0.003	0.010	0.010	0.004	0.004	0.004
<b>N<sub>3</sub></b>	-	4.0	4.7	-	4.3	4.3
<b>R<sub>3</sub> Ni-Ni (<math>\theta = 140</math>)</b>	-	4.967	5.028	-	4.95	4.88
<b><math>\sigma^2</math></b>	-	0.007	0.013	-	0.010	0.010
<b>N<sub>4</sub></b>	-	5.0	5.0	-	4.2	2
<b>R<sub>4</sub> Ni-Ni (<math>\theta = 180</math>)</b>	-	5.686	5.704	-	5.686	5.651
<b><math>\sigma^2</math></b>	-	0.012	0.018	-	0.008	0.007

## References

- (1) Cavani, F.; Trifirò, F.; Vaccari, A. *Catal. Today* **1991**, *11* (2), 173.
- (2) Suntivich, J.; Gasteiger, H. a.; Yabuuchi, N.; Shao-Horn, Y. *J. Electrochem. Soc.* **2010**, *157* (8), B1263.
- (3) Grimaud, A.; May, K. J.; Carlton, C. E.; Lee, Y.-L.; Risch, M.; Hong, W. T.; Zhou, J.; Shao-Horn, Y. *Nat. Commun.* **2013**, *4* (May), 2439.
- (4) Suntivich, J.; May, K. J.; Gasteiger, H. A.; Goodenough, J. B.; Shao-Horn, Y. *Science (80-. )*. **2011**, *334* (6061), 1383.
- (5) Diaz-Morales, O.; Ledezma-Yanez, I.; Koper, M. T. M.; Calle-Vallejo, F. *ACS Catal.* **2015**, No. 5, 5380.

## 5. Summary

Our civilization is facing one of the biggest challenges in its entire history: the energy transition. The growing demand for energy, the scarcity of resources and climate change are the three main factors driving the change. Firstly, the world population is expected to keep on growing, and many poor countries are projected to experience rapid economic development in the near future, which calls for the continued growth of global energy supply. Secondly, fossil fuels, the back-bone of the current energy-infrastructure, while still sufficient in quantity for the upcoming decades, are finite. In addition, the combustion of these fossil fuels is leading to global climate change, which is a great threat to humanity as we know it, in environmental, economical, political and sociological terms. Thus, a move away from relying on fossil fuels and towards renewable, clean and sustainable energy resources like the Sun, is both necessary and inevitable.

Harvesting solar energy entails several scientific and technical challenges, the most significant being the intermittence of the Sun. The momentary, daily and seasonal variability in sunlight demands for a storage solution, such that the solar energy harvested during the sunny days can be released upon demand to provide a steady baseload supply of electricity. In this thesis, we investigate photoelectrochemical (PEC) water splitting as a possible solution for the conversion and storage of solar energy into chemical fuels. PEC water splitting allows for direct conversion of solar to chemical energy via the production of hydrogen. This approach allows for the sustainable production of solar fuels from only water and sunlight, and thereby provides a pathway towards a carbon-free economy.

Solar water splitting can be realized with PEC cells, built with semiconducting photoelectrodes and metal counter-electrodes immersed in an electrolyte solution. The photoelectrodes facilitate light absorption to generate charge carriers, which are then separated and transported to the corresponding solid/liquid electrode/electrolyte interfaces, to drive the water oxidation and reduction half-reactions. Out of these two water splitting half-reactions, water oxidation is the more complex and difficult to drive, since it involves the transfer of four protons and four electrons (where hydrogen production only uses 2 protons and electrons), and goes through three different



intermediates (only one for hydrogen). Thus, the understanding and improvement of the oxygen evolution reaction (OER) efficiency remains the biggest challenge in overall water splitting. Consequently, in this thesis we focus on the materials that perform electrochemical and photoelectrochemical oxygen evolution: semiconductor photoanodes and metal oxide oxygen evolution catalysts (OECs). Specifically, we investigate bismuth vanadate ( $\text{BiVO}_4$ ), an n-type semiconducting photoanode material, and nickel oxyhydroxide ( $\text{NiOOH}$ ), a Ni-based highly efficient OEC.

Firstly, we developed a new technique to improve the surface and bulk limitations of  $\text{BiVO}_4$  photoanodes. Specifically, we introduced a novel in-situ PEC technique called “photocharging” (PC), which comprises prolonged exposure of a photoanode to solar illumination in an open circuit configuration and while immersed in an electrolyte. The PC treatment yields superior PEC activity of  $\text{BiVO}_4$  electrodes: record high photocurrents for undoped and uncatalyzed  $\text{BiVO}_4$  of  $4.3 \text{ mAcm}^{-2}$  @  $1.23 V_{\text{RHE}}$ , very low onset potential of  $0.25 V_{\text{RHE}}$ , very steep photocurrent onset, enhanced catalytic efficiency in a broad potential range, doubled photovoltage and greatly improved quantum efficiency (75 % external and 95 % internal, average in the  $440 \text{ nm} > \lambda > 330 \text{ nm}$  range). Thus, we have provided a new simple photoelectrochemical tool, that can be used as a powerful post-synthetic technique which has the potential to improve the water splitting performance of (metal oxide) photoelectrodes (yet to be determined for materials other than  $\text{BiVO}_4$ ).

Secondly, we investigated how different electrochemical conditions affect the PEC properties of  $\text{BiVO}_4$ , in particular the properties of  $\text{BiVO}_4$  subjected to PC treatment. We found a strong correlation between the pH of the electrolyte and PEC properties: alkaline conditions facilitate the PC effect while acidic conditions prevent it from developing. This strong pH dependence of the PC effect hints towards the importance of the semiconductor-liquid junction (SLJ), which clearly plays a key role in photocharging. Moreover, our results suggest that any enhancements of the bulk-related functionalities are mediated by phenomena occurring at the surface, highlighting the importance of the SLJ for the efficiency of PEC devices.

To gain further insights to the photocharging process, several in-situ and operando spectroelectrochemical techniques were used to study the  $\text{BiVO}_4$  photoanodes. Our results suggest that PC is related to a light-driven alteration of the SLJ, which is preferential in alkaline conditions. Those changes result in the formation

of a  $\text{BiVO}_4$  surface with activity superior for OER, i.e. requiring a lower overpotential to drive the reaction and showing higher efficiency. The UV-vis, XPS and XAS results suggest that those changes may include: the formation of extra surface hydroxyl groups, intercalation of hydrogen, formation of oxygen vacancies, and the reduction of surface vanadium species from 5+ down to 4+. These phenomena have been independently demonstrated to increase donor density and cause the Fermi level to shift towards the conduction band edge – beneficial from the standpoint of water splitting efficiency, and visible in our electrochemical impedance spectroscopy (EIS) and PEC results. Furthermore, according to our EIS study, the PC treatment causes a capacitive layer to form on the surface of the electrodes. Such a capacitive layer has the ability to accumulate photogenerated holes that can facilitate suppressed surface recombination, and thus improved water oxidation. Overall, the PC mechanism seems to be a combination of multiple phenomena that give rise to  $\text{BiVO}_4$  with superior OER properties.

In addition to studying  $\text{BiVO}_4$  photocharging, we also attempted to gain new insights into the mechanism of water oxidation on  $\text{Ni(Fe)OOH}$  catalysts using several in-situ spectroelectrochemical techniques. Our results suggest that  $\text{Ni(Fe)OOH}$  gets negatively charged prior to OER. We believe that those charged sites on the catalyst surface are OER precursor species. To the best of our knowledge it is the first experimental evidence of the “active oxygen” species in  $\text{Ni(Fe)OOH}$ . Moreover, we propose that the formation of those “active oxygen” sites occurs via a deprotonation process. Our SERS data does not allow for unequivocal assignment of the chemical identity of those species, though it suggests peroxidic or superoxidic nature. Thus, we were able to improve the general understanding of the mechanism of OER on  $\text{Ni(Fe)OOH}$ . Next, we looked into the impact of electrolyte on the efficiency and mechanism of OER on  $\text{Ni(Fe)OOH}$ . Our electrochemical data clearly shows that highly alkaline conditions promote high catalytic activity (low Tafel slope) and also positively affect the thermodynamics (lower onset potential and lower potential for  $\text{Ni}^{2+}/\text{Ni}^{3.x+}$  transition). However, we believe that in moderately alkaline pHs ( $\text{pH} < 10$ ) this inhibitory effect is primarily due the  $\text{BO}_3^{3-}$  preferential adsorption on the surface of the catalyst. In highly alkaline pHs ( $\text{pH} > 11$ ) the presence of borate anions does not seem to play a role anymore. Importantly, looking at our electrochemical and SERS data, we were able to correlate high OER activity in high pHs with formation of the “active oxygen species”. These results clearly demonstrate that the deprotonating effect in

strongly alkaline media has an important effect on the catalytic activity of nickel-based compounds, and should be carefully considered in addition to the Fe content, if one would like to develop Ni-based electrocatalysts meant to catalyze the OER at moderate pHs. Correspondingly, at moderate pHs the deprotonation effect plays a key role, such that even Fe-activated NiOOH is poorly active in near-neutral conditions. Our work clearly shows that a catalyst should not be studied separately from its environment; in Ni-based OECs the phase-nature and activity of the catalyst is strongly dependent on the electrolyte properties and therefore such a system should be studied as a whole. Lastly, we showed that there are virtually no structural and functional differences between Ni(Fe)OOH and Ni(Fe)-B<sub>i</sub>,

Overall this thesis demonstrates different strategies towards the understanding and improvement of the water oxidation half-reaction realized via electrochemical and photoelectrochemical water splitting, as well as new insights into this process. While the energy transition itself is inevitable, the way we arrive at the new energy landscape is still unknown and yet to be determined. There are several different strategies taking part in this race: direct PEC water splitting, PV + electrolysis, CSP, world-wide electricity grid, CO<sub>2</sub> reduction, NH<sub>3</sub> storage, nuclear fusion etc. Regardless which one prevails, one thing is quite certain: given the future demise of fossil fuels and increasing electrification, (photo)electrochemistry will quite certainly become one of the main technologies of the chemical industry. Therefore, studying the electrochemical and photoelectrochemical splitting of water can be nothing but beneficial for the challenges that lie ahead of us.

## 6. Samenvatting

Onze beschaving staat voor een van de grootste uitdaging in de geschiedenis: de energietransitie. De stijgende vraag naar energie, de beperking van grondstoffen en de klimaatverandering zijn de drie belangrijkste drijvende factoren voor de verandering. Ten eerste wordt verwacht dat de wereldbevolking blijft toenemen, en veel arme landen zullen naar verwachting een snelle economische ontwikkeling ondervinden in de nabije toekomst, dat vraagt om de verdere groei van de wereld-energievoorziening. Ten tweede, de fossiele brandstoffen, de ruggengraat van de huidige energie infrastructuur, waarvan de hoeveelheid nog steeds voldoende is voor de komende decennia, zijn beperkt. Bovendien leidt het verbranden van deze fossiele brandstoffen tot een wereldwijde klimaatverandering, wat een grote bedreiging is voor de mensheid zoals we kennen in ecologische, economische, politieke en sociologische termen. Het overgaan van fossiele brandstoffen naar een hernieuwbare, schone en duurzame energiebron als de zon, is dus zowel noodzakelijk als onvermijdelijk.

Het oogsten van zonne-energie brengt verschillende wetenschappelijke en technische uitdagingen met zich mee, het belangrijkste is de onderbreking van de zon. De tijdelijke, dagelijkse en seizoensgebonden variabiliteit van het zonlicht eist voor een opslag oplossing, zodat de zonne-energie die geoogst wordt tijdens de zonnige dagen kan op aanvraag worden vrijgegeven om een constante levering van elektriciteit te voorzien. In dit proefschrift onderzoeken we foto-elektrochemische (PEC) watersplitsing als een mogelijke oplossing voor de conversie en opslag van zonne-energie in chemische brandstoffen. PEC-watersplitsing zorgt voor een directe conversie van zonne-energie in chemische energie via de productie van waterstof. Deze aanpak maakt de duurzame productie van zonne-brandstoffen uit alleen water en zonlicht mogelijk, en biedt daarmee een route naar een koolstofvrije economie.

Watersplitsing met behulp van zonlicht kan worden gerealiseerd met PEC cellen, gemaakt van halfgeleidende foto-elektrodes en metaal tegen-elektrodes ondergedompeld in een elektrolytoplossing. De foto-elektrodes vergemakkelijken lichtabsorptie om de ladingdragers te genereren. De ladingdragers worden dan gescheiden en getransporteerd naar de overeenkomstige vaste stof/vloeistof

elektrode/elektrolyt grensvlakken om de oxidatie van water en de reductie halfreactie aan te drijven. Van deze twee halfreacties is de water oxidatie reactie complexer en moeilijker aan te drijven, omdat bij deze halfreactie de overdracht van vier elektronen en vier protonen betrokken is (terwijl voor de productie van waterstof maar slechts twee protonen en elektronen nodig zijn), en deze halfreactie heeft drie verschillende tussenproducten (slechts één voor waterstof). Het begrijpen en het verbeteren van de zuurstof vormingsreactie (OER) efficiëntie blijft de grootste uitdaging voor de totale watersplitsing. Daarom richten we ons in dit proefschrift op materialen die elektrochemisch en foto-elektrochemisch zuurstof kunnen vormen: foto-anodes van halfgeleider en zuurstof vormingskatalysatoren (OECs) van metaaloxide. Specifiek onderzoeken we bismut vanadaat ( $\text{BiVO}_4$ ), een n-type halfgeleidende foto-anode materiaal, en nikkel oxyhydroxide ( $\text{NiOOH}$ ), een Ni gebaseerde zeer efficiënte OEC.

Ten eerste hebben we een nieuwe techniek ontwikkeld om de oppervlakte- en bulkbeperkingen van  $\text{BiVO}_4$  foto-anodes te verbeteren. We hebben een nieuwe in-situ PEC-techniek geïntroduceerd genaamd “photocharging” (PC), waarbij een foto-anode in een open-circuit configuratie en ondergedompeld in een elektrolyt langdurig blootgesteld wordt aan zonneverlichting. De PC-behandeling levert uitstekende PEC activiteit van  $\text{BiVO}_4$  elektrodes op: hoge fotostroom van  $4.3 \text{ mAcm}^{-2}$  @  $1.23 \text{ V}_{\text{RHE}}$  voor niet gedoteerde en niet gekatalyseerde  $\text{BiVO}_4$ , lage onset potentiaal van  $0.25 \text{ V}_{\text{RHE}}$ , zeer steile fotostroom onset, verbeterde katalytische efficiëntie in een breed potentiaal bereik, verdubbelde fotospanning en sterk verbeterde kwantum efficiëntie (75% extern en 95% intern, gemiddeld in  $440 \text{ nm} > \lambda > 330 \text{ nm}$  bereik) zijn opgenomen. We hebben dus een nieuwe eenvoudige foto-elektrochemische tool gevonden, die gebruikt kan worden na de synthese als een krachtige techniek om de prestatie van water splitsing van (metaaloxide) foto-anodes (nog te bepalen voor andere materialen dan  $\text{BiVO}_4$ ) te kunnen verbeteren.

Ten tweede hebben we onderzocht hoe verschillende elektrochemische omstandigheden de PEC-eigenschappen van  $\text{BiVO}_4$  beïnvloeden, met name de eigenschappen van  $\text{BiVO}_4$  onderworpen aan PC-behandeling. We hebben een sterke correlatie gevonden tussen de pH van de elektrolyt en PEC-eigenschappen: alkalische milieu bevordert het PC-effect terwijl zure omstandigheden verhindert dat het PC-effect zich ontwikkelt. Deze sterke pH afhankelijkheid van het PC-effect wijst op het belang van halfgeleider-vloeistof overgang (SLJ), die zeker een belangrijke rol speelt in

photocharging. Bovendien suggereren onze resultaten dat elke verbeteringen van de bulkgerelateerde functionaliteiten worden bemiddeld door de verschijnselen aan de oppervlakte, en dit benadrukt het belang van de SLJ voor de efficiëntie van PEC toestel.

Om verder inzicht te verkrijgen in het photocharging proces, werden verschillende in-situ en operando spectro-elektrochemische technieken gebruikt om  $\text{BiVO}_4$  foto-anode te onderzoeken. Onze resultaten suggereren dat PC is gerelateerd aan een verandering van SLJ aangedreven door licht, wat bij alkalische omstandigheden de voorkeur heeft. Deze veranderingen resulteren in de vorming van  $\text{BiVO}_4$  oppervlakte met een superieure activiteit voor OER, dat wil zeggen lagere overpotentiaal is vereist om de reactie aan te drijven en de efficiëntie is verbeterd. De UV-vis, XPS en XAS resultaten suggereren dat deze veranderingen de volgende kunnen zijn: de vorming van extra hydroxyl groepen op het oppervlak, de intercalatie van waterstof, de vorming van zuurstof vacancy, en de reductie van vanadium deeltjes op het oppervlak van 5+ naar 4+. Deze verschijnselen zijn onafhankelijk aangetoond om donor dichtheid te verhogen en veroorzaakt de verschuiving van de Fermi-niveau richting de rand van de geleidingsband – gunstig vanuit het oogpunt van water splitsing efficiëntie en zichtbaar in onze elektrochemische impedantie spectroscopie (EIS) en PEC resultaten. Volgens onze EIS-studie, de PC-behandeling zorgt ervoor dat een capacitieve laagje gevormd wordt op het oppervlak van de elektrodes. Een dergelijk capacitieve laagje heeft het vermogen om de foto-gegenereerde elektronengaten op te vullen, de onderdrukte oppervlakte-recombinatie te kunnen bevorderen en kan dus leiden tot een verbeterde oxidatie van water. De PC-mechanisme blijkt een combinatie te zijn van verschillende verschijnselen die de OER-eigenschappen van  $\text{BiVO}_4$  superieur laat stijgen.

Naast het onderzoeken van photocharging van  $\text{BiVO}_4$ , hebben we ook geprobeerd om nieuw inzicht te verkrijgen in het mechanisme van wateroxidatie op  $\text{Ni(Fe)OOH}$  katalysator door gebruik van verschillende in-situ spectro-elektrochemische technieken. Onze resultaten stellen voor dat  $\text{Ni(Fe)OOH}$  negatief geladen wordt voorafgaand aan OER. Wij geloven dat deze geladen plekken op de katalysator oppervlakte uitgangsstoffen zijn van OER. Voor zover wij weten is dit het eerste experimentele bewijs van “actieve zuurstof” deeltjes in  $\text{Ni(Fe)OOH}$ . Bovendien stellen we voor dat de vorming van deze “actieve zuurstof” plekken plaatsvinden via deprotonatie proces. Onze SERS gegevens geeft geen eenduidige toewijzing van de

chemische identiteit van deze deeltjes, maar het suggereert peroxidisch of superoxidisch aard. We waren dus in staat om het algemene begrip van het mechanisme van OER op Ni(Fe)OOH te verbeteren.

Vervolgens hebben we gekeken naar de invloed van elektrolyt op de efficiëntie en mechanisme van OER op Ni(Fe)OOH. Onze elektrochemische gegevens hebben duidelijk aangetoond dat sterke alkalische omstandigheden de katalytische activiteit stimuleren (lage Tafel-helling) en ook de thermodynamica positief beïnvloeden (lagere onset potentiaal en lagere potentiaal voor  $\text{Ni}^{2+}/\text{Ni}^{3.x+}$  transitie). We geloven echter dat in een gematigd alkalische pH's ( $\text{pH} < 10$ ), dit remmend effect voornamelijk is vanwege de preferentiële adsorptie van  $\text{BO}_3^{3-}$  op het oppervlakte van de katalysator. Bij hoge alkalisch pH's ( $\text{pH} > 11$ ), de aanwezigheid van boraat anionen lijkt geen rol meer te spelen. Belangrijker nog, als we kijken naar onze elektrochemische en SERS gegevens, dan zijn we in staat om de hoge OER activiteit in hoge pH's te correleren aan de vorming van de "actieve zuurstof deeltjes". Deze resultaten tonen duidelijk aan dat het deprotonatie effect in sterk alkalische media een belangrijk effect heeft op de katalytische activiteit van nikkel gebaseerde verbindingen, en moet naast het Fe-gehalte zorgvuldig overwogen worden als men Ni gebaseerde elektro-katalysator voor OER bij gematigd pH wil ontwikkelen. Bij gematigd pH's speelt het deprotonatie effect een belangrijke rol, zodanig dat FE geactiveerde NiOOH zwak actief is in bijna neutrale omstandigheden. Ons werk laat duidelijk zien dat een katalysator niet los van zijn milieu moet worden bestudeerd; in Ni gebaseerde OECs, de phase-nature en de activiteit zijn sterk afhankelijk van de elektrolyt eigenschappen en daarom moet een dergelijk systeem in zijn geheel worden bestudeerd.

Ten slotte hebben we laten zien dat er vrijwel geen structurele en functionele verschillen zijn tussen Ni(Fe)OOH en Ni(Fe)-B<sub>i</sub>. De SERS, UV-vis, XAS, XRD en XPS data suggereren dat de Ni-B<sub>i</sub> systeem nauwelijks onderscheidbare tegenhangers heeft in de Ni(OH)<sub>2</sub>/NiOOH systeem. Bovendien vertonen Ni(Fe)OOH en Ni(Fe)-B<sub>i</sub> bijna identiek elektrochemisch gedrag naar OER. Daarnaast konden we geen overtuigend bewijs vinden voor het belang van boor, aanwezig in de structuur van Ni(Fe)-B<sub>i</sub>. Daarom stellen we op basis van de experimentele data verzameld gedurende dit werk voor dat Ni(Fe)-B<sub>i</sub> en Ni(Fe)OOH chemisch hetzelfde zijn, namelijk vormen van NiOOH.

Dit proefschrift toont verschillende strategieën aan voor het begrijpen en het verbeteren van de water oxidatie half-reactie via elektrochemische en foto-elektrochemische watersplitsing, en ook nieuwe inzichten in dit proces. Hoewel de energietransitie onvermijdbaar is, de manier waarop wij de nieuwe energielandschap bereiken is nog niet bekend en moet nog bepaald worden. Er zijn diverse strategieën die deelnemen aan deze race: directe PEC-watersplitsing, PV + elektrolyse, CSP, wereldwijde energienet, CO<sub>2</sub>-reductie, NH<sub>3</sub> opslag, kernfusie etc. Ongeacht welke leidt, één ding is vrij zeker: gezien de toekomstige ondergang van fossiele brandstoffen en toenemende elektrificatie, (foto-)elektrochemie zal zeker een van de belangrijkste technologieën van de chemische industrie worden. Daarom zal het bestuderen van elektrochemische en foto-elektrochemische splitsing van water, zeer waarschijnlijk gunstig zijn voor de uitdagingen die voor ons liggen.



## 7. Acknowledgements

Completing a PhD is not something that comes easy. And while there's only a single name on the cover, there's a large group of people that make the final success possible. Here I take a brief moment to acknowledge everyone that participated in my Delft journey.

First and foremost, I want to thank **Wilson**, the best boss one could possibly imagine. It's been quite of a ride and I wouldn't have made it without all your support and motivation! Thanks for all the patience when confronted with missed deadlines, thanks for all time invested in teaching me about the solar water splitting (and more!), thanks for always giving me a kick of positivity! Secondly, a big thanks to **Bernard**, for teaching me about what being a real scientist means, for being critical when necessary and for challenging me to questioning my own ideas. Next, huge thanks to **Herman and Joost**; you made our labs work like a charm! A lot of my experiments wouldn't have been possible without your help! Also big thanks to all the other support staff in ChemE: **Ruben, Marcel, Ben, Bart, John, Jan, Nayyar and Edwin. Heleen** – you were always of great help with all the administration affairs, working behind the scenes. Thank you for all the warmth and help, thank you so much! And in case of emergency I could always count on **Wiel, Noortje or Rajshree** - thanks! It was a great privilege to be a part of a group with so many great minds (and voices!): **Joop, Wim, Hans, Andreas, Fokko and George** – thank you for all the inspiring discussions and jokes! Also special thanks to **Roel**, who hired me and gave the opportunity to come to Delft. Too bad we never actually had a chance to work together! I also want to thank all the great scientists with whom I collaborated or got inspired by: **Sixto, Mark, Dunwei, John, Daniel, Henning, Morgan, Daniel, Heinz, Ib, Wolfram, Shannon, Leif, Kevin, Nathan, Guido, Laurens, Tom, Arjan, Juan, and Monika**. Special thanks to **Alessandro** and the rest of the ESRF crew (**Flo!**), it was a great pleasure working with you! All the 5 times in Grenoble were super inspiring and enjoyable!

Without a slightest doubt, now I have to acknowledge **Moreno, Digda and Ma Ming**. You guys were my 3 best friends here and all what we've experienced is legendary! I would need an extra booklet to describe all the stupid jokes we've made over the years. Let me just say: Gei wo kan yi kan ni de...! **Fatwa** – you were like a

lighthouse to me when I joined the group – thanks for teaching me a great deal about PEC and being such an awesome guy! **Divya**, thanks for always being an amazing companion to take a break, drink some coffee and talk about anything! **Diana**, rok w którym byłaś częścią grupy zapisał się złotymi zgłoskami, dzięki! Let me also acknowledge the rest of the MECS team, all the wonderful people that were around me, the old crew: **Petra, Peter, Ruud, Kohta, Arjen, Martin, Lennard, Anca, Tsveta, Qingping, Vijayshankar Dandapani, Christian, Sarmila**, the PEC team: **Marco, Nienke, Kai, Nathan, Anirudh, Vermeer, Marijn, Recep, Kailun, Sanjana, Tom, Dowon**, the photochromic team: **Fahimeh, Steffen, Trang, Giorgio** the nano team: **Jicheng, Tobias, Aaike, Anne, Kostis, Julien**, the battery team: **Bernhard, Yaolin, Audrey** and the most mecsinized students: **Yingying, Jenny, Isaac, Mercedes, Andrea, Melanie, Lucas**. I want to thank all my students for having enough patience to deal with a supervisor like me: **Joppe, Max, Tom, Timo, Eva, Eline, Tetsuro, Gijs, Robbie, Quentin**. Especially big thanks goes to **Tets** who was super helpful with the translation of the Samenvatting! I also want to thank all my friends and colleagues in the other ChemE groups, especially **Roman, Simge, Matija, Manu, Dainius, Elena, Karolis, Serhii, Jos, Wouter, Tomasz, Emma, Maria, Francesca, Yu Bi, Ryan, Damla, The Angry Guy, Jara, Laura, Sumit, Max, Dima, Anping, Piotr, Łukasz, Durgesh, Fabio, Aris, Bengisu, Georgiy, Angie, Ben, Qian**. It was great knowing you! I want to acknowledge all the people that I collaborated with, or simply had some great time with during multiple conferences: **Nishant, Paula, Oscar, Janneke, Rick, Sun-Yun, Isis, Roger, Anthony, Gede, Leo, Felix, Soren, Ieva, Yasmine, Ben, Sandheep, Isaac, Ewa, Carolin, Marlene, Saim**. I also want to acknowledge all the people that I lived together with, during my Delft era: **Roy, Shiromani, Maria, Davide, Julian, Fai-Tong, Merve, Trista, Elke, Danbi, Jay, Giorgio, Kuan-Ling, Mengchu, Michael, Marta, Noemi, Mike, Eva, Caterina, Belen, Carme, Anastasia, Luka, Dasha**. You made my stay a lot more fun and there are many stories that we share together! Dancing was a big part of my life throughout all those years, so let me acknowledge some of my friends from the SoSalsa society: **Michiel, Tamara, Didi, Rebecca, Eline, Linde, Marijn, Diego, Ana, Marius, Dylan, Karolis, Murali, Daniel, Jeroen, Jason, Joy, David, Ravi, Dhruva, Aydin, Chiwei, Jan, Ignacio, Terrie, Sofia, Rebecca, Marielle, Verena, Eline, Guusje, Vicki, Regina, Milena, Vivian, Areti, Melody, Dilara, Louise, Arnela, Daphne, Suzan, Suzana, Aurinke, Zsofi**. Another important part of my life was climbing, and there's a number of people that helped me to grow as a climber: **Kuba, Mani, Adam, Chris, Peter, Joane, Roos, Sinai, Tim, Jara, Monika**,

**Weronika, Mateusz, Ola, Magda, JD** and again **Roman, Ryan and Frank**. There were also a lot of other friends that made my time in Delft so memorable: **Frank, Michelle, Cathy, Laura, Anja, Antia, Cora, Gaby, Anna, Charlie, Marijke, Tomiris, Ilaria, Marlijn, Andrea, Eliza, Alex, Adonia, Mandar, Michał**. Huge thanks, lots of love and kisses for my girlfriend **Chara** who gave me a lot of motivation to finalize this endeavour! Ela! Daxi! Filakia! Na koniec parę słów po polsku. Dzięki **Wojtek**, że jak wpadałem to zawsze gdzieś uderzaliśmy w tango. Dzięki wszystkim ze starej paczki, że jeszcze się trzymamy: **Winiak, Olo, Bizon, Banan, Mierzwa, Ble, Ola, Ania, Basia, Danusia, Graszka, Kinga, Misia, DKC, Paweł**. Dzięki mojej rodzinie: **Babci, Basi, Markowi, Mateuszowi**. Dzięki **Brat** że żyjesz, tym razem obeszło się bez Twojej pomocy ;) Dzięki Wam kochani **Rodzice** za wszystko!

## 8. List of Publications

- (1) Lamm, B.;\* **Trzeźniewski, B. J.**;\* Döscher, H.; Smith, W. A.; Stefik, M. Emerging Postsynthetic Improvements of BiVO<sub>4</sub> Photoanodes for Solar Water Splitting. *ACS Energy Lett.* **2018**, *3*, 112–124, \*equal contribution
- (2) **Trzeźniewski, B. J.**; Digdaya, I. A.; Nagaki, T.; Ravishankar, S.; Herraiz-Cardona, I.; Vermaas, D. A.; Longo, A.; Gimenez, S.; Smith, W. A. Near-Complete Suppression of Surface Losses and Total Internal Quantum Efficiency in BiVO<sub>4</sub> Photoanodes. *Energy Environ. Sci.* **2017**, *10*, 1517–1529.
- (3) **Trzeźniewski, B. J.**; Smith, W. A. Photocharged BiVO<sub>4</sub> Photoanodes for Improved Solar Water Splitting. *J. Mater. Chem. A* **2016**, *4*, 2919–2926.
- (4) **Trzeźniewski, B. J.**;\* Diaz-Morales, O.;\* Vermaas, D. A.; Longo, A.; Bras, W.; Koper, M. T. M. M.; Smith, W. A. In Situ Observation of Active Oxygen Species in Fe-Containing Ni-Based Oxygen Evolution Catalysts: The Effect of pH on Electrochemical Activity. *J. Am. Chem. Soc.* **2015**, *137*, 15112–15121, \*equal contribution
- (5) Nesbitt, N. T.; Ma, M.; **Trzeźniewski, B. J.**; Jaszewski, S.; Tafti, F.; Burns, M. J.; Smith, W. A.; Naughton, M. J. Au Dendrite Electrocatalysts for CO<sub>2</sub> Electrolysis. *J. Phys. Chem. C* **2018**, acs.jpcc.8b01831.
- (6) Digdaya, I. A.; **Trzeźniewski, B. J.**; Adhyaksa, G. W. P.; Garnett, E. C.; Smith, W. A. General Considerations for Improving Photovoltage in Metal–Insulator–Semiconductor Photoanodes. *J. Phys. Chem. C* **2018**, acs.jpcc.7b11747.
- (7) Digdaya, I. A.; Adhyaksa, G. W. P.; **Trzeźniewski, B. J.**; Garnett, E. C.; Smith, W. A. Interfacial Engineering of Metal-Insulator-Semiconductor Junctions for Efficient and Stable Photoelectrochemical Water Oxidation. *Nat. Commun.* **2017**, *8*, 15968.
- (8) Ma, M.; **Trzeźniewski, B. J.**; Xie, J.; Smith, W. A. Selective and Efficient Reduction of Carbon Dioxide to Carbon Monoxide on Oxide-Derived Nanostructured Silver Electrocatalysts. *Angew. Chemie Int. Ed.* **2016**, *55*, 9748–9752.

- (9) Szilágyi, P. Á.; Westerwaal, R. J.; Lansink, M.; van Montfort, H. I.; **Trześniewski, B. J.**; Garcia, M. V.; Geerlings, H.; Dam, B. Contaminant-Resistant MOF–Pd Composite for H<sub>2</sub> Separation. *RSC Adv.* **2015**, *5*, 89323–89326.
- (10) Kumar, N.; Abdi, F. F.; **Trzesniewski, B.**; Smith, W. A.; Planken, P. C. M.; Adam, A. J. L. Investigation of Terahertz Emission from BiVO<sub>4</sub>/Au Thin Film Interface. *J. Infrared, Millimeter, Terahertz Waves* **2015**, *36*, 1033–1042.
- (11) Szilágyi, P. Á.; Weinrauch, I.; Oh, H.; Hirscher, M.; Juan-Alcañiz, J.; Serra-Crespo, P.; de Respinis, M.; **Trześniewski, B. J.**; Kapteijn, F.; Geerlings, H.; *et al.* Interplay of Linker Functionalization and Hydrogen Adsorption in the Metal–Organic Framework MIL-101. *J. Phys. Chem. C* **2014**, *118*, 19572–19579.

## 9. Curriculum Vitae

Bartek Trześniewski was born on 17 October 1987 in Kraków, Poland, to Piotr Trześniewski and Maria Trześniewska (née Dąbrowa), both chemists. He attended the Jan III Sobieski High School in Kraków. In 2011 he graduated from AGH University of Science and Technology in Kraków, with a degree of Bachelor of Science, majoring in Materials Science and Engineering and earning Diploma Summa Cum Laude. He completed his graduation project, Design of a micro-thermogravimetric apparatus for high temperature corrosion tests in water vapour environments, under the supervision of Prof. Zbigniew Grzesik. He followed with master studies at AGH and in 2012 he graduated with a degree of Master of Science in Materials Science and Engineering, with a Specialization in Functional Materials, earning Diploma Summa Cum Laude again. He completed his graduation project, Monolithic thermoelectric heat flux sensor, under the supervision of Prof. Krzysztof Wojciechowski. Additionally, he completed 1 year of extra-curricular bachelor studies in Mathematics and in Computer Science, both at the Jagiellonian University in Kraków. Since 2012 he has been a PhD researcher in the Materials for Energy Conversion and Storage Group at Delft University of Technology, at the Department of Chemical Engineering, working under the supervision of Dr. Wilson A. Smith. During this period, he has been working on designing, synthesis and investigation of materials and devices for solar fuels production, specifically coupling the photo-absorbers and oxygen evolution catalysts for water splitting cells.



